

3309

JNCASR
Acc No. 3309
LIBRARY

De Bony

JNCASR
JNCASR
620.5 P03
3309

Mesoscopic organization and properties of nanocrystals of metals, metal oxides and other materials

A Thesis submitted in partial fulfillment
of the requirements of the degree of
Doctor of Philosophy

By
P. John Thomas



Chemistry and Physics of Materials Unit
Jawaharlal Nehru Centre for Advanced Scientific Research (A Deemed University)
Bangalore – 560 064 (INDIA)
May 2003

620.11

p03

Dedicated to my parents...

Declaration

I hereby declare that this thesis entitled “**Mesoscopic organization and other properties of nanocrystals of metals, metal oxides other materials**” is an authentic record of research work carried out by me under the supervision of Prof. C. N. R. Rao, FRS and Prof. G. U. Kulkarni at the Chemistry and Physics of Materials Unit, Jawaharlal Nehru Centre for Advanced Scientific Research, Bangalore, India.

In keeping with the general practice of reporting scientific observations, due acknowledgement has been made whenever work described here has been based on the findings of other investigators. Any oversight due to error of judgement is regretted.



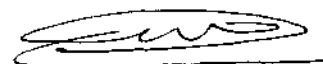
P. John Thomas

Certificate

Certified that the work described in this thesis titled "Mesoscopic organization and properties of nanocrystals of metals, metal oxides and other materials" has been carried out under our supervision at the Chemistry and Physics of Materials Unit, Jawaharlal Nehru Centre for Advanced Scientific Research, Bangalore, India



Prof. C. N. R. Rao



Prof. G. U. Kulkarni

Acknowledgements

The pleasure of doing science under the tutelage of Prof. C. N. R. Rao can hardly be adequately described. Prof. Rao, with his passionate zeal, unbounded exuberance, keen sense of purpose and seemingly boundless frontiers of knowledge set about charting the course of this investigation. He has provided guidance, inspiration and direction to this work. My association with him will always be a source of inspiration to me. Prof. G. U. Kulkarni with his cheery demure, incisive questioning ability and knack for marshalling resources and forging teams has provided guidance and direction to this work. I shall cherish pleasant memories of my association with him. I am indebted to Prof. Rao and Prof. Kulkarni for teaching me the methods of Science.

It is a pleasure to thank Dr. K. V. Sarathy, C. P. Vinod, Dr. P. Saravanan, Dr. M. Rajamathi, Dr. P. V. Vanitha, Dr. S. Berchmans, T. A. Jose and Ved varun agrawal with whom I have collaborated. Many thanks are due to Prof. E. V. Sampathkumar of TIFR (Mumbai) for help with SQUID measurements. I sincerely thank Dr. A. R. Raju for providing several valuable inputs and advice. I thank Prof. J. Chandrasekar, my faculty advisor for providing useful advice.

I am thankful to the faculty members belonging to JNC and the chemical sciences division of the Indian Institute of Science for courses that have been extremely beneficial to this study. In particular, I would like to thank Prof. S. Bhattacharya, Prof. V. Krishnan, Prof. S. Chandrasekaran, Prof. K. L. Sebastian, Prof. S. Yashonath, Prof. T. N. Guru row, Prof. P. Balaram, Prof. M. S. Hegde of IISc and Prof. K. S. Narayan, Prof. S. Natarajan, Dr. A. R. Raju, Dr. N. Chandrabhas, Dr. S. Balasubramanian, Prof. S. Narashiman, Dr. U. Waghmare of JNC.

My labmates, former and present - Hari, CP, Vijay, Neena, Ved and Girish have been instrumental in maintaining a cheery atmosphere in the lab. I thank all of them. I sincerely thank Dr. A. Govindaraj for being very helpful.

The help of Mrs. Usha with TEM, Srinath, Srinivas and Srinivasa Rao with various instruments in Nano lab, Anil with X-ray diffraction, Vasu with TGA and

IR and Basvaraj with SEM and EDAX have been valuable to this study. My ardent thanks are due to all of them. I wish to thank Dr. G. N. Subbana and M. K. Renganathan for help with electron microscopic measurements. I also thank Arokyanathan for assistance at the workshop.

I thank my friends, seniors and colleagues Hari, CP, Mini, Gopalan, Satish, Santhosh, Anupama, Sachin, Gargi, Acharya, Gautam, Neena, Manoj, Biru, Deepak, Sudhee, Pattu, Motin, Swami, Jaya, Balu, Kapoor, Ashish, Vaidhya, Manashi, Vivek and Behera for help and cheerful company.

I am extremely thankful to the staff of complab for maintaining state of the art computing facilities at JNC. I have derived a lot of benefit from it. I thank the former heads of complab Prof. G. U. Kulkarni, Dr. S. Balasubramanian and the current head Dr. U. Waghmare. I also thank the complab personnel, Rajesh in particular for maintaining the facilities in complab.

I am grateful to the administrative and library staff members of JNC for all the help they have provided. I am thankful to Mrs. Shashi, Gowda and Xavier at Prof. Rao's office.

A special note of thanks is due to Lakshmi and Vanitha for making my stay in Bangalore pleasant and memorable.

Among the several teachers who have inspired my pursuit of science, Prof. K. V. Raman and Dr. N. Xavier occupy a prominent place. I offer my sincere thanks to them and all my other teachers.

I wish to express my gratitude to my parents and my brother Paul and sister Bobby for without their support and encouragement, this study wouldn't have been possible.

Preface

The thesis presents the results of investigations on mesoscalar organization and other properties of nanocrystals of metals and metal oxides. Section 1 contains a brief overview of nanocrystals and their mesoscopic organization. The scope of the investigations is described in Section 2. Preparation and characterization of the materials forms Section 3, followed by a discussion of results in Section 4.

Synthetic routes to gram quantities of Co, Ni, Co-Ni alloy particles of sizes 100 – 600 nm as well as of free standing films of Au nanocrystals are described. The role of the particle diameter, and of the ligand chain length in determining the nature of mesoscalar organization in a series of Pd nanocrystals, including magic nuclearity Pd₅₆₁ and Pd₁₄₁₅ nanocrystals is discussed at length. Self-assembly of magic nuclearity Pd nanocrystals into giant clusters, containing a magic number of the original nanocrystals has been investigated. Layer-by-layer assembly of metal and semiconductor nanocrystals capped by thiols is discussed. The ability of core-shell Pd-Ni and Pd-Ni-Pd nanocrystals as well as of γ -Fe₂O₃, Fe₃O₄ and Co₃O₄ nanocrystals to form two-dimensional arrays is examined by means of transmission electron microscopy. Magnetic studies on drop cast films of nanocrystals of γ -Fe₂O₃ as well as on other materials are presented. Interaction of metal nanocrystals capped by thiocarboxylic acids with metal ions has been investigated by means of UV-visible spectroscopy. Scanning tunnelling microscopy and spectroscopy have been employed to study the coulomb blockade in polymer coated Au and Pd nanocrystals of different diameters. An atomic force microscopy based method to pattern metal nanocrystals on flat substrates is presented.

Contents

Declaration	i
Certificate	iii
Acknowledgements	v
Preface	vii
Summary	1
1 Overview of nanocrystals and their assemblies	5
1.1 Introduction	5
1.2 Synthesis of nanocrystals	6
1.2.1 Dispersion methods	7
1.2.2 Reduction methods	7
1.2.3 Shape control	12
1.2.4 Tailoring the ligand shell	13
1.3 Geometric structure of nanocrystals	14
1.4 Electronic properties of nanocrystals	18
1.4.1 Single electron effects in nanocrystals	21
1.5 Optical properties of nanocrystals	23
1.6 Magnetic properties of nanocrystals	28
1.7 Programmed assemblies	33
1.7.1 One-dimensional arrangements	34

1.7.2	Two-dimensional arrays	35
1.7.3	Three-dimensional superlattices	38
1.7.4	Colloidal crystals	39
1.7.5	Collective properties	39
1.8	Emerging applications	41
2	Scope of the Present Investigations	43
2.1	Submicron-sized particles of Co, Ni and Co-Ni alloys	43
2.2	Films of Au nanocrystals at liquid-liquid interfaces	43
2.3	Effect of size on the Coulomb staircase behaviour in Au and Pd nanocrystals	44
2.4	Two-dimensional arrays of Pd nanocrystals	45
2.5	Giant clusters of magic nuclearity Pd nanocrystals	46
2.6	Mesoscopic organization of magnetic nanocrystals	46
2.7	Layer-by-Layer assembly of metal and semiconductor nanocrystals .	47
2.8	Interaction of lipoic acid capped metal nanocrystals with metal ions	47
2.9	Atomic force microscopy based method for patterning nanocrystals	48
3	Experimental and related aspects	49
3.1	Preparation of Nanocrystals	49
3.1.1	Co, Ni and Co-Ni alloy particles	49
3.1.2	Films of Au nanocrystals	50
3.1.3	Pd nanocrystals	51
3.1.4	Pd-Ni nanocrystals	53

3.1.5	Thiolization of Pd and Pd-Ni nanocrystals	53
3.1.6	CdS nanocrystals	54
3.1.7	Pt nanocrystals	54
3.1.8	Au and Ag nanocrystals	55
3.1.9	Magnetic oxide nanocrystals	56
3.2	Characterization of the nanocrystals	57
3.2.1	Transmission electron microscopy	57
3.2.2	Scanning tunnelling microscopy and spectroscopy	58
3.2.3	Atomic force microscopy	58
3.2.4	Scanning electron microscopy and Energy dispersive analysis of X-rays	60
3.2.5	Magnetic measurements	60
3.2.6	X-ray photoelectron spectroscopy	61
3.2.7	X-ray diffraction	61
3.2.8	Other miscellaneous techniques	61
4	Results and Discussion	63
4.1	Submicron particles of Co, Ni and Co-Ni alloys	63
4.2	Films of Au nanocrystals at liquid-liquid interfaces	71
4.3	Effect of size on the Coulomb staircase behaviour in Au and Pd nanocrystals	79
4.4	Two-dimensional arrays of Pd nanocrystals	86
4.5	Giant clusters of magic nuclearity Pd nanocrystals	103
4.6	Mesoscopic organization of magnetic nanocrystals	109

4.7	Layer-by-Layer assembly of metal and semiconductor nanocrystals .	131
4.8	Interaction of metal ions with lipoic acid capped Au and Ag nanoparticles	134
4.9	Atomic force microscopy based method for patterning nanocrystals .	144

Summary

The results obtained from the various investigations that are a part of this thesis are summarized below.

A synthetic scheme based on the polyol process adaptable to prepare a few grams of magnetic submicron sized particles of Co, Ni and Co-Ni alloys has been devised. The diameters of the particles obtained are dependent on the metal ion:reducing agent ratio employed and were tunable in the range of 100 – 600 nm. These particles were rendered air stable by coating them with poly(vinylpyrrolidone) (PVP) during synthesis. The diamagnetic shell of PVP does not have a detrimental effect on the magnetic properties of these particles which continue to exhibit behaviour characteristic of fine particle magnets.

The constrained environs of the interface between two liquids (water and toluene) have been harnessed to synthesize free standing films of nanocrystalline Au. The diameter of the nanocrystals and their coverage in the films are dependent on time of contact between the two liquids and concentration of the reactants. The nanocrystals at the interface are readily extracted into either the aqueous or the organic medium by use of appropriate capping agents such as mercaptoundecanoic acid, dodecanethiol. The hydrosol and the organosol so obtained consist of particles with diameters similar to those at the interface. From the interface, the nanocrystals could readily be transferred to solid substrates such as mica or a polymer film by simply lifting the substrate across the interface. This technique has been extended to obtain granular thin films of Au.

Coulomb staircases in polymer-covered Pd and Au nanocrystals of varying diameters in the 1.7 – 6.4 nm range has been investigated by employing tunnelling conductance measurement. Charging up to several electrons is observed at room temperature in the I-V spectra. Small nanocrystals show charging steps exceeding 200 mV while the larger ones exhibit smaller steps. Significantly, the charging energies follow a scaling law of the form, $U = A + B/d$, where d is the diameter of

Summary

the nanocrystal and A and B are constants. Further, the line widths in the derivative spectra also vary inversely with the diameter.

PVP covered Pd have been made by alcoholic reduction and thiolized (capped with alkanethiols) using a ligand exchange reaction to obtain alkanethiol capped Pd nanocrystals. These monodisperse nanocrystals self-assemble into ordered two-dimensional arrays upon drying on a flat substrate such as a TEM grid. The effect of the nanocrystal diameter (d) and the thiol chain length (ℓ) on the nature of the obtained arrays has been studied by employing Pd nanocrystals with diameters in the range of 1.8–6.0 nm and thiols of varying lengths (butanethiol to hexadecanethiol). A phase diagram based on the d/ℓ ratio has been obtained. It has been found that nanocrystals with the d/ℓ ratios in the range 1.5–3.0 readily form crystalline arrays. These experimental observations are supported by empirical calculations that treat capped nanocrystals as soft spheres. As a part of this study, two-dimensional arrays of magic nuclearity five and seven shelled Pd nanocrystals have been obtained and constitute the first report of arrays obtained from magic nuclearity nanocrystals.

Giant clusters (cluster of clusters) formed by mesoscale self-assembly of PVP covered Pd₅₆₁ nanocrystals have been observed. Giant clusters with one, two, three and five closed shells corresponding to nuclearities of 13, 55, 147 and 561 have been characterized by transmission electron microscopy. This is the first direct observation of giant clusters formed by magic nuclearity nanocrystals. Theoretical work predicting that size effects are probably invariant under scaling are supported by the experimental observation.

PVP covered Pd-Ni core shell nanocrystals with compositions Pd₅₆₁Ni_n ($n = 38, 280, 561, 1500, 3000, 4500$) have been obtained by using magic nuclearity Pd₅₆₁ nanocrystals as seeds. These particles when capped with octane or dodecanethiol, self-assemble into two-dimensional arrays. The arrays of Pd-Ni nanocrystals are well-ordered with the particles containing higher Ni percentage tending to form multilayers. Pd₅₆₁Ni₃₀₀₀ nanocrystals have been further covered with a layer of Pd to obtain nanocrystals of the form Pd₅₆₁Ni₃₀₀₀Pd₁₅₀₀. The three layered Pd₅₆₁Ni₃₀₀₀Pd₁₅₀₀ particles also self-assemble into two-dimensional arrays when

capped with octanethiol. It has been possible to replace the PVP shell of the Pd-Ni nanocrystals with a layer of octylamine and obtain two-dimensional arrays of amine capped particles. A marked change in the nature of assembly is observed with the change in the head group from thiol to amine. The amine capped nanocrystals assemble into regular two-dimensional arrays with higher coverage and exhibit no tendency to form multilayers unlike the arrays obtained with corresponding thiols. A study of the magnetic properties of the Pd-Ni nanocrystals revealed that the magnetic moment scales with Ni concentration. Nanocrystals of metal oxides - γ - Fe_2O_3 , Fe_3O_4 , CoFe_2O_4 and MnFe_2O_4 , Co_3O_4 capped with octylamine have been prepared by thermal decomposition of the metal cupferron complexes in high boiling organic solvents. Co_3O_4 nanocrystals prepared by this method self-assemble into two-dimensional arrays. Close packed arrangements with short range order have been obtained with γ - Fe_2O_3 and Fe_3O_4 nanocrystals. Citrate capped γ - Fe_2O_3 yield exceptionally smooth films when drop cast on Si(100) substrates. In such films, the particles self-assemble with their easy axis of magnetization perpendicular to the substrate. The films, therefore exhibit a perpendicular magnetic anisotropy that depends on film thickness.

Superlattices consisting of arrays of CdS and Pt nanocrystals interspersed with dithiols have been obtained on Au substrates using the layer-by-layer deposition technique. The formation of the superlattices is studied by means of X-ray photoelectron spectroscopy and Scanning tunnelling microscopy. Superlattices consisting of three alternating layers of Pt and CdS nanocrystals have been prepared.

The effect of chelation of metal ions by lipoic acid molecules bound to the surface of Au and Ag nanocrystals have been investigated by studying the plasmon band of nanocrystals. Three distinct regimes of interaction based on the concentration of metal ions have been identified. The regime of low metal ion concentration is associated with reversible chelation and dampening of the plasmon band. Aggregation and irreversible chelation accompanied by an increase in the flocculation parameter characterizes the next regime of intermediate metal ion concentration. The high concentration regime is marked by precipitation. In the low metal ion concentration regime, the rate of dampening of the plasmon band is

Summary

unique and characteristic of a metal ion and does not depend on nature of the nanocrystals or their size.

The water meniscus that forms spontaneously between a scanning atomic force microscopic tip and the substrate has been exploited to form nanostructured patterns of tetrakis(hydroxymethyl)phosphonium chloride capped Au and PVP covered Pd₅₆₁ nanocrystals on mica substrates. The unique features of this study are the findings that the meniscus can indeed be used to transport high molecular mass substances like capped nanocrystals and that the weak noncovalent forces of interaction between the mica substrate and the nanocrystals are sufficient to limit lateral spread of the generated patterns. The latter observation significantly broadens the choice of substrates and nanocrystals amenable to such patterning studies.*

*Papers based on this study have appeared in Bull. Mater. Sci. (2001); J. Phys. Chem. (2003); Chem. Phys. Lett. (2000); J. Phys. Chem. (2000); J. Phys. Chem. (2001); J. Nanosci. Nanotech. (2001); Pramana - J. Phys. (2002); J. Phys. Chem. (1999); J. Phys. Chem. (2002); Pure and Appl. Chem. (2002); Pure and Appl. Chem. (2000).

1. Overview of nanocrystals and their assemblies

1.1 Introduction

Solids owe much of their properties to the order originating from the periodic arrangement of atoms that extends many orders of magnitude higher than the reach of the electrons. The behavior of matter, innately solid but of smaller dimensions, in which the electrons begin to feel the effects of the shorter order, has been a subject of intense research of late. These particles are denoted by several names - clusters, nanoparticles or nanocrystals. Nanocrystals measure a few nanometers in diameter and could contain up to a few hundred atoms. Electrons suffer quantum confinement in such clusters and cause the nanoparticles to behave in a manner distinct from both the constituting atoms and the corresponding bulk. Much of the fascination in nanoscience is due to the fact that nanocrystals and other nano-objects such as tubes and wires possess properties that depend on the size of the system. Size has an active role in determining the electronic, chemical, optical and magnetic properties of nanocrystals.

Clusters of metals are known from ancient times. They were employed to dye glass and fabrics and as a therapeutic aid in treatment of arthritis. Purple of cassius, a popular purple dye in olden days was subsequently found to be made of tin oxide and Au nanocrystals. The secret behind the colour of the Lycurgus cup, a roman glass artifact dated to 4 AD, that appears red in transmitted light and green in reflected light was found to be due to Au and Ag nanocrystals impregnated in glass. The foundation of modern colloid science was laid by Michael Faraday as early as 1857 [1]. He established that several dyes were indeed made of metal particles. After a thorough study of gold sols, Faraday concluded “... *the gold is reduced in exceedingly fine particles which becoming diffuse, produce a beautiful fluid... the various preparations of gold, whether ruby, green, violet or blue... consist of that substance in a metallic divided state*”. Thus, colloidal metal particles in sols came to be known as divided metals. At its inception, the science of colloids did not quite catch popular fancy. It remained the domain of a few

individuals. For example, Ostwald's 1915 book on colloids is titled "The world of neglected dimensions" [2]. Thus, the theoretical works of Mie [3], Gans [4, 5] and Kubo [6] which were successful in predicting the optical properties and electronic structure of metal particles and Einstein's success in relating brownian motion to diffusion coefficient [7] were largely ignored. Heralded by the visionaries such as Feynman [8], the science of colloids staged a gradual revival in the 1980s. Since then, significant advances in both experimental and theoretical aspects have led to a veritable explosion of interest in the areas of nanoscience and nanotechnology and have set the scene for a renaissance in colloid science. The study of nanocrystals and other nanosystems is now called nanoscience. The recent explosion of interest has been so profound that several modern practitioners of nanoscience are not aware of its colloidal ancestry.

1.2 Synthesis of nanocrystals

Clusters are inherently unstable because a large fraction of the constituent atoms are present at the surface. Simple geometrical arguments lead to the approximate expression $6d/D$ for the fraction of atoms at the surface of a nanocrystal [9]. Here, d is the atomic diameter and D , the diameter of the nanoparticle (the expression is valid when $d \ll D$). Thus, Au nanocrystals of ~ 4 nm diameter ($d = 0.23$ nm) have a third of their atoms at their surfaces. Nanoparticles are therefore inherently reactive and possess a natural ability to coagulate to larger particles. Another issue pertinent to synthesis of nanocrystals is size control [10]. It is desirable to limit the distribution in the diameters of the obtained nanocrystals to facilitate the study of the size-dependent properties of nanocrystals. Nanocrystals can in principle be made by two different means:

- By continuous division of matter in bulk (*the dispersion method*)
- By controlled growth of the constituents starting from atoms (*the reduction method*)

1.2.1 Dispersion methods

The breaking down method typically involves evaporation of the bulk metal in high vacuum by resistive evaporation, laser ablation or arc discharge. Nucleation takes place starting from the plume and continues till a solid substrate comes in its way. Control of particle size is achieved by tuning the rate of evaporation and the distance between the substrate and the source of atoms.

The above crude method may be modified by altering the design of the cluster source, for e.g., clusters may be produced by injection of a high pressure inert gas into a cavity containing metal vapor (produced by pulsed laser or arc discharge) and subsequent expansion in the form of a supersonic jet across a narrow nozzle under the right temperature and flow conditions. The emerging beam can be directed to a *time of flight mass spectrometer to analyze the mass of the clusters produced* and also to produce beams of size selected clusters. The problem associated with the deposition of the cluster so produced onto a solid support is the excess Kinetic energy possessed by the clusters in the beam (around 10 KeV for a 5 nm Silver cluster). The dissipation of this kinetic energy after impact on a surface may well involve formation of islands, fragmentation etc. Clusters of noble metals, Pd, Ni, Cu, Zn, Cd and several other metals have been made by the above method. Clusters of GaN and AlN and other semiconducting material can be obtained by reacting the cluster beams *in-situ* with reactive gases such as ammonia.

Soft landing methods involve the nucleation of clusters in a stream of Argon in a low vacuum (10^{-2} torr) followed by landing on a cold substrate covered with a bed of argon. This method yields particles which are more spherical and uniform in size. Cluster beams may also be produced by field emission, particle or photon impacts. The produced cluster beams can also be encapsulated in a polymer or other dielectric material like solid CO₂, SiO₂ or Al₂O₃.

1.2.2 Reduction methods

Reduction methods yield a dispersion of nanocrystals in liquids (the sols) and involve a premium - the need for a ligand shell or a capping layer to

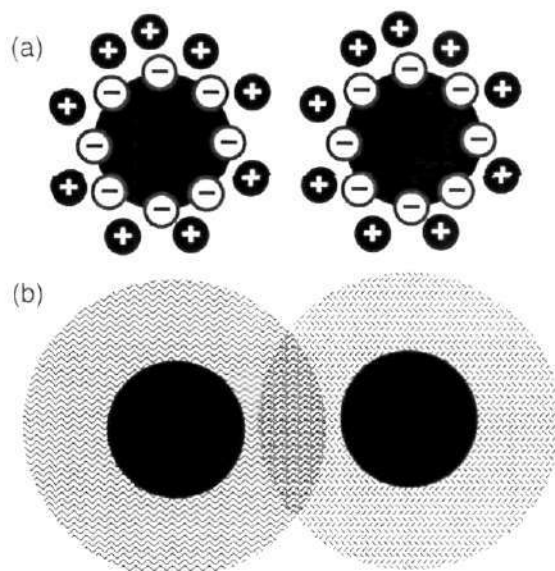


Figure 1.1: Schematic illustration of factors leading to stability to a colloidal dispersion. (a) An electric double layer and (b) the loss of conformational freedom of chain-like ligands

prevent aggregation. Typical ligands or capping agents employed are ionic species like sodium citrate, polymers such as poly(vinylpyrrolidone) (PVP) and poly(vinylalcohol) (PVA), fatty acids, long chain thiols or amines. The details of how a ligand shell stabilizes a nanocrystal are illustrated in Figure 1.1. Sols can be stabilized either by steric or electrostatic forces [10]. Electrostatic stabilization involves the formation of an electric double layer around the nanoparticles. For example, the surface of a Au nanocrystal capped with sodium citrate consists of adsorbed chloride and citrate anions, which attract a layer of cations around them forming a electric double layer with a Coulomb potential, thereby preventing aggregation. The double layer is affected by factors such as ionic strength of the solvent and the temperature. The steric bulk of the ligand shell around a metal cluster can also be useful in stabilizing a colloidal dispersion, especially in organic or non-polar liquids, which do not permit the charge acquisition. van der Waals attraction between metal particles tend to make the nanocrystals come close. When clusters are sufficiently close, the chain like ligands around the particles interpenetrate and suffer a loss in the accessible conformations, making

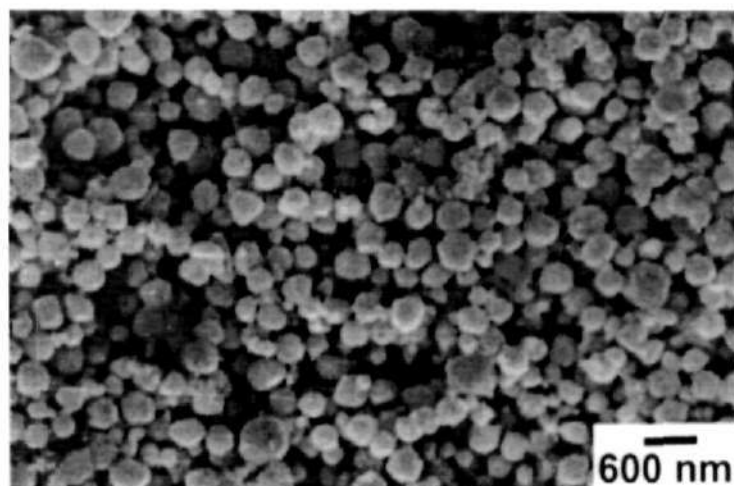


Figure 1.2: Scanning electron microscopic image of Au nanoparticles prepared by the polyol method.

the arrangement entropically unstable. In addition to this, the solvent perceives an increase in the local concentration of the ligands and seeks to get the local concentration on par with the bulk, thereby ripping the particles apart.

The understanding of the above methods of stabilization of clusters have aided in the formulation of many schemes for synthesizing nanocrystals. Nanocrystals of metals can generally be made by controlled reduction of the corresponding metal salts. These reactions rely on two competitive reactions. The first of which is the nucleation and growth of the cluster matter. The other is the reaction between the metal and the ligand. Once the latter proceeds, the metal atom is no longer available for coordination to other species and this reaction on the surface of a growing particle inhibits further growth. A variety of reducing agents have been employed for the reduction of metal salts. These include alcohols, glycols, metal borohydrides and certain specialized reagents such as Li or Na naphthalide and tetrakis(hydroxymethyl)phosphonium chloride. Various metal particles with sizes ranging from a few nanometers to a few microns have been made by the polyol process [11, 12] in which metal salts are reduced with high boiling alcohols such as ethylene glycol (see Figure 1.2). Nanocrystals of various noble and semi-noble metals such as Au, Ag, Pt, Rh, Pd, transition and rare earth metals such as Pb, Gd and Rh have been made employing the above techniques. The fact that these

reactions can be tuned to near perfection to yield monosized clusters has been demonstrated by the making of $[\text{Pt}_{38}(\text{CO})_{44}\text{H}_2]^{2-}$ [10], $\text{Au}_{55}[\text{P}(\text{C}_6\text{H}_5)_3]_{12}\text{Cl}_6$ [13], $\text{Pd}_{561}\text{phen}_{36}\text{O}_{200\pm 20}$ (phen - 1,10-Phenanthroline) [14] and $\text{Pt}_{309}\text{phen}_{36}\text{O}_{\sim 30}$ [10]. Long chain thiols, amines and fatty acids have emerged as capping agents of choice for metal nanocrystals. Semiconductor nanoparticles could be obtained by kinetic control of precipitation reactions [9, 15]. Nanocrystals of inorganic oxides and hydroxides are generally obtained by controlled hydrolysis [16]. CdS, PbS, AgI, CdSe, $\gamma\text{-Fe}_2\text{O}_3$, Fe_3O_4 and other nanocrystals have been obtained. The nanocrystals so obtained are normally capped with ions and possess a broad distribution in diameters. Thermolysis methods involving the decomposition of organometallic precursors in high boiling organic solvents such as Tri-n-octylphosphine lead to a variety of semiconductor and oxide nanocrystals with narrow size-distribution [17, 18]. Nanocrystals obtained by the above route include InP, CdSe, ZnSe, PbSe, $\gamma\text{-Fe}_2\text{O}_3$ and Fe_3O_4 . These nanocrystals are generally capped with long chain organic amines.

Soft-chemical routes

Means of obtaining nanocrystals under near ambient conditions have been gaining in importance in recent times. Micro-organisms such as bacteria and fungi have been harnessed to synthesize both metal and semiconductor nanocrystals [19–21]. Nanocrystals have been made in constrained environments such as surfactant micelles, reverse micelles, vesicles, bi-layers, micro-emulsions, nanoporous alumina [22]. A Reverse or inverted micelle is a particularly elegant template for making nanoparticles [23]. The inverted micelle contains a few droplets of water, in the form of a sphere stabilized by a surfactant in a non-polar medium. Ions when introduced into this system move on to the water pools. Micelles with anions and cations can be prepared starting from the salt of the metal with the surfactant. The surfactants which aid the formation of the micelle are chosen carefully so that they can also bind to the surface of the particles when they are formed in the water pool. Mixing suitable amounts of cationic and anionic micelles yield nanoparticles of semiconductors. Reducing a cationic micelle yields metal nanoparticles. After the

synthesis of the nanoparticles, the dispersion medium (the organic solvent) can be evaporated and the excess surfactant washed away. The radius of the water pool(D), that controls the diameter of the nanoparticle produced is related to W, the ratio of the [H₂O] and [surfactant] as: $D = kW$ where k is a constant obtainable from the phase diagram of the micellar system. For example, the value of k was found to be 0.3 for AOT (Dioctylsulfosuccinate) / heptane system.

Hybrid methods

Several groups have sought to combine physical and chemical means of cluster production in a single synthetic route to nanocrystals. Reetz et al. [24] have produced Pd nanocrystals soluble in a mixture of acetonitrile/tetrahydrofuran by electrolysis of Pd sheet with a electrolyte containing Tetraoctylammonium bromide, the capping agent. In order to obtain nanocrystals in solution, Harfenist et al. [25] steered a mass-selected Ag cluster beam through a toluene solution of thiol and capped the vacuum prepared particles. Alternatively, sols of Au and Ag have also been obtained by laser abalating [26] a metal strip immersed in a solution containing the capping agent. Lasers have been used to alter the size distribution of the nanocrystalline sols [27,28].

Other chemical techniques for the preparation of nanocrystals involve radiolytic or sonochemical reactions [9,29]. Besides the above, hydrothermal routes have also been successfully adapted to synthesise nanocrystals [16].

Single crystals of large clusters

While the dream of obtaining single crystals of nanocrystals still remains elusive, large clusters possessing sol like properties have been obtained as single crystals. Thus, single crystals of clusters such as $\text{Cu}_{147}\text{Se}_{73}(\text{PEt}_3)_{22}$ [30], $[\text{Cd}_{10}\text{S}_4(\text{SPh})_{16}]^{4-}$ [31], $\text{Cd}_{32}\text{S}_{14}(\text{SC}_6\text{H}_5)_{36}\text{DMF}_4$ [31], $\text{Cd}_{17}\text{S}_4(\text{SCH}_2\text{CH}_2\text{OH})_{26}$ [31], $\text{Cd}_{32}\text{S}_{14}(\text{SCH}_2\text{CH}(\text{CH}_3)\text{OH})_{36}$ [32], $\text{Hg}_{32}\text{Se}_{14}(\text{SeC}_6\text{H}_5)_{36}$ [33] have been obtained. The chemical routes to the above clusters are fairly demanding and are not yet adaptable to yield large quantities of such clusters. The optical properties of

the solutions of the above clusters prompt one to wonder at what size of the solute does the dispersion change from solution to a sol.

Purification

Nanoparticles of choice, prepared by any of the chemical methods described above, can be further purified to get rid of impurities or big particles. Removal of unreacted matter or other impurities can be brought about by dialysis through a semipermeable membrane. Poly-dispersity in the sizes of the nanocrystals could be reduced by size selective precipitation. Size selective precipitation is carried out with two miscible solvents, only one of which is capable of dissolving the nanoparticle. To a nanocrystalline dispersion the solvent incapable of dissolving the nanocrystals is added in small quantities. This solvent mixture, induces precipitation of nanoparticles, starting with particles of the largest diameter. By collecting various fractions of nanocrystals at different solvent compositions, size selective precipitation can be effected. Ultra-centrifugation is another means of accomplishing size-selection and purification.

1.2.3 Shape control

The properties of nanocrystals follow from the confinement of electrons to the physical dimensions of nanocrystals and so, it would be interesting to confine electrons to non-spherical shapes and study the properties of the resulting nano-objects. Nanocrystals of different shapes, in addition to spheres have been noticed previously [34]. However, it is only in the recent past that chemical methods of synthesis have become sophisticated enough to yield a reasonable fraction of non-spherical nanoparticles. CdSe nanocrystals in the form of rods, arrows, teardrops and tetrapods have been obtained by careful control of thermolysis conditions such as ratio of surfactant to the reactants and injection volumes [35,36]. Triangular CdS nanocrystals have been obtained by inverse micelle methods [37]. Large tetrahedral Si nanocrystals as exclusive products have been obtained by careful control of the silane reduction conditions [38]. By controlling decomposition conditions, MnS nanocrystals of various shapes such as wires and cubes have been obtained [39].

Nanoscale disks and cubes of Ag have been obtained by a surfactant mediated growth process [40, 41]. Murphy's group has pioneered a solution state method to obtain long nanorods of Au and Ag [42–44]. Their method involves a seed mediated growth of nanocrystals into nanorods and is an easy method to produce large quantities of nanorods. Besides the above, channels of cationic micelles [45] and the polyol process [46] have been adapted to yield nanorods of Au or Ag. Punter et al. [47] have obtained nanorods of Co by carefully decomposing cobalt carbonyl in high boiling organic solvent. Efforts are currently underway to elucidate the properties of such non-regularly shaped particles.

1.2.4 Tailoring the ligand shell

Nanocrystals in their native form are dominated by the surface species - the capping agents employed play an important role in determining the property of the nanocrystals. Hence, in addition to controlling the size and the shape of the nanocrystals it is also necessary to tailor its surface with the right capping agent. In addition to traditional capping agents that include ions, surfactants and polymers, a new breed of ligands- dendrimers, hydrogen bonding fragments of protein, DNA and dyes- with pendent thiol groups as well as silica layers have been used as capping agents [48–50]. In some cases, a layer of a noble metal is used as a buffer between the core nanocrystal and the ligand shell [51]. For example, a layer of gold lends special stability to Fe nanocrystals and helps prevent oxidation and in preserving the magnetic properties of Fe. Coating of a wider band gap material over a semiconductor nanocrystal is known to enhance the light emitting properties of semiconductor nanocrystals [15, 52].

Of special interest with regard to tailoring the ligand shells are reactions that enable the total replacement of one set of ligands with another [53–60]. These reactions also typically enable the transfer of nanocrystals from one phase to another and are accompanied by vivid interchange of colours between the two phases. Ag nanoparticles of 8 nm diameter were transferred from water to cyclohexane by the use of sodium oleate and NaCl [53]. Au₅₅ nanocrystals were transferred from dichloromethane to water by utilizing the ability of triphenylphosphine sulfonate

to displace the initial triphenylphosphine ligands at the surface [10]. Such a transfer has also been accomplished with other ligands [54, 55]. Brown and coworkers found that the phase transfer was accompanied by growth of nanocrystals [54]. A novel method of thiol-derivatizing hydrosols of metal sols such as Au, Ag and Pt has been developed by Sarathy et al. [56, 57]. The procedure involves mixing vigorously a hydrosol containing metal particles of the desired size distribution with a toluene solution of an alkane thiol in the presence of a strong acid or reducing agent. A simple modification of this technique is shown to be effective in the case of CdS nanocrystals [58]. Caruso and co-workers have been successful in transferring different metal nanocrystals from organic to aqueous phase by the use of dimethylaminopyridine as a phase transfer and capping agent [59, 60].

1.3 Geometric structure of nanocrystals

In the reduced dimensions of nanoparticles, forces responsible for packing of atoms are different. Surface tension, the cost of maintaining a surface plays an important role in determining the properties of the nanocrystals. The bond distance typically reduces with the nanoparticle diameter. Further, nanoparticles tend to exhibit faceted structures like tetrahedra, octahedra or their truncated forms like the cuboctahedron (a octahedron truncated by a cube, see Figure 1.3a). These structures can be obtained in a straightforward manner starting from close packed hard spheres. In addition to the above, small clusters adopt icosahedral (see Figure 1.3b) or dodecahedral shapes. These shapes have a five fold symmetry, which is inconsistent with the packing requirements of regular crystalline lattices and therefore involve a loss of the packing efficiency. Atoms in these shapes can still be described starting from crystalline arrangements [61]. For example, the icosahedron which has twenty triangular faces and twelve vertices consists of the following fcc like close packing. Each of the twenty triangular faces of an icosahedron can be considered as a base of a tetrahedron, whose apex is at the inversion center (see Figure 1.4a). A tetrahedron $OA'B'C'$ in Figure 1.4b joining three face centered atoms and an atom at the base of a fcc unit cell has an angle, $\alpha = 60^\circ$. These angles can be distorted to 63.43° , to obtain the tetrahedron (OABC) which forms the building block of

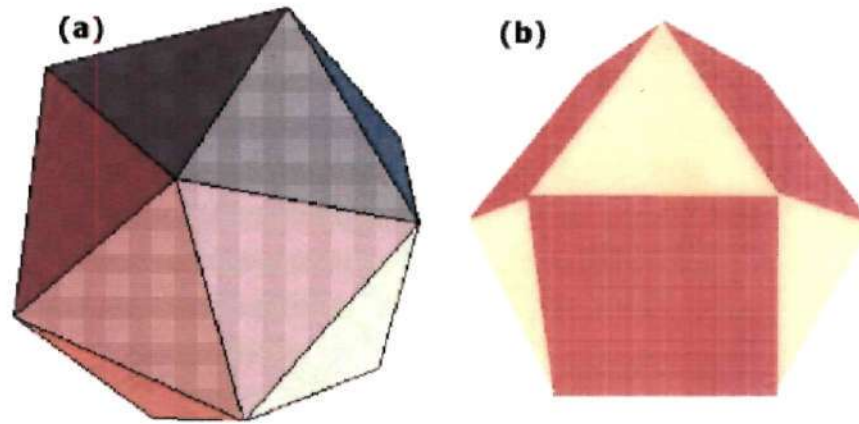


Figure 1.3: Common shapes adopted by small nanocrystals. (a) Cuboctahedron and (b) Icosahedron.

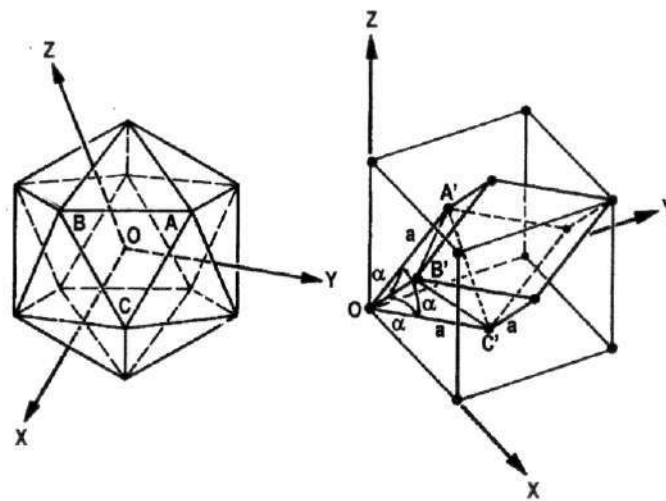


Figure 1.4: The regular icosahedron is made up of twenty irregular tetrahedra like OABX. The rhombohedral cell in a fcc lattice ($OA'B'C'$) has $\alpha = 60^\circ$. When α is distorted to 63.43° , $OA'B'C'$ and $OABC$ become similar. Small nanocrystals distort in a similar manner from regular fcc lattice to adopt the icosahedral shape.

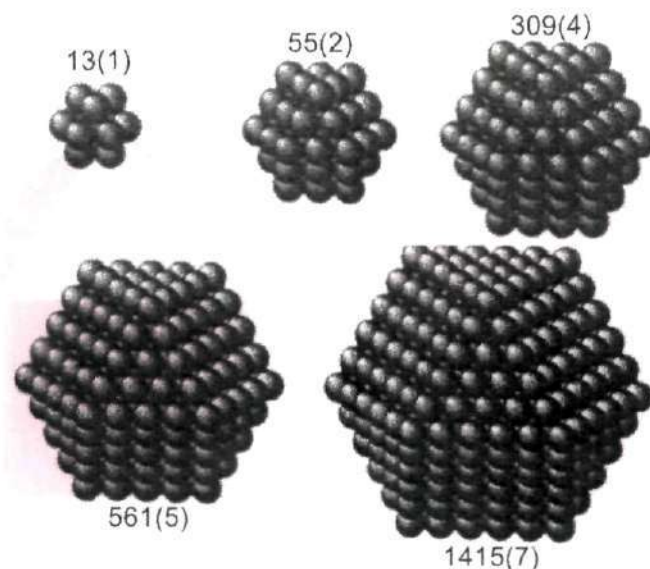


Figure 1.5: Nanocrystals in closed-shell configurations with magic number of atoms. The numbers beside correspond to the nuclearities and the numbers in parenthesis refer to the number of shells.

an icosahedron. Such a distortion reduces the packing fraction from 0.74080 to 0.68818. The unusual preference for this shape by small clusters has been attributed to the surface forces and elastic strain [61]. In a similar manner, a decahedral particle can also be obtained starting from a fcc lattice.

The properties of nanocrystals are additionally influenced by the formation of shells which occur at definite nuclearities. These nuclearities called “magic” endow a special stability to nanocrystals. Nuclear physicist first observed magic nuclearities while studying the nucleus and proposed an explanation assuming a spherical shape for the nucleus. These theories have since been discarded by them but their adapted versions continue to be useful in describing the structure of metal clusters and provide a rational basis for the shell structure observed in metallic and non-metallic clusters [62]. The magic nuclearities depend on the packing adopted by the solid, but are the same for the cases of the bcc and fcc solids and are illustrated in Figure 1.5. Nanocrystals with fully filled shells are special in many ways and are similar to atoms that have reached an outer shell octet configuration. For example in a recent study, Boyen et al. [63] found that magic nuclearity Au_{55} nanocrystals

are specially stable and are not amenable to oxidation, even under conditions where bulk Au is oxidized.

Magic nuclearity alkali metal nanocrystals with 13, 55 and higher nuclearity have been generated using cluster beam methods [62]. Chemical routes leading to magic nuclearity metal nanocrystals have been reported [10]. Schmidt et al. have successfully made Au, Pt, Ru and Rh sols consisting of 55 metal atoms and have assigned them the formula $M_{55}[PPh_3]_{12}Cl_6$. This cluster has an icosahedral shape and has two shells. Schmid has also made $Pt_{309}phen_{36}O_{\sim 30}$ [10] cluster consisting of four completed shells. $Pd_{561}phen_{36}O_{200\pm 20}$ was first made by Zamareev et al. [14]. It consists of five full shells. All the above clusters are believed to have an icosahedral shape. Sols consisting of these nanocrystals exhibit more stability than other sols and can be distinguished from other sols containing polydisperse nanocrystals.

It is expected that closed shell configurations can extend in dimensions to reach superclusters - giant clusters made up of clusters and beyond. Thus, closed shell configurations lend stability to a cluster of clusters, the giant cluster, and a cluster of giant clusters. So, the formation of superclusters by condensation of clusters could be similar to that of fractal growth - invariant under scaling.

Structure determination of the colloidal crystallites should ideally follow from X-ray diffraction, but small particles do not diffract well owing to limited size and as mentioned before, do not crystallize. Structural studies have therefore been based on HRTEM (High resolution transmission electron microscopy), EXAFS (Extended X-ray absorption fine structure) and STM (Scanning tunnelling microscopy).

HRTEM with its ability to image atomic distributions in real space has emerged as a popular method. After extensive TEM studies, it is now fairly well established that the larger metal particles, (radius > 3.0 nm) follow the bulk metal structure i.e., they are essentially silhouettes of the bulk metal. The preference of small clusters to adopt a icosahedral structure has been directly observed and evidence for twinning required to transform a crystalline arrangement to an icosahedron has been also obtained [61]. It has been possible to simulate the images observed by

HRTEM [64, 65]. Characterization by TEM, however, has its own problems: the ligands are stripped from the clusters under the beam, the high energy of the beam could induce phase transitions, dynamic events under the beam like quasi-melting, lattice reconstructions have been observed [66]. Multiple twinning exhibited by nanocrystallites makes structural elucidation difficult. The fact that ligands desorb from the clusters has made this technique unsuitable to follow events like the change in atomic packing with the change in the ligand shell. For example, the Pd₅₆₁ cluster is known to show different structure when OAc⁻ ligands are replaced with PF₆⁻ ligands.

STM though a good probe to look at the sizes and the morphology of the clusters, suffers from the disadvantage of the inability to probe the internal structure of the cluster matter, especially if the cluster is covered with a ligand shell. Reetz et al. have shown that the diameters of nanocrystals obtained by STM includes the thickness of the ligand shell [67] by imaging their electrochemically prepared Pd nanocrystals. EXAFS scores over the other techniques because it provides an ensemble average. HREM, which probes the local structure is an ideal complimentary tool for EXAFS.

It is now apparent from the studies based on the above techniques that the nanoparticles largely follow the bulk crystalline order and are therefore being called nanocrystals. However, in the case of semiconductor and oxide nanoparticles, the above statement is not always true. The nanoparticles prepared by low temperature methods such as arrested precipitation incorporate several defects in the lattice and ion occupancy [17]. Further, the surface structure of these nanoparticles could be different from the corresponding bulk. Amorphous nanoparticles are sometimes obtained by sonochemical and other rapid quenching means [18].

1.4 Electronic properties of nanocrystals

The study of the electronic structure of the nanoparticles has been a focus of intense research. Bulk metal possess a partially filled electronic band and their ability to conduct electrons is due to the availability of a continuum of

energy levels above E_F , the fermi level. These levels can easily be populated by applying an electric field and the electrons now behave as delocalised Bloch waves ($\lambda \sim 5 - 10 \text{ \AA}$) [68]. However when bulk metal is broken down, the continuum of the electronic states breaks down and the sample ultimately becomes insulating. The emerging discreteness of energy levels would not manifest themselves as long as the gap is less than $k_b T$. However the discreteness can be measured in terms of average spacing between the successive quantum levels, δ is given by

$$\delta = \frac{4E_F}{3n} \quad (1.1)$$

and is known as the Kubo gap [6]. Here, n is the number of valence electrons in the cluster (a contribution of one valence electron per constituent atom is assumed). The E_f in the case of semi-conductors is in between two bands, one of which is filled. As the size of the system decreases, the energy levels at the band edges become discrete, with a similar interlevel spacing as in metals. This effectively increases the band gap of the semiconductor. Thus, the Kubo gap is manifest in both metals and semiconductors (see Figure 1.6).

The band gap closure, the emergence of the metallic state from the cluster regime has been followed by techniques such as photoelectron spectroscopy and tunneling conductance measurements. For example, the groups of Chesnovsky [70] and Rademann [71] have studied mass selected Hg clusters by means of photoelectron spectroscopy. They found that a small Hg particle with atoms in the $6s^2 6p^0$ configuration is held together by relatively weak van der Waals forces and is essentially nonmetallic. As the nanoparticle grows in size, the atomic $6s$ and $6p$ levels broaden into bands and an insulator-metal transition appears to occur - driven by the physical dimensions of the individual particle. They found that the size-induced metal-insulator transition takes place when the number of atoms in the cluster is around 400.

Direct information on the gap states in nanocrystals of metals and semi-conductors is obtained by scanning tunneling spectroscopy (STS). This technique provides the desired sensitivity and spatial resolution making it possible to carry out tunneling spectroscopic measurements on individual particles. A systematic STS

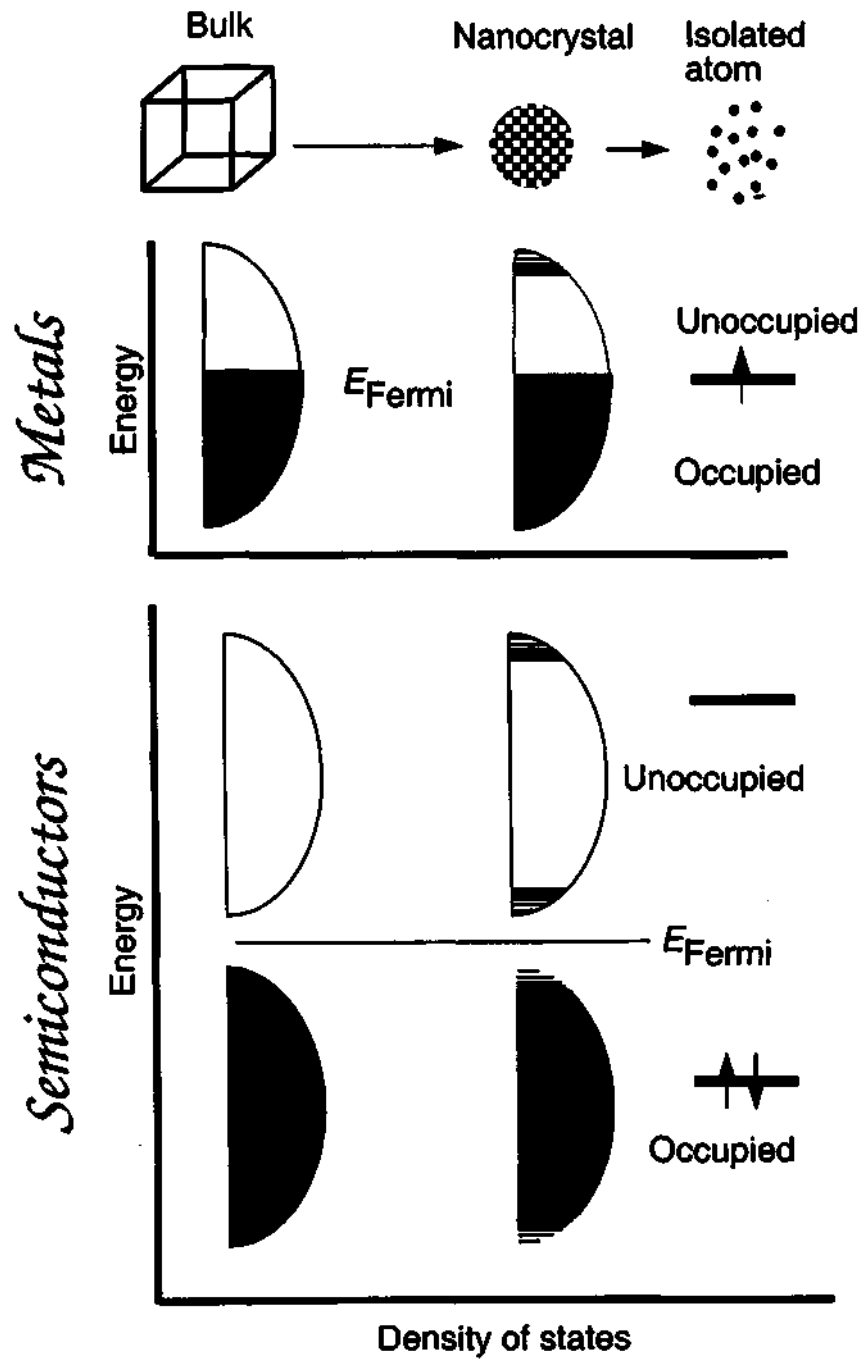


Figure 1.6: Schematic illustration of the density of states for metal and semiconductor nanocrystals.

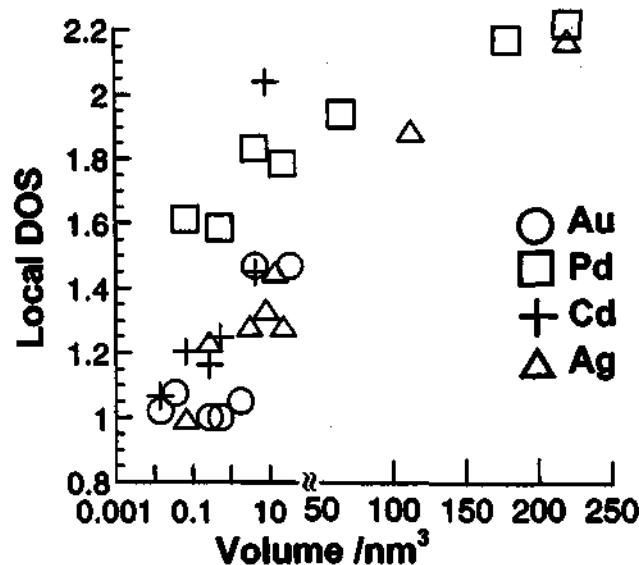


Figure 1.7: Variation of the nonmetallic band gap with nanocrystal size in various metal nanocrystals.

study of Pd, Ag, Cd and Au nanoparticles of varying sizes deposited on a graphite substrate has been carried out under ultrahigh vacuum conditions by C. P. Vinod et al. [72]. They found that I-V spectra of bigger particles were featureless while those of the small particles (< 1 nm) showed well-defined peaks on either side of zero-bias due to the presence of a gap. It was seen that small particles of ~ 1 nm diameter are in fact non-metallic (see Figure 1.7).

Theoretical calculations of the electronic structure of metal and semiconductor nanocrystals throw light on the size-induced changes in the electronic structure. Rosenblit and Jortner [69] calculated the electronic structure of a model metal cluster and predicted electron localization to occur in a cluster of diameter ~ 0.6 nm. In the case of semiconductor nanocrystals, it is shown using tight binding approximation that the band gaps nearly reach the bulk values at sizes of around 5 nm.

1.4.1 Single electron effects in nanocrystals

In a bulk metal, the energy required to add or remove an electron are equivalent and is called its work function. In contrast, in case of a molecule, the correspond-

ing energies, electron affinity and ionization potential are nonequivalent. Since nanocrystals are intermediary, it is expected that two energies differ only to a small extent, the difference being called the charging energy (U). This is a Coulombic energy state and is different from the electronic energy gap. U is dependent on the particle diameter and the chemical identity of the material. The Coulombic states can be similar for both semiconductor and metallic nanocrystals unlike the electronic states [73]. One of the experimental ways of determining the charging energy is from the capacitance of the nanocrystals, which is derived from current-voltage spectra. The capacitance (C) is related to the charging energy U by the relation:

$$C = \frac{U}{2e} \quad (1.2)$$

Small nanocrystals of metals with organic ligand shells acting like a dielectric spacer can exhibit capacitances as low as 10^{-18} F. When electrons are allowed to tunnel through a potential barrier in to the cluster, the capacitance of the cluster changes sufficiently to block the entry of the next electron till an observable change in the potential of the charging field is applied. This leads to the observation of the coulomb gap and the Coulomb staircase in the I-V spectra [74, 75].

For current to flow through a nanocrystal, an external voltage V_{ext} greater than $e/2C$ is required. This phenomena of current exclusion across zero bias is called Coulomb blockade. When the Coulomb blockade barrier is broken applying sufficient voltage, the electrons tunnel into the nanocrystal. Electrons tunneling in thus immediately tunnel to the next junction (residence time ~ 100 ps). This time is however, long enough to provide a voltage feedback to prevent an additional electron from tunneling simultaneously. A continuous one electron current (I) given by

$$I = \frac{e}{2RC_t} \quad (1.3)$$

(C_t is the total capacitance) flows through the circuit. To place an additional electron, a full e/c increase in voltage is required. Thus, steps are visible in the I-V curves and such I-V curves are said to exhibit Coulomb staircase.

Scanning tunneling spectroscopy had been the only method to investigate such phenomena. However, recently Chen et al. [76] demonstrated the use of differential

pulse voltammetry on an ensemble of mass selected Au nanocrystals covered with alkane thiols to follow such events. They observed a transition to molecule like charging in clusters with mass less than 14 kD (diameter ~ 1.2 nm). Since then, numerous electrochemical studies have been carried out. It has been said that minute changes on the surface of the nanocrystal can drastically change the charging energy of the cluster. Oxidation of ferrocene terminated alkane thiols attached to gold clusters were studied using a rotated disk voltametry. The average capacitance was found to increase by a factor of 8 when a redox reaction took place on the surface of the cluster [77]. Electrons stored in these quantum capacitors have been used to facilitate electron transfer reactions [78].

1.5 Optical properties of nanocrystals

The electronic absorption spectra of nanocrystals is dominated by the surface plasmon band which arises due to the collective coherent excitation of the free electrons within the conduction band [79–81]. A schematic illustration of the electric field component of an incoming light wave inducing a polarization of the free or itinerant electrons with respect to the heavier core is shown in Figure 1.8. The species present at the surface of the nanocrystals confine the plasmons and also contribute to altering the direction of polarization. Figure 1.8 corresponds to the dipolar surface plasmon excitation mode which is the most relevant for particles whose diameters are much less than the wavelength of light. However, higher order excitations are possible and come into play for nanocrystals with diameters in the range of tens of nanometers.

As mentioned before, the theory of optical absorption of small particles was proposed by Mie in 1908 [3]. Mie's electrodynamic solution to the problem of light interacting with particles involved solving Maxwell's equations with appropriate boundary conditions and leads to a series of multipole oscillations for the extinction (C_{ext}) and scattering (C_{scat}) cross sections of the nanoparticles. Thus,

$$C_{\text{ext}} = \frac{2\pi}{k^2} \sum_{n=1}^{\infty} (2n+1) \text{Re}(a_n + b_n) \quad (1.4)$$

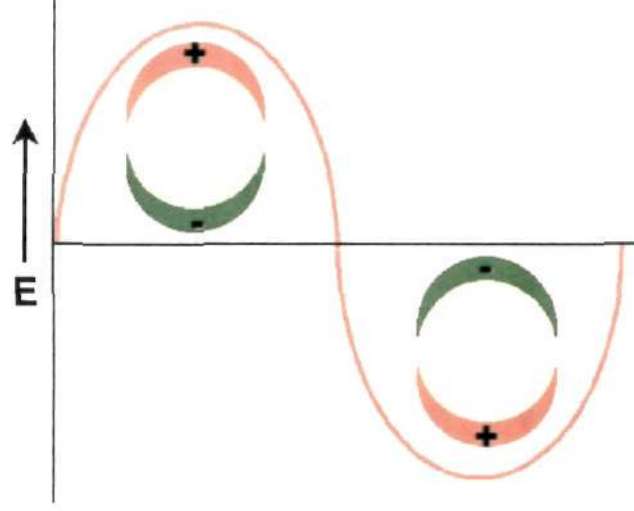


Figure 1.8: A schematic illustration of the excitation of the dipole surface plasmon oscillation by the electric field component of the light wave. The dipolar oscillation of the electrons has the same frequency as that of the incoming light wave.

$$C_{\text{sca}} = \frac{2\pi}{|k|^2} \sum_{n=1}^{\infty} (2n+1) \text{Re}(|a_n|^2 + |b_n|^2) \quad (1.5)$$

where, ϵ_m is the dielectric constant of the surrounding medium, $k = \frac{2\pi\sqrt{\epsilon_m}}{\lambda}$, a_n and b_n are Ricatti-Bessel functions that depend on the wavelength and the nanoparticle radius (R). For small particles, the scattering term and the higher order extinction terms are negligible. So, the extinction coefficient is given by

$$C_{\text{ext}} = \frac{24\pi^2 R^3 \epsilon_m^{3/2}}{\lambda} \frac{\epsilon'}{(\epsilon + 2\epsilon_m)^2 + \epsilon'^2} \quad (1.6)$$

where ϵ and ϵ' are the real and imaginary part of the frequency dependent dielectric constant of the substance. The dielectric constants can either be obtained from the Drude free electron model or from experiments. The Drude model relates the dielectric constant to the bulk plasmon frequency (ω_p) and the dampening frequency (ω_d), which are given by

$$\omega_p = \frac{Ne^2}{m\epsilon_0} \quad (1.7)$$

$$\omega_d = \frac{v_f}{L} \quad (1.8)$$

where N is the concentration of the free electrons, m the effective mass of the electron, v_f the velocity of the electrons at the fermi level and L , the mean free

path. Small particles with diameters comparable to the mean free path exhibit a diameter dependent L , given by

$$\frac{1}{L_{\text{effective}}} = \frac{1}{2R} + \frac{1}{L} \quad (1.9)$$

Thus, metal nanocrystals of various sizes exhibit characteristic colors depending on their diameters. In the case of semiconductor and other particles, the free electron concentration is much smaller and the plasmon absorption band is shifted to the infrared region. Mathematical methods have been developed to accurately compute the higher order terms in Mie's theory [82]. Several off the shelf programs are available to apply Mie's theory and its extensions to a variety of nanoparticles [83]. One such program called "BHCOAT" and presented in the book by Bohren and Huffman [84] is an extremely popular and freely available code.

The fairly complicated nature of the surface plasmon excitation and its dependence on a variety of factors such as the surrounding medium and the distribution in the particle diameters have thwarted attempts to derive fundamental physical quantities and quantitative information about the electronic structure of fine particles based on plasmon resonance spectroscopy. Initial studies such as due to Kreker and Kreibig have been instrumental in verifying the validity of the Mie's theory for noble metal particles such as Au and Ag [85, 86]. Qualitative estimates can however be easily made based on the observed plasmon resonance band. For example, the plasmon band shifts to red with the decrease in the particle diameter (see Figure 1.9). Loose, reversible association of particles (aggregation) blue-shifts the plasmon band.

The peculiar features of the plasmon band - its dependence on the dielectric constant of the surrounding medium and the number of free electron present in the nanocrystals has found interesting uses. It is possible to probe changes taking place in the vicinity of nanoparticles using the plasmon resonance band. Experiments indicate an unusually high sensitivity of the plasmon band intensity to small changes in the surrounding dielectric. Events that alter the surrounding dielectric such as binding of molecules to the ligand shell and the solvent refractive index have been successfully studied using the plasmon resonance band [79, 87, 88]. Chemisorption

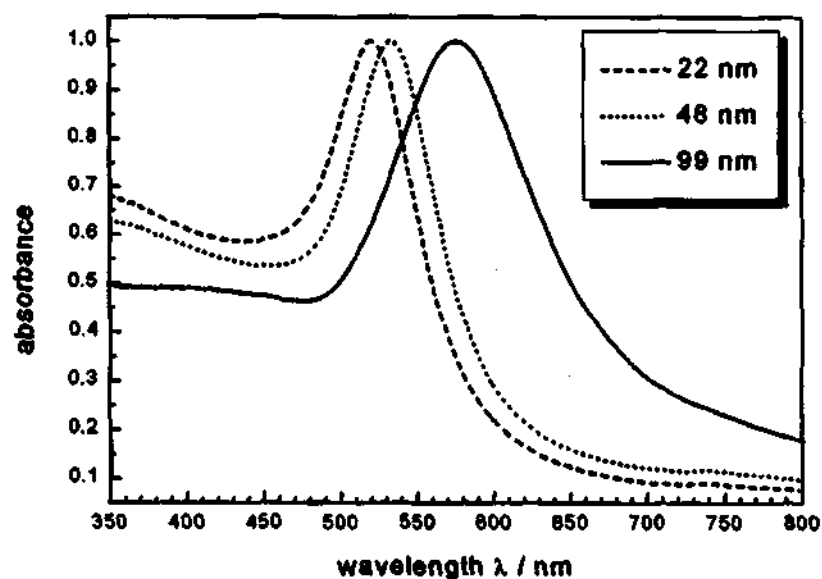


Figure 1.9: Absorption spectra of Au nanocrystals of various diameters.

taking place at the surface of the nanocrystals alters both the surrounding medium dielectric constant and the number of free electrons (by charge transfer), thereby leading to striking changes in the plasmon band [9, 80].

Brus and others recognized the inadequacy of Mie's theory in explaining the electronic absorption spectra of semiconductor nanocrystals and proposed an independent theory to describe the absorption spectra of semiconductor nanocrystals based on the effective mass approximation [89, 90]. They proposed that the absorption band in the visible region is due to excitons. Thus, CdS a yellow solid, exhibits an excitonic absorption around 600 nm, which gradually shifts into the UV region as the nanocrystal diameter is varied below 10 nm. The absorption band can be systematically varied across ranges of a few 100 nm by changing the size of the semiconductor nanocrystal. As an example, the absorption spectra of CdSe nanocrystals of various sizes is shown in Figure 1.10. The excitonic nature of the absorption band permits direct correlation of the band gap of the semiconductor nanocrystal with the absorption edge. In Figure 1.11, the variation of the band gap, derived from the absorption edge as a function of the diameter is

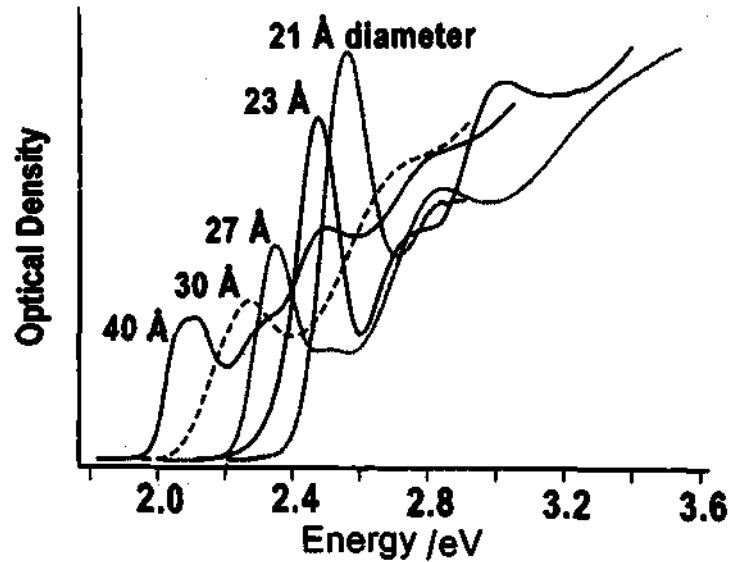


Figure 1.10: Absorption spectra of CdSe nanocrystals of various diameters.

shown. Theories have now grown in sophistication and rigour to include key effects like surface structure and coupling of electronic states and are able to accurately reproduce experimental observations [91, 92]. However, the understanding of the optical properties of semiconductor nanocrystals is still incomplete and careful experiments on monodisperse nanocrystals are currently being pursued to unravel the mystery [15].

In addition to interesting absorption properties, the semiconductor nanocrystals also exhibit luminescent behaviour. The emission from mono-disperse semiconductor nanocrystals such as CdSe is intense, narrow and can be brought about by excitation in a broad range of wavelengths [52]. The emission can be tuned by altering the diameter of the nanocrystal. Further control over the emission can be exercised by varying the surface structure and controlling diameter distribution. The above factors have led to the exploration of a wide range of applications for luminescent semiconductor nanocrystals.

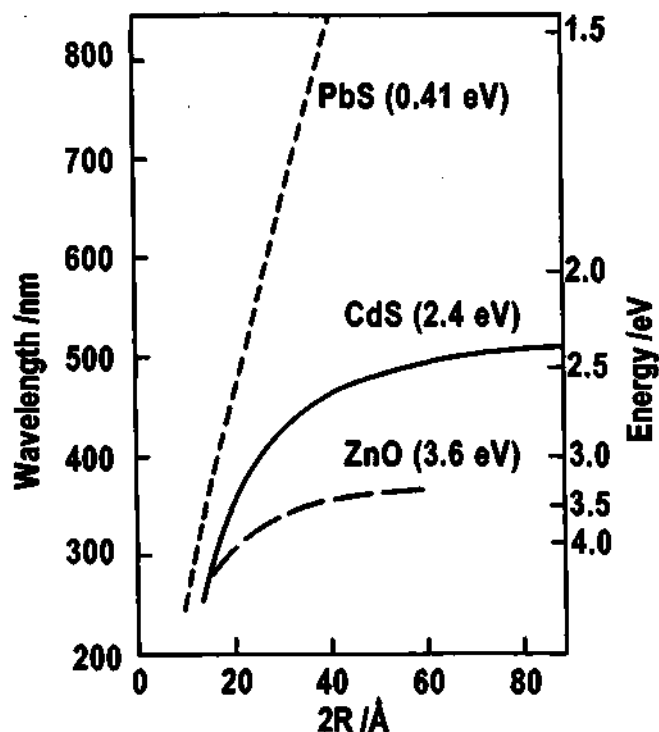


Figure 1.11: Wavelength of the absorption threshold and band gap as a function of the particle diameter for various semiconductors. The corresponding bulk energy gap is given in parenthesis.

1.6 Magnetic properties of nanocrystals

The study of magnetic properties of nanoparticles have a long and colourful history [93–95]. Size effects were perhaps first noticed in magnetic measurements carried out on the so called “fine particles” - particles with diameters in the 10–100 nm range [93]. Much of the attraction towards fine particles is due to their single domain nature, which simplifies the theoretical treatment and leads to experimental understanding.

Magnetizing a sample involves induction of free magnetic poles at its ends. These magnetic poles give rise to a demagnetizing field (H_d) - a magnetic field in a direction opposite that of magnetization, in the sample. H_d is proportional to the intensity of magnetization (I) and is given by the expression

$$H_d = \frac{NI}{\mu_0} \quad (1.10)$$

1.6. Magnetic properties of nanocrystals

where, N is the dimensionless demagnetizing factor. N depends on the shape of the sample and can be calculated exactly only for the cases of ellipsoids [95]. A proper consideration of the demagnetizing fields is essential in understanding the magnetic behaviour of a system. For the case of spherical nanocrystals and their aggregates the value of N is 0.33. Thin films are considered as infinite cylinders and N is 0 when the magnetic field is along either of the long axis.

Materials in general, exhibit strong and often complex anisotropic behaviour when subject to magnetization. The simplest form of anisotropy is the uniaxial anisotropy where the anisotropic energy (E) is only dependent on the angle (θ) the magnetic field vector makes with the easy axis of the sample. The anisotropic energy is expressed in the form

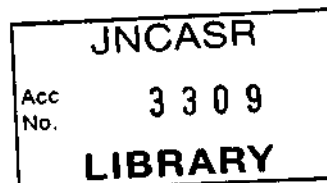
$$E = K_{u1} \sin^2 \theta_0 + K_{u2} \sin^4 \theta_0 + \dots \quad (1.11)$$

Here K_{u1}, K_{u2} are the anisotropy constants. Practically, the K_{u1} term suffices to describe the observed anisotropy. The ideal magnetization curves obtainable at various θ values from samples possessing uniaxial anisotropy is shown in Figure 1.12. Square loops are obtained when the direction of magnetization is parallel to the easy axis and straight line loops are obtained when the field direction is perpendicular to the easy axis direction [94].

In order to understand the size-dependent magnetic properties, it is instructive to follow the changes in coercivity as the size of the nanocrystals is decreased from a few microns to a few nanometers (see Figure 1.13). With the decrease in the diameter, the coercivity (H_c), increases initially till a particular diameter, D_s , and thereafter begins to decrease. The critical diameter, D_s , marks a diffuse region wherein the particle changes from being a multi-domain particle to a single-domain particle. The value of D_s is normally a few tens of nanometers. Below D_s , H_c tends to decrease due to thermal effects and typically follows a relation of the form

$$H_c = g - \frac{h}{D^{3/2}} \quad (1.12)$$

where g and h are constants [96]. Below a critical diameter D_p , the coercivity becomes zero as the thermal energy is now sufficient to demagnetize the particles.



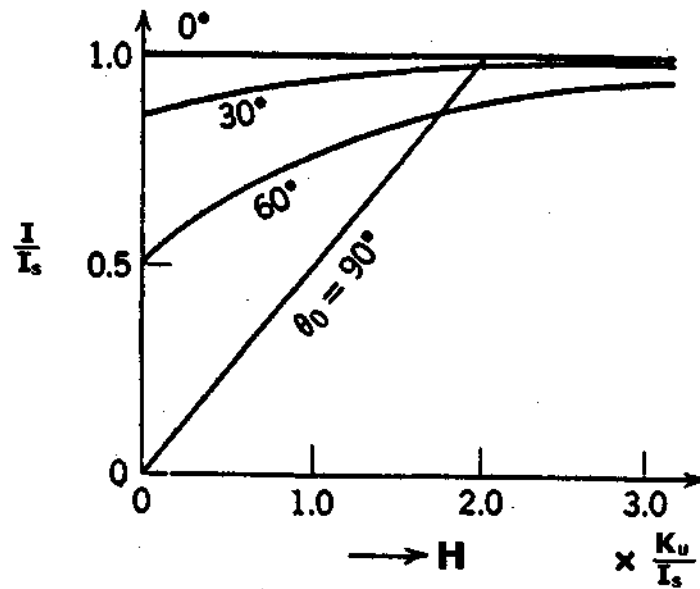


Figure 1.12: Magnetization curves obtained at various θ values from sample possessing uniaxial anisotropy.

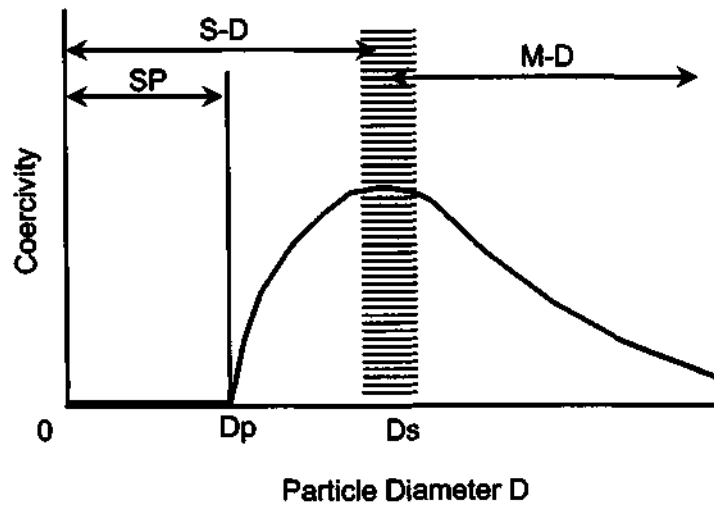


Figure 1.13: Schematic illustration of the changes in the coercivity of a magnetic particle with change in the diameter. SP denotes the superparamagnetic regime, S-D the single-domain regime and M-D the multi-domain regime.

Nanocrystals below a critical diameter, D_p (~ 10 nm) exhibit such behaviour and are said to be superparamagnetic. Each of the above critical regimes adopt different paths to the magnetized state. The paths leading to magnetized state are often complex and not well understood [96].

Superparamagnetic behaviour, as indicated before is caused by thermal flipping of the anisotropic barrier to magnetization reversal. Below a certain temperature called blocking temperature, the temperature induced flipping or relaxation can be arrested and the nanocrystals acquire a finite coercivity. The superparamagnetic behaviour was first modelled by Neel in the 1950s [97]. For the case of nanoparticles with uniaxial anisotropy, Neel's theory suggests that the temperature induced relaxation (τ_N) varies exponentially with temperature and scales with the sample volume (V) in the following manner:

$$\tau_N^{-1} = \tau_0^{-1} e^{-\alpha} \quad (1.13)$$

where,

$$\alpha = \frac{K_{ul} V}{k_b T} \quad (1.14)$$

τ_0 , is a pre-exponential factor that involves the young's modulus, the demagnetization factor and the gyromagnetic ratio. Though the simple scaling with volume suggested by Neel's theory is largely followed in the uniaxial cases, the actual blocking behaviour of magnetic nanocrystals, especially those of the oxides are quite complicated. Effects such as those due to the ligand shell and lattice defects are thought to be responsible for the observed deviation.

Experimentally, superparamagnetism may be probed by a variety of techniques such as Neutron scattering, Mössbauer spectroscopy, magnetization and susceptibility measurements. It is to be noted that each of these techniques have a characteristic timescale of measurement and can therefore indicate a different blocking temperature.

In addition to superparamagnetic behaviour, nanocrystals possess other size dependent magnetic properties such as enhanced atomic magnetic moments and

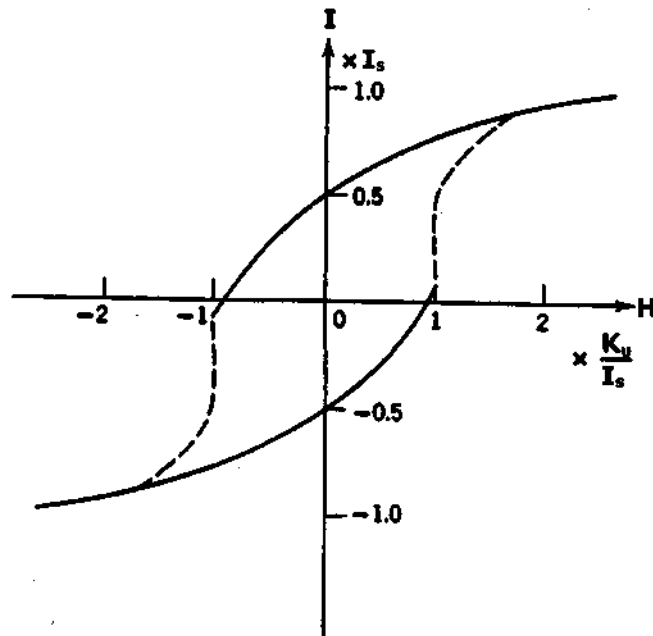


Figure 1.14: Magnetization curve of an aggregate of single domain fine particles with uniaxial anisotropy.

higher magnetic anisotropy. Surface effects, due to the high surface to volume ratios leading to a break down in the magnetic order, could cause certain nanoparticles to behave like spin glasses [93].

An ensemble of interacting superparamagnetic nanoparticles have been obtained in numerous ways such as freezing a sol containing a known fraction of magnetic nanoparticles or dilution in a polymer matrix. Such magnetic structures have been subjects of a large number of theoretical and experimental investigations [94,98,99]. The magnetization curve of an aggregate of spherical single domain nanocrystals with uniaxial anisotropy and random orientation of the easy axis is shown in Figure 1.14. From the critical ratios such as the squareness ratio (the ratio of the remanent to the saturation magnetization) and coercivity derived from the such curves, it is possible to infer the nature of the sample anisotropy and its anisotropy constant.

Recent synthetic advances have yielded high quality defect free monodisperse nanocrystals on either side of the superparamagnetic divide. Further, recent self-

assembly based routes lend unprecedented control over assemblies of nanoparticles. Spurred by the above and technological demands, there has been renewed interest in the properties of aggregates of magnetic nanocrystals.

1.7 Programmed assemblies

Attempts to build ordered assemblies of nanoparticles have been driven by both technological and fundamental implications these assemblies are likely to have. It has now been realized, that if ever nanotechnology has to be ushered in, means of rapid and controlled synthesis of assemblies of nanoparticles are essential. The cooperative or collective properties of assemblies like the path of free electrons, optical properties and interparticle coupling are of fundamental importance.

The self assembly route has been the method by which all known assemblies of nanocrystals have been built. It has been used to build one, two and three dimensional solids. In assemblies such as these, the size of the particles and the interparticle spacing can be varied nearly continuously. In the words of J. R. Heath “Experiments have been performed where covalency is an experimentally controlled, continuously variable parameter”. These assemblies are prospective candidates to yield materials with tunable structural, magnetic, optical and transport properties.

The fabrication and alignment of one dimensional wires and channels consisting of metal nanocrystals have till now met only with limited success. Such assemblies require the ordering forces to be constrained in a single dimension and consequently are difficult to realize. When a dispersion of nanoparticles coated with appropriate ligands like thiols, silanes, phospholipids, phosphines or fatty acids are allowed to evaporate on a solid substrate, the nanoparticles spontaneously organize themselves into two dimensional lattices. The above method of obtaining nanocrystal arrays has met with a lot of success and has been reviewed recently [73, 100–102]. Exploiting the formation of a self-assembled monolayer on noble metal surfaces by dithiols and other such organizations, three dimensional arrangements of nanocrystals could be obtained.

1.7.1 One-dimensional arrangements

Many groups have attempted to fabricate wire like arrangement of particles by using atomic steps on crystalline surfaces where the particles are preferentially absorbed. However, the preparation of distinct steps on ordered surfaces require complicated nano-fabrication procedures which take away the promise of a cheap method of assembling clusters. Hornayak et al. have made nanowires by filling the pores of nanoporous alumina [103]. They demonstrate that by varying the pore size, the clusters from size 1.4 to 2.5 nm can be arranged in the pores, although perfectly close packed structures were not obtained. It is also possible to prepare one-dimensional arrangement of other nanocrystals by use of similar porous alumina template. Strands of DNA of desired length, with their ends thiol derivatised were bound to gold nanoparticles and the particles were brought together by allowing complimentary strands of DNA to hybridize to produce one-dimensional structures [104]. Electrostatic interaction between DNA chain and Au nanocrystals were found to be suitable to cause organization of the nanocrystals into linear arrays [105]. A one dimensional structure has also been made by drawing HDPE (high density polyethylene) impregnated with Ag nanocrystals over a hot shoe [106]. This material was also found to exhibit polarization dependent optical absorbance. It is also known that many plant fibrils contain such nanowires. Heath and coworkers [107] have fabricated wires of Ag nanocrystals by compressing a dispersion of Ag (4.5 nm) nanocrystals in toluene. The wires were one nanocrystal thick, a few nanocrystals wide and extended in length from 20–300 nm. The interwire separation distance as well as the alignment of the wires could be controlled by compressing the film. Based on preliminary experimental observations, it has been suggested that tobacco mosaic virus tubules could serve as templates for growth of 1D lattice of quantum dots [110]. Liquid crystalline phases of a genetically engineered virus-ZnS nanocrystal hybrid material was used as a template to obtain linear arrays of ZnS nanocrystal aggregates [108]. Similarly, Pt nanocrystals in the form of ribbons have been obtained using cholesteric liquid crystalline templates [109].

1.7.2 Two-dimensional arrays

Arrays of metal nanocrystals

Gold nanoparticles were first organized into a two dimensional lattice by Schiffrin et al. by employing a sol obtained by reduction of gold ions in the presence of thiols [111]. Whetten et al. [113] size-selected an organosol consisting of poly-disperse Au nanocrystals and separated out fractions containing nanocrystals of different mean sizes and prepared well-ordered two-dimensional arrays of nanocrystals. Harfenist et al. [25] steered a cluster beam of mass selected Ag nanocrystals into a solution of alkane thiol dispersed in toluene and found that the resulting thiol-capped nanocrystals formed extended two-dimensional arrays. Sarathy and coworkers have obtained well-ordered arrays of several thiol capped metal nanocrystals by first thiol-derivatizing the corresponding hydrosols [56,57]. A two-dimensional array of Au nanocrystals, obtained by the above method is shown in Figure 1.15. Fitzmaurice and coworkers [114] and others [115] have obtained two-dimensional arrays of alkanethiol covered Ag nanocrystals. By varying the amount of the deposited sol, it is possible to obtain a three dimensional superlattice consisting of layers of two-dimensionally ordered nanocrystals [25]. Long chain fatty acids have also been used for ligating and assembling metal nanocrystals. Colloidal dispersion of Co nanocrystals capped with fatty acids were found to self-assemble to yield hexagonally ordered arrays similar to those obtained with alkanethiols [116, 117]. Ag nanocrystals capped with fatty acids were prepared by thermal decomposition of silver salts of fatty acids and were found to self-assemble to cubic or hexagonal close-packed structures [118, 119]. Well-ordered two-dimensional arrays of Au nanocrystals have also been obtained by employing alkylamines [120]. Methods to organize non-spherical metal nanocrystals into two-dimensional arrays have met with some success. Hexagonal Pt as well as elongated silver nanocrystals have been organized into ordered two-dimensional arrays [56, 121]. Ordered two dimensional lattices containing thiolized spherical Au particles of two different sizes have been reported by Kiely et al. [122], who found that the nanocrystals of different radii follow the radius ratio rules formulated

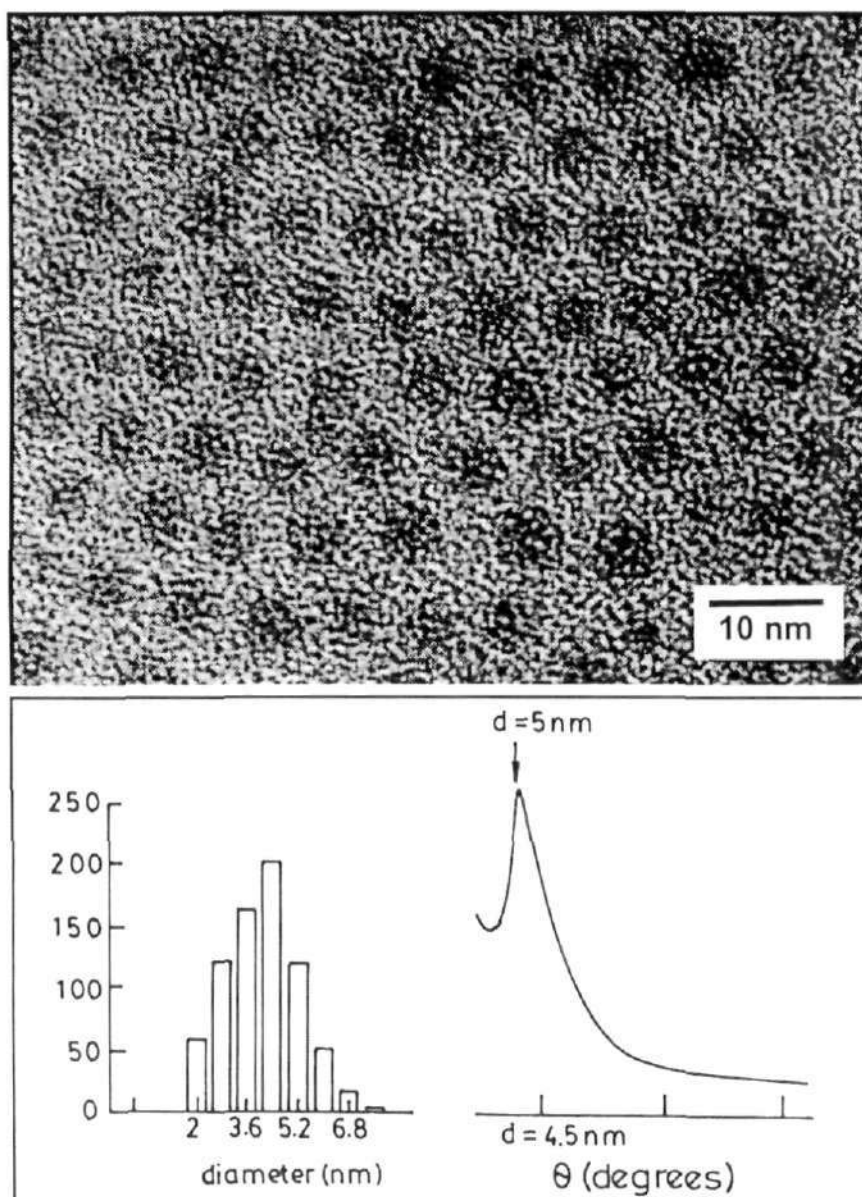


Figure 1.15: Transmission electron micrograph of a two-dimensional array of Au nanocrystals of size ~ 4.2 nm. The histogram showing the size-distribution and an X-ray diffraction pattern revealing a peak corresponding to the interparticle spacing observed in the TEM image above is also shown alongside.

for alloying of metals with similar atomic radii ratios. Alloy arrays consisting of Au and Ag nanocrystals of different sizes have also been made [123].

Arrays of semiconductor nanocrystals

By size-selecting CdSe nanocrystals prepared by thermolysis means, Bawendi et al. have obtained a superlattice consisting of several layers two-dimensionally ordered layers [125]. Motte et al. have obtained hexagonally ordered two-dimensional arrays of Ag₂S nanocrystals synthesized by reverse micelle method [74]. InP nanocrystals prepared by the thermolysis method have also been organized into two-dimensional arrays [126]. Au nanocrystals as well as CdSe-ZnS core-shell nanocrystals of various sizes have been organized into two-dimensional lattices using a protein (chaperonin) template [127].

Arrays of oxide nanocrystals

The very first report of two-dimensional arrays of nanocrystals were of Fe₃O₄ nanocrystals [128]. Bentzon et al. observed that the ferrofluid obtained by thermolysis of ironpentacarbonyl upon drying (over a period of several weeks) yielded well ordered two-dimensional arrays of Fe₃O₄ nanocrystals. Since then, quicker methods have been devised to obtain arrays of Fe₃O₄ nanocrystals [129]. In contrast to metal nanocrystals, attempts to organize non-spherical oxide nanocrystals have met with reasonable success. Thus, tetrahedral CoO nanocrystals have been organized into extended two-dimensional arrays [130]. A rectangular superlattice made of prismatic BaCrO₄ has been observed [131]. More complex arrays such as those consisting of a mixture of nanocrystals of different sizes have been obtained using Fe₃O₄ and Fe-Pt nanocrystals [132]. The mixed arrays were obtained by evaporating a binary mixture of the metal oxide organosols.

Other two-dimensional arrangements

When certain monodisperse nanocrystals such as thiol-capped Au [133–135], barium hexaferrite [136] were evaporated on a substrate, the nanocrystals, quite surprisingly assembled into micrometer-sized rings with walls consisting of a few

layers of nanocrystals. Heath and co-workers proposed that such structures arise due to solvent de-wetting effects that come into play during solvent evaporation [134]. It was shown by Pileni and co-workers, that such rings and other related structures could be obtained from a variety of nanocrystals by varying the solvent evaporation rate and exploiting the resulting fluid instabilities (the Marangoni effect) that occur during evaporation [137, 138].

1.7.3 Three-dimensional superlattices

Multilayer assemblies using monothiols such as the ones discussed above are generally fragile and are not suited for use in functional devices. One of the means of obtaining robust structures involves multilayer deposition of nanocrystals and has been drawing a good deal of attention over the last few years as they provide a convenient, low-cost means to prepare ultra-thin films of controlled thickness, suited for device applications. Such assemblies rely on a variety of monolayer forming species which include alkanethiols, amines, long chain fatty acids and silanes. In a typical experiment, one end of a monolayer forming bifunctional spacer, is tethered to flat substrates such as gold, aluminium, indium tin oxide or glass, leaving the other end free to anchor nanocrystals. Subsequent layers can be introduced by dipping the substrate sequentially into the respective spacer molecule solution and the nanocrystal dispersion, with intermediate steps involving washing and drying. The formation of the multilayer assembly can be monitored using a variety of spectroscopy and microscopy tools. Brust et al. [139] have reported the formation of multilayers of Au nanoparticles using dithiols. These workers have confirmed the layer-by-layer deposition of particle arrays by employing UV-vis spectroscopy and ellipsometry. Such assemblies can also be obtained by employing polyelectrolytic spacers such as poly(diallyldimethylammonium chloride) (PDDA), poly(ethyleneimine) (PEI), poly(allylamine hydrochloride) (PAH) and polymers such as poly(phenylenevinylene) (PPV) as well [140–143]. Thus, multilayers such as those of CdTe nanocrystals spaced with PDDA, CdSe spaced with PPV have been prepared.

1.7.4 Colloidal crystals

The tendency of monodisperse nanocrystals to arrange into ordered three dimensional arrays extending to a few microns, has been noticed [144]. The crystallites are typically obtained by slow, controlled evaporation of the solvent over periods of a few months. Careful tuning of crystallization conditions have yielded crystallites of micrometer dimensions consisting of Au₅₅ nanocrystals and Fe-Pt alloy nanocrystals (4.5 nm). Micron sized crystals consisting of TOPO capped CdSe nanocrystals have been obtained by the groups of Bawendi and Weller [125, 145]. However, it was observed that the nanocrystal arrangement in all the above crystallites was polymorphous. It is believed that such crystallites, consisting of ordered nanocrystals could prove to be the best candidates to study the collective properties of an ensemble of nanocrystals.

1.7.5 Collective properties

The fact that the physical properties of nanocrystal organizations could be different from that of the isolated particles is being realized. Pellets of monodisperse nanocrystals, obtained by the use of bifunctional ligands that bind to more than one nanocrystal or by applying pressure on dried nanocrystalline matter, have been used for electrical transport measurements [146–149]. Pellets made of small Au and Pd nanocrystals exhibit non-metallic behavior with specific conductivities in the range of $10^6 \Omega^{-1}\text{cm}^{-1}$ [146–148]. The conductivity however increases dramatically with an increase in the diameter of the nanocrystals. An insulator metal transition has indeed been reported from pellets made of ~ 12.5 nm Au and Ag nanocrystals [149]. Electrical transport measurements on layer-by-layer assemblies of nanocrystals on conducting substrates have been carried out by adopting a sandwich configuration [150–152]. Nanocrystalline films with bulk metallic conductivity have been realized with Au nanocrystals of 5 and 11 nm diameter spaced with ionic and covalent spacers [151, 152]. The conductivity of monolayered two-dimensional arrays of metal nanocrystals have been studied with patterned electrodes [153–158]. Structural disorder and inter-particle separation

distance are identified as key factors that determine the conductivity of such layers [153–156]. It was found that the conductivity of such layers can be enhanced by replacing alkane thiol with an aromatic thiol *in-situ* [157, 158]. That the interaction energy of nanocrystals in such organizations can be continually varied by changing the interparticle distance was exploited by Heath and co-workers [159, 160], who prepared a monolayer of Ag (~ 3 nm) nanocrystals at air/water interface in a LB trough and varied the interparticle distance by applying pressure. A host of measurements including reflectivity and non-linear optical spectroscopic techniques were carried out *in-situ*. This study led to the observation of a reversible Mott-Hubbard metal-insulator transition in the nanocrystal ensemble wherein the Coulomb gap closes at a critical distance between the particles. Tunnelling spectroscopic measurements on films of 2.6 nm Ag nanocrystals capped with decanethiol reveal a Coulomb blockade behavior attributable to isolated nanocrystals [160]. On the other hand, nanocrystals capped with hexane and pentane thiol exhibit characteristics of strong inter-particle quantum mechanical exchange. Similar behavior was observed in the case of self-assembled two-dimensional arrays of Co nanocrystals and Au nanocrystals [161, 162].

Optical properties of a superlattice of semi-conductor nanocrystals are different from that of the individual nanocrystals due to interparticle interactions [15]. When present in close-packed organization, the absorption spectra of the semiconductor nanocrystals is broadened and red shifted. This change has been attributed to interparticle dipolar interactions [163]. Bawendi and co-workers have studied such changes in ensemble of CdSe nanocrystals of different diameters and have obtained evidence for long range resonance transfer of electronic excitation from smaller to bigger nanocrystals due to dipolar interactions [164]. In a noteworthy experiment, Weller and co-workers, prepared drop cast films of giant CdS clusters of the form $\text{Cd}_{17}\text{S}_4(\text{SCH}_2\text{CH}_2\text{OH})_{26}$ and $\text{Cd}_{32}\text{S}_{14}(\text{SCH}_2\text{CH}(\text{CH}_3)\text{OH})_{36}$ with diameters of 1.4 and 1.8 nm, respectively. Further, an integrating sphere was used to collect absorption data, thereby virtually eliminating errors from inhomogeneities and size distributions [165]. The experiments due to Weller also support the idea of dipolar interaction leading to the red shift and broadening. Signatures of such

interactions have also been seen in the case of CdS multilayer deposits [142]. The interparticle interactions, however, could range from weak dipolar interactions to strong exchange interactions based on the interparticle separation. Delocalization of the electronic states of nanocrystals in ensembles due to exchange interactions have been observed in experiments with CdSe nanocrystals. Gaponenko and co-workers have shown that the optical properties of an ensemble of small (~ 1.6 nm) CdSe nanocrystals are similar to that of bulk CdSe due to complete delocalization of the electronic states of individual nanocrystals [166].

Nanocrystals of Co when organized into two-dimensional arrays exhibit a higher superparamagnetic blocking temperature compared to isolated nanocrystals [167]. Sun and co-workers report a lattice of nanocrystals each consisting of a Fe core and a Pt shell prepared by heating Fe-Pt alloy nanocrystals [168]. Following phase segregation, the interaction between the nanocrystals increased leading to a ferromagnetic films capable of supporting high density magnetization reversal transitions. Exchange spring magnets - nanocomposites that consist of magnetically hard and soft phases interacting via magnetic exchange coupling, have been made by carefully annealing the mixed nanocrystal array consisting of Fe-Pt and Fe_3O_4 [132].

1.8 Emerging applications

Several applications have been envisaged for nanocrystals, ranging from simple dyes to magnetic resonance imaging contrast agents [171], as components of electronic circuitry [172, 173] and magnetic media, as ingredients in catalyst and sensors, and so on. All the above applications seek to exploit the tunability provided by size-dependent properties of the nanocrystals. Nanocrystals are thought of as important in single electron devices, operating at room temperature, such as super sensitive electrometers and memory devices [173, 174].

Exploratory devices have been made from polymer/polyelectrolyte-nanocrystal hybrids, seeking to exploit their electro and photoluminescent properties. Device fabrication in all these cases is by low cost self-assembly based techniques and

utilize either multilayer deposition or drop/spin casting methods. For example, a photochemical device that acts like a “solar cell” has been made from poly(2-hexylthiophene)-CdSe nanorod multilayers [169], White light emission has been obtained from drop cast films consisting of a mixture CdSe-ZnS, CdS-ZnS and polyaurlymethacrylate [170].

Ordered arrays of nanocrystals, in principle, could be thought of as arrays of single electron transistors (SET), where the electrostatic interaction between neighboring SETs acts as wireless communication means. It has been suggested by Korotkov [175] and Lent [176] that simple logical operations can be performed on a circuitry consisting of arrays of SETs in the form of chains or cells with suitable insulating spacers. An electric field applied in one direction polarizes the strings into either the 0 or the 1 state. Lent’s scheme, named quantum cellular automata, instead uses a square cell consisting of five nanocrystals to denote the state of polarization. Preliminary experiments to evaluate the schemes are currently being pursued.

The realization that self-assembly driven fabrication process is not capable of producing defect free structures, has fuelled a search for algorithms that can compute even with defective circuitry. Heath and co-workers [177] have developed Teramac, a computer that works despite a high concentration of defects in its bank of microprocessors. A more radical solution called amorphous computing aims to “engineer pre-specified, coherent behavior from cooperation of large numbers of unreliable parts interconnected in unknown, irregular and time varying ways” [178–180].

2. Scope of the Present Investigations

The study of electronic properties of individual nanocrystals and structural aspects of their assembly assumes significance against the backdrop of emerging applications of nanocrystalline materials. The fabrication of electronic nanodevices touted as substitutes to today's microdevices requires extensive study of the components and the means of putting them together to make a functional device. The present study was undertaken to address a few such issues.

2.1 Submicron-sized particles of Co, Ni and Co-Ni alloys

Large scale synthesis of metal particles is invariably carried out using chemical routes. Of the many procedures, the polyol process is especially suitable for the synthesis of metal particles with sizes ranging from a few nanometers to a few microns [11, 12]. Magnetic nanocrystals such as those of Pd-Ni, Fe-Ni and Co-Fe, prepared by the above process, have been attracting wide interest due to their microwave absorption properties and for potential use as electromagnetic radiation absorbers [181–183].

The bare magnetic particles obtained by the polyol process, are not stable in air and are prone to oxidation. We considered that a polymer coating such as PVP should improve the stability of the particles with respect to atmospheric oxygen. PVP is ideal because it contains a ring nitrogen atom which can bind to the metal particles and yet not affect the magnetic properties of the nanocrystals [10, 184]. We have prepared PVP coated submicron sized particles of Co, Ni and Co-Ni alloys by the polyol process. In order to ascertain that the PVP coating has no detrimental effect on the properties of the particles, we have studied the magnetic properties of the particles.

2.2 Films of Au nanocrystals at liquid-liquid interfaces

Soft chemical methods have been gaining in prominence as means of synthesizing nanocrystals [185]. These methods rely on constrained environment such as the

confines of a reverse micelle or a phase boundary to limit the growth of particles. By exposing Langmuir-Blodgett films of Pb and Cd salts of fatty acids to H_2S , CdS and PbS nanocrystals have been prepared [186]. As discussed previously, a variety of nanocrystals have been obtained using inverted micelles. Thiol capped Au nanocrystals have been prepared by using the phase boundary between water and toluene to limit the diffusion of the aqueous reducing agent into the organic phase containing the Au precursor [111].

We have employed the liquid-liquid interface to synthesize free standing films of Au nanocrystals. The interface of two liquids not only serves to limit diffusion but also acts as a constrained growth medium for nanocrystals. This technique can readily be extended to prepare granular thin films of Au. The use of the liquid-liquid interface in this case is similar to the use of air-water interface in the the Langmuir-Blodgett technique. This liquid-liquid interface technique could lead to a new and a universal route to synthesize various nanomaterials.

2.3 Effect of size on the Coulomb staircase behaviour in Au and Pd nanocrystals

Small metal nanocrystals prepared by wet-chemical means have been found to exhibit coulomb staircases in their I-V spectra. Thus, the charging energy of $Pt_{309}phen_{36}O_{20}$ has been reported to vary between 50 and 500 meV depending on the way the cluster is oriented on the substrate [172]. Scanning tunnelling spectroscopy carried out on pellets of $Au_{55}(PPh_3)_{12}Cl_6$ showed I-V characteristics that reflect single electron transport [187]. Similar effects have been observed in the case of monolayers of Co nanocrystals [188]. The charging energies of CdS particles of different sizes present in a LB film have also been measured [189].

To our knowledge, there has been no known experimental investigation of the coulomb staircase phenomenon in isolated metal nanocrystals, especially with respect to the effect of particle size. We have therefore investigated the Coulomb staircase behavior in Au and Pd nanocrystals of varying size (1.7 – 6.4 nm), protected by PVP. In this size range, the nanocrystals are small enough to have

discrete charging energies, yet being well within the metallic regime [72].

2.4 Two-dimensional arrays of Pd nanocrystals

Metal nanocrystals suitably capped self-organize into two and three dimensional assemblies. Appropriate ligands, a narrow size distribution and a slow evaporating solvent are the required conditions for the lattices to be formed. The nanocrystals capable of forming ordered arrays have traditionally been regarded as hard spheres, with no interactions between them. The stability of the lattices obtained have been attributed to entropic packing considerations. Accordingly, nanocrystals of definite size ratios crystallize into entropically stabilized bimodal assemblies [122]. However, the observations that the obtained organizations are influenced by the substrate, capping agent and solvent composition cannot be explained by simple hard sphere model. The importance of interparticle attractions has been pointed out by Ohara et al. [190]. They observed that the net long range attractions between dodecanethiol stabilized Au nanocrystals induce them to order in form of opals. Further, most nanocrystal assemblies do not satisfy the Alder and Wainwright critical volume criteria for entropic stabilization - the volume fractions of ordered nanocrystal have always been lower than the required minimum of 0.49 [191]. Korgel et al. have proposed a soft-sphere model to describe the energetics of nanocrystal assembly [114]. This model provides reasonable explanation of the experimental observations.

We sought to understand the nature and stability of two-dimensional crystalline arrays of thiol-covered metal nanocrystals in terms of the particle diameter (d) and the ligand chain length (ℓ). It has been suggested that the d/ℓ ratio is a relevant parameter [192, 193]. We have studied the two-dimensional arrays formed by Pd nanocrystals of varying diameter in the range 1.8 – 6.0 nm by employing alkane thiols of different chain lengths (butyl to hexadecyl). This study enabled us to obtain an experimental stability diagram in terms of d and ℓ . We have compared the experimental results with those from empirical calculations based on a soft sphere model.

2.5 Giant clusters of magic nuclearity Pd nanocrystals

The possibility that magic nuclearities associated with the formation of nanocrystals could also extend to their growth and beyond was theoretically predicted on the basis of the embedded atom approximation by Fritsche et al. [194]. Secondary ion and plasma desorption mass spectrometry on dried samples of magic nuclearity Au₅₅ nanocrystals has provided evidence for such a growth process [195]. However, no clear preference for the magic nuclearities were observed and further, these clusters were not discernable outside of the mass spectrometer.

We have examined the mesoscopic assembly of Pd nanocrystals by employing electron microscopic techniques. For this purpose, we prepared monodisperse Pd₅₆₁ nanocrystals capped with PVP and examined the aggregates obtained on standing, in aqueous dispersions of these nanocrystals.

2.6 Mesoscopic organization of magnetic nanocrystals

In the family of magnetic nanocrystals, nanocrystals of metal oxides occupy a prominent place because they are probably the only ones stable in air. Mesoscopic organizations of magnetic metal oxide and other nanocrystals result in materials with new and interesting magnetic properties [132,167,168]. Such organizations are being considered for potential uses in magnetic recording technology. Experiments on drop cast films of magnetic nanocrystals suggest that the easy magnetic axis of nanocrystals can be aligned by applying a magnetic field during evaporation of the sol on a substrate. The resulting films consist of nanocrystals with their easy axis aligned parallel to the substrate and exhibit parallel magnetic anisotropy [196,197].

Magic nuclearity Pd₅₆₁ nanocrystals have been used as seeds to obtain monodisperse Pd-Ni core-shell nanocrystals with varying Ni loading. These core-shell nanocrystals have been thiolized adopting the procedure described earlier and the resulting ordered lattices studied. New routes for the synthesis of magnetic metal oxide nanocrystals such as CoFe₂O₄ and Fe₃O₄ have been explored and their mesoscopic organization examined. We have also examined the magnetic order

in drop-cast films of citrate and octylamine capped γ -Fe₂O₃ nanocrystals on Si substrates.

2.7 Layer-by-Layer assembly of metal and semiconductor nanocrystals

The layer-by-layer technique permits the building up of robust multi-layers consisting of arrays of nanocrystals and spacers. It is believed that such organizations are best suited for making functional devices from nanocrystals. CdS and Au nanocrystals have been deposited on a gold substrate by making use of dithiol molecules [139, 198]. The formation of such layers were confirmed by measurements such as UV-spectroscopy. Layers of CdS nanocrystals were found to yield small photocurrents upon irradiation with white light. However, no detailed investigations based on electron spectroscopic and microscopic techniques have been carried out in the above cases. We have attempted to prepare hetero-structures consisting of metal and semiconductor nanocrystals on Au substrates by employing dithiols as spacers and have studied them using STM and X-ray photoelectron spectroscopy (XPS).

2.8 Interaction of lipoic acid capped metal nanocrystals with metal ions

Mercaptocarboxylic acids when employed as capping agents for metal nanocrystals render the nanocrystals water soluble and self-assemble on their surfaces with the thiol end bound to the nanocrystal and the carboxyl end sticking out radially. It is possible to chelate metal ions to carboxyl end and study the binding by the use of the plasmon resonance band of the metal nanocrystals. It has been suggested by Hupp et al. that such nanocrystals could be useful in sensing heavy metal ions [199]. Further, pH titrations of Simard and co-workers reveal the reversible nature of aggregates produced by chelation [200].

We have investigated the effect of chelation of various metal ions on α -

lipoic acid capped Au and Ag nanocrystals by means of UV-visible spectroscopy and transmission electron microscopy. We have made use of the flocculation parameter defined by Whitesides et al. to follow some of the changes induced by chelation [201].

2.9 Atomic force microscopy based method for patterning nanocrystals

It is being increasingly realized that to harness nanocrystals in functional devices, methods to position nanocrystals and to generate patterns of nanocrystals in arbitrary locations on surfaces are important. A soft lithography based technique has been developed by Whitesides and co-workers to generate patterns of Pd nanocrystals on a variety of substrates [202]. The smallest width of the pattern possible using this technique is of the order of a few hundred nanometers. Dip-pen nanolithography utilizes the water meniscus formed between a scanning probe microscopic cantilever and the substrate to transport matter from the tip to the sample and create patterns on the substrate. Patterns with widths of the order of a few nanometers can be routinely generated by using this technique. Demers and Mirkin patterned dithiols on Au substrates and used the patterns of dithiols to organize metal nanocrystals [203].

We have adopted the dip-pen nanolithographic technique to create patterns of Au and Pd nanocrystals, by employing the weak forces between the substrate and the nanocrystals. Our method significantly broadens the choice of substrates and the nanocrystals available for patterning.

3. Experimental and related aspects

3.1 Preparation of Nanocrystals

Nanocrystals of metals, semiconductors and oxides were made by chemical means. The nanocrystals obtained were “capped” by a variety of surfactants or capping agents. In Figure 3.1, the capping agents employed are illustrated. The glassware used for the preparation of nanocrystals were etched with a “glass etching” mixture consisting of 50% v/v of 40% HF and lab detergent. Care was taken to avoid glassware and pellets with scratches to avoid precipitation of the prepared sols.

3.1.1 Co, Ni and Co-Ni alloy particles

Particles of Co and Ni were prepared by refluxing an ethylene glycol solution of their acetates or sulphates containing PVP ($M_w \sim 40,000 \text{ gmol}^{-1}$). In a typical reaction, 2 g of PVP, 0.5 g of the metal precursor were dispersed in 50 ml of ethylene glycol and the resulting solution refluxed at 198 °C for 10 h. In all reactions involving Ni, the pH was adjusted to 9 – 11 by addition of NaOH prior to reduction. The total metal ion concentration was held constant at 0.1 M for all the preparations. Particles of Co and Ni alloys were obtained by co-reducing the corresponding salts. Thus, to obtain alloy particles of the composition $\text{Co}_{0.9}\text{Ni}_{0.1}$, 1.12 g of $\text{Co}(\text{ac})_2 \cdot 4\text{H}_2\text{O}$ and 0.124 g of $\text{Ni}(\text{ac})_2 \cdot 4\text{H}_2\text{O}$ were dissolved in 50 ml of ethylene glycol and were refluxed at 198 °C overnight. In all the above cases, the solution turned black within a few minutes of reaching 198 °C. At the end of the reaction, the particles were precipitated from the solution by adding excess water or acetone and isolated by centrifugation. The particles were subsequently washed with water several times to remove excess PVP and unreduced matter if any. Finally, the obtained black precipitates were dried in vacuum to obtain waxy solids.

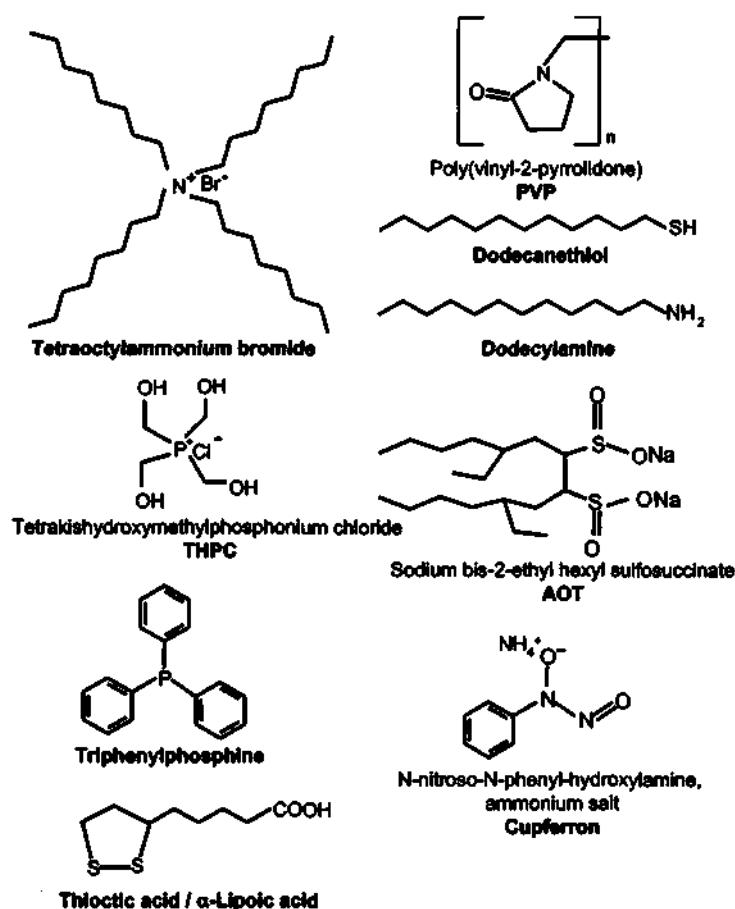


Figure 3.1: Structure of the various surfactants that were used as capping agents.

3.1.2 Films of Au nanocrystals

Au(PPh₃)Cl (Ph - phenyl) was obtained following a reported procedure [204] starting from HAuCl₄. In a typical preparation, 10 ml of 1.5 mM solution of Au(PPh₃)Cl was allowed to stand in contact with 16 ml of 6.25 mM aqueous alkali in a 100 ml beaker at room temperature. Once the two layers stabilized, 330 μ l of 50 mM THPC was injected into the aqueous layer using a syringe with minimal disturbance to the toluene layer. The onset of reduction was marked by a faint pink colouration of the liquid-liquid interface. The reduction thus initiated was allowed to proceed without disturbance for several hours. With the passage of time, the colour became more vivid, finally resulting in a robust elastic film at the liquid-liquid interface (see Figure 3.2).



Figure 3.2: Photograph showing a film of Au nanocrystals formed at the interface of water and toluene.

3.1.3 Pd nanocrystals

Pd nanocrystals have been studied because of their catalytic properties and consequently, many synthetic schemes have been devised for their preparation. We prepared Pd nanocrystals in the size range 1 – 10 nm following various reported methods. These nanocrystals were employed in the study of the coulomb staircase phenomena, the lithography study as well as in the studies of the mesoscopic organization of nanocrystals.

Small and medium sized Pd nanocrystals coated with PVP were obtained according to a method detailed by Teranishi [205]. This method involves the reduction of H_2PdCl_4 with ethanol in the presence of PVP. A 250 ml of 2.0 mM stock solution of H_2PdCl_4 was prepared by adding 1.73 ml of 0.58 N HCl (1.0 mM) to 88.7 mg of PdCl_2 (0.5 mM) in water. 15 ml of this solution and 35 ml of ethanol-water mixture containing PVP was used for making different sols. The diameters of the nanocrystals obtained depended on the amount of ethanol used. A batch of Pd

nanocrystals were made with a 40% mixture of ethanol and a PVP/Pd ratio of 40 (molar ratio calculated on the basis of monomer weight of PVP - 111.11 gmol^{-1}). Magic nuclearity Pd_{561} nanocrystals were prepared by employing 20% ethanol and a PVP/Pd ratio of 10. In a similar way, seven-shelled Pd_{1415} nanocrystals were prepared by employing a 25% solution of ethanol. To obtain still bigger Pd nanoparticles, the magic nuclearity Pd_{561} nanocrystals were used as seeds to induce growth of another layer of Pd. 25 ml of fresh H_2PdCl_4 in a 2:3 ethanol-water mixture was added to 25 ml of the sol and further reduction was carried out. All sols obtained by the above method could be dried and redispersed in water, ethanol and dimethylformamide. The prepared particles were insoluble in toluene, heptane and dichloromethane.

Magic nuclearity Pd_{561} nanocrystals capped with phenanthroline were prepared by employing the method of Schmid et al. [206]. Accordingly, 100 mg of $\text{Pd}(\text{ac})_2$ in 50 ml of acetic acid containing 11 mg of 1,10-Phenanthroline monohydrate was reduced by careful addition of gaseous H_2 . The formation of the sol was seen by a sudden change in colour from orange-yellow to brown-black during the passage of the hydrogen gas. The reduction was continued till a clear black precipitate was seen. A small quantity of gaseous oxygen was then added to liberate the hydrogen molecules coordinated to the surface of the nanocrystals. The sol was filtered by decantation and the filtrate centrifuged with 3 – 4 fold excess benzene to obtain Pd nanocrystals in solid form. The nanocrystals were soluble in acetic acid, water, dichloromethane, ethanol and were insoluble in heptane and toluene.

Large Pd nanocrystals covered with PVP were prepared following the method of Porta et al. [207]. Accordingly, 33.5 mg of $\text{Pd}(\text{ac})_2$ was reduced with 125 ml of ethanol in the presence of 190 mg of PVP. The reduction was brought about by refluxing the mixture in air for two hours, followed by rapid cooling over an ice bath. The formation of the sol was seen by the change in the colour from orange-yellow to brown-black and occurred within five minutes. However, prolonged periods of refluxing was required to drive the reaction to completion.

The nanocrystals employed for single electron tunnelling and lithographic

Table 3.1: Details of the starting compositions and synthetic conditions. The total metal ion/PVP ratio was 10 in all cases.

Nanocrystal composition	Metal ion	Concentration μM	Solvent volume/ composition
Pd_{561}	Pd^{2+}	750	20% v/v aq. Ethanol, 50 ml
$\text{Pd}_{561}\text{Ni}_{138}$	$\text{Pd}_{561} + \text{Ni}^{2+}$	25	Propanol, 100 ml
$\text{Pd}_{561}\text{Ni}_{280}$	$\text{Pd}_{561} + \text{Ni}^{2+}$	187	Propanol, 100 ml
$\text{Pd}_{561}\text{Ni}_{561}$	$\text{Pd}_{561} + \text{Ni}^{2+}$	375	Propanol, 100 ml
$\text{Pd}_{561}\text{Ni}_{800}$	$\text{Pd}_{561} + \text{Ni}^{2+}$	535	Propanol, 100 ml
$\text{Pd}_{561}\text{Ni}_{1500}$	$\text{Pd}_{561} + \text{Ni}^{2+}$	1003	Propanol, 100 ml
$\text{Pd}_{561}\text{Ni}_{3000}$	$\text{Pd}_{561} + \text{Ni}^{2+}$	2005	Propanol, 100 ml
$\text{Pd}_{561}\text{Ni}_{4500}$	$\text{Pd}_{561} + \text{Ni}^{2+}$	3008	Propanol, 100 ml
$\text{Pd}_{561}\text{Ni}_{3000}\text{Pd}_{1500}$	$\text{Pd}_{561}\text{Ni}_{3000} + \text{Pd}^{2+}$	2005	20% v/v aq. Ethanol, 50 ml

studies were further purified to rid the sols of free ions and starting material. For this purpose, the sols were repeatedly precipitated by adding diethyl ether. Each time the filtrate was filtered employing a Gelman 0.45 μm nylon membrane filter and the precipitate redispersed in ethanol.

3.1.4 Pd-Ni nanocrystals

PVP capped $\text{Pd}_{561}\text{Ni}_n$ nanocrystals were prepared by employing Pd_{561} nanocrystals as seeds and adopting a method reported by Teranishi and co-workers [205]. Sols of magic nuclearity Pd_{561} nanocrystals, prepared as detailed above were dried and redispersed in 100 ml of Ar-purged 1-Propanol followed by the addition of the required amount of $\text{Ni}(\text{ac})_2 \cdot 4\text{H}_2\text{O}$ and PVP (see Table 3.1). The mixture was reduced by refluxing under an Ar flow for 3 hrs. Particles of the type $\text{Pd}_{561}\text{Ni}_{3000}\text{Pd}_{1500}$ were obtained by refluxing $\text{Pd}_{561}\text{Ni}_{3000}$ with required quantities of H_2PdCl_4 and PVP (see Table 3.1).

3.1.5 Thiolization of Pd and Pd-Ni nanocrystals

Thiolized Pd and Pd-Ni nanocrystals (i.e., nanocrystals capped with alkane thiols) were essential for the formation of the two-dimensional lattices and were

obtained by thiol-derivatizing PVP capped nanocrystals following the procedure of Sarathy et al. [56, 57]. Accordingly, to 3 ml of the aqueous sol consisting of a few micromoles of the metals, 0.4 ml of toluene and 10 μ l of an alkanethiol were added. The two layers were thoroughly mixed in a vortex mixer. To this dispersion, 3 ml of *Con. HCl* was added over a period of three minutes accompanied by vigorous stirring. This resulted in a complete transfer of nanocrystals to the organic medium and was marked by a complete drain of colour from the aqueous layer. The nanocrystals in the organic layer could be isolated by slow evaporation of the organosol. All thiolized nanocrystals acquired a different solubility behaviour.

3.1.6 CdS nanocrystals

CdS nanocrystals capped with AOT were prepared by the reverse micelle method using the procedure reported by Lianos and Thomas [208]. Two 50 ml dispersions containing inverted AOT micelles in heptane of sodium sulphide nonahydrate and cadmium perchlorate hexahydrate were mixed under Ar atmosphere in darkness. The W ratio ($[\text{water}]/[\text{AOT}]$) was maintained at 5, with $[\text{AOT}] = 1.8 \text{ mM}$. The concentration of aqueous S^{2-} and Cd^{2+} was maintained at 1 mM. Before use, AOT was dehydrated by dissolving in petroleum ether and evaporating (with rotary evaporator) the obtained solution. The AOT foam thus obtained was dissolved in heptane and used immediately. The AOT micelles were made stirring a mixture of heptane, AOT and aqueous solution of cadmium perchlorate or sodium sulphide for one hour. The two micelles were mixed and the stirring continued in the dark for one hour to obtain the CdS nanocrystals. Excess AOT can be removed by precipitating the nanocrystals with acetone. The precipitate was washed with water and redispersed in heptane to get pure CdS nanocrystals.

3.1.7 Pt nanocrystals

Pt nanocrystals were prepared by transferring Pt^{4+} ions to the organic phase by the use of a phase transfer catalyst - tetraoctylammonium bormide, followed by borohydride reduction. The reduction proceeds at the interface of the two liquids. In a typical preparation, 10 ml of toluene consisting of 35.5 mg of tetraoctylammonium

bromide was added to 5 ml of 2.6 mM H_2PtCl_6 . The two liquids are thoroughly shaken, till the organic layer acquires a orange-yellow colour and the aqueous layer is completely drained of colour. To this dispersion 5 ml of freshly prepared 26 mM NaBH_4 solution was rapidly added to obtain Pt nanocrystals in the organic layer. The aqueous layer was drained and the organic layer was washed with water several times to remove unreacted NaBH_4 .

Films of the above nanocrystals were made by depositing alternate layers of 1,10-decanedithiol and particles on a polycrystalline Au substrate. The Au substrates were made by depositing Au by resistive evaporation onto freshly cleaved mica substrates maintained at 500 °C in a vacuum. The substrate was first immersed in a 50 mM solution of 1,10-decanedithiol in toluene. After 2 hrs, the substrate was washed thoroughly with toluene and dried in air. The dithiol covered substrate was immersed in a dilute dispersion of nanocrystals for 12 hrs. These steps were repeated to obtain multilayers of nanocrystals.

3.1.8 Au and Ag nanocrystals

Au nanocrystals capped with PVP were prepared by a photoreduction method [209]. This method yields ion free, polydisperse Au nanocrystals, ideal for the study of the coulomb staircase phenomena. Thus, 15 ml of 0.5 mM solution of HAuCl_4 in formamide containing 2 mM of PVP was irradiated with UV light from a mercury vapor lamp (60 W) for 3 hrs to effect the reduction. During the course of reduction, the colour changed from orange to pale violet and the overall temperature of the precursor increased by ~ 10 °C.

Lipoic acid capped Au and Ag nanocrystals utilized for the study of interaction of metal ions with nanocrystals were prepared based on a method reported by Maya et al. [210]. In a typical preparation, 15 ml of 2.5 mM NaBH_4 was added to a 15 ml aqueous solution consisting of 75 μmols each of HAuCl_4 and α -lipoic acid. Upon addition of NaBH_4 , the colour of the solution instantly turned to wine red indicating the reduction of HAuCl_4 . The sol was thoroughly aerated and repeatedly extracted with dichloromethane to remove unreacted products. Nanocrystals of Ag

were prepared in a similar manner, starting with AgNO_3 . The colour of the sol in the case of Ag was yellow. The mean diameters of the nanocrystals could be varied by changing the metal/lipoic acid ratios. In addition to the reactions with the 1:1 metal/lipoic acid mole ratios, Au nanocrystals were prepared with a metal/lipoic acid 1:2.5 ratio. Ag nanocrystals were prepared with metal/lipoic acid ratio of 1:5 as well.

3.1.9 Magnetic oxide nanocrystals

Citrate-capped $\gamma\text{-Fe}_2\text{O}_3$ nanocrystals were prepared by a procedure that is a modification of the one described by Ngo and Pileni [211]. In a typical preparation, to 50 ml aqueous solution containing 1.96 g (0.005 mol) of ferrous ammonium sulphate and 2.78 g (0.01 mol) of sodium dodecylsulphate, 40 ml of 40% aqueous solution of dimethylamine was added under vigorous stirring. The brown black precipitate obtained after stirring for two hours was centrifuged, washed with 2 M HNO_3 , followed by water until it was free from ions. The solid was then re-dissolved in an aqueous solution of trisodium citrate (0.06 M, 100 ml) with half an hour stirring. To the brown sol thus obtained, 100 ml acetone was added to yield a fluffy brown precipitate. The precipitate consisting of citrate-capped $\gamma\text{-Fe}_2\text{O}_3$ nanocrystals was centrifuged, washed with acetone and dried in air at 25 °C. The brown powder so obtained was freely dispersible in water and upon dispersion yielded a brown ferrofluid which was stable for several weeks.

Metal cupferronates were used as precursors in the synthesis of a series of metal oxide nanoparticles. The cupferron complexes were obtained by known methods [212]. Thus, iron, cobalt and manganese cupferronates were prepared by slow addition of aqueous cupferron to a aqueous solution of the respective chlorides. The pH of the solution was maintained at 2.0 for the preparation of iron cupferronate. The solids were recrystallized from alcohol and were brown, greyish brown or red for Fe, Mn and Co respectively. Nanoparticles of $\gamma\text{-Fe}_2\text{O}_3$, Fe_3O_4 , Co_3O_4 , CoFe_2O_4 and MnFe_2O_4 were prepared by thermal decomposition of the metal cupferronates. In a typical reaction yielding $\gamma\text{-Fe}_2\text{O}_3$, 9.0 ml of 0.3 mM solution of $\text{Fe}(\text{cup})_3$ in n-octylamine was injected into 9.0 ml of tri-n-

octylamine that was maintained at 300 °C and was being vigorously stirred. The onset of the reaction was marked by brisk effervescence. The contents of the flask were maintained at ~ 225 °C and the stirring continued for another 45 mins. To obtain Fe₃O₄ particles, the decomposition was carried out in H₂ atmosphere and the contents of the flask were maintained at ~ 250 °C in H₂ atmosphere till the contents of the flask changed colour from brown to black. Co₃O₄ particles were obtained starting from Co(cup)₂. A 1:2 mixture of Co and Fe cupferronates yielded CoFe₂O₄ nanoparticles. Similarly, a 1:2 mixture of Mn and Fe cupferronates yielded MnFe₂O₄ nanoparticles. All the nanoparticles obtained were freely soluble in toluene and could be precipitated (reversibly) using methanol.

Films of magnetic nanocrystals were prepared by drop casting the sols obtained above. For this purpose, Si(100) wafers (0.5 cm x 2.0 cm) were mechanically thinned from the rear to a thickness of a few hundred microns and cleaned by washing with water, followed by sonication in methanol. No attempt was made to remove the native oxide layer on the substrate. Nanocrystal films of varying thickness were prepared by successive addition of 20 μl droplets of 0.35% aqueous or toluene sols. The deposition process was monitored by a Cahn microbalance to determine the mass of the nanocrystals transferred to the substrate.

3.2 Characterization of the nanocrystals

The prepared nanocrystals were characterized by adopting several spectroscopic and microscopic techniques such as TEM, Scanning electron microscopy (SEM), Atomic force microscopy (AFM), Scanning tunnelling microscopy and spectroscopy (STM/STS). In the following paragraphs, the details of instruments used and the sample preparation methods adopted are described.

3.2.1 Transmission electron microscopy

The nanocrystal dispersions were examined with a JEOL-3010 Transmission electron microscope (TEM), operating at 300 KV, with a line to line resolution of 1.7 Å. Selected area electron diffraction (SAED) measurements were also carried

out on the same microscope. Samples for TEM and SAED were prepared by depositing a drop of the sol on a holey carbon copper grid, allowing it to dry in air and in a desiccator overnight. The diameters of the nanocrystals were obtained from transmission electron micrographs and generally represent averages obtained from a few hundred nanocrystals.

3.2.2 Scanning tunnelling microscopy and spectroscopy

Scanning tunnelling microscopy and tunnelling conductance measurements were carried out using a Digital instruments Nanoscope-II scanning tunnelling microscope operating at room temperature in air. The scanner was initially calibrated against the (0001) surface of highly oriented pyrolytic graphite (HOPG) using an Au tip prepared by electrochemical means [213]. High impedance of 2.5 MW (bias, 500 mV; set-point current, 2 nA) was used for imaging to prevent tip induced damage and capture of metal particles by the tip. Samples for conductance measurements were prepared by depositing a few drops of the dilute metal sol on freshly cleaved HOPG and allowing it to dry in vacuum. The layer-by-layer films of nanocrystals were imaged as prepared employing wire cut Pt-Ir tips.

I-V data were collected in the spectroscopy mode with the feedback loop turned off. Initially, large areas typically 200 nm² were scanned to locate isolated nanocrystals. After obtaining a stable, non-drifting image of an isolated nanocrystal, 200 I-V data points were collected in a typical voltage sweep of ± 750 mV across zero, with a delay of 100 msec between successive sweeps. The I data points were then normalized with respect to the set-point current. Imaging of the area was repeated after the I-V measurement to ensure that the nanocrystal had not drifted away. We have carried out measurements under the same conditions of bias and current (500 mV, 2 nA) on the various Pd and Au nanocrystals.

3.2.3 Atomic force microscopy

Atomic force microscopy experiments were carried out using Digital instruments multimode head attached to Nanoscope-IV controller (see Photograph in



Figure 3.3: Photograph of the atomic force microscope (Digital instruments multimode head).

Figure 3.3). Tapping and contact (lateral force) mode imaging was carried out using standard etched Si or Si_3N_4 cantilevers. The scanner was calibrated using a standard Pt coated Au grid with a pitch of $1\ \mu\text{m}$ and against the (0001) surface of HOPG (operating in STM mode). Au films from the interface were transferred to Si(100) substrates by gently lifting the substrate across the interface and were imaged in the tapping mode. Drop cast films of magnetic nanocrystals on Si(100) substrates were imaged in the tapping mode. For the lithographic study, freshly cleaved mica substrates were employed. The cantilevers were coated with nanocrystals by dipping the cantilever assembly in the nanocrystal sol and subsequently blow drying the cantilever with hot air. Contact mode imaging was carried out for this study.

3.2.4 Scanning electron microscopy and Energy dispersive analysis of X-rays

Scanning electron microscopy (SEM) was carried out with a Leica S-440i scanning electron microscope. Energy dispersive analysis of X-rays was performed with a Oxford microanalysis group 5526 system attached to the SEM employing Links (ISIS) software and a Si(Li) detector. Samples for SEM and EDAX were prepared by depositing a drop of the sol on an aluminum stub and allowing it to evaporate in air. EDAX analysis was carried out in the spot profile mode with a beam diameter of 1 μm at several places on the sample. The compositions reported represent averages of about 10 profiles.

3.2.5 Magnetic measurements

Magnetic measurements were carried out either a vibrating sample magnetometer (VSM 7300, Lakeshore) or a Quantum design superconducting quantum interference device (SQUID). The VSM was capable of reaching fields of upto 10 kOe, while the SQUID could reach upto 5 T. Magnetic measurements were carried out with a VSM on dried Co, Ni and Co-Ni alloy particles. For this purpose, about 20 mg of the sample was mounted on a perspex holder. Magnetic moments were measured as the samples were being cooled under a field of 0.5 kOe. Hysteresis measurements were carried out at the lowest temperature (50 K). Magnetic measurements were also carried out on oxide nanocrystals in a similar manner. Samples of Pd-Ni nanocrystals were prepared by sealing 1.5 ml (containing 0.9 μmoles of Pd ions) of thiolized nanocrystals dispersed in toluene in glass tubes. Zero field cooled (ZFC) measurements were carried out by cooling the sample down to 5 K in the absence of a field and measuring the magnetic moment in the heating cycle employing a field of 50 kOe. Field cooled (FC) measurements were carried out by cooling the sample in a field (50 or 0.5 kOe) and measuring the magnetic moment in the heating cycle.

Drop cast films of nanocrystals were held either parallel or perpendicular to the magnetic field direction and allowed to cool to the lowest temperature in the

remnant field. Hysteresis measurements were carried out during the heating cycle with a sweep time of 5 minutes. After reaching room temperature, the orientation of the film was changed and the cycle repeated to obtain hysteresis loops from the other orientation. A large sweep time was employed for the SQUID measurements.

3.2.6 X-ray photoelectron spectroscopy

X-ray photoelectron spectroscopy (XPS) was carried out with ESCA LAB MKIV spectrometer employing Al $K\alpha$ radiation (1486.6 eV). Samples for XPS were prepared by depositing a few drops of the sol on a graphite or a polycrystalline Au surface and drying in a vacuum. The reported binding energies are relative to the 84.0 eV Au($4f_{7/2}$) level.

3.2.7 X-ray diffraction

Powder X-ray diffraction measurements were carried out using Siemens Seifert 3000 X-ray diffractometer employing either Cu $K\alpha$ or Co $K\alpha$ radiation. Samples were prepared by depositing the nanocrystals in the form of films on a glass slide.

3.2.8 Other miscellaneous techniques

Thermogravimetric analysis were carried out with a Mettler Toledo instrument in the temperature range 100 – 900 °C under N₂ or O₂ atmosphere at a heating rate of 5 °C/min, typically using 25 mg of the sample in solid form mounted on a porcelain boat. UV-visible spectroscopy measurements were carried out with a Perkin-elmer lambda 900 spectrometer.

4. Results and Discussion

4.1 Submicron particles of Co, Ni and Co-Ni alloys

Sub-micron sized particles of Co, Ni and Co-Ni alloys have been successfully prepared by adopting a modified polyol process as detailed in the experimental section. The various experimental parameters such as the metal ion:reducing agent ratio and the metal ion:PVP ratio have been systematically varied over a range to ascertain their effect on the characteristics of the prepared particles. This variation in range has been facilitated by the fact that in the polyol reduction process, ethylene glycol acts both as a reducing agent and as a solvent and therefore the synthesis can be carried out over a wide range of the metal:reducing agent ratios especially in the reducing agent rich regime. Thus, the Ni^{2+} :ethylene glycol mole ratio was varied from 0.008:1 to 0.0045:1 and the Co^{2+} :ethylene glycol ratio varied from 0.005 to 0.0022. The metal:PVP weight ratios was varied in the range 1:4-1:20. The above reaction was carried out with $\text{Ni}(\text{SO}_4)$ instead of $\text{Ni}(\text{ac})_2$ as well.

Ni particles in the size range of 10 nm were obtained (see TEM image in Figure 4.1), when $\text{Ni}(\text{SO}_4)$ was used as Ni source instead of $\text{Ni}(\text{ac})_2$. SEM images obtained from a range of Co, Ni and CoNi alloy particles are shown in Figure 4.2. The images reveal that the particles are generally spherical in shape with a uniform diameter. In some portions of the images, agglomerated particles are seen - perhaps due to their magnetic nature. Typical histograms are shown in Figure 4.3. It is seen that the particles are monodisperse with $\sigma \sim 15 - 20\%$. By varying the Ni^{2+} :ethylene glycol mole ratio from 0.008:1 to 0.0045:1, the mean diameter of the particles could be varied from 520 nm to 750 nm. Similarly, in the case of Co, a change in the Co^{2+} :ethylene glycol ratio from 0.005:1 to 0.0022:1 resulted in a change of the particle diameters from 410 nm to 550 nm. We have verified that a *intermediatory choice of metal ion:reducing agent yields particles with diameters linearly proportional to the ratio in all the above cases*. A variation in the metal:PVP weight ratios however, produced no change in the obtained particle diameters.

XRD measurements confirmed the crystalline nature of the particles. All the

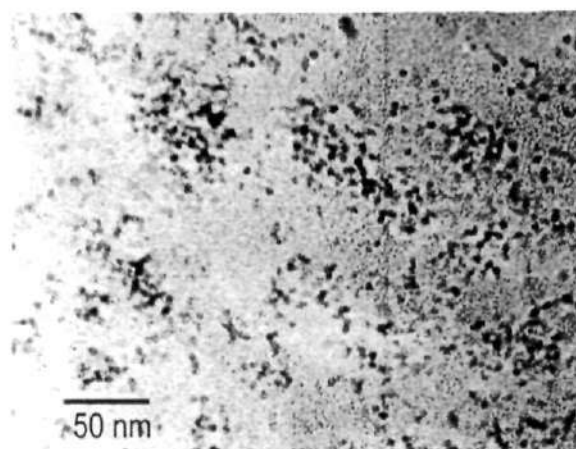


Figure 4.1: Transmission electron micrograph of small PVP covered Ni particles produced by reduction of Ni(SO₄).

Table 4.1: Properties of Co-Ni alloy particles

Metal salt feed ratio	Composition of the particles by EDAX	Phases as seen by XRD	Diameter	
			SEM (nm)	XRD (nm)
Co _{0.10} Ni _{0.90}	Co _{0.13} Ni _{0.87}	fcc	200	190
Co _{0.30} Ni _{0.70}	Co _{0.31} Ni _{0.69}	fcc	350	342
Co _{0.50} Ni _{0.50}	Co _{0.53} Ni _{0.47}	fcc	450	440
Co _{0.70} Ni _{0.30}	Co _{0.69} Ni _{0.31}	fcc + hcp	-	-
Co _{0.90} Ni _{0.10}	Co _{0.88} Ni _{0.12}	fcc + hcp	190	170

Ni particles were found to exhibit a fcc structure, similar to bulk Ni. The Co particles on the other hand, exhibited a hcp structure. The alloy particles, rich in Co exhibited both fcc and hcp peaks, while those with higher Ni content exhibited only fcc peaks. However, owing to the small difference in the lattice spacings of Ni and Co (Co = 0.35477 nm, Ni = 0.35238 nm), the peaks could not be definitively assigned to a solid solution of Co and Ni. These results are similar to the ones obtained with uncoated CoNi alloy particles obtained by other workers [182]. The diameter of the particles (d) could be estimated from the width of the X-ray peaks, by using the Debye-Scherrer relation which is give by:

$$d = \frac{0.91\lambda}{\beta \cos\theta} \quad (4.1)$$

where, λ is the X-ray wavelength, β , the peak width at half maximum and θ , the

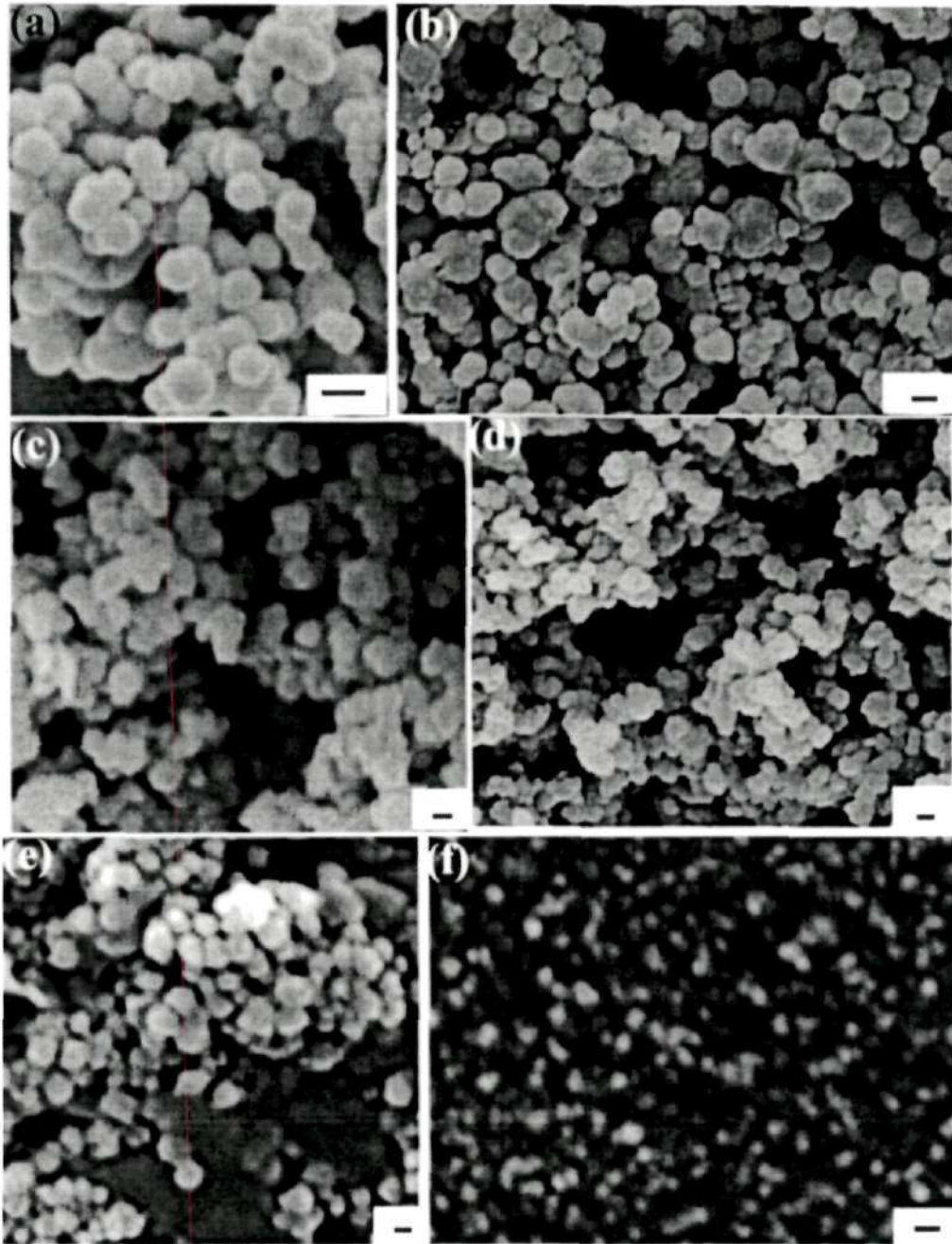


Figure 4.2: SEM micrographs of Co, Ni and Co-Ni alloy particles. (a) and (b) Co Particles; (c) and (d) Ni particles; alloy particles of composition (e) $\text{Co}_{0.50}\text{Ni}_{0.50}$ and (f) $\text{Co}_{0.90}\text{Ni}_{0.10}$. The scale bars on the images correspond to 500 nm

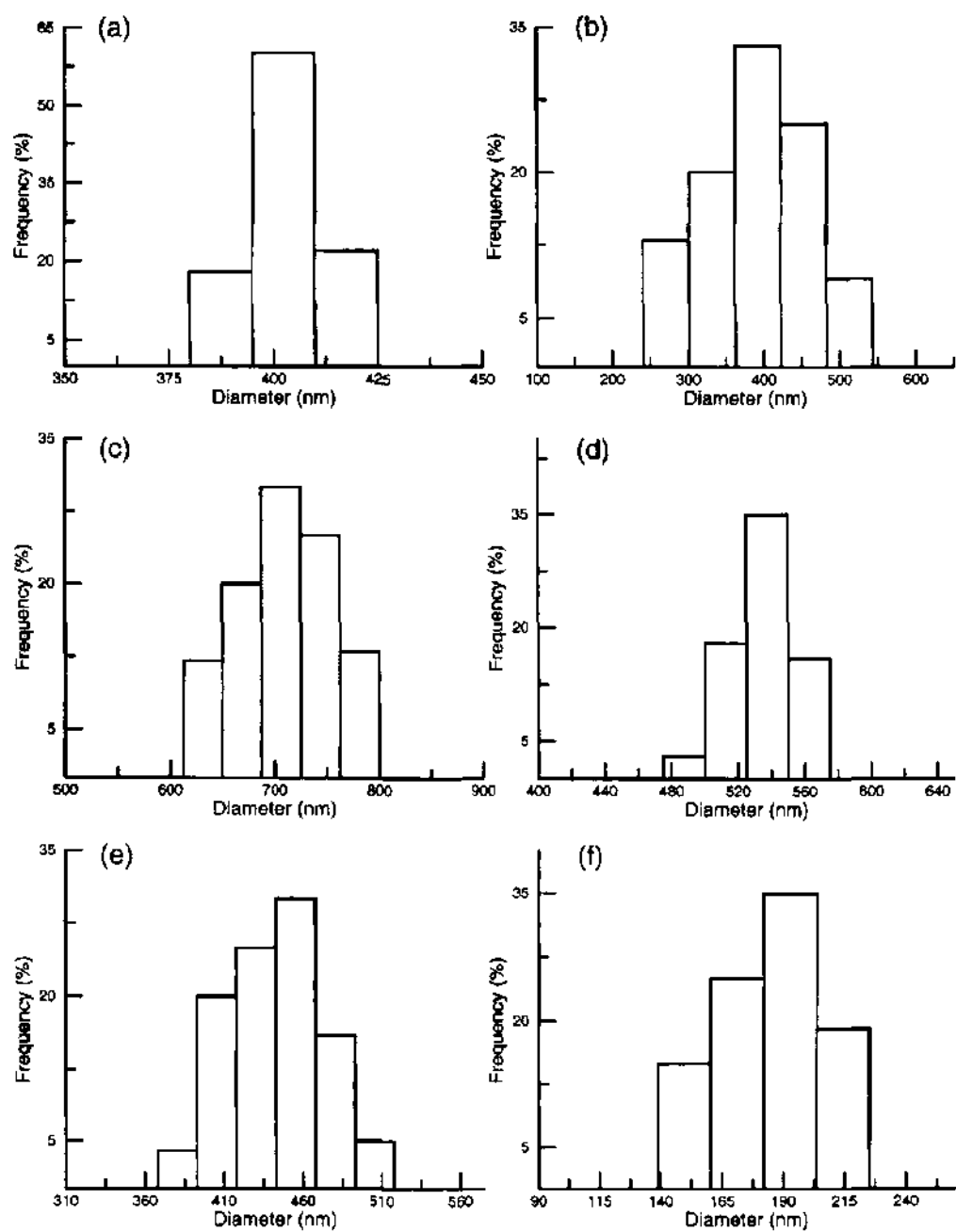


Figure 4.3: Histograms showing the size distribution of the Co, Ni and Co-Ni alloy particles. (a) and (b) Co Particles; (c) and (d) Ni particles; alloy particles of composition (e) $\text{Co}_{0.50}\text{Ni}_{0.50}$ and (f) $\text{Co}_{0.90}\text{Ni}_{0.10}$.

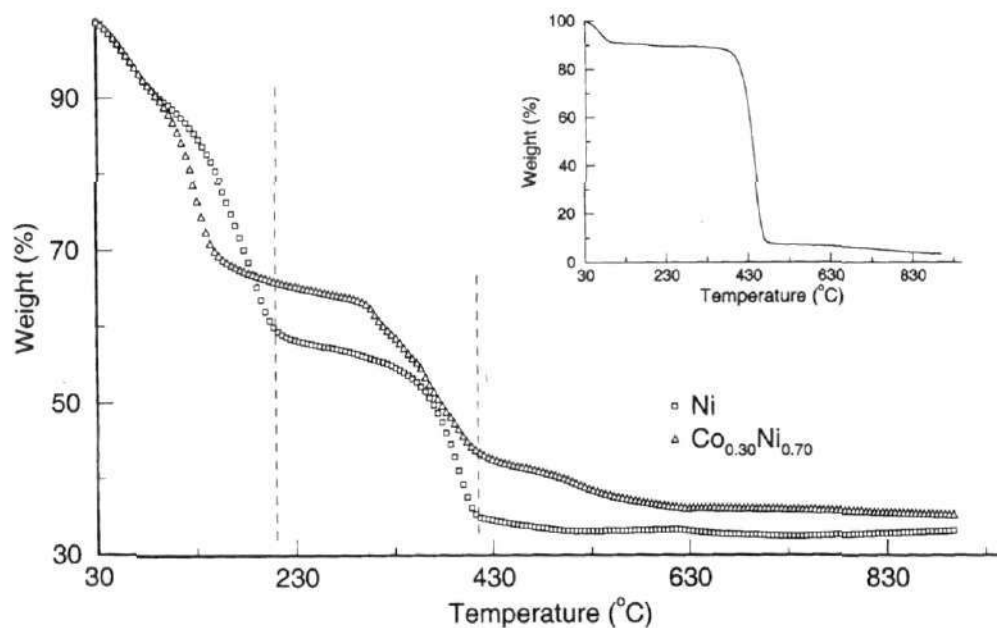


Figure 4.4: TG curves of Ni and $\text{Co}_{0.30}\text{Ni}_{0.70}$ alloy particles. The vertical lines demarcate the regions of weight loss corresponding to the solvent at ~ 200 °C and PVP at ~ 410 °C. Inset shows the TGA curve of PVP.

bragg angle. Accordingly, Ni and Co particle diameters were estimated based on the widths of the (111) and (011) peaks. The alloy particles were further analyzed by EDAX. Line and spot profile analyses yielded compositions within 2% of the feed ratio of the metal salts. The feed ratios, compositions determined by EDAX, the phase, the diameters determined by XRD and the diameters estimated from the SEM micrographs are given by way of summary in Table 4.1. The X-ray diameters are lower than those obtained from SEM as they do not include the PVP shell and correspond only to the diameter of the metal core.

In order to arrive at the actual metal content in polymer covered particles, TGA measurements were carried out under either nitrogen or oxygen gas flow. The TG curves for both Ni and CoNi alloy particles (in N_2 atmosphere) showed a two-step weight-decline pattern with the inflexion points at around 156 °C and 372 °C (see Figure 4.4), the former corresponding to the desorption of the solvent molecules and the latter, due to degradation of the PVP shell. The thermal decomposition temperature of PVP is ~ 375 °C, as seen in an independent measurement. Typically,

we have observed weight losses of $\sim 30\%$ for the solvent and $\sim 40\%$ for the PVP layer. In case of Co, a weight gain of $\sim 30\%$ was noticed at $\sim 250\text{ }^\circ\text{C}$ in a O_2 atmosphere. The metal content in this case was estimated, assuming complete oxidation of Co to Co_3O_4 . XRD analysis of the heat-treated sample confirmed complete oxidation of Co to Co_3O_4 .

Typical curves obtained in a M vs H sweep with submicron sized monometal particles, along with the measurement on corresponding bulk ingots are shown in Figure 4.5. The hysteresis loops tend to saturate in cases of Ni, while in case of Co, saturation was not observed. The saturating magnetic field was similar to the corresponding bulk metal and showed little dependence on size, in good agreement with studies of similar metal particles obtained by physical methods [214]. The coercivities, however, were different from the bulk, owing to small size of the particles [95] (see table 4.1). In case of both Co and Ni, a consistent increase in the coercivity value with size is noticed. In the case of Co, the coercivity of 550 nm particle is 512 Oe, significantly higher than the bulk coercivity (235 Oe). Further, it increases from 312 Oe to 512 Oe for a 240 nm change in the average particle diameter. Similarly, in case of Ni, the observed coercivity change is ~ 146 Oe for a change in diameter of 230 nm. The observed increase in coercivity with size indicates that the particles consist of a single magnetic domain [95]. (also see section 1.6)

In the case of Co-Ni alloy particles, the Ni rich compositions tend to saturate, while the Co rich compositions display no tendency for saturation (see Figure 4.6). In order to estimate the changes in the magnetic moment with composition, the magnetization at 8.5 kOe were examined (see inset of Figure 4.6). It was found that these values increase progressively to reach bulk Ni value. This trend is similar to the trend exhibited by bulk CoNi alloys.

We found that the PVP covered particles are stable in air for extended periods of time (few months) as against the naked Co and Ni particles. This could readily be seen by the fact that the particles were strongly attracted to a magnet, months after the preparation and could be confirmed by X-ray diffraction.

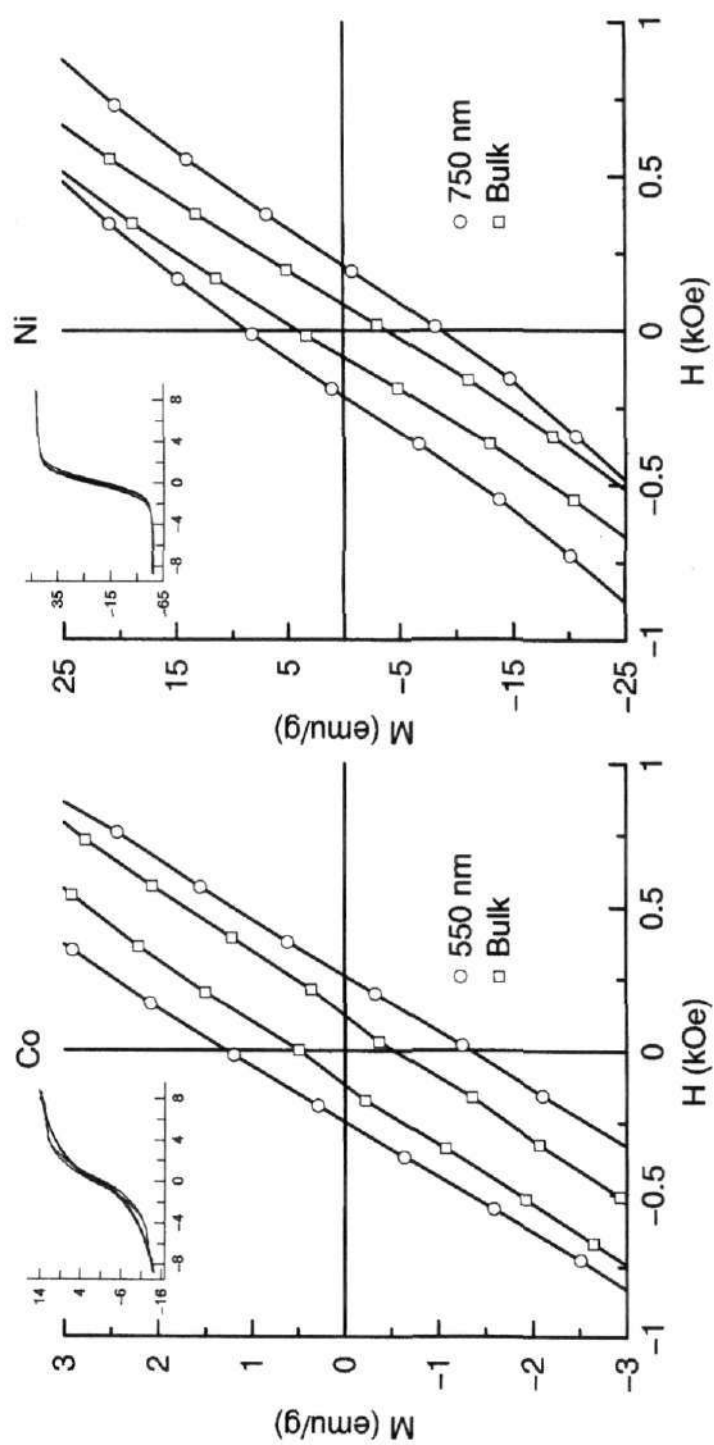


Figure 4.5: The area around zero field in M vs H sweep, showing the coercive field for Co and Ni particles along with that of the bulk. Inset shows the overlapping hysteresis loops of Co and Ni particles with their bulk analogues.

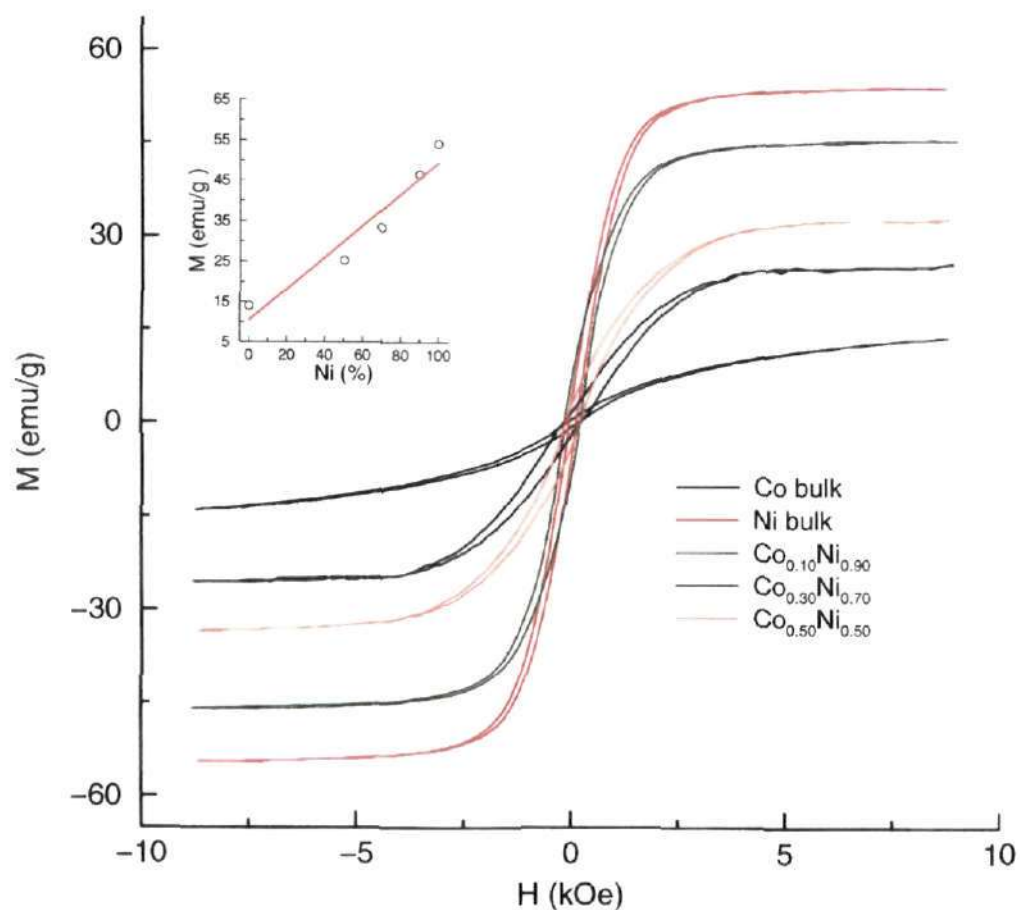


Figure 4.6: Hysteresis loops of Co-Ni alloy particles along with those obtained with ingots of pure Co and Ni. Inset shows the change in the magnetization value at 8.5 kOe field with composition.

In conclusion, magnetic sub-micron sized Co, Ni and CoNi alloy particles (with diameters in the range 100 – 600 nm) were prepared by a modified polyol method wherein a layer of polyvinylpyrrolidone protects the particles. The size of the particles could be varied by altering the metal:reducing agent ratio. The particles thus obtained were stable under ambient conditions, without undergoing oxidation. Further, the PVP coating does not significantly influence the magnetic properties of the Co, Ni and CoNi alloy particles.*

*A paper based on this study has appeared in Bull. Mater. Sci. (2001).

Table 4.2: Magnetic properties of Co and Ni particles

Sample	Diameter (nm)	M at 8.5 kOe (emu/g)	Coercivity (kOe)
Co bulk	-	13.9	235
Co	410	14.5	312
Co	450	13.6	410
Co	550	13.5	512
Ni bulk	-	54.1	176
Ni	520	53.5	280
Ni	690	54.3	378
Ni	750	54.0	426

4.2 Films of Au nanocrystals at liquid-liquid interfaces

It occurred to us that it should be possible to exploit a liquid-liquid interface to synthesize and cast metal nanocrystals into a film *in-situ*. For this purpose, we have made use of two immiscible liquids such as toluene and water, with the metal precursor in the organic layer and the reducing agent in the aqueous layer, as detailed in the experimental section. By this procedure, we have been able to obtain Au nanocrystals in the form of a film at the interface. The nature of the emerging film was examined by systematically varying factors such as contact time at the interface, the relative amounts of reducing agent and the Au precursor. Furthermore, the free-standing films obtained by the present method could be converted either to an organosol or a hydrosol by using appropriate capping agents.

In Figure 4.7, a photograph showing nanocrystalline Au at the interface along with those wherein the nanocrystals have been dispersed as organosols by using dodecanethiol and as hydrosols by using mercaptoundecanoic acid is presented. It can be readily seen that by the use of dodecanethiol and mercaptoundecanoic acid as capping agents, the nanocrystals at the interface can be completely transferred to the organic and the aqueous medium respectively. We believe that such a transfer is accomplished by the strong ligands containing the thiol group, displacing the



Figure 4.7: Nanocrystalline film of Au formed at the toluene-water interface (middle). Gold is introduced as a toluene solution of $\text{Au}(\text{PPh}_3)\text{Cl}$ while partially hydrolysed THPC (tetrakis(hydroxymethyl)phosphoniumchloride) in water acts as a reducing agent. The film is obtained when the two layers are allowed to stand for several hours. When dodecanethiol is added to the toluene layer, the film breaks up forming an organosol (left) while mercaptoundecanoic acid added to water produces a hydrosol (right).

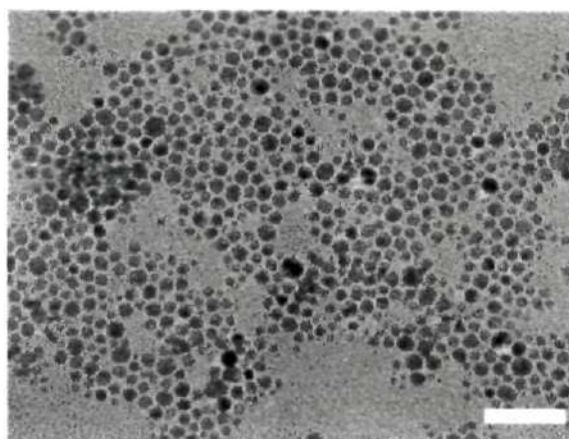


Figure 4.8: TEM micrograph of the as-prepared standard film obtained after 24 hours from a liquid-liquid interface containing 1.5 mM toluene solution of $\text{Au}(\text{PPh}_3)\text{Cl}$ and 330 ml of 50 mM THPC in 16 ml of 6.25 mM aqueous NaOH solution. The scale bar corresponds to 50 nm.

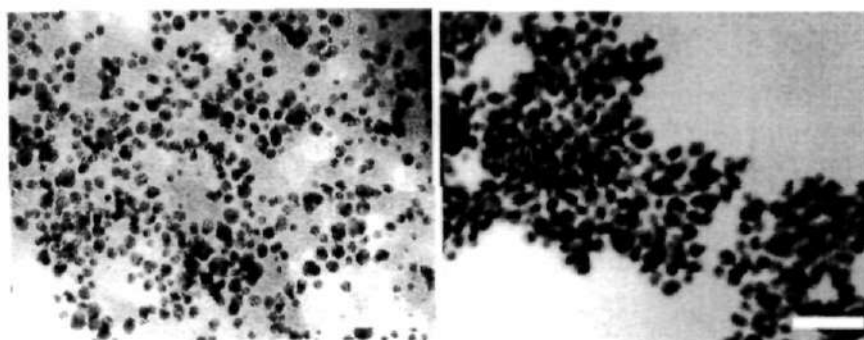


Figure 4.9: TEM micrographs of dodecanethiol capped nanocrystals (left) in the organosol and mercaptoundecanoic acid capped nanocrystals in the hydrosol (right). The scale bar corresponds to 50 nm.

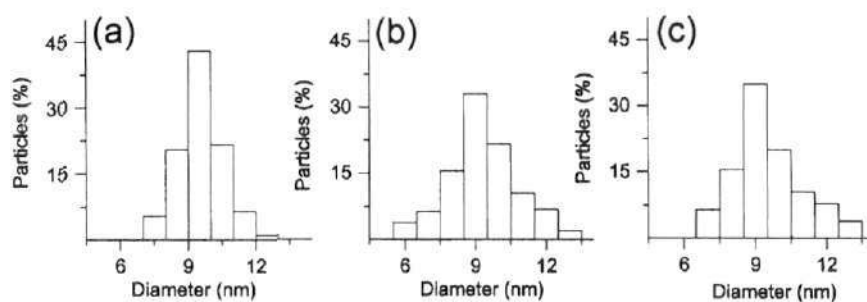


Figure 4.10: Histograms of the diameter distribution obtained from (a) the film at the interface; (b) the hydrosol obtained with mercaptoundecanoic acid and (c) the organosol obtained with dodecanethiol.

weaker ligand that are initially bound to the nanocrystal surface. The transfer can be effected by using other alkane thiols and amines as well.

In Figure 4.8, we show a TEM image of an as-prepared film of Au nanocrystals, obtained after maintaining the organic-aqueous interface with the reactants for 24 hours. The as-prepared film consists of nanocrystals with diameters in the range 5.5 to 14 nm with a mean of ~ 9 nm. The nanocrystals are present in a close packed arrangement with typical interparticle distance of 1.5 nm. A lower magnification image revealed that the film essentially consists of a monolayer of nanocrystals with a high coverage ($> 75\%$). Aggregates and multilayered films were seen in a few areas of the grid. The organosol and the hydrosol were examined by TEM and were seen to consist of Au nanocrystals (see Figure 4.9), however, the close packing of

nanocrystals present in the film is not seen in the case of the sols. Further, the particles transferred to sols possessed similar average diameters, but a somewhat wider size distribution (see Figure 4.10). TEM investigations reveal that a number of *multiply twinned particles* are present in these cases.

In Figure 4.11, TEM images of the films sampled after a contact times of 3, 6 and 9 hours respectively are shown. These images may be compared with that of the standard film shown in Figure 4.8 corresponding to a contact time of 24 hours. Clearly, an increase in contact time increases the coverage of the film on the substrate, with no observable change in the average diameter of the nanocrystals. Such a change is surprising since, it is generally expected that with time, the particle growth should take place monotonously, reaching higher and higher diameters. Although a more detailed study on the growth of nanocrystals is essential, our observations seem to suggest that the particle growth reaches saturation with time while fresh nucleation sites are constantly being created, thereby inhibiting the monotonous growth.

Use of high concentrations of the reducing agent results in less uniform films with altered distributions in the particle diameter as can be seen from a comparison of Figure 4.12 with Figure 4.8. When the concentration of THPC was doubled, the distribution was somewhat narrower with the average diameter of ~ 9.5 nm (Figure 4.12a). A further increase in the concentration of the reducing agent results in broader distributions in diameters (Figure 4.12b). We notice that the close-packing of the particles seen in Figure 4.8 is lost at higher concentrations of the reducing agent. The films formed at higher concentrations of the reducing agent also exhibit a distinct tendency to form multilayers.

The choice of the ingredients deserves a mention. It seems important that the right choice of the metal precursor and the reducing agent is employed to obtain stable films at the liquid-liquid interface. For instance, Au^{3+} ions complexed with tetraoctylammonium bromide in toluene did not form a film at the interface, but yielded an organosol. Similarly, more powerful reducing agents such as sodium borohydride fail to produce uniform nanocrystalline films. The choice of the

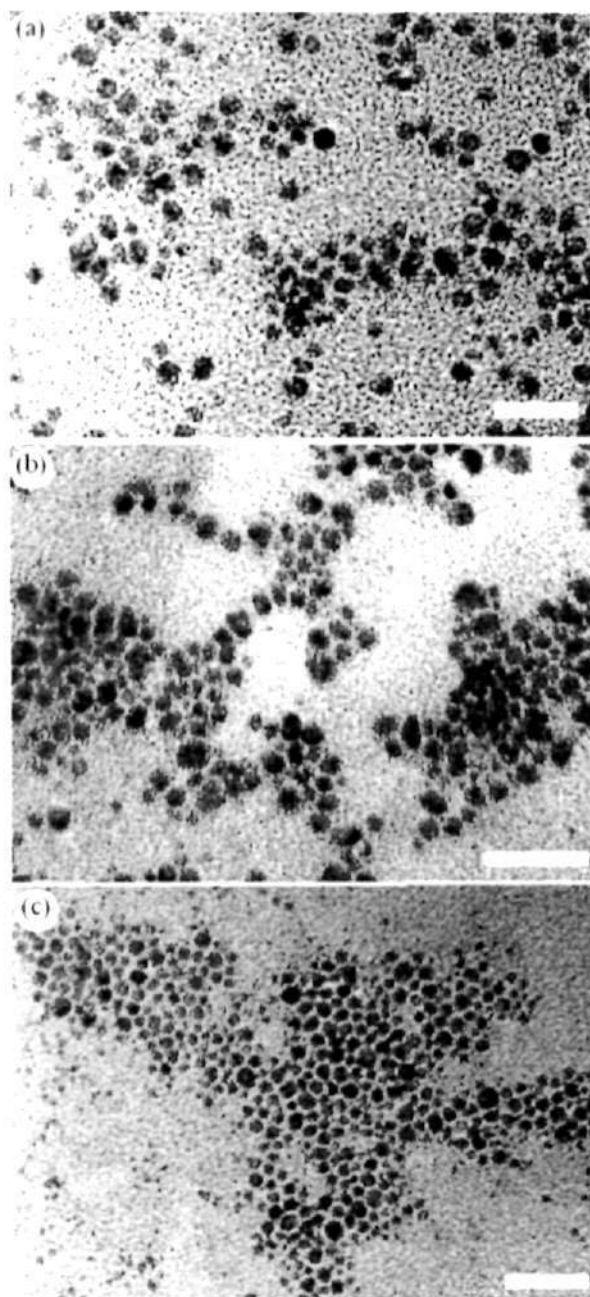


Figure 4.11: TEM micrographs of the films collected from a liquid-liquid interface containing 1.5 mM toluene solution of $\text{Au}(\text{PPh}_3)\text{Cl}$ and 330 μl of 50 mM THPC in 16 ml of 6.25 mM aqueous NaOH solution, with different contact times - (a) 3 hours (b) 6 hours and (c) 9 hours. The scale bars correspond to 50 nm.

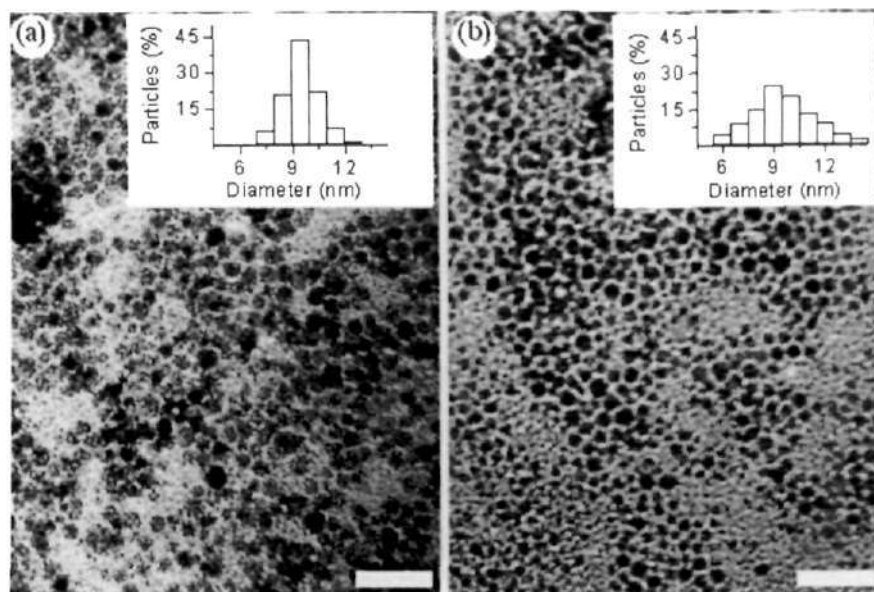


Figure 4.12: TEM micrographs of films collected after 24 hours from a liquid-liquid interface containing 1.5 mM toluene solution of $\text{Au}(\text{PPh}_3)\text{Cl}$ and 16 ml 6.25 mM aqueous NaOH solution with (a) 660 μl and (b) 1200 μl of 50 mM THPC. The concentrations correspond the metal:reducing agent ratios of 1:2 and 1:4 respectively. The scale bars correspond to 50 nm. Insets show histograms of the diameter distribution.

organic solvent also seems important. While we were able to obtain stable films with benzene and dichloromethane, solvents such as octanol were deterrent to film formation.

UV-Visible spectra of the as-prepared Au film as well as of the hydrosol and organosol are shown in Figure 4.13. All the spectra exhibit bands due to the surface plasmon, the position and intensity depending on several factors such as the diameter of the nanocrystals, the nature of the ligand and the refractive index of the surrounding medium [79,80]. The film on quartz substrate exhibits a broad band centered at 575 nm, while the sols show plasmon bands at ~ 530 nm. The band due to the octylamine-capped nanocrystals (organosol) is more intense compared to that of the MUA capped nanocrystals from the hydrosol, probably due to a dampening of the surface plasmon by the thiol. The higher wavelength of the plasmon band of the film could be due to the relatively higher dielectric constant of the surrounding medium.

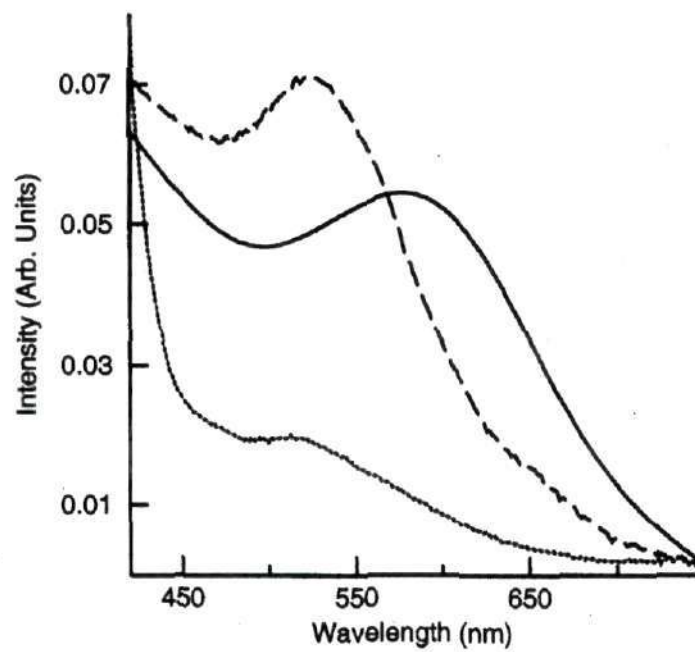


Figure 4.13: UV-Visible spectra of the as prepared standard film on a synthetic quartz substrate (dark line), octylamine capped nanocrystals in toluene (dashed line) and mercaptoundecanoic acid capped nanocrystals in water (dotted line).

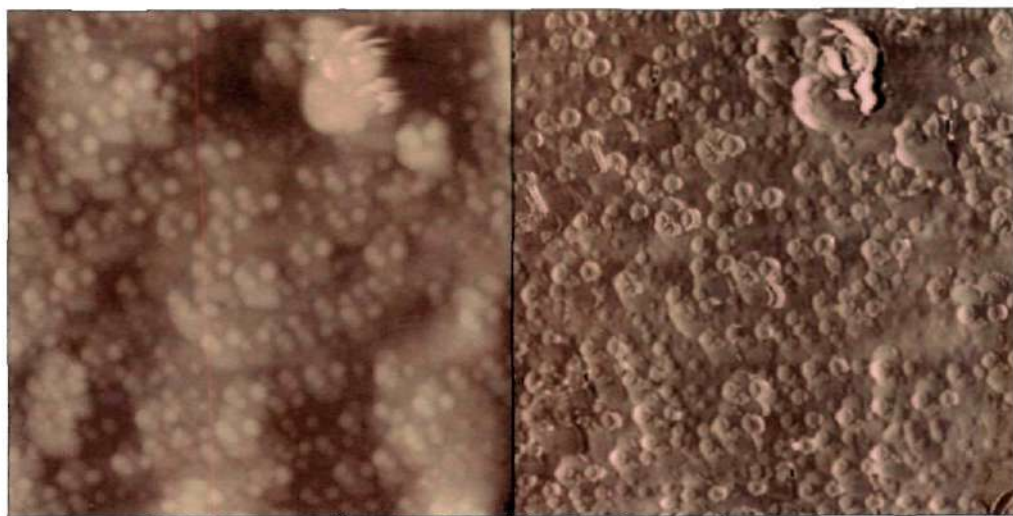


Figure 4.14: Tapping mode AFM images of the as prepared film in amplitude mode (left) and phase mode (right). The imaged area is 500 * 500 nm.

Tapping mode AFM images of the as prepared Au film reveals several features which are mostly spherical in nature (Figure 4.14), with diameters between 7 – 16 nm, somewhat higher than those from the TEM measurements. It is therefore possible that the nanocrystals consist of a layer of the organic ligand which are invisible in the TEM measurements [67, 215]. AFM images also reveal regions where the nanocrystals are aggregated. Wider scans covering few microns yielded a r.m.s roughness of ~ 35 nm with the maximum peak to valley distance of 80 nm. The surface composition of the film was probed using core-level XPS. The Au(4f) spectra showed a broad doublet, which could be fitted to two Au species with $4f_{7/2}$ binding energies of 84 and 85.2 eV. This is consistent with the picture of a metallic core surrounded by a layer of Au atoms bound to the capping agents [216]. The latter may consist of triphenylphosphine ligands and ionic species from THPC. The spectrum revealed the presence of phosphorous and chlorine in the film.

The free-standing nanocrystalline Au films can be lent some extra strength with the help of solid supports which may also attribute additional properties. Use of polystyrene support, for example, yields flexible and transparent films. We found that a few drops of a toluene dispersion of the polymer added to the layer atop the interface yielded the desired film upon evaporation of the solvent. The film thus obtained was continuous and contained a high density of nanocrystals. We envisage several potential applications of such films in color filters and radiation shields.

By simultaneously increasing both the Au precursor and the reducing agent concentration, thin films of Au with high luster were obtained at the interface. XRD diffraction measurements confirmed the crystalline nature of these films. In Figure 4.15, a typical AFM image of such a film transferred to a HOPG substrate is presented. The AFM image reveals that the film is made up of granules of Au, with typical r.m.s surface roughness of 35 nm. The inset in Figure 4.15, shows a photograph of a glass slide coated with the lustrous Au film.

In conclusion, preparation of films of nanocrystals of Au at the liquid-liquid interface has been accomplished by taking $\text{Au}(\text{PPh}_3)\text{Cl}$ in organic layer and partially hydrolyzed THPC in the aqueous layer. The particle diameters and the film coverage

4.3. Effect of size on the Coulomb staircase behaviour in Au and Pd nanocrystals

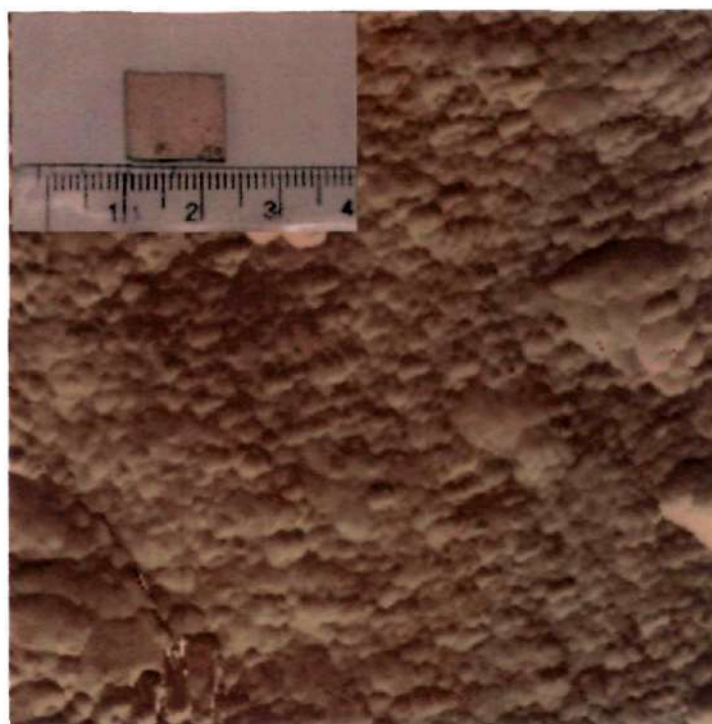


Figure 4.15: Tapping mode AFM images (in phase contrast mode) of the lustrous Au films transferred to a highly oriented pyrolytic graphite substrate. The imaged area is $1.84 \mu\text{M}^2$. The film was prepared starting with 10 mM solution of $\text{Au}(\text{PPh}_3)\text{Cl}$ in toluene. Inset shows a picture of a similar film transferred on a glass substrate.

are dependent on the contact time and the concentration of the reactants. The films show surface plasmon bands characteristic of Au nanocrystals. The nanocrystals in the films are readily extracted to aqueous or organic layers by adding suitable capping agents. This method can be extended to prepare thin granular films of Au. A particularly noteworthy aspect of the study is that the nanocrystalline film at the interface can be easily transferred onto a solid support.[†]

4.3 Effect of size on the Coulomb staircase behaviour in Au and Pd nanocrystals

In Figure 4.16, typical STM images of Pd and Au nanocrystals dispersed on a HOPG substrate are shown. I-V spectra were obtained by positioning the tip atop

[†]A paper based on this study is set to appear in *J. Phys. Chem.* (2003).

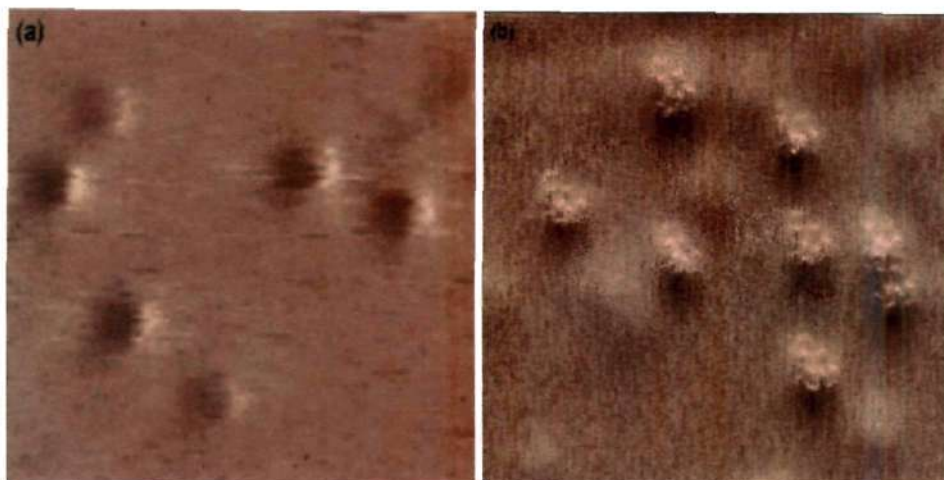


Figure 4.16: STM images of (a) PVP covered Pd₅₆₁ and (b) dodecanethiol capped Au nanocrystals. The scanned area in each case is 25 nm². In a, the observed diameters are (3.4 ± 0.2) nm and the imaging conditions are - sample bias: 0.2 V, setpoint current: 2 nA. In b, the imaging conditions are - sample bias: 200 mV, setpoint current: 2 nA. The features seen on each nanocrystals are the head-groups of thiol molecules.

such nanocrystals as described in the experimental section. In Figure 4.17, the I-V spectra obtained with Pd nanocrystals of 3.3, 4.4 and 6.4 nm diameter are shown. The curves are characteristic of metal-insulator-metal (MIM) junctions [217], modulated on either side of the zero bias by a series of current-voltage steps. The 3.3 nm nanocrystal, corresponding to the magic nuclearity five shell Pd₅₆₁ exhibits a step width of 208 mV or a charging energy of 208 meV. The voltage range studied ± 750 mV was wide enough to allow charging of the nanocrystal up to several electrons. What is striking is that both the step width and the number of steps vary with the nanocrystal diameter. The step width, which is 208 mV for the 3.3 nm nanocrystal, decreases to 158 mV in the case of the 4.4 nm nanocrystal, and to 116 mV for the 6.4 nm nanocrystal. The 3.3 nm nanocrystal exhibits three steps on either side of the zero bias which amounts to three times the electronic charge on it. The 4.4 and 6.4 nm nanocrystals display five and seven steps, respectively in the same voltage range. We also notice that the overall current is higher for the larger metal cores [72]. The derivative spectra shown in Figure 4.17 reveal uniformly spaced peaks corresponding to the steps in the I-V data.

4.3. Effect of size on the Coulomb staircase behaviour in Au and Pd nanocrystals

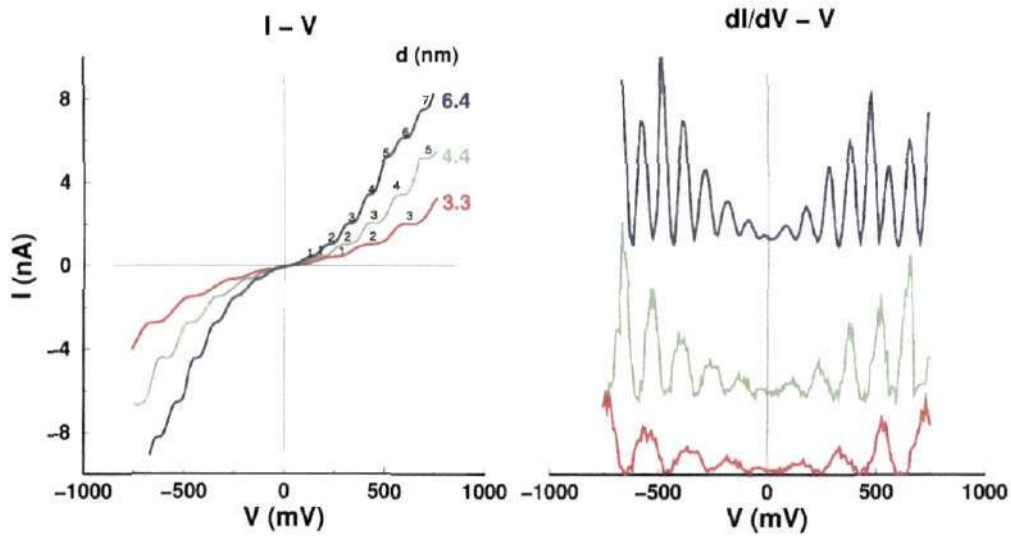


Figure 4.17: I-V spectra of isolated Pd nanocrystals of different sizes. The derivative spectra are shown alongside.

A model proposed by Amman et al. [218] has been used to describe the observed Coulomb staircase behavior and to relate the I-V curves to physical quantities. This model called the semi-classical model is schematically illustrated in Figure 4.18. It is based on a double junction of capacitors and provides a means by which the observed capacitance (C) can be resolved into two components C_1 and C_2 , and the resistance (R) into R_1 and R_2 , such that $C = C_1 + C_2$ and $R = R_1 + R_2$ (see Figure 4.18b). For $C_1 \ll C_2$ and $R_1 \ll R_2$, the model predicts steps in the measured current to occur at critical voltages,

$$V_c = \frac{n_c e}{C} + \frac{q_0 + e/2}{C} \quad (4.2)$$

where q_0 is the residual charge. The fit obtained in the case of the 3.3 nm Pd nanocrystal is shown in Figure 4.19. Noticeable deviations from the model are seen specially at higher voltages. Considering that the measurements were carried out at room temperature, it is actually surprising that the semi-classical model yields such reasonable fits. The analysis gave estimates for the circuit constants as follows: $C_1 = 0.07$ aF, $C_2 = 0.7$ aF, $R_1 = 0.5$ M Ω , $R_2 = 255$ M Ω , $q_0 = 0$ e. These values are typical of ligated metal clusters [218]. The capacitance of a metal nanocrystal can be estimated from the classical expression for the capacitance of a metal sphere

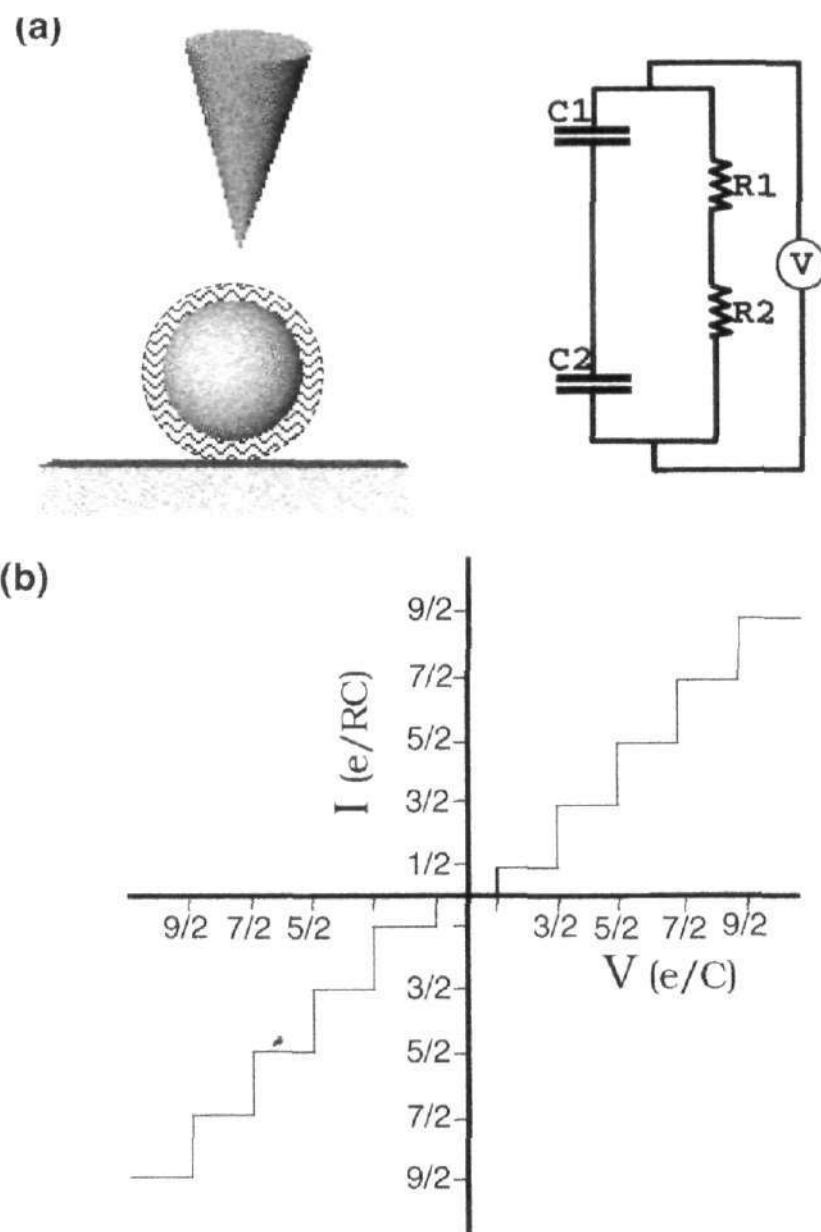


Figure 4.18: Schematic illustration of (a) a single electron tunnel junction formed by a nanocrystal held between the STM tip and the substrate. The particle diameter varies between 1.7 and 6.4 nm and the thickness of the PVP coating is ~ 1 nm. The "equivalent" circuit is shown alongside. (b) I-V spectra showing a Coulomb staircase.

4.3. Effect of size on the Coulomb staircase behaviour in Au and Pd nanocrystals

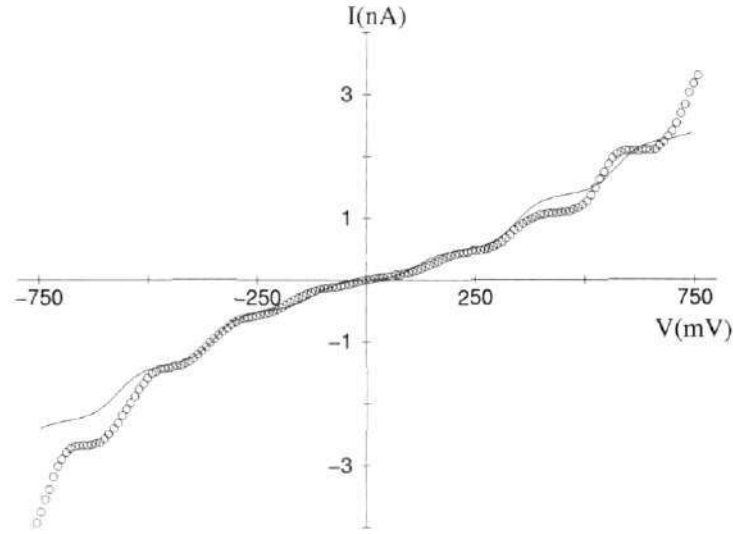


Figure 4.19: I-V characteristic of an isolated 3.3 nm Pd nanocrystal (dotted line) and the theoretical fit (solid line) obtained with the semiclassical model.

(C_d) in a dielectric medium

$$C_d = 2\pi\epsilon_0\epsilon d \quad (4.3)$$

Here d is the diameter of the particle [74]. Assuming $\epsilon_{\text{PVP}} = 3$ [219], we obtain $C_{3.3 \text{ nm}} \sim 0.6 \text{ aF}$ which matches closely with the tunnelling measurement. Similar results were obtained with other nanocrystals.

The I-V data obtained with the Au nanocrystals are shown in Figure 4.20. The smallest nanocrystal studied (1.7 nm) exhibits a three-step Coulomb staircase with a step width of 229 mV. Larger nanocrystals display a larger number of steps with smaller widths, just as the Pd nanocrystals. The MIM characteristics in Figure 4.20 are somewhat distorted specially in the case of smaller nanocrystals, possibly due to an unfavorable ratios of the capacitances and resistances [187].

The measurement of energies of free metal clusters has led to a scaling law, which relates the measured charging energy to the diameter of the cluster. Further theoretical treatment resulted in a scaling law of the form

$$U = A + \frac{B}{d} \quad (4.4)$$

where A and B are constants [220]. In order to examine whether the charging energies obtained from the above data follow a scaling law of the above form, we

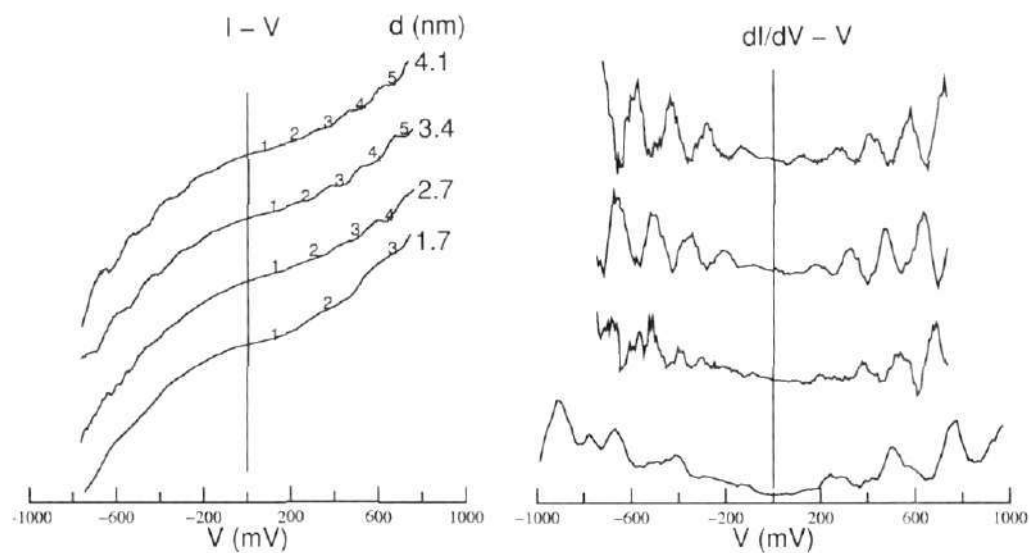


Figure 4.20: I-V spectra of isolated Au nanocrystals of different sizes. The derivative spectra are shown alongside.

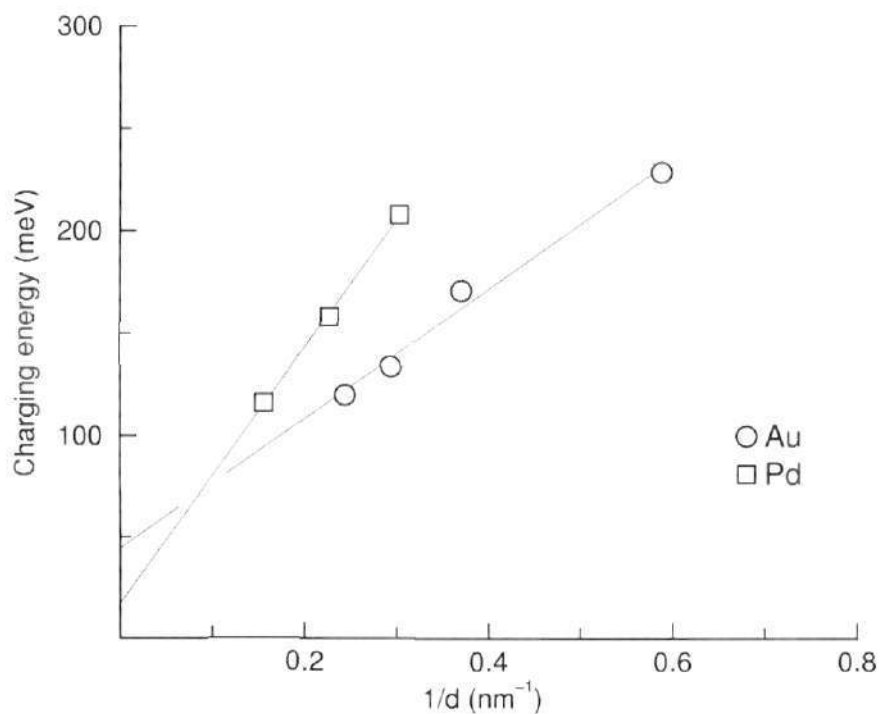


Figure 4.21: Variation of the charging energies of Pd and Au nanocrystals with inverse diameter.

4.3. Effect of size on the Coulomb staircase behaviour in Au and Pd nanocrystals

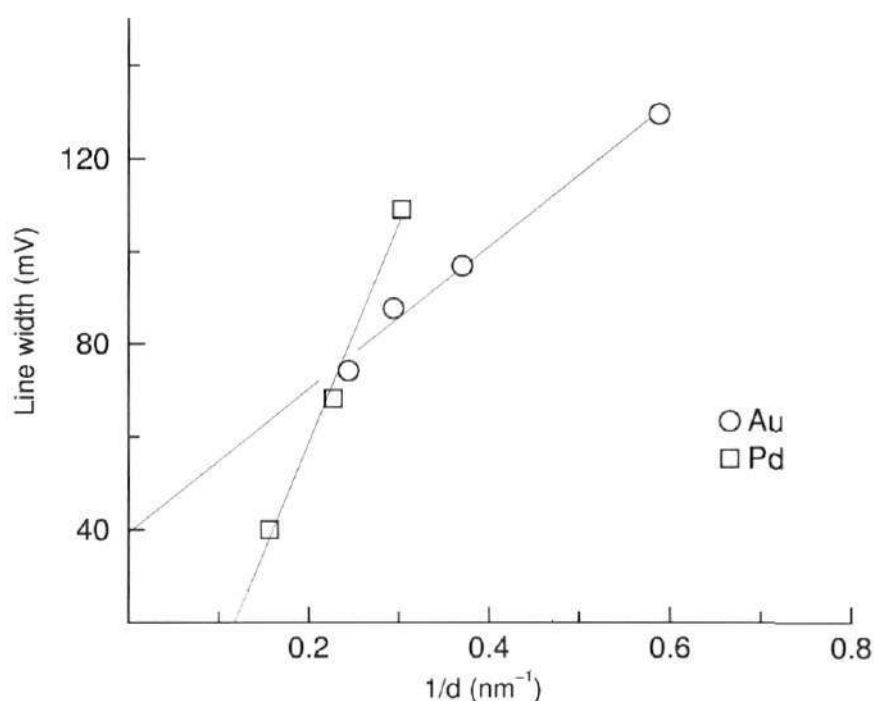


Figure 4.22: Variation of the line width of the derivative spectra of Pd and Au nanocrystals with inverse diameter.

have plotted the charging energy against $1/d$ in Figure 4.21. We see that the plots are linear showing that the scaling law is indeed obeyed. The intercepts for the Pd and Au nanocrystals are quite close (17 and 40 meV respectively). The slopes (B) are, however, different 627 and 318 meVnm^{-1} respectively. The model predicts a significantly higher value of the slope (1440 meVnm^{-1}). The difference between the model and the experimental observation may be due to the presence of the polymer coating and also possibly due to interaction of the nanocrystal with the substrate. The values of the intercepts are related to the bulk inner band energies.

An interesting observation from the derivative spectra in Figures 4.17 and 4.20 is that the line width, which is a representation of the diffused nature of a Coulomb step, varies with the nanocrystal size. The line width for the 3.3 nm Pd nanocrystal is $\sim 107 \text{ mV}$ while for 4.4 and 6.4 nm nanocrystals, the widths are 72 and 38 mV, respectively. A similar trend is seen in the case of Au nanocrystals (Figure 4.20). It is possible that such smearing of the I-V data occurs due to thermal excitations in the tunnel junction at room temperature. However, the observed systematics points to a

size effect. It is noteworthy that the line width also exhibits a linear relationship with the inverse diameter, much like the charging energy itself (See Figure 4.22). The two systems of nanocrystals exhibit different slopes and intercepts. We do not have an explanation for the size dependence of the line width at this stage. It is possible that the observed line broadening could arise due to tunnelling from the vicinity of the Fermi level of the nanocrystal to the substrate, the tunnel barrier decreasing with decreasing nanocrystal size [221]. This effect could also arise, in principle, due to an off-centered tip. We, however, believe this not to be the case in the present study.

We made attempts to study the Coulomb staircase phenomenon in thiolized Au nanocrystals and the magic nuclearity Au₅₅ nanocrystal. Both the systems showed no evidence for single electron tunnelling at room temperature. This is possibly because the ligands do not form sufficiently insulating tunnel barriers.

In conclusion, we have observed Coulomb staircases at room temperature in tunnel junctions formed by PVP ligated nanocrystals of Pd and Au. Our observations relate to the charging effects of a classical conducting particle, the charging energy obeying a scaling law with respect to the inverse of the diameter. The observed differences in charging energies of Au and Pd nanoparticles may originate from the inherent differences in the electronic structure of Pd and Au systems (viz., 5d¹⁰ and 5d¹⁰6s¹ respectively). The different way of interaction of the metal with the ligand shell should also be taken into account, to arrive at a viable explanation.[‡]

4.4 Two-dimensional arrays of Pd nanocrystals

Arrays formed by Pd nanocrystals of various dimensions capped with thiols of different chain lengths have been studied. For this purpose, hydrosols of Pd were prepared as detailed in the experimental section. The Pd hydrosol obtained with 40% ethanol consisted of nanocrystals with a mean diameter of 1.8 nm. The distribution in the particle diameter was quite narrow ($\sigma \sim 15\%$). The diameters of magic nuclearity Pd₅₆₁ and Pd₁₄₁₅ nanocrystals were 2.5 and 3.2 nm (see Figure 4.23),

[‡]A paper based on this study has appeared in *Chem. Phys. Lett.* (2000).

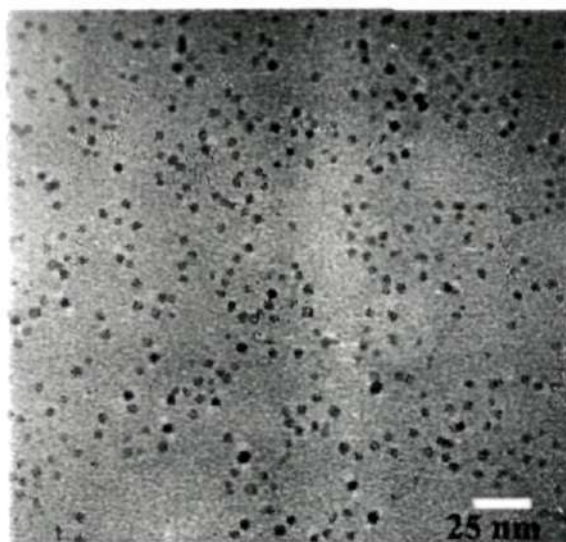


Figure 4.23: TEM image as prepared PVP covered Pd₅₆₁ nanocrystals.

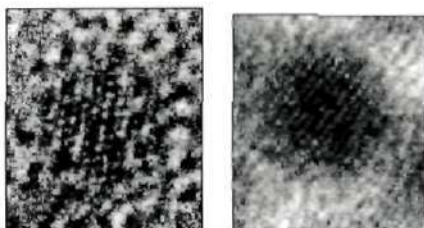


Figure 4.24: HRTEM images of Pd₅₆₁ (left) and Pd₁₄₁₅ (right) nanocrystals.

with narrow size distributions ($\sigma \sim 6$ and 7% respectively). High resolution TEM images of Pd₅₆₁ reveal the icosahedral shape of the particles and the characteristic 11 [111] lattice fringes (see Figure 4.24). In the case of Pd₁₄₁₅ nanocrystals, 15 [111] lattice fringes are seen (see Figure 4.24). The average diameter of Pd nanocrystals obtained by the two stage growth process was found to be 4.5 nm (see Figure 4.25). The average diameter of Pd nanocrystals obtained by the method of Porta et al. [207] was 6.0 nm ($\sigma \sim 14\%$). The smaller diameter distribution in the case of magic nuclearity Pd₅₆₁ nanocrystals is noteworthy.

The PVP covered nanocrystals were thiolized to obtain nanocrystals capable of forming arrays. The PVP and thiol covered nanocrystals were studied by means of XPS (see Figure 4.26). The binding energy of Pd(3d_{5/2}) core level was at 334 eV comparable to metallic Pd in both cases - before and after thiolization. However,

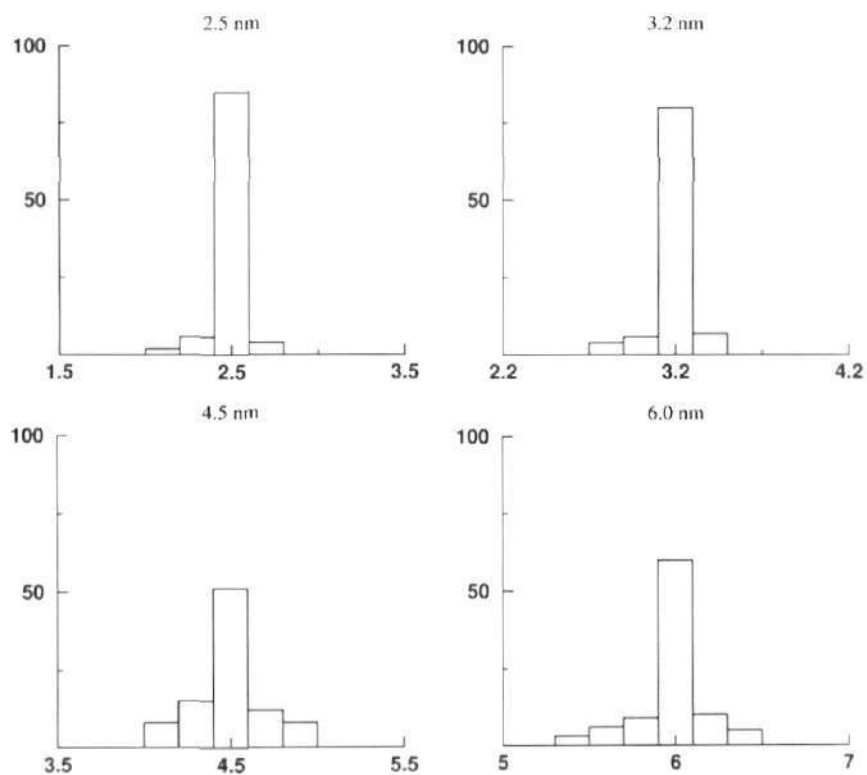


Figure 4.25: Histograms showing the distribution in the diameters of Pd hydrosols.

the N(1s) feature at ~ 400 eV present in the PVP capped nanocrystals was not seen after thiolization. Instead a new feature at 163.5 eV due to S(2p) was seen, showing that the thiol molecules were chemisorbed on the surface of the Pd nanocrystals in the organosol. Thus, the thiolization process results in complete replacement of the PVP ligand shell with a thiol layer.

In Figure 4.27, TEM micrographs showing lattices formed by nanocrystals of diameters 2.5 and 3.2 nm derivatized with octanethiol and dodecanethiol are presented. Organized arrays extending to several microns are seen in the images. *The honey-comb like ordering of the nanocrystals propagates a few tens of nanometers before being interrupted by a line or point defect [100].* With the change of thiol from octanethiol to dodecanethiol, the packing of the nanocrystals looks somewhat different (compare a and c with b and d of Figure 4.27). The self-assembly of thiol molecules on the faceted nanocrystal surface perhaps

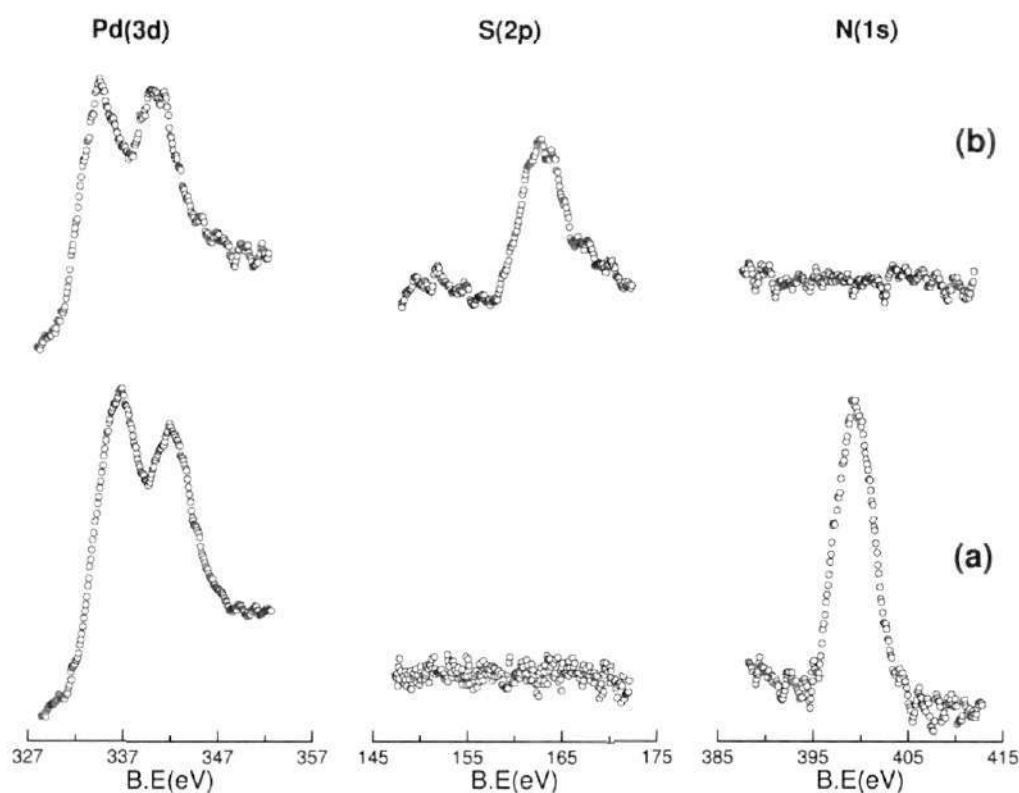


Figure 4.26: X-ray photoelectron spectra of Pd₅₆₁ nanocrystals (a) before and (b) after thiolization.

determines the structure of the organization [114]. The 2.5 nm particles coated with octanethiol (Figure 4.27a) exhibit a pattern where a nanocrystal at the center of the hexagonal arrangement is more prominent compared to the surrounding ones. The 3.2 nm particles coated with dodecanethiol (Figure 4.27d) also organize in a similar fashion. These are essentially bilayered structures [222] where the nanocrystals in the top layer occupy the 2-fold saddle sites to form a hexagon which is rotated by 30° with respect to the hexagon below (see Figure 4.28). On the other hand, the hexagonal arrays shown in Figure 4.27b (2.5 nm/dodecanethiol) and Figure 4.27c (3.2 nm/octanethiol) are more commonly observed [111–120]. A special feature of the above four arrays is that they are composed of magic nuclearity nanocrystals. This study constitutes the first report of organization of magic nuclearity nanocrystals into ordered arrays. Schmid et al. [223] have recently reported the formation of ordered two-dimensional monolayers of Au₅₅ nanocrystals

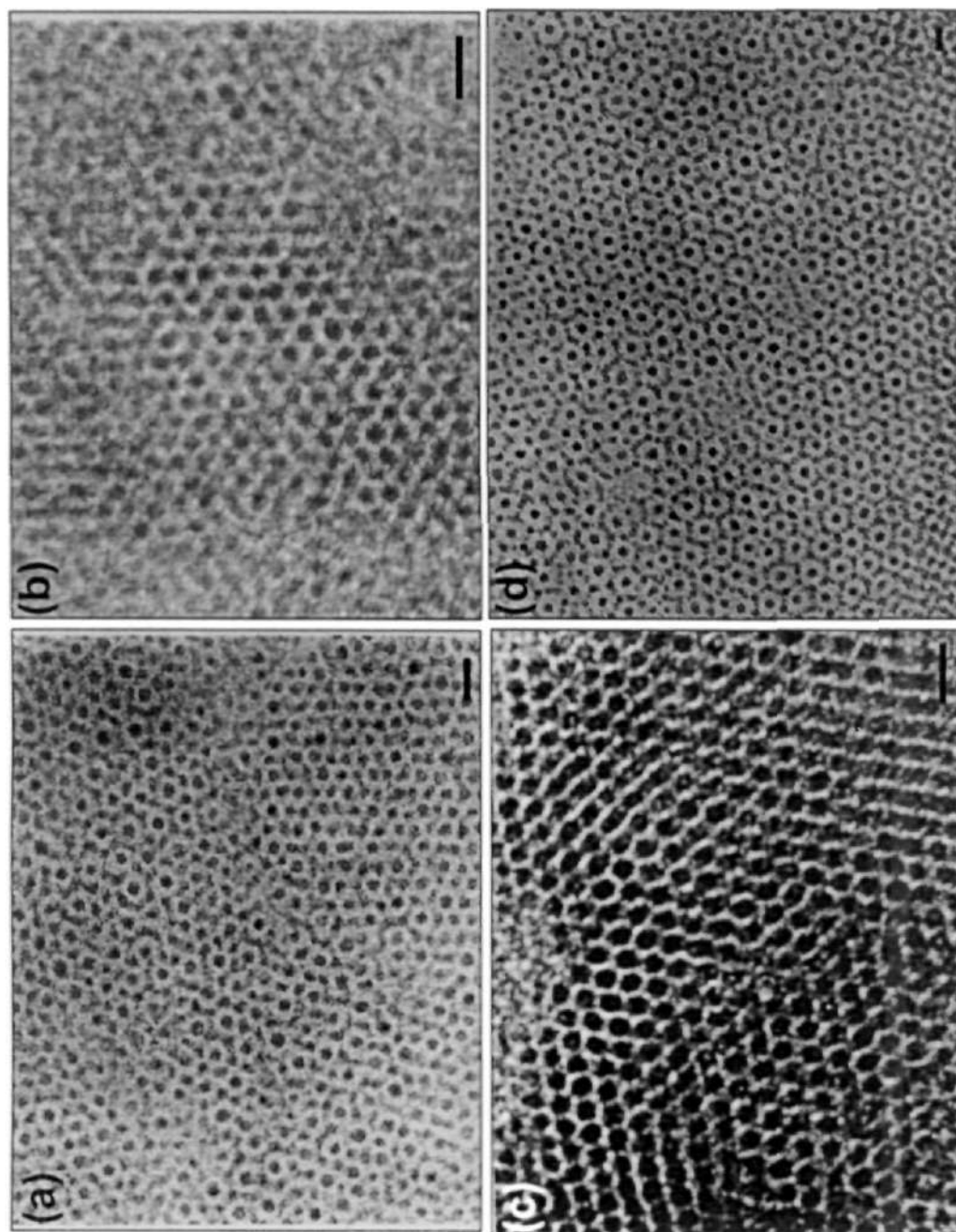


Figure 4.27: TEM micrographs showing hexagonal arrays of thiolized Pd nanocrystals: (a) 2.5 nm, octanethiol (b) 2.5 nm, dodecanethiol (c) 3.2 nm, octanethiol, and (d) 3.2 nm, dodecanethiol. The scale bars correspond to 10 nm.

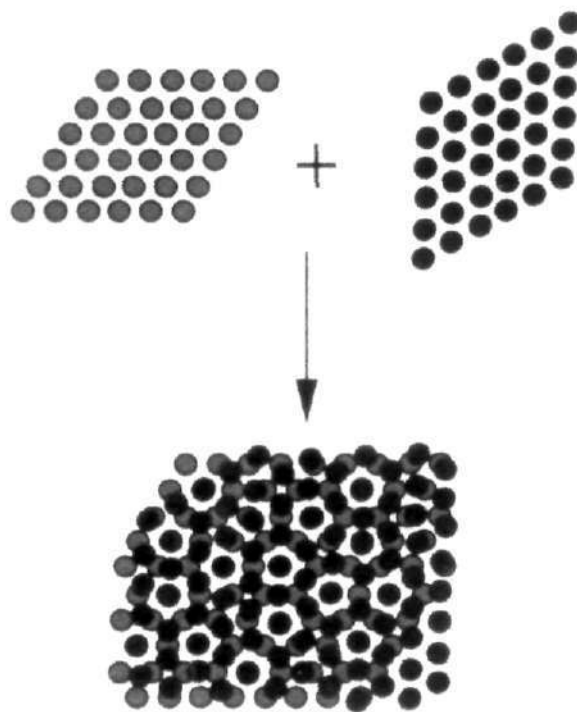


Figure 4.28: Schematic illustration showing multiple ring sequences formed by overlap of two hexagonal ABCABC rafts, one of which is rotated by 30° with respect to the other. Such a rotation places the top hexagonal raft at the 2-fold saddle sides on the bottom hexagonal raft.

on a polymer film. In the present study, however, nanocrystals of choice are thiolized and organized.

We have analyzed the two-dimensional lattices of thiolized nanocrystals in terms of the distribution in the center to center nearest neighbour distance " c " and an angle α , subtended by a pair of nearest neighbours using a computer code developed by us. c and α are schematically illustrated in Figure 4.29. Six nearest neighbors of a given nanocrystal were considered to determine the distribution in c . The angles subtended by all possible pairs of the nearest neighbors were analyzed and six angles closest to 60° were chosen to calculate the distribution in α . For an ideal lattice, c and α would have to be single line histograms and this was used to test input to the code. The distributions in c and α for the lattices illustrated in Figure 4.27 are depicted in Figure 4.30. The mean values of c and α for the 2.5 nm particles coated with dodecanethiol: $c = 4.1$ nm ($\sigma = 8\%$) and $\alpha = 60^\circ$ ($\sigma = 13\%$). Assuming a

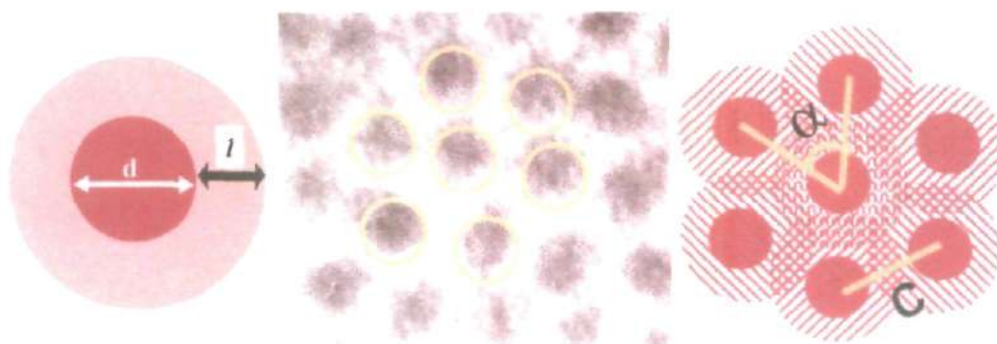


Figure 4.29: Schematic illustration of the various parameter used to characterize the nanocrystal arrays: d -the nanocrystal diameter, l -the ligand chain length, c -the nearest neighbour distance, α -the angle subtended between two nearest neighbours.

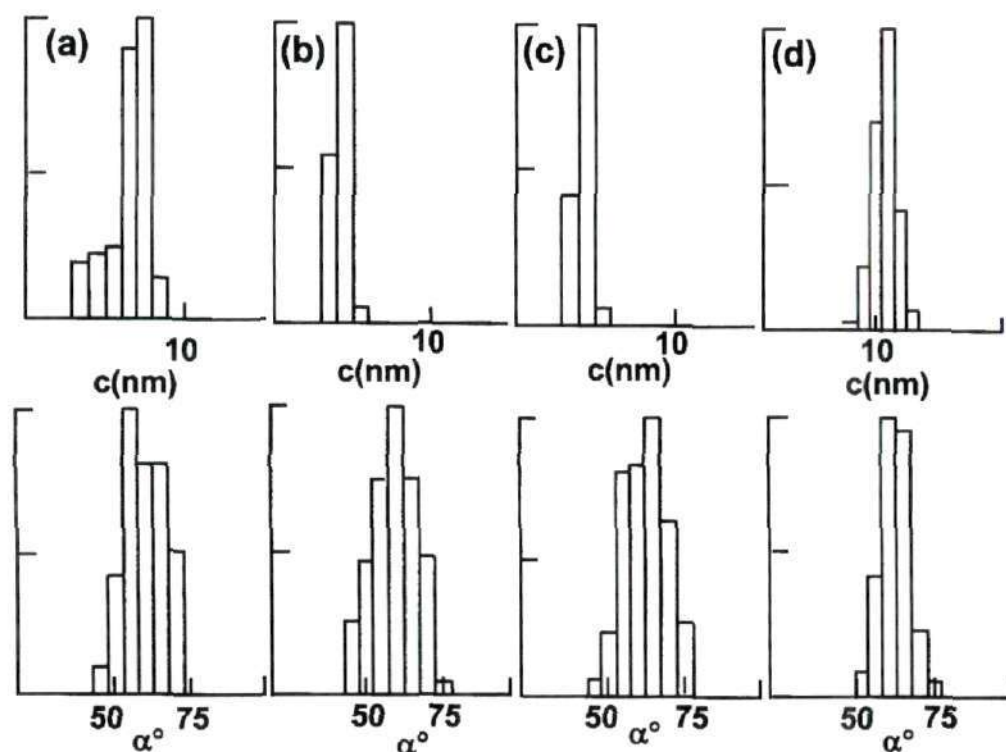


Figure 4.30: Histograms showing the distribution (normalized to 100%) in the nearest neighbour distance, (d), and the angle, α for the cases of (a) 2.5 nm, octanethiol (b) 2.5 nm, dodecanethiol (c) 3.2 nm, octanethiol, and (d) 3.2 nm, dodecanethiol.

fully extended all trans conformation of the dodecanethiol molecule inclined 30° on the particles surface, its projected chain length, ℓ is ~ 1.7 nm [192]. Accordingly, the expected c value (diameter plus twice the chain length) is ~ 5.9 nm. The observed value of 4.1 nm is considerably smaller due to interpenetration of the ligand shells of the neighbouring nanocrystals. A reduction in the c value of 1.8 nm amounts to 53% interdigitation of the thiol molecule. On the contrary, the octanethiol molecules on the 3.2 nm particles (Figure 4.27c) exhibit 25% interdigitation ($c = 5.0$ nm, $\ell = 1.2$ nm). The histograms in Figure 4.30a and d refer to the second neighbours, and the interdigitation of the thiol molecules in these cases is estimated to be 48% and 31% respectively. From the histograms in Figure 4.30, we observe that the distribution in α is somewhat narrower in the case of dodecanethiol-assisted organizations.

The effect of the thiol chain length on nanocrystal organization is illustrated in Figure 4.31 in the case of the 4.5 nm nanocrystals. The butanethiol-coated nanocrystals form agglomerates, 20–40 nm in size, with little internal order (Figure 4.31a). In many regions, the particles do not show distinct boundaries. The mean diameter estimated from the isolated particles in the thiolized sol is similar to that of the pristine sol. Longer chain thiols, on the other hand, give rise to close-packed arrays (Figure 4.31b-d) spread over micron-sized areas similar to those shown in Figure 4.27. The contrasting behavior of butanethiol (Figure 4.31a) is clearly due to its short chain length ($\ell = 0.8$ nm) and is not related to the concentration of the sol, since similar conditions of preparation were used in all the cases. The role of the thiol chain length becomes more apparent when we closely examine the organizations in Figure 4.31b-d. The 4.5 nm nanocrystals covered with octanethiol form a honeycomb lattice (Figure 4.31b) which is relatively less dense compared to the lattices in Figure 4.27. We observe short-range order limited to three or four hexagons of nanocrystals. The packing is facilitated in many places by a curved arrangement of the nanocrystals. The nearest neighbour distance, c calculated from relatively dense areas is ~ 6.2 nm ($\sigma = 11\%$), which amounts to thiol interdigitation of 30%. On the other hand, the 4.5 nm sol derivatized with dodecanethiol and hexadecanethiol, crystallize in close packed structures as shown

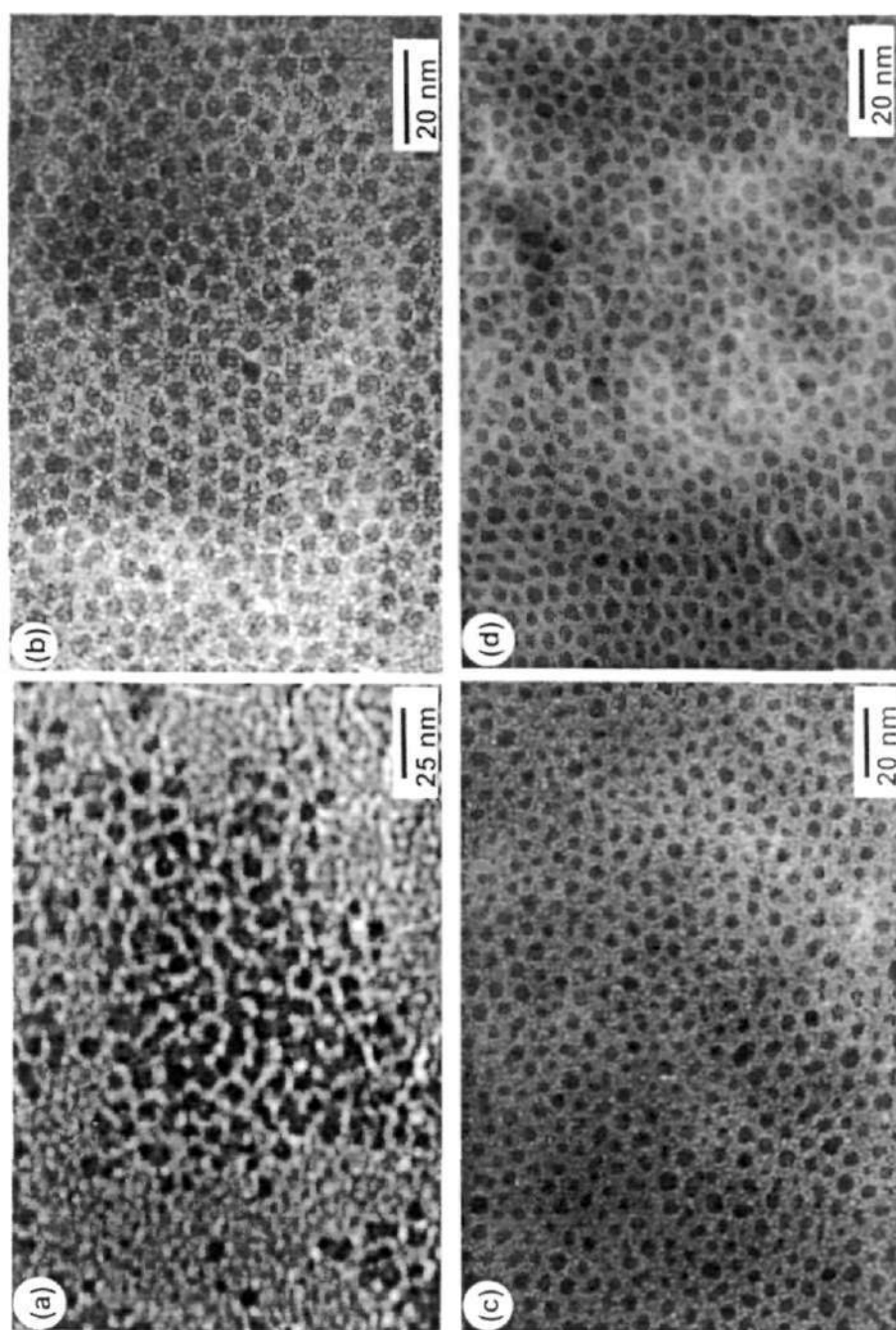


Figure 4.31: TEM micrographs showing Pd nanocrystals of mean diameter 4.5 nm organized into two-dimensional lattices using different thiols: (a) butanethiol, (b) octanethiol, (c) dodecanethiol, (d) hexadecanethiol.

in parts c and d, respectively, of Figure 4.31. The nanocrystals are, however, not uniform in size. The mean sizes are similar to the pristine sol, but the distributions have considerably widened ($\sigma = 20\%$ and 18%), respectively. Unlike the magic nuclearity particles, the 4.5 nm particles exhibit wider size distribution in the hydrosol and are more susceptible to change in size and shape after thiolization. Despite the variations in shape and size, the nanocrystals organize into close-packed arrays, as shown in Figure 4.31c,d. The corresponding c values are 7.3 nm ($\sigma = 14\%$) and 7.7 nm ($\sigma = 12\%$), the interpenetration of thiol molecules being 18% and 24%, respectively. These organizations are different from the opal structures observed by Ohara et al. [190] and resemble more closely the jammed arrangements of polydisperse spheroids [224].

The results discussed above suffice to demonstrate that the nature of nanocrystal organization depends on both the particle diameter, d , and the thiol chain length, ℓ . On the basis of our study of the nanocrystal organizations obtained with different values of d and ℓ , we have arrived at the phase diagram shown in Figure 4.32. In this figure, the bright area in the middle is the most favorable d/ℓ regime, corresponding to extended close packed organizations of nanocrystals such as those illustrated in Figures 4.27 and 4.31. The d/ℓ values in this area are in the range 1.5 – 3.8. The area shaded dark in Figure 4.31 includes the d/ℓ regime giving rise to various short-range aggregations, formed when the particles are small and the chain length is large, or vice versa. As an example, we show a TEM image of 6 nm/octanethiol ($d/\ell \sim 5.0$) assembly in Figure 4.33 which exhibits no long-range order. However, the nanocrystals are isolated from one another unlike those in Figure 4.27. This assembly is similar to a collapsed monolayer of metal particles observed in the LB films on applying excess pressure [192].

To shed further light on the above experimental observations, we invoke the soft-sphere model proposed by Korgel et al. [114]. In this model, the total potential energy (E) is considered to be a result of two types of forces between the nanocrystals,

$$E = E_{steric} + E_{vdW} \quad (4.5)$$

The van der Waals interaction due to the polarization of the metal cores constitutes

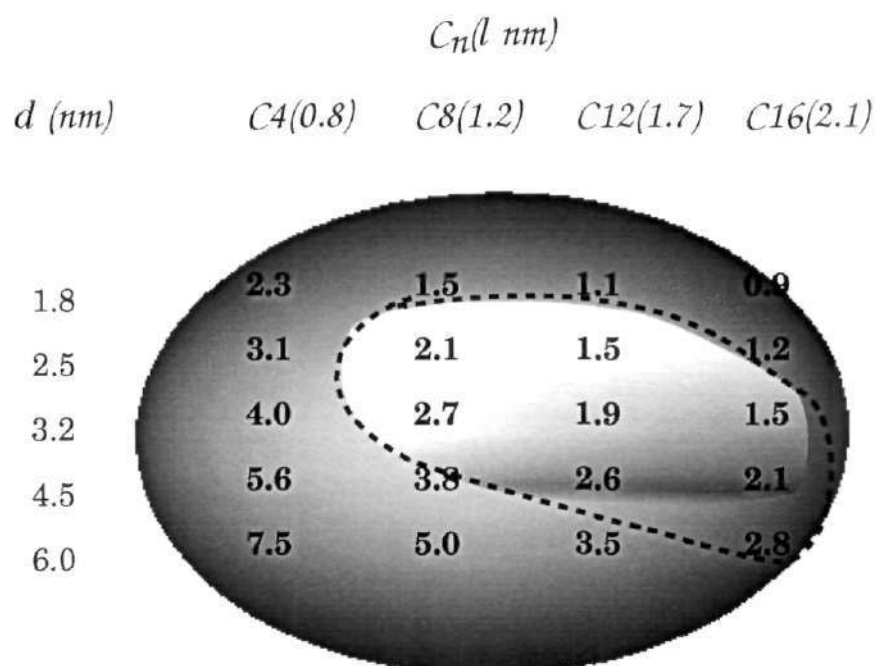


Figure 4.32: The $d - \ell$ phase diagram for Pd nanocrystals thiolized with different alkane thiols. The mean diameter, d , was obtained from the TEM measurements on as prepared sols. The length of the thiol chain, ℓ , is estimated by assuming an all trans conformation of the alkane chain. The thiol is indicated by the number of carbon atoms, C_n . The bright areas in the middle encompasses systems which form close-packed organizations of nanocrystals. The surrounding darker area includes disordered or low-order arrangements of nanocrystals. The area enclosed by the dashed line is derived from calculations from the soft sphere model.

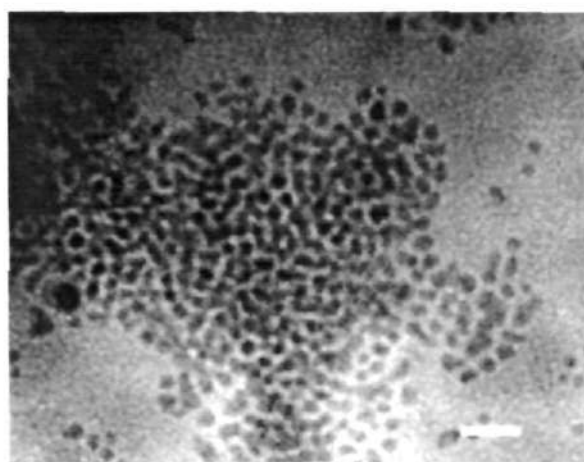


Figure 4.33: TEM micrograph showing disordered arrangement of 6 nm particles coated with octanethiol ($d/\ell = 5.0$). The scale bars corresponds to 20 nm.

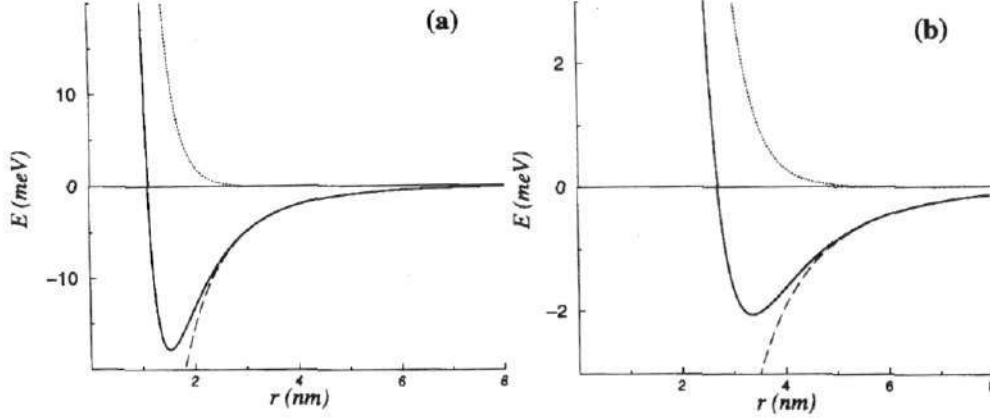


Figure 4.34: Variation of the two components and the total potential energy versus the separation distance between two Pd nanocrystals of 4.5 nm diameter coated with (a) octanethiol or (b) dodecanethiol.

the attractive term and the steric interaction between the thiol molecules on the two surfaces forms the repulsive term,

$$E_{vdW} = \frac{A}{12} \left\{ \frac{d^2}{\tau^2 - d^2} + \frac{d^2}{\tau^2} + 2 \ln \left[\frac{\tau^2 - d^2}{t^2} \right] \right\} \quad (4.6)$$

$$E_{steric} = \frac{50d\ell^2}{(\tau - d)\pi\sigma_a^3} kT e^{-\pi(\tau - d)} \quad (4.7)$$

where τ is the interparticle distance. The Hamaker constant, A , for Pd nanocrystals, in toluene has been estimated to be 1.95 eV [225]. The calculated diameter of the area occupied by the thiol molecule (σ_a) on the particle surface is $\sim 4.3 \text{ \AA}$ [114]. The total energy is attractive over a range of interparticle distances, the magnitude increasing with fall in distance. There could be range of interparticle distances where the attractive energy from the van der Waals term exceeds the repulsive energy due to the steric factor, giving rise to net stabilization of the two-particle system. This is illustrated in Figure 4.34 in the case of 4.5 nm particles. Stabilization energies of 17 and 2 meV were obtained from the calculation for particles coated with octanethiol and dodecanethiol respectively.

In Figure 4.35, we depict the stabilization energies for the d/ℓ values corresponding to the experimentally investigated systems. The points fall in two regions

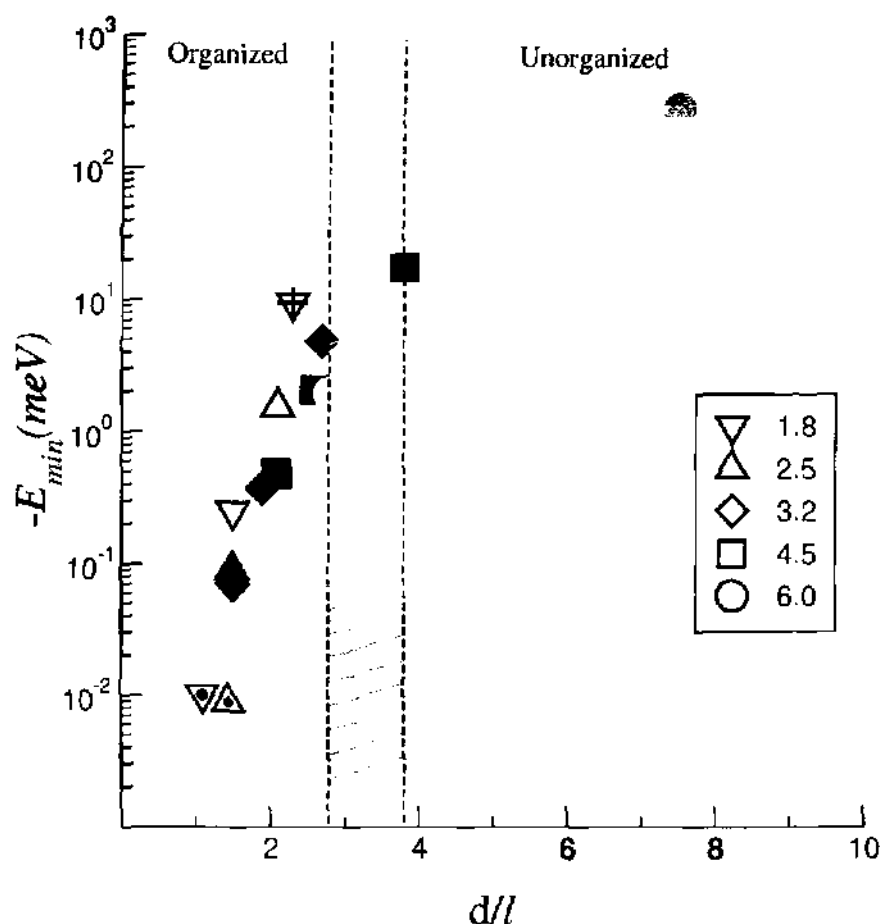


Figure 4.35: Variation of the stabilization energy against d/l for various nanocrystal-thiol systems: filled squares, crystalline organizations; plus, dimers and trimers; centered, 1-D string; gray, disordered organization. The organized and unorganized are delineated with the hatched area indicating an intermediate region.

corresponding to organized and unorganized arrays. With shorter thiol chain lengths or larger metal cores ($d/l > 3$), steep potential energy wells in the range of tenths of meV, are observed implying agglomeration of the particles. For $d/l < 2.5$, the two-particle system exhibits a shallow minimum with negligible stabilization, corresponding to a situation where long thiol chains shield the attractive interactions between the metal cores. An organization involving metal nanocrystals of this kind is influenced more by the directional property of the thiol chain resulting in lower order structures. For (d/l) values in the range $\sim 2.0 - 3.0$, the stabilization energies have moderate values comparable to the thermal energy of the nanocrystals. This

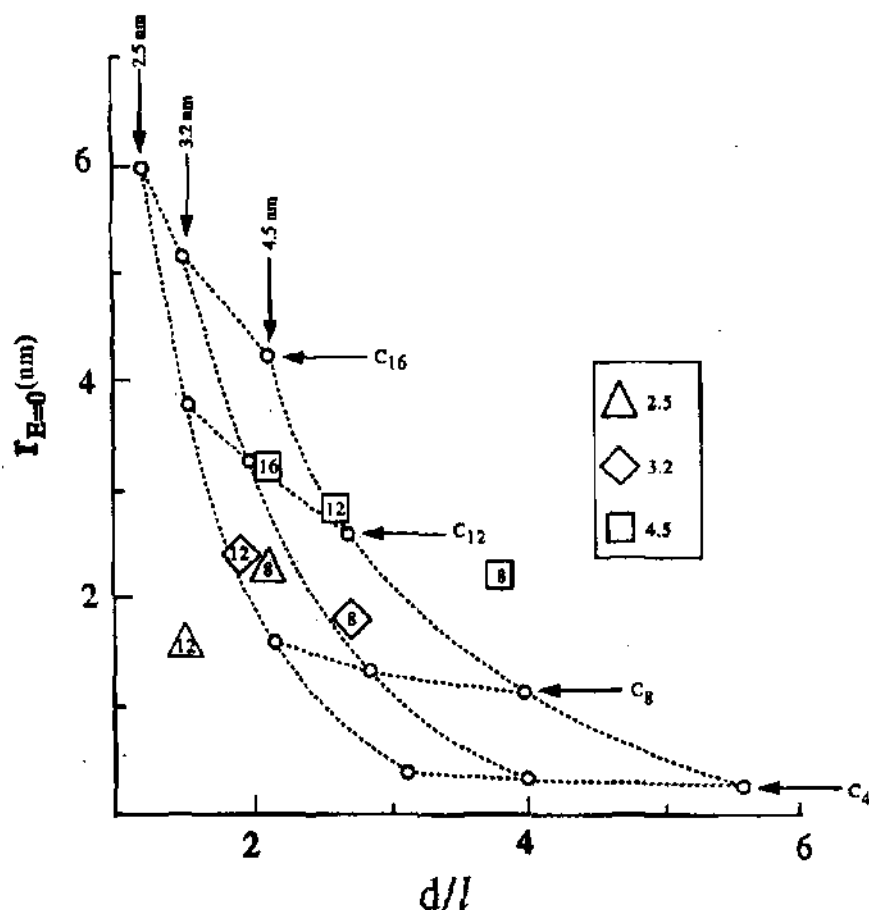


Figure 4.36: Separation distance at the zero crossover of the total potential ($r_{E=0}$) against d/ℓ for various nanocrystal-thiol systems. The separation distances in close-packed organizations of nanocrystals obtained from TEM are also shown.

energy is just adequate to bring the metal particles close enough to form an extended array. This is similar to the case of hard spheres where the interaction energy is negligible till the spheres come in contact and then the repulsion is asymptotic [226]. Thiolized nanocrystals in the hard sphere limit are guided mainly by the entropy, leading to the honeycomb organizations.

In Figure 4.36, we present the separation distances obtained in the hard sphere limit ($r_{E=0} = c_{E=0} - d$) for different nanocrystals and thiols in the form of a grid against (d/ℓ) . For a given thiol, the separation distance increases as the nanocrystal diameter decreases, more steeply when the thiol chain is longer. Compared to these results, our experimental values lie between 1.5 and 3.2 nm. It is clear

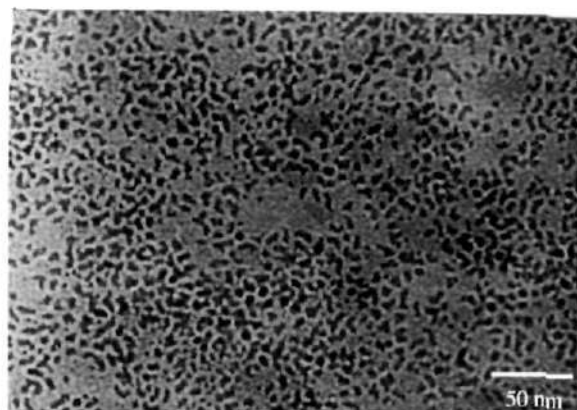


Figure 4.37: TEM micrographs showing aggregates of 1.8 nm particles covered with butanethiol.

from Figure 4.36 that our calculations underestimate the distance in the case of octanethiol, the deviations being 44%, 13% and 25% for 2.5, 3.2 and 4.5 nm particles, respectively. The values are overestimated by as much as 50% for the longer thiols. In other words, the thickness of the thiol shell, $\hat{\ell}$, estimated from the experimental separation distances ($2\hat{\ell} = c - d$) is different compared to the projected lengths (ℓ). Accordingly, the ratio $d/\hat{\ell}$ for the experimental crystalline lattices falls in the range 2.5 – 4.0 as compared to the (d/ℓ) range of 1.5 – 3.8. Clearly, the extent of interdigitation of thiol molecules plays a major role in attributing hardness to the ligated nanocrystal, which in turn decides the nature of the two-dimensional organization.

We now briefly examine organizations in systems where the dimensions of the metal core and of the thiol reach have extreme values, as in the case of 1.8 nm nanocrystals coated with butanethiol (Figure 4.37). The (d/ℓ) value in this case is 2.3 and the stabilization energy is relatively high, (> 10 meV; see Figure 4.35). We see from Figure 4.37 that the nanocrystals are engaged locally in small aggregates to form dimers, trimers, or occasionally even tetramers. The aggregates mingle with one another to give rise to what could be efficient packing under the given constraints. Clearly, the butanethiol molecule, despite being attached to a small nanocrystal (1.8 nm) fails to prevent agglomeration of the metal cores. In extreme cases such as this, the (d/ℓ) criterion alone would not suffice for the

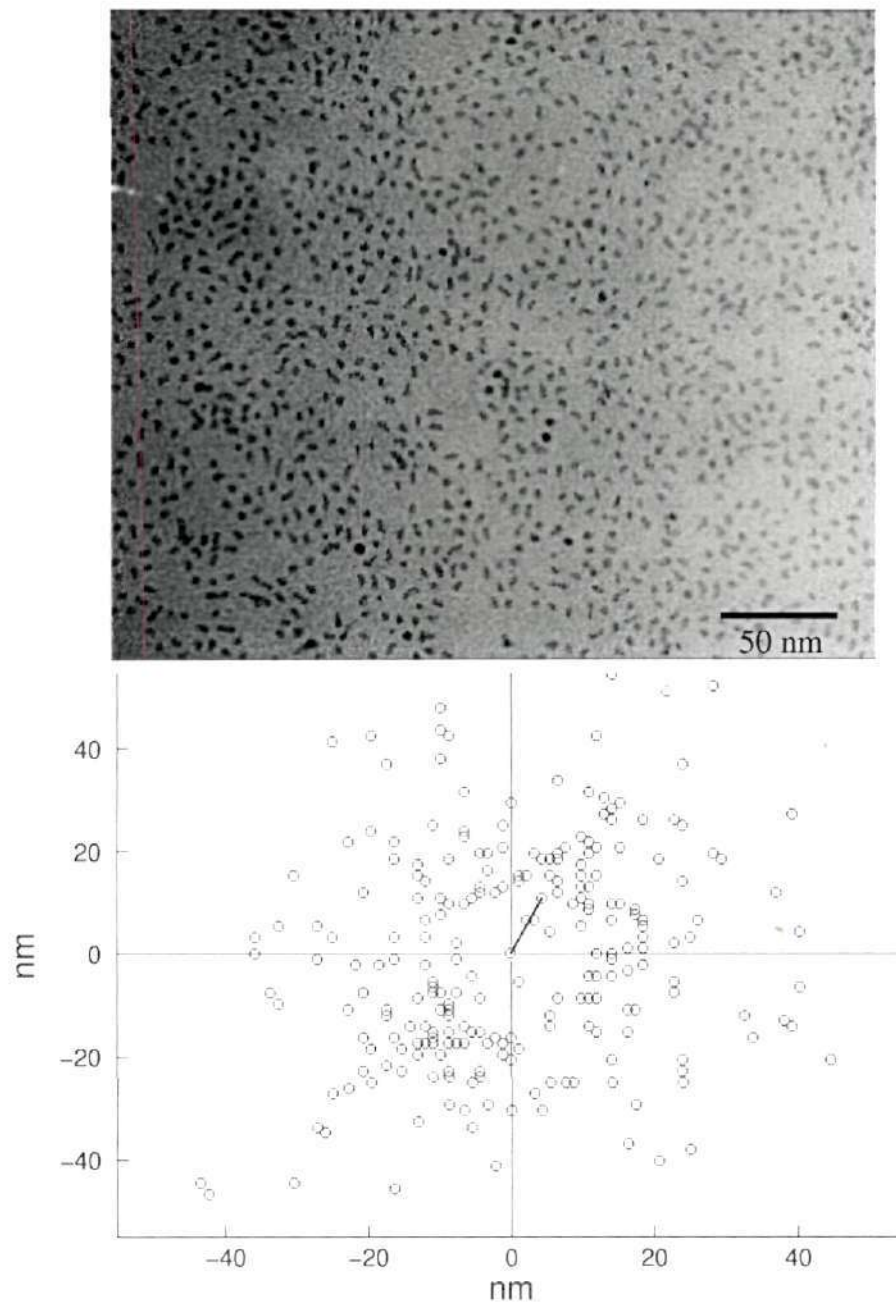


Figure 4.38: TEM micrograph showing 1-D strings of 3.2 nm particles held by hexadecanethiol. In the plot below are shown the vectors depicting the length and direction of the strings with the center of the picture as the origin. The resultant obtained by adding all the vectors is indicated as a thick line.

formation of a nanocrystal array. Another interesting arrangement is seen in the case of the 3.2 nm particles covered by hexadecanethiol ($d/\ell = 1.5$), the stabilization energy of which is very small (see Figure 4.35). The metal nanocrystals are not sufficiently big to attract hexagons of partners but instead form a loose structure filled with 1-D strings, as shown in Figure 4.38. Each string is identified with a series of nearly equally spaced ($c \sim 6.3$ nm, $\sigma \sim 14\%$) nanocrystals, corresponding to 26% of interdigitation of the hexadecanethiol molecules. The length of the string varies between 15 and 65 nm (3 and 12 particles, respectively) with the mean at 35 nm (6 particles). A vector sum of the strings gives a small residue (6 nm), implying that the arrangement is indeed random. This type of arrangement is observed, though less prominently, in the case of 1.8 and 2.5 nm particles covered with hexadecanethiol.

A critique of the d/ℓ model would be in order at this stage. This model takes account of competing forces arising from the attraction between the metal cores and the steric repulsion from the surface ligands. The question as to how good the d/ℓ is an operational parameter is debatable. As shown earlier, the d/ℓ ratio for crystalline arrays is in the range 1.5 – 3.8, the only strong exception being the 1.8 nm/butanethiol system ($d/\ell = 2.3$) which forms a low dimensional organization. Nanocrystal systems such as 1.8 nm/dodecanethiol and 6.0 nm/butanethiol, with d/ℓ far outside this range, exhibit disordered structures. It is, therefore, gratifying that the simple d/ℓ model accounts for the experimental observations reasonably satisfactorily, except at the boundary values. Clearly, there is a need to examine thiol interdigitation and related problems associated with the nanocrystalline arrays.

In conclusion, thiolized Pd nanocrystals self-assemble to give rise to different types of organizations depending on the particle diameter, d and the alkane chain length, ℓ . The experimental observations relating the stability of the two-dimensional arrays to the d/ℓ ratios find support from empirical calculations based on a soft sphere model. Nanocrystals with stabilization energies comparable to the thermal energy (a few millielectronvolts) give rise to close-packed hexagonal crystalline arrays whose d/ℓ values are in the range 1.5 – 3.8. Large nanocrystals

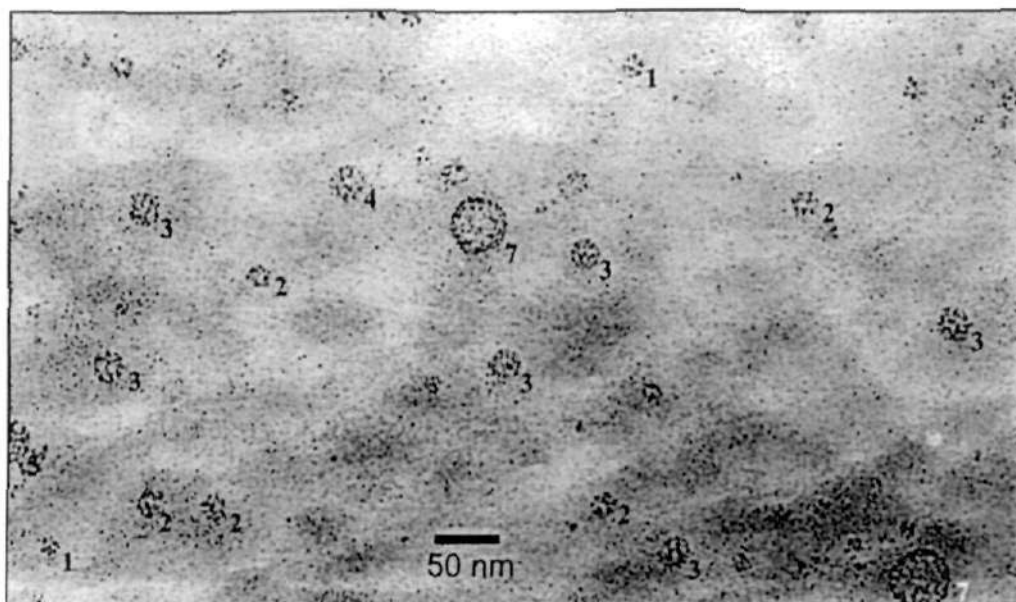


Figure 4.39: TEM image of Pd₅₆₁ nanocrystals forming aggregates. The numbers correspond to the proposed number of nanocrystal shells, n in each of the aggregate.

($d/\ell > 3$) with high stabilization energies (> 10 meV) form collapsed structures while those attached to longer chain thiols ($d/\ell \leq 1.5$) are associated with little stabilization and exhibit low-order structures. The interparticle distances estimated from the soft sphere model deviate to some extent from the experimental values due to interdigitation of thiol molecules chemisorbed on the curved nanocrystal surfaces.[§]

4.5 Giant clusters of magic nuclearity Pd nanocrystals

The ligand shells that adorn the metal nanocrystals influence their behaviour. Thus, thiolized metal nanocrystals form ordered aggregates in two-dimensions as described in the previous section. Polymer coated nanocrystals on the other hand are covered with a sheath of ligands isotropic in all directions, which effectively magnify the facets of the nanocrystals. The isotropic ligand brings about a different type of nanocrystal organization.

[§]Papers based on this study have appeared in *J. Phys. Chem.* (2000); *Pure and Appl. Chem.* (2000).

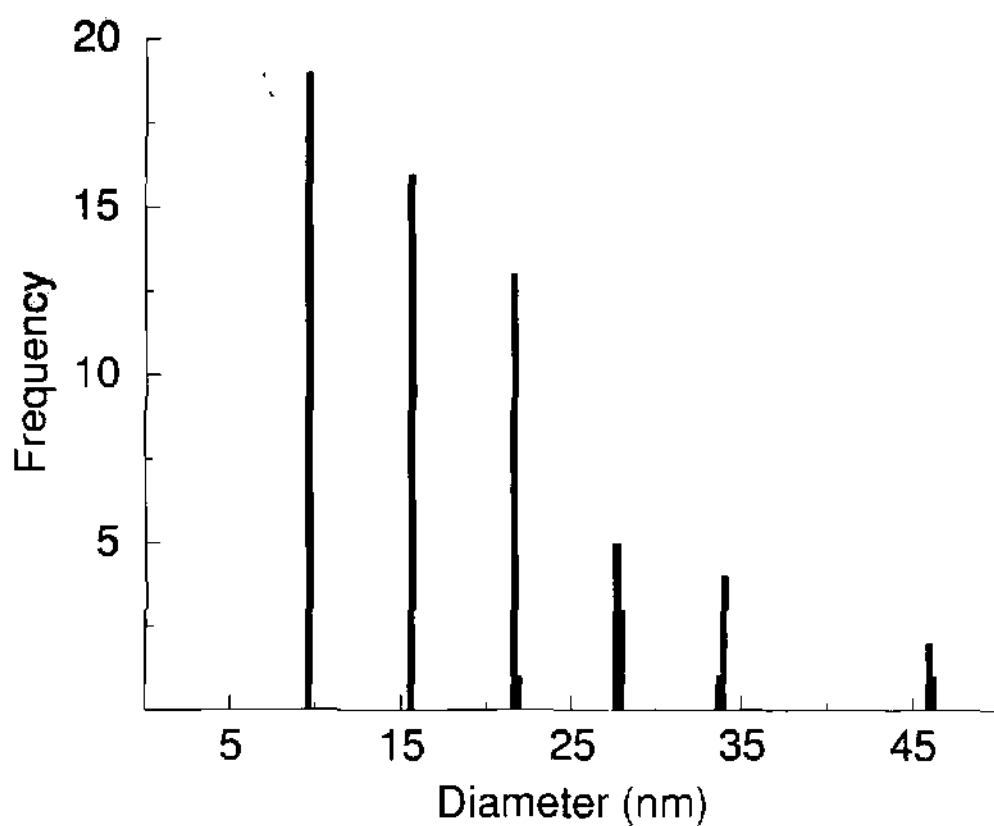


Figure 4.40: Histogram showing the distribution in the diameters of the obtained aggregates.

Table 4.3: Giant clusters of Pd₅₆₁ nanocrystals

Diameter measured (nm)	No. of nanocrystals
9.6 ± 0.1	13 ± 1
15.6 ± 0.1	55 ± 6
21.6 ± 0.1	147 ± 16
27.7 ± 0.1	309 ± 34
33.8 ± 0.1	561 ± 61
46.0 ± 0.15	1415 ± 156

In the experiments with magic nuclearity Pd₅₆₁ nanocrystals- wherein a drop of the nanocrystals were slowly evaporated on a TEM grid, aggregates of nanocrystals were observed. A scan of the grid revealed the presence of a large number of uniform spherical particles. Figure 4.39 shows a typical TEM image of the dispersion. In addition to isolated nanocrystals, bigger features resembling aggregates of nanocrystals are seen in the image. A histogram showing the distribution of the observed diameters is given in Figure 4.40. Evidently, the giant clusters exhibit a preference for specific diameters - 9.6, 15.6, 21.6, 27.7, 33.8 and 46.0 nm, with the smaller aggregates being more abundant. To estimate the number of nanocrystals present in these aggregates, the effective volume of a nanocrystal was calculated on the basis of the distance between adjacent nanocrystals (that are not a part of the aggregate) in TEM images. The pairs of particles were chosen carefully such that the two metal cores were distinct. The mean value obtained from hundred such measurements was 4.1 ± 0.1 nm. This value is more suitable than the diameter of an isolated nanocrystal, the latter being 3.3 nm as estimated by STM measurements. We assume that the effective volume thus estimated takes into account the free volume in the nanocrystal aggregate. In other words, the particle pair is taken to adequately describe the interactions in the bigger aggregates. In Table 4.5, we list the observed diameters of the aggregates along with the estimates of the nuclearities. The aggregates are indeed giant containing tens to hundreds of nanocrystals and consists of nuclearities that quite surprisingly are exceptionally close to the magic nuclearities. In Figure 4.41, the calculated perimeters are projected against different giant clusters. The close agreement between the observed and calculated diameters is indeed apparent.

The giant aggregates obtained are distinct from the two-dimensional rings obtained by other groups. To establish the spherical nature of the giant clusters, they were imaged at different tilts ($\pm 17.5^\circ$) along two perpendicular axes in the focal plane. Figure 4.42 shows such images obtained with a giant cluster of nuclearity 561. The projected image appears circular over the entire tilt range of 35° , along both the directions. A series of such tilt experiments confirmed the spherical nature of the aggregates. Furthermore, lattice resolved images of individual Pd₅₆₁

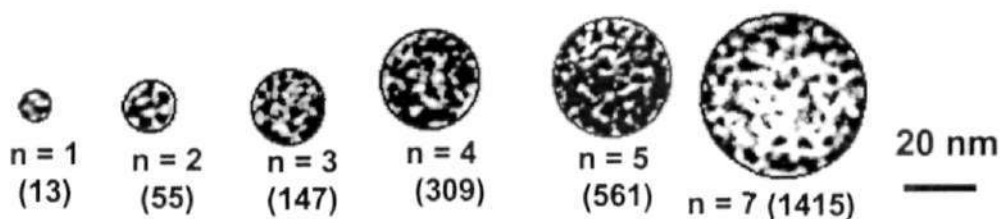


Figure 4.41: Giant clusters of different magic nuclearities, $(\text{Pd}_{561})_n$, the circles corresponding to the diameters of the clusters calculated on the bases of the effective volume of an individual nanocrystal.

nanocrystals constituting the giant cluster reveal the characteristic 11 [111] lattice fringes. Attempts to image the internal structure of the giant clusters were however, not successful probably because of the interference from the ligand shell of the nanocrystals.

As mentioned in Section 2.5, the process of self-assembly of such monodisperse nanocrystals to yield giant clusters was theoretically predicted using the embedded atom approximation by Fritsche et al. [194]. They proposed that when the ligands are stripped from the nanocrystals by some process, it would be energetically favourable for the nanocrystals to form giant clusters (see Figure 4.43). Such a process is facilitated by the facets present on the surface of the nanocrystal. In our case, the icosahedral Pd_{561} nanocrystals self-assemble into giant clusters, even in the presence of the ligand shell (PVP), due to fact that the shell being polymeric is isotropic and thereby facilitates an assembly that is dominated by the facets on the surface of the nanocrystals.

Attempts to investigate the process of self-assembly of nanocrystals of a different magic nuclearity (Pd nanocrystals of diameter 3.2 nm corresponding to a nuclearity of 1415), yielded giant clusters with possible nuclearities of 147 and 309, as shown in Figure 4.44. However, the slightly wider distribution in the pristine nanocrystal diameter, (probably due to a mixture of 7 and 8 shelled clusters) seems to hinder the facile formation of uniform giant clusters. A majority of these clusters ($\sim 60\%$) display elongation along the axis. A narrow distribution in the initial nanocrystal sol appears to be essential for the formation of the magic nuclearity giant clusters.

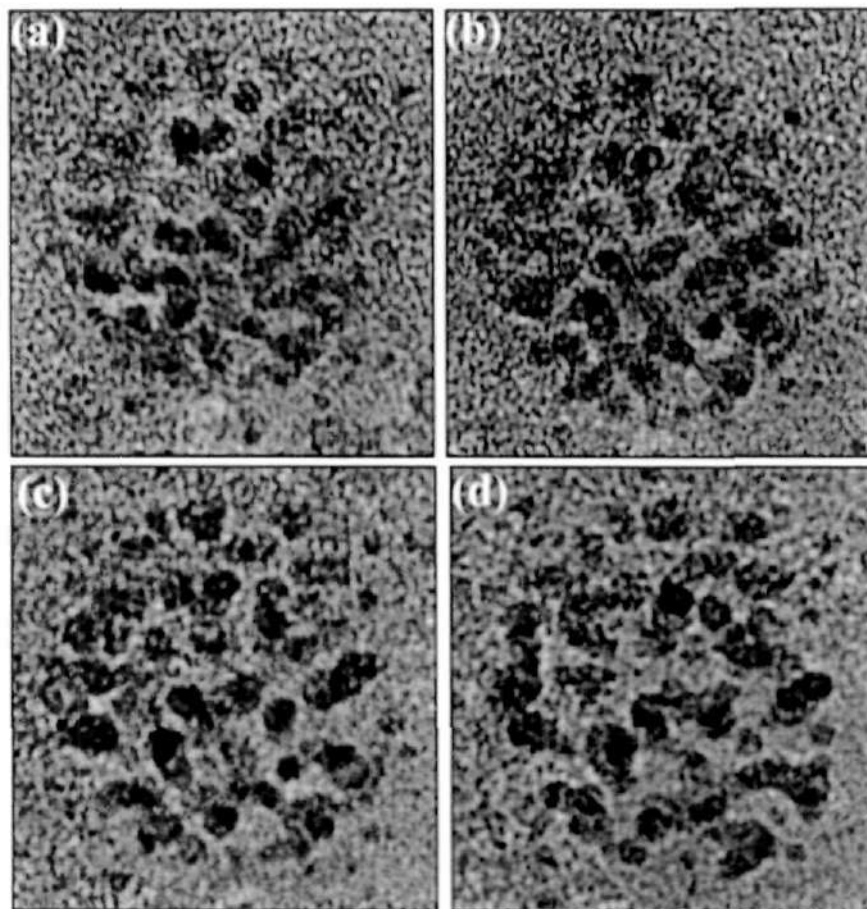


Figure 4.42: A $(\text{Pd}_{561})_{561}$ giant cluster imaged at various tilt angles along two perpendicular axes in the focal plane: (a) $-18.7^\circ, 1.4^\circ$; (b) $-7.3^\circ, -1.4^\circ$; (c) $0^\circ, 1.4^\circ$; (d) $12.4^\circ, -1.4^\circ$

In conclusion, giant clusters of Pd nanocrystals are obtained by the mesoscopic assembly of nanocrystals of uniform size. This observation provides an illustration of the principle of self-similarity. These clusters of metal nanocrystals are perhaps bound by the same laws that endow special stability to magic numbered nanocrystals. It would therefore appear that these laws are invariant under scaling. The giant clusters of Pd_{561} are different from other types of ligand directed nanocrystal aggregates which are formed mostly due to the directional nature of the ligand shell.[†]

[†]A paper based on this study has been published in *J. Phys. Chem.* (2001).

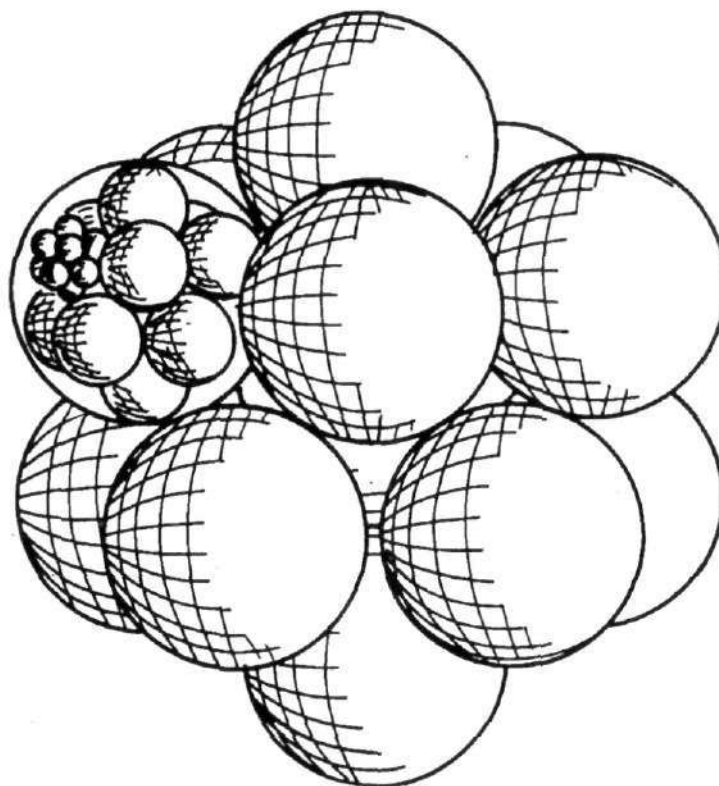


Figure 4.43: Self-similarity: Schematic illustration of the formation of a cluster of metal atoms (*nanocrystal*) and a cluster of *nanocrystals* (*giant clusters*) and *giant clusters* forming larger aggregates. The size effects operating could be invariant to scaling.

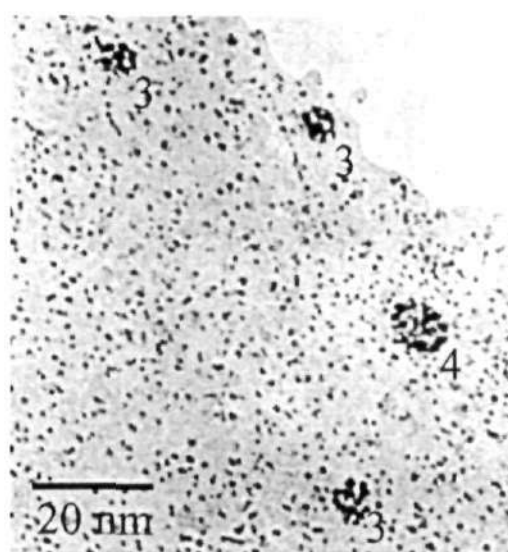


Figure 4.44: TEM image of giant clusters of Pd₁₄₁₅ nanocrystals. The numbers correspond to the proposed number of nanocrystal shell, *n*.

Table 4.4: Optical density (at 400 nm) of Pd-Ni core-shell nanocrystal sols of different compositions.

Nanocrystal composition	[Pd ²⁺] μM	[Pd ²⁺] μM	Absorbance (arb. units)
Pd ₅₆₁	375	0	0.212
Pd ₅₆₁ Ni ₃₈	375	25	0.212
Pd ₅₆₁ Ni ₂₈₀	375	187	0.336
Pd ₅₆₁ Ni ₅₆₁	375	375	0.463
Pd ₅₆₁ Ni ₈₀₀	375	535	0.575
Pd ₅₆₁ Ni ₁₅₀₀	375	1003	0.886
Pd ₅₆₁ Ni ₃₀₀₀	375	2005	1.561
Pd ₅₆₁ Ni ₄₅₀₀	375	3008	2.282
Pd ₅₆₁ Ni ₃₀₀₀ Pd ₁₅₀₀	1378	2005	2.122

4.6 Mesoscopic organization of magnetic nanocrystals

PVP capped Pd₅₆₁Ni_n (n=38, 280, 561, 800, 1500, 3000 and 4500 atoms) core-shell nanoparticles were prepared and subsequently thiolized with octane and dodecane thiol, as described in section 3.1.5. The composition of the particles were studied using EDAX analysis and XPS. Ni loading on the Pd core could also be followed by monitoring the optical density (OD) of the nanocrystals. Pd nanocrystals exhibit featureless absorption throughout the visible range, coating with Ni, results in a uniform increase in OD. Table 4.4 list the changes in the OD at 400 nm as a function of Ni loading. It is readily seen that the OD increases linearly with Ni coating.

The mean diameters (obtained from TEM measurements) of the Pd-Ni core-shell nanocrystals, Pd₅₆₁Ni₂₈₀, Pd₅₆₁Ni₅₆₁, Pd₅₆₁Ni₁₅₀₀, Pd₅₆₁Ni₃₀₀₀ and Pd₅₆₁Ni₄₆₀₀ were 2.7, 2.9, 3.3, 4.9 and 5.5 nm respectively. In case of Pd₅₆₁Ni₃₀₀₀Pd₁₅₀₀ nanocrystals, the mean size was 5.5 nm. The size of the nanocrystals did not change noticeably on thiolization. The compositions of the Pd₅₆₁Ni_n particles were analyzed by XPS before and after thiolization. The spectra in Pd(3d) and Ni(2p)

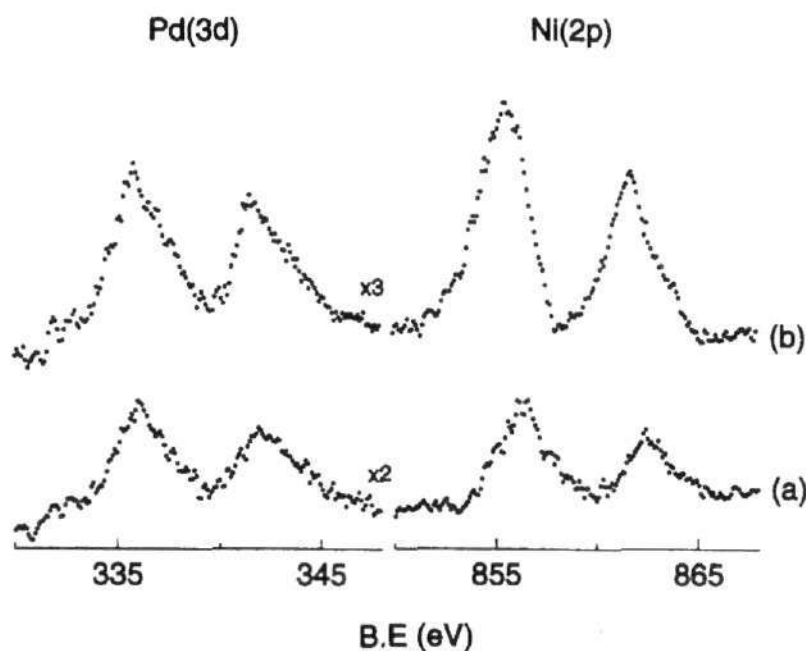


Figure 4.45: X-ray photoelectron spectra of thiolized (a) Pd₅₆₁Ni₂₈₀ and (b) Pd₅₆₁Ni₁₅₀₀ nanocrystals in the Pd(3d) and Ni(2p) levels.

regions for thiolized Pd₅₆₁Ni₈₀₀ and Pd₅₆₁Ni₁₅₀₀ samples are shown in Figure 4.45. The binding energies of the core-levels are shifted to higher values with respect to the bulk (Pd(3d_{5/2}) - 335.6 eV; Ni(2p_{3/2}) - 853.0 eV) more so in case of Ni. The small shift is due to thiol ligation and particle size effect. The compositions, estimated by a method described previously by Rao and co-workers [227], were Pd₅₆₁Ni₈₅₈ and Pd₅₆₁Ni₁₅₄₀, in close agreement with the starting ratios of the metal salts employed. EDAX also yielded Pd-Ni ratios conforming to the values estimated by XPS. In the case of Pd₅₆₁Ni₃₀₀₀Pd₁₅₀₀, EDAX yielded a Pd to Ni ratio of 0.727 instead of the expected value of 0.695. There was no significant change in the composition upon thiolization. Thiolized Pd₅₆₁Ni_n nanocrystals were stable in air for long periods extending to a few months, without undergoing any change in size or composition. Furthermore, there is no observable oxide formation during the ligand replacement.

The zero-field cooled (ZFC) measurements for octanethiol coated Pd₅₆₁Ni₁₅₀₀ and Pd₅₆₁Ni₄₅₀₀ nanocrystals are shown in Figure 4.46. The field-cooled mea-

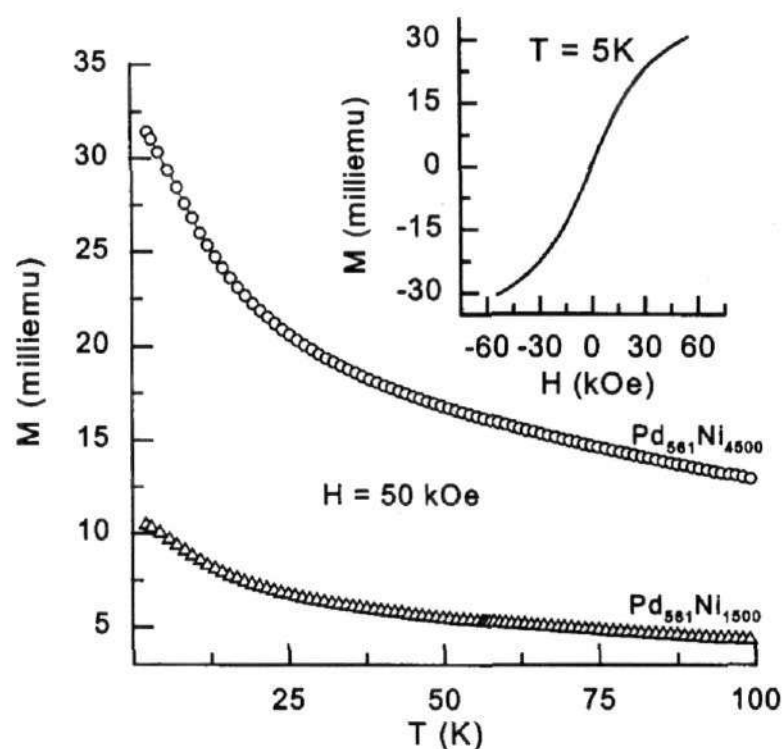


Figure 4.46: Temperature dependence of magnetization for Pd₅₆₁Ni_n core-shell nanocrystals with $n = 1500$ and $n = 4500$ under an applied field of 50 kOe. The values were corrected for contributions from the solvent and the glass tube. The inset shows the change in magnetization (uncorrected) as a function of magnetic field for $n = 4500$ at 5 K.

measurements yielded curves overlapping with the ZFC curves. The ratio of the measured magnetic moments (Pd₅₆₁Ni₄₅₀₀/Pd₅₆₁Ni₁₅₀₀) is ~ 3 at all temperatures, indicating that the moment changes linearly with Ni loading. The Pd-Ni core shell nanocrystals, however do not exhibit hysteresis even at 5 K (see inset of Figure 4.46). The reason for the nanocrystal not exhibiting a blocking behaviour is not clear at present. It is possibly due to ligands induced disorder in the magnetic spins.

TEM images of two-dimensional arrays of Pd₅₆₁Ni_n nanocrystals thiolized with octanethiol are shown in Figure 4.47 in the case of $n = 280$, 561 and 1500 compositions. With the Pd₅₆₁Ni₂₈₀ nanocrystals, order is seen in small regions against the background of a collapsed layer. Similar lattices were obtained in

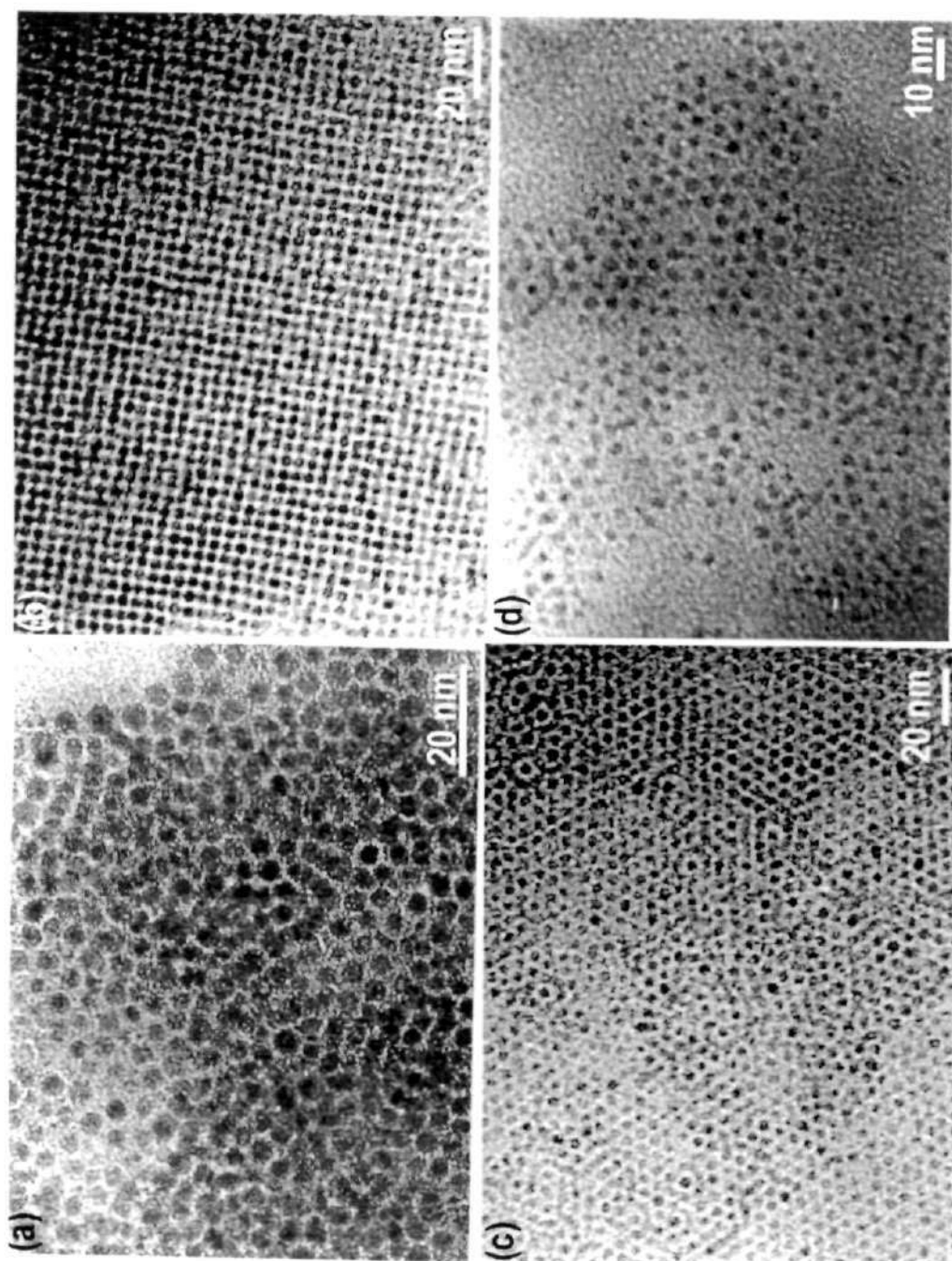


Figure 4.47: TEM images of ordered arrays of Pd₅₆₁Ni_n core-shell nanocrystals; (a) n = 280, octanethiol; (b) n = 561, octanethiol; (c) n = 1500, octanethiol; (d) n = 38, dodecanthiol.

the case of $\text{Pd}_{561}\text{Ni}_{38}$. Considering that thiolized Pd_{561} nanocrystals themselves form good two-dimensional arrays (see Figure 4.27 and discussions therein), it is interesting that even a small Ni coating on Pd_{561} perturbs the crystallinity. Nanocrystals with higher Ni loadings, $\text{Pd}_{561}\text{Ni}_{561}$ and $\text{Pd}_{561}\text{Ni}_{1500}$, however, form extremely well-ordered arrays extending to a few microns. The arrays seen in the TEM images for the cases of $\text{Pd}_{561}\text{Ni}_{561}$ and $\text{Pd}_{561}\text{Ni}_{1500}$ (Figure 4.47c and d) correspond to the $\langle 100 \rangle$ and $\langle 101 \rangle$ projections of a bcc lattice. In the case of $\text{Pd}_{561}\text{Ni}_{1500}$, some portions of the array exhibit a bilayered structure similar to the case of Pd_{561} nanocrystal capped with octanethiol. The interparticle separation distances are ~ 1.0 and 1.2 nm for $n = 561$ and 1500 , respectively, suggesting a significant interdigitation of the alkyl chains of the adjacent particles. In the case of $\text{Pd}_{561}\text{Ni}_{38}$, a good array could be obtained when dodecanethiol was used instead of octanethiol (Figure 4.47d).

In Figure 4.48, we show the TEM images obtained with $\text{Pd}_{561}\text{Ni}_{3000}$ and $\text{Pd}_{561}\text{Ni}_{4500}$ nanocrystals coated with octanethiol. Both these systems show a strong tendency towards self-organization into extended arrays like those with lesser Ni content (Figure 4.47). Significantly, in some portions of the images (Figure 4.48), multi-layered structures are seen in the form of tapes and wires. $\text{Pd}_{561}\text{Ni}_{4500}$ tends to form small three-dimensional crystallites (~ 200 nm) as shown in Figure 4.48b. An additional layer of Pd atoms on top of the nanocrystals however brings about a distinct change in the nature of extended arrays. The nanocrystals no longer form multilayers, but instead form two-dimensional layers as can be seen in Figure 4.49. Further, the observed coverage of the $\text{Pd}_{561}\text{Ni}_{3000}\text{Pd}_{1500}$ lattice is poorer and the extent of organization is smaller. It was found by us that the transfer of $\text{Pd}_{561}\text{Ni}_{3000}$, from aqueous to organic phase could be accomplished by the use of octylamine as well. As in the case of thiols, there was no observable change in composition or size upon capping with the amine. In Figure 4.50, typical TEM micrographs of octylamine covered $\text{Pd}_{561}\text{Ni}_{3000}$ nanoparticles are shown. It is seen that the nanocrystals of 3.3 nm diameter arrange in a well-ordered hexagonal array with a nearest neighbour spacing of 1.7 nm, indicating upto 30% interdigitation of the amine chains. Such an array is strikingly different from the one obtained from

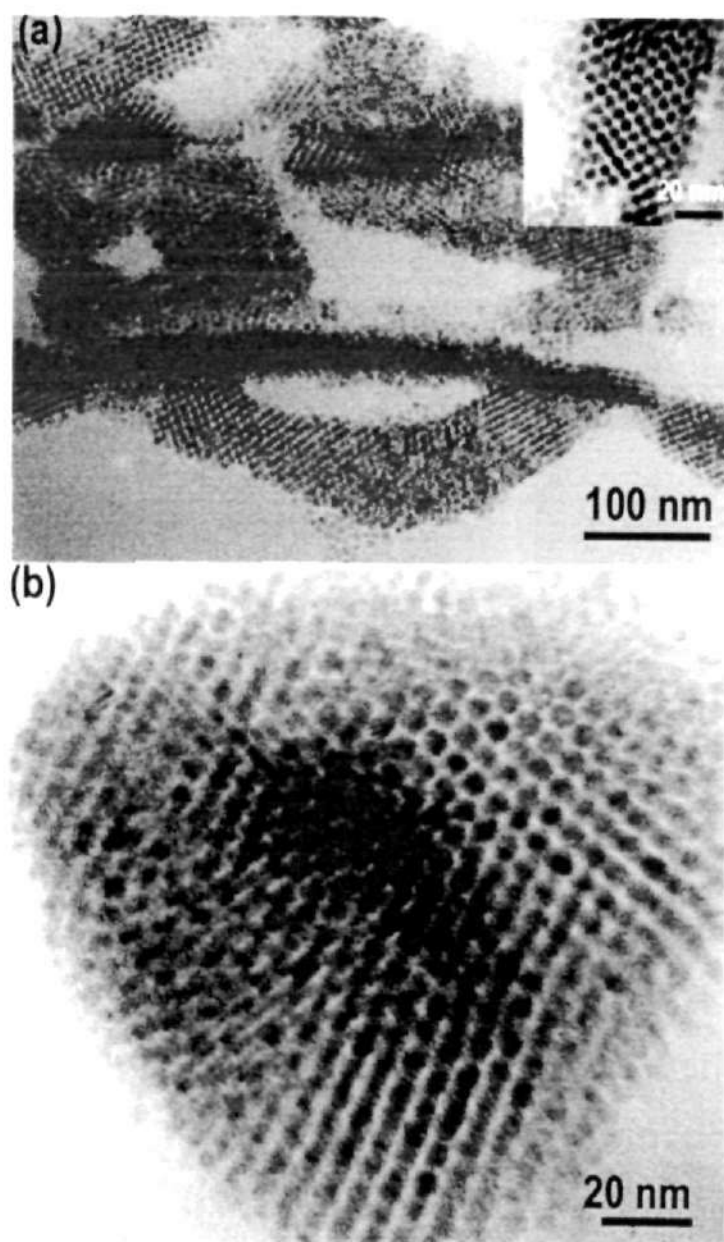


Figure 4.48: TEM images of ordered arrays formed by $\text{Pd}_{561}\text{Ni}_n$ core-shell nanocrystals, coated with octanethiol: (a) $n = 3000$ and (b) $n = 4500$. The inset in (a) shows the structure of the wire like nanocrystal assembly.

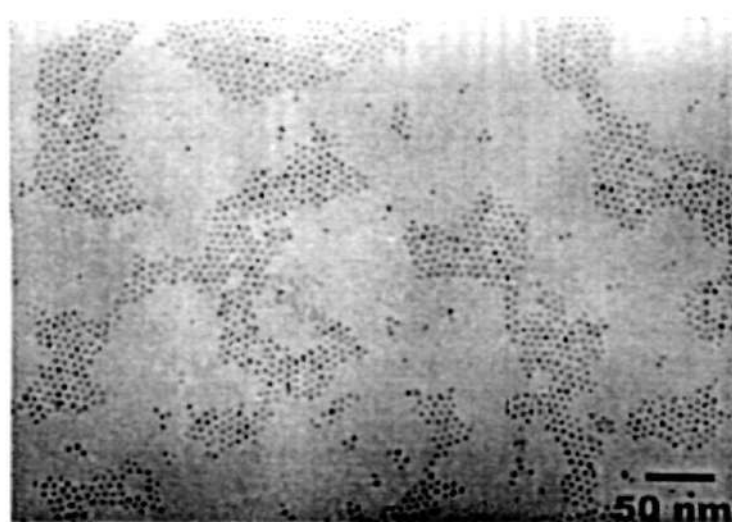


Figure 4.49: TEM images of the arrays formed by octanethiol coated $\text{Pd}_{561}\text{Ni}_{3000}\text{Pd}_{1500}$ core-shell nanocrystals.

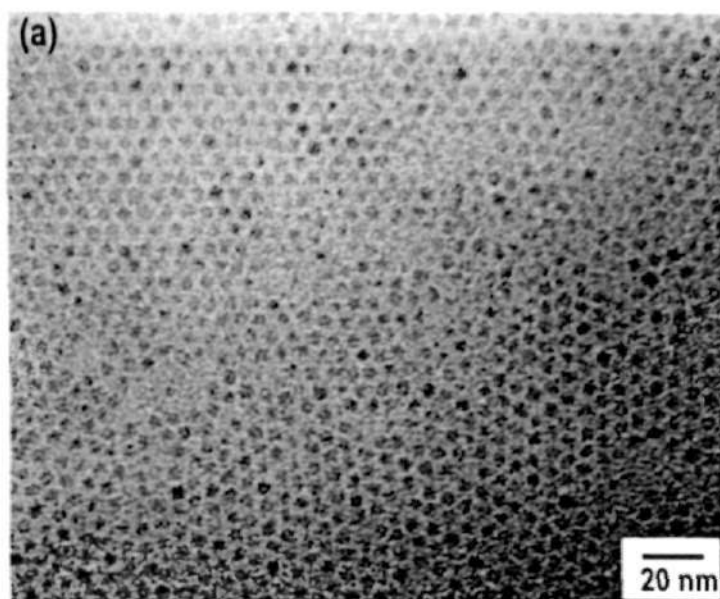


Figure 4.50: TEM images of the arrays formed by octylamine coated $\text{Pd}_{561}\text{Ni}_{3000}$ core-shell nanocrystals.

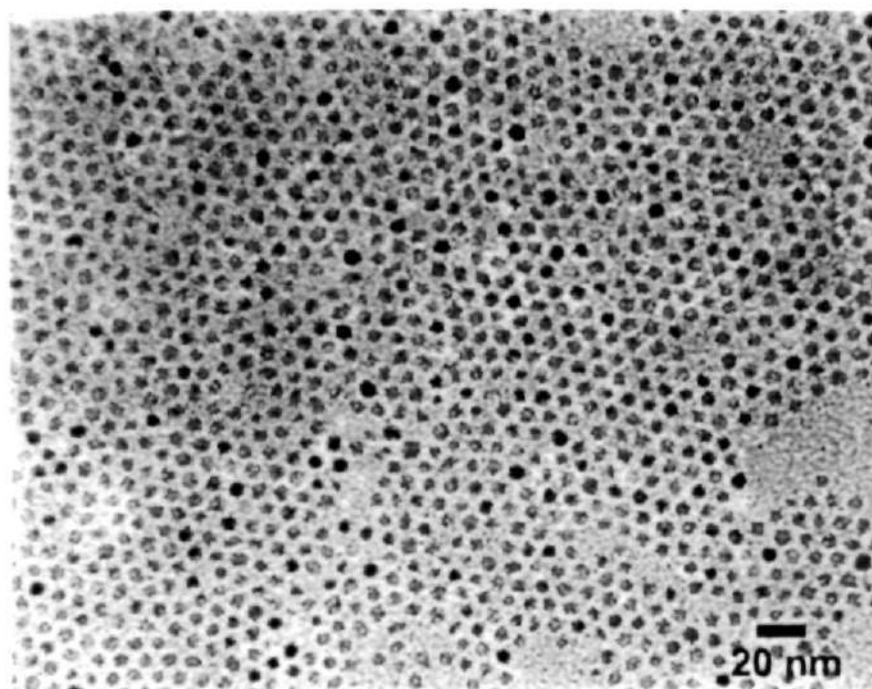


Figure 4.51: TEM images of the arrays formed by octylamine coated $\text{Pd}_{561}\text{Ni}_{3000}\text{Pd}_{1500}$ core-shell nanocrystals.

the corresponding thiol (see Figure 4.48a), where multilayered structures were seen. In Figure 4.51, arrays obtained from octylamine capped $\text{Pd}_{561}\text{Ni}_{3000}\text{Pd}_{1500}$ nanocrystals are shown. It is seen that the nanocrystals retain their pristine diameter of 5.5 nm and self-assemble into a dense two-dimensional array with upto 25% of the amine chains. When compared to the corresponding lattice obtained with octanethiols (see Figure 4.49), the amine capped particles exhibit a higher coverage and a larger extent of organization (with the order extending to a few microns). It is interesting to note that a change in the head group of the surfactant from a thiol to an amine (with identical chain lengths) can bring about such pronounced changes in the nature of the organization.

After being successful in organizing the weakly magnetic Pd-Ni nanocrystals into ordered arrays, we considered that it would be interesting to obtain ordered arrangements of some strongly magnetic systems such as those of metal oxides. We sought to prepare monodisperse nanocrystals of $\gamma\text{-Fe}_2\text{O}_3$, Fe_3O_4 - two of the oldest magnetic systems as well as those of ferrimagnetic CoFe_2O_4 and

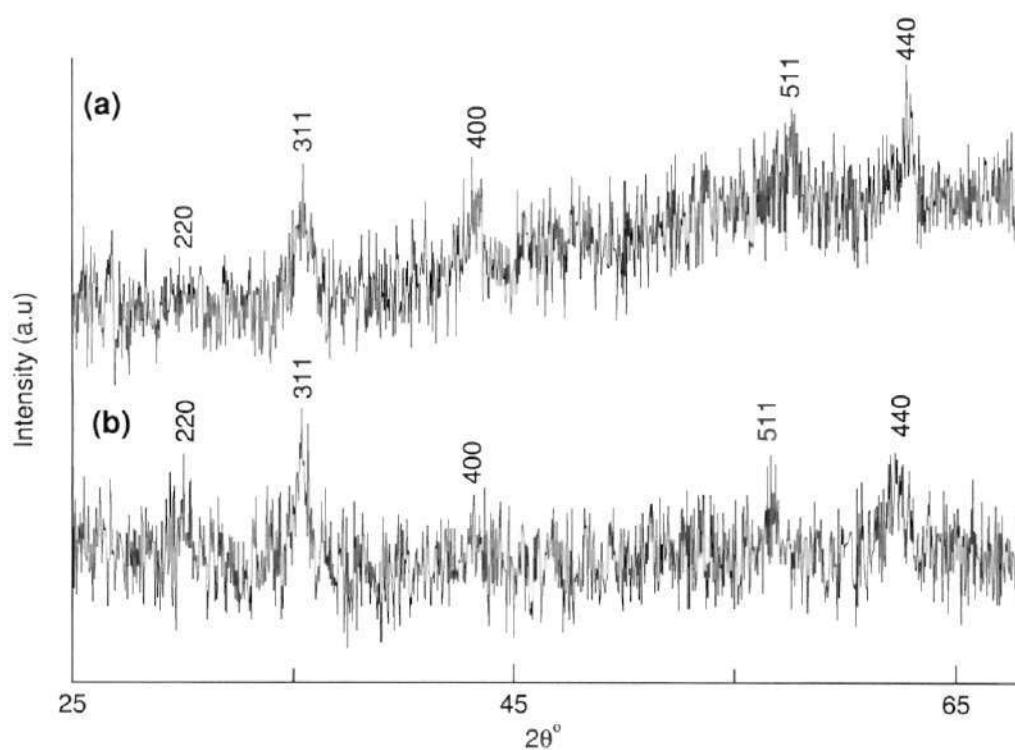


Figure 4.52: X-ray diffraction pattern of (a) $\gamma\text{-Fe}_2\text{O}_3$ and (b) Fe_3O_4 nanocrystals.

MnFe_2O_4 nanocrystals by thermal decomposition methods. The high temperature methods were chosen because they are known to yield defect free, monodisperse nanocrystals. Accordingly, amine capped particles of $\gamma\text{-Fe}_2\text{O}_3$, Fe_3O_4 , CoFe_2O_4 and MnFe_2O_4 as well as Co_3O_4 were prepared by thermal decomposition of metal cupferron complexes as detailed in the experimental section. The X-ray diffraction patterns of $\gamma\text{-Fe}_2\text{O}_3$ and Fe_3O_4 nanocrystals (see Figure 4.52) exhibit slightly broadened peaks. Reflections due to the (220), (311), (400), (511) and (440) planes with d-spacings of 2.930, 2.490, 2.060, 1.590, 1.464 Å are seen in the case of $\gamma\text{-Fe}_2\text{O}_3$ nanocrystals. In the case of Fe_3O_4 nanoparticles, these reflections are observed at 2.960, 2.530, 2.098, 1.612, 1.471 Å. The above values are characteristic of $\gamma\text{-Fe}_2\text{O}_3$ and Fe_3O_4 and indicate that both the particles are monophasic [228]. The diameters estimated from the broadening of the X-ray peaks using the Debye-Scherrer (see equation 4.1) formula was 5.9 nm for the $\gamma\text{-Fe}_2\text{O}_3$ and 5.8 nm for Fe_3O_4 nanoparticles. EDAX studies on CoFe_2O_4 and MnFe_2O_4 particles yielded Co(Mn):Fe ratios of 2.2 and 1.9 close to the expected value of 2.00. X-ray

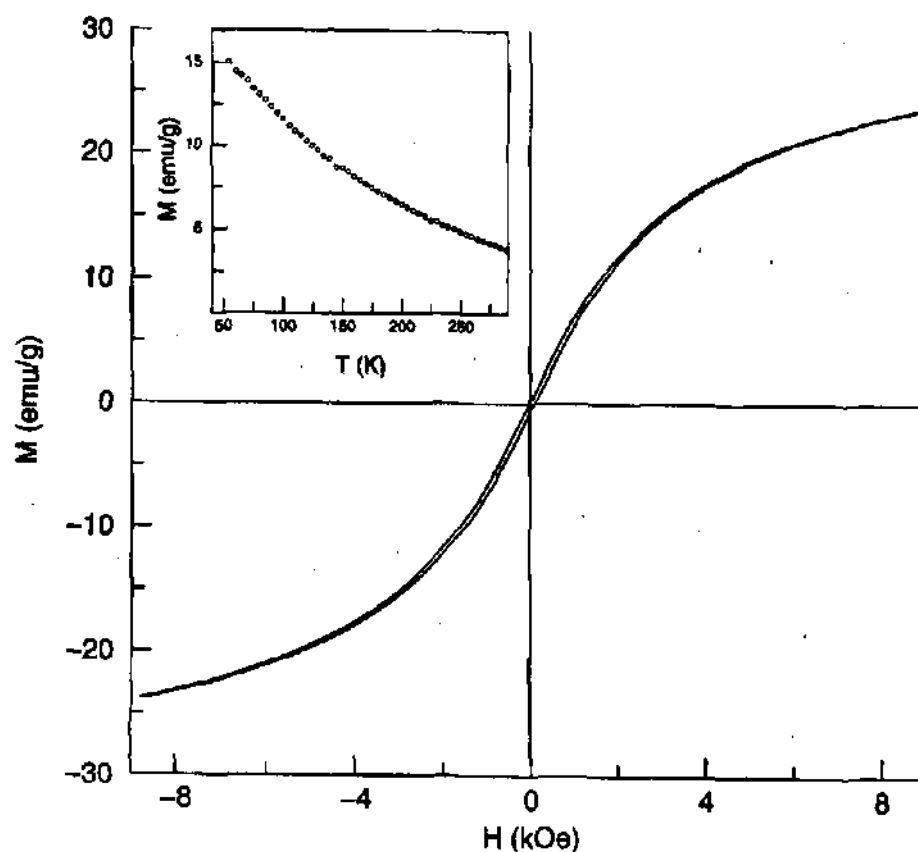


Figure 4.53: Hysteresis loops exhibited by octylamine $\gamma\text{-Fe}_2\text{O}_3$ nanoparticles. Inset shows the temperature dependence of the paramagnetic moment (under a field of 0.5 kOe).

diffraction patterns revealed the monophasic nature of these particles. Magnetic measurements carried out on octylamine capped $\gamma\text{-Fe}_2\text{O}_3$ nanocrystals are presented in Figure 4.53. It is seen that the magnetic moment of the nanocrystals increases with temperature and that nanocrystals are superparamagnetic even at 50 K. In the temperature range studied, (300 to 50 K), the other ferrite nanocrystals also exhibited similar behaviour.

TEM images of octylamine capped Fe_3O_4 , CoFe_2O_4 and $\gamma\text{-Fe}_2\text{O}_3$, along with the SAED patterns are presented in Figure 4.54. The average diameters for the cases of Fe_3O_4 , CoFe_2O_4 and $\gamma\text{-Fe}_2\text{O}_3$ were 5.0, 4.8 and 4.5 nm respectively. The diameters obtained from TEM measurements are in reasonable agreement with those estimated from broadening of the X-ray peak. The MnFe_2O_4 particles were

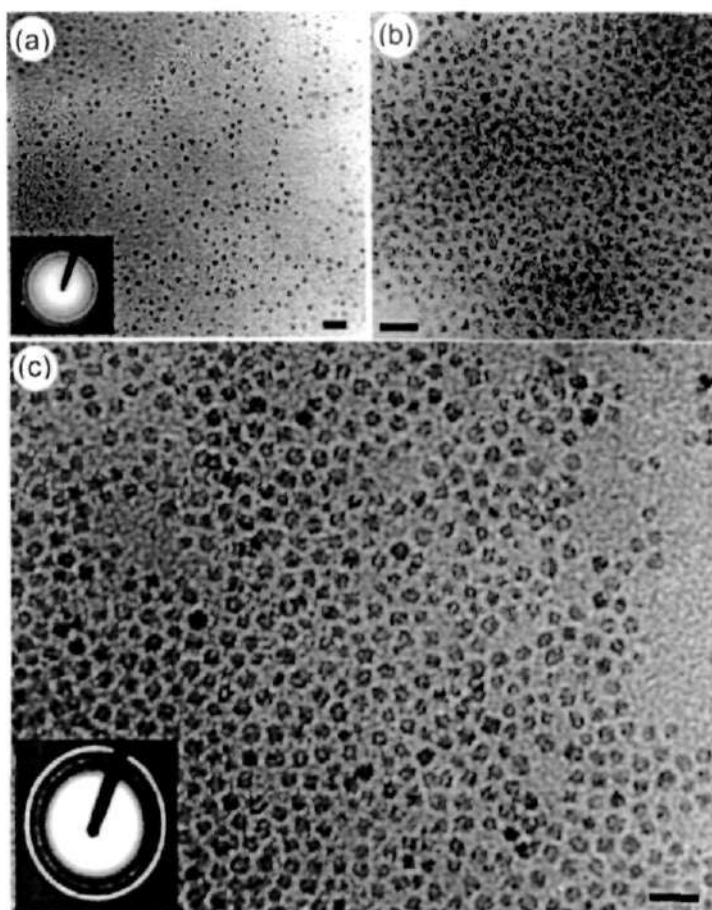


Figure 4.54: TEM micrographs of octylamine capped (a) Fe_3O_4 , (b) CoFe_2O_4 and (c) $\gamma\text{-Fe}_2\text{O}_3$ nanoparticles. The scale bars correspond to 20 nm. The insets in (a) and (c) show the obtained SAED patterns.

smaller with diameters in the range of 2 to 4 nm. Nanocrystals separated from each other are seen in the case of Fe_3O_4 (see Figure 4.54a). In contrast, close packed aggregates of nanocrystals are seen in the cases of CoFe_2O_4 and $\gamma\text{-Fe}_2\text{O}_3$ (see Figure 4.54b,c). In the case of $\gamma\text{-Fe}_2\text{O}_3$, short range order of nanocrystals, extending to one or two hexagons is seen.

Dodecylamine capped Fe_3O_4 were prepared by carrying out decomposition of the cupferron complex in dodecylamine instead of octylamine. The obtained nanocrystals were larger with a mean diameter of 8.6 nm and exhibit a tendency to form close packed arrays (see Figure 4.55). The arrangement seen in this case

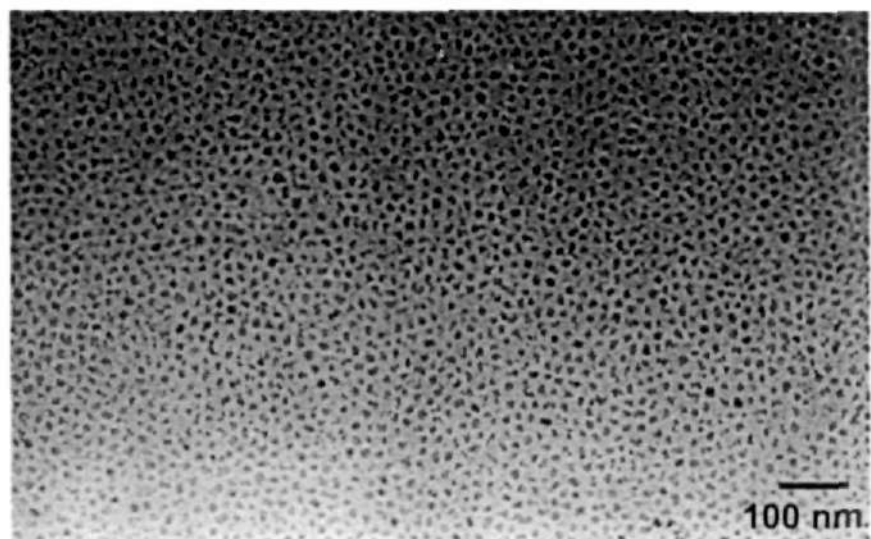


Figure 4.55: TEM micrographs showing Fe_3O_4 nanoparticles capped with dodecylamine.

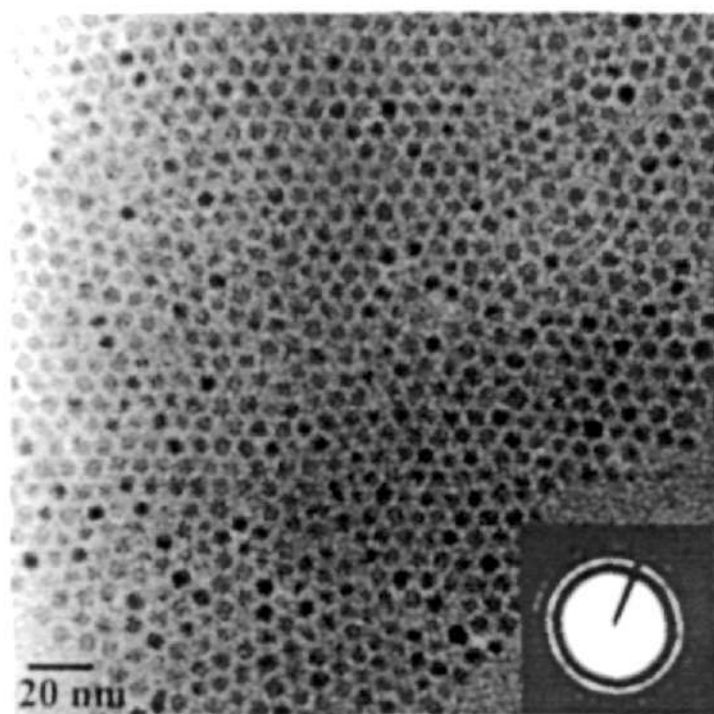


Figure 4.56: TEM micrographs showing Co_3O_4 nanoparticles capped with octylamine. Inset shows the SAED pattern.

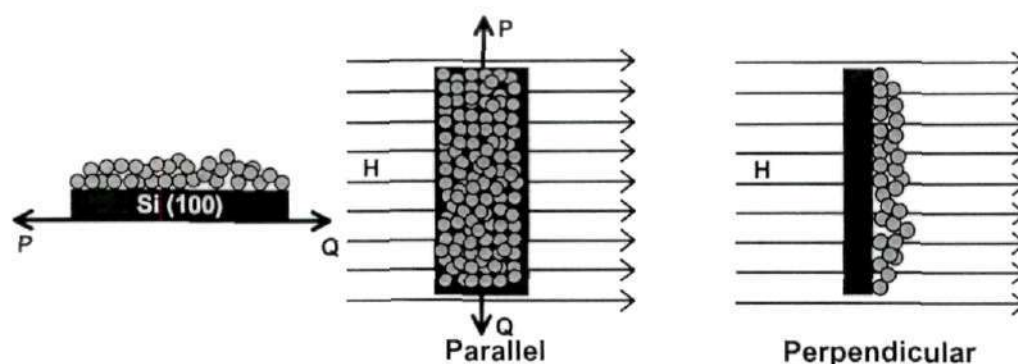


Figure 4.57: Schematic illustration of the two different orientations along which magnetic measurements were carried out. The change in the orientation was brought about by rotating the film along the PQ axis.

bears a remarkable resemblance to the arrays obtained from Pd nanocrystals at extremal d/ℓ values (see for example, Figure 4.38). Due to the significant number of faceted particles, it has not been possible to obtain reliable center to center interparticle distances. However, the average interparticle surface to surface distance obtained is ~ 3.2 nm and indicates 6% interdigitation of the dodecylamine chains. By adopting the thermal decomposition method, we have also been able to obtain monodisperse Co_3O_4 nanocrystals. The octylamine capped Co_3O_4 nanocrystals with a mean diameter of 5 nm, readily self-assemble into well ordered two-dimensional arrays similar to Pd and Pd-Ni nanocrystals (see Figure 4.56). Amine chain interdigitation of upto 17% was observed in these arrays.

Having obtained ordered arrangements of magnetic nanocrystals, we attempted to study collective magnetic properties. For this purpose, core-shell Pd-Ni, octylamine capped $\gamma\text{-Fe}_2\text{O}_3$ as well as citrate capped $\gamma\text{-Fe}_2\text{O}_3$ nanocrystals were cast into films on Si(100) surface by allowing droplets of the sol to evaporate slowly on the Si(100) substrate. The loading of the nanocrystals on the substrates was followed by the aid of a Cahn microbalance. Films of citrate capped $\gamma\text{-Fe}_2\text{O}_3$ with loadings of 454, 720 and 1400 μg , octylamine capped $\text{Pd}_{561}\text{Ni}_{3000}$ with a loading of 510 μg and octylamine capped $\gamma\text{-Fe}_2\text{O}_3$ with a loading of 300 μg were prepared. When cast into films, the nanocrystals retained their identity and were not aggregated. This can be readily ascertained by the fact that the nanocrystals can be

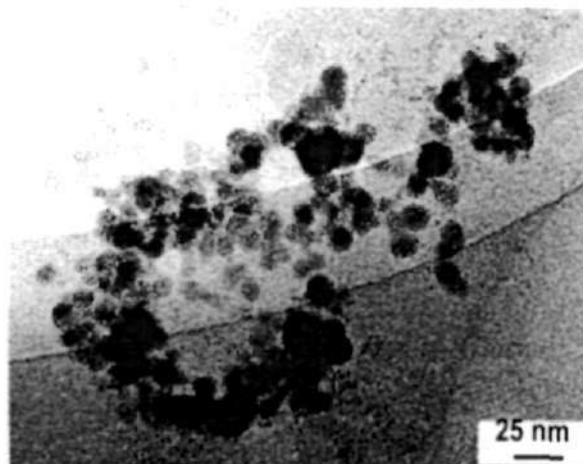


Figure 4.58: TEM micrographs of citrate capped $\gamma\text{-Fe}_2\text{O}_3$ nanoparticles.

recovered without any change in size or shape by simply immersing the substrate in appropriate solvents. The magnetic structure of the films was studied by carrying out magnetic hysteresis measurements along parallel and perpendicular directions as a function of temperature. In figure 4.57, the two orientations of the film with respect to the magnetic field is schematically illustrated.

The average diameter of the citrate capped $\gamma\text{-Fe}_2\text{O}_3$ nanocrystals was found to be 10.8 nm (see TEM image in Figure 4.58). Figure 4.59 shows the SEM images of typical films, revealing a large coverage of the magnetic particles over the substrate with no cracks and discontinuities. It is seen that octylamine capped $\text{Pd}_{561}\text{Ni}_{3000}$ nanocrystals yield films that are made up of dendritic outgrowths against a smooth background (see Figure 4.59a). It is to be noted that the dendritic outgrowths and the background are both made up of $\text{Pd}_{561}\text{Ni}_{3000}$ nanocrystals. An increase in the film loading increases the density of the dendritic outgrowths. The octylamine capped $\gamma\text{-Fe}_2\text{O}_3$ nanocrystals yield rough films with spherical agglomerates (see Figure 4.59b). The spherical agglomerates were seen, regardless of the film loading. Citrate capped $\gamma\text{-Fe}_2\text{O}_3$ nanocrystals, on the other hand, yield exceptionally smooth films. At a loading of $454\ \mu\text{g}$, one observes smooth films extending to tens of microns (see Figure 4.59c). The microstructure is different from that on HOPG substrates, where rough films consisting of spherical agglomerates are observed [196, 197]. As the nanocrystal loading is increased to $1400\ \mu\text{g}$

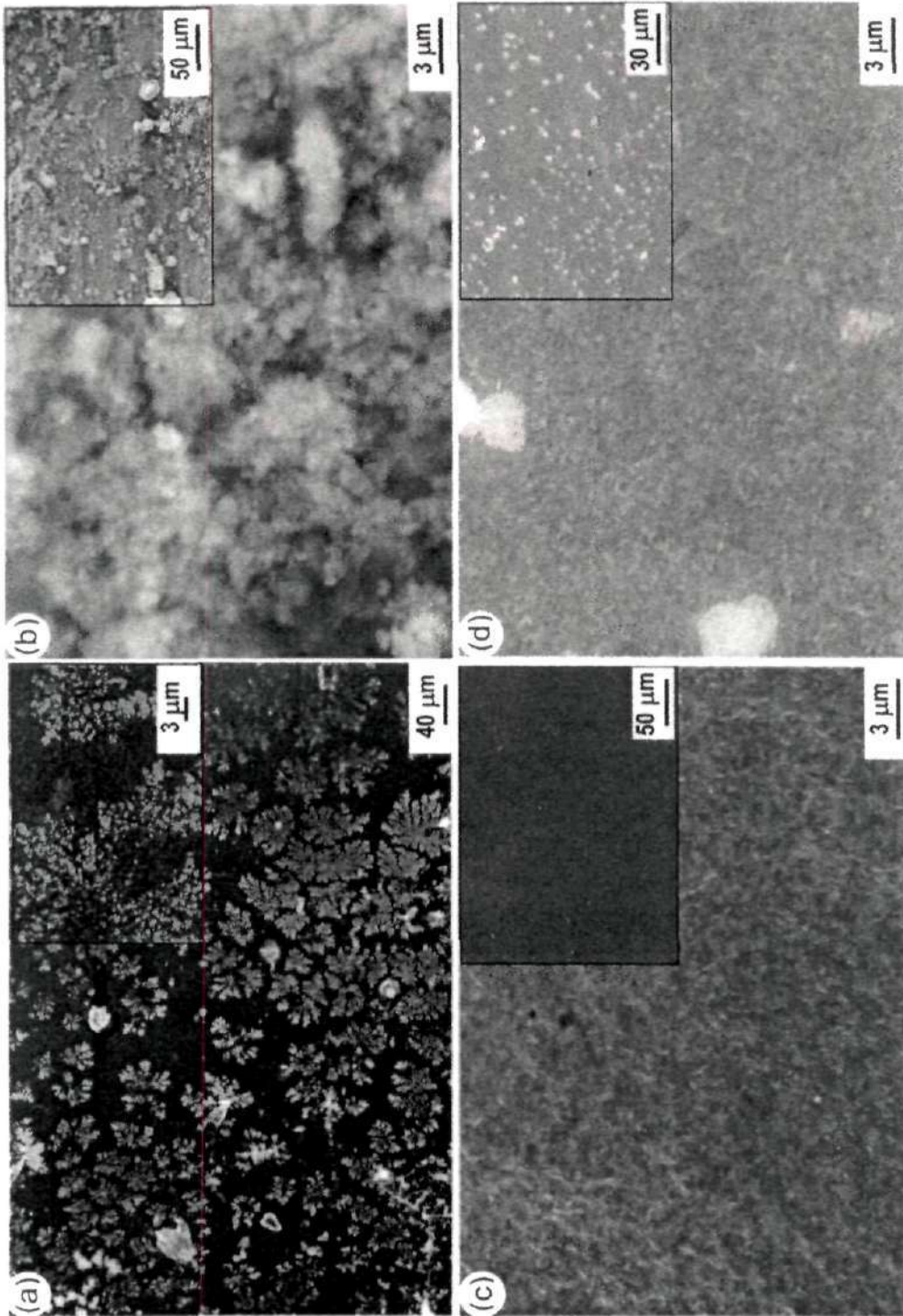


Figure 4.59: SEM images showing drop-cast films of (a) 510 μg of octylamine capped $\text{Pd}_{561}\text{Ni}_{30000}$ nanocrystals, (b) 300 μg of octylamine capped $\gamma\text{-Fe}_2\text{O}_3$ nanocrystals, (c) 454 μg of citrate capped $\gamma\text{-Fe}_2\text{O}_3$ nanocrystals, (d) 1400 μg of citrate capped $\gamma\text{-Fe}_2\text{O}_3$ nanocrystals. The inset (a) shows a higher resolution SEM image showing the details of a dendritic outgrowth. The insets in (b), (c), (d) show images from larger areas (lower resolution).

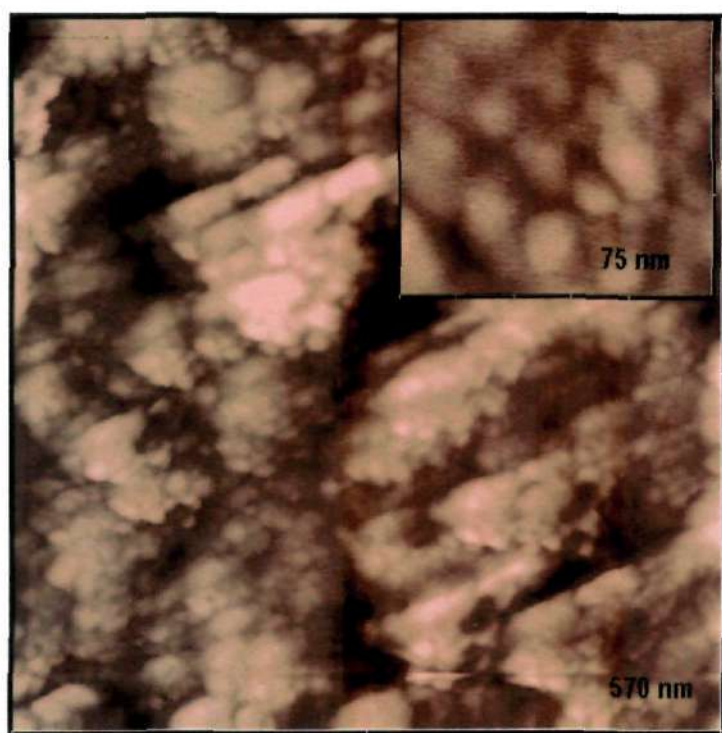


Figure 4.60: Tapping mode atomic force microscopic images of 720 μg citrate capped $\gamma\text{-Fe}_2\text{O}_3$ nanocrystal film. The inset shows a higher resolution image.

(Figure 4.59d), a few spherical agglomerates of tightly packed nanocrystals are seen against a smooth background. Tapping mode AFM measurements on films of citrate-capped nanocrystals revealed that the films were made of spherical particles with an average diameter of 12 nm (see Figure 4.60). The difference in the diameters (of 1.2 nm) between TEM and AFM measurement is due to the thickness of the capping citrate layer. The r.m.s roughness value obtained by AFM of a film (with 720 μg loading) estimated from a region of $3\mu^2$ was ~ 50 nm, the maximum surface trough to valley distance being 115 nm. SEM and AFM images revealed no changes in the microstructure of the films after the completion of magnetic measurements. Based on the observed surface roughnesses, the films made up of citrate capped $\gamma\text{-Fe}_2\text{O}_3$ nanocrystals were chosen for detailed magnetic studies.

The citrate capped nanocrystals in the powder form are superparamagnetic at room temperature and exhibit hysteresis on cooling to 5 K as shown in Figure 4.61. The saturation field and the coercivity values are similar to the values reported

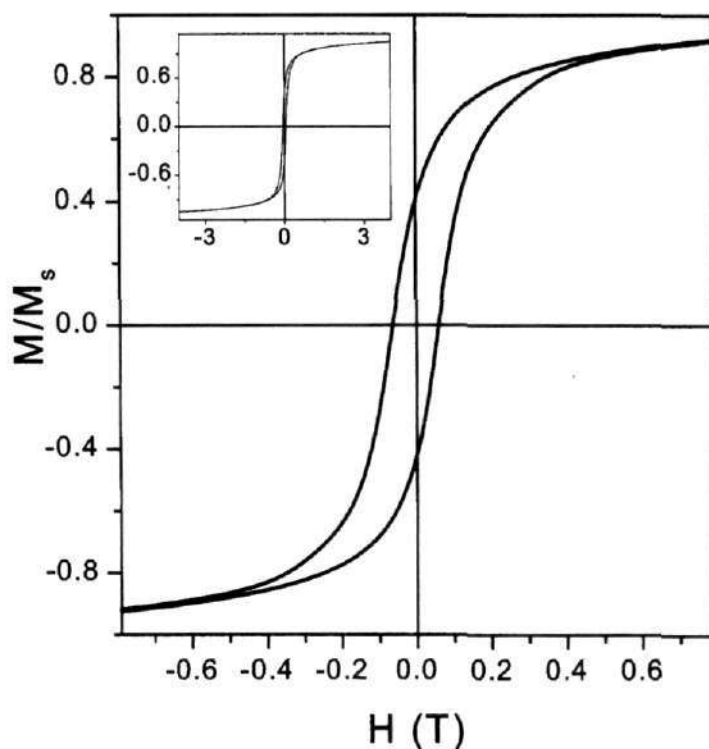


Figure 4.61: Hysteresis loop at 5 K ($H = 4$ T) from citrate capped $\gamma\text{-Fe}_2\text{O}_3$ nanocrystals in powder form. The inset shows the hysteresis loop in the full range.

for iron oxide nanocrystals of similar dimensions. The squareness ratio for the powder sample was 0.42, a value close to that expected (0.5) for randomly oriented single domain magnetic particles with uniaxial anisotropy [94]. Such an anisotropy has been observed earlier for iron oxide nanocrystals of similar sizes, based on ferromagnetic resonance and magnetization measurements [196, 229].

Figure 4.62 shows the hysteresis loops from the 720 μg film of citrate capped $\gamma\text{-Fe}_2\text{O}_3$ nanocrystals obtained along parallel and perpendicular orientations at various temperatures. The film exhibits hysteresis even at 300 K in contrast to the powder sample which is superparamagnetic at room temperature. As the temperature is lowered from 300 to 50 K, the coercivity of the film increases from 1.52 to 3.10 kOe along the perpendicular orientation (Figure 4.62a) and from 1.20 to 1.66 kOe along the parallel orientation (Figure 4.62b). The hysteresis loops from the perpendicular orientation are steeper and wider than those from the parallel orientation and

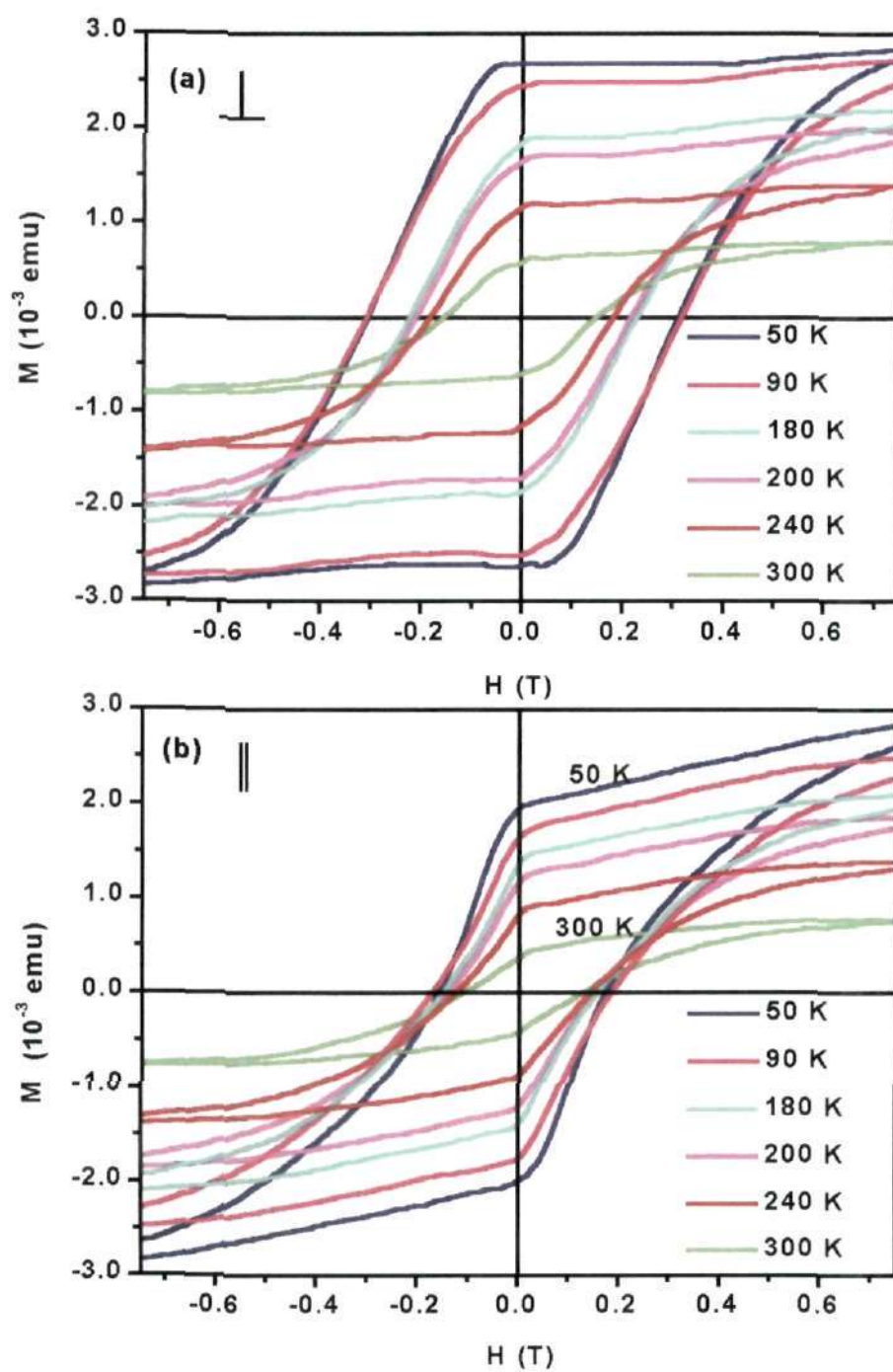


Figure 4.62: Hysteresis loops from the $720 \mu\text{g}$ of citrate capped $\gamma\text{-Fe}_2\text{O}_3$ film at various temperatures with the substrate held (a) perpendicular and (b) parallel to the applied field direction.

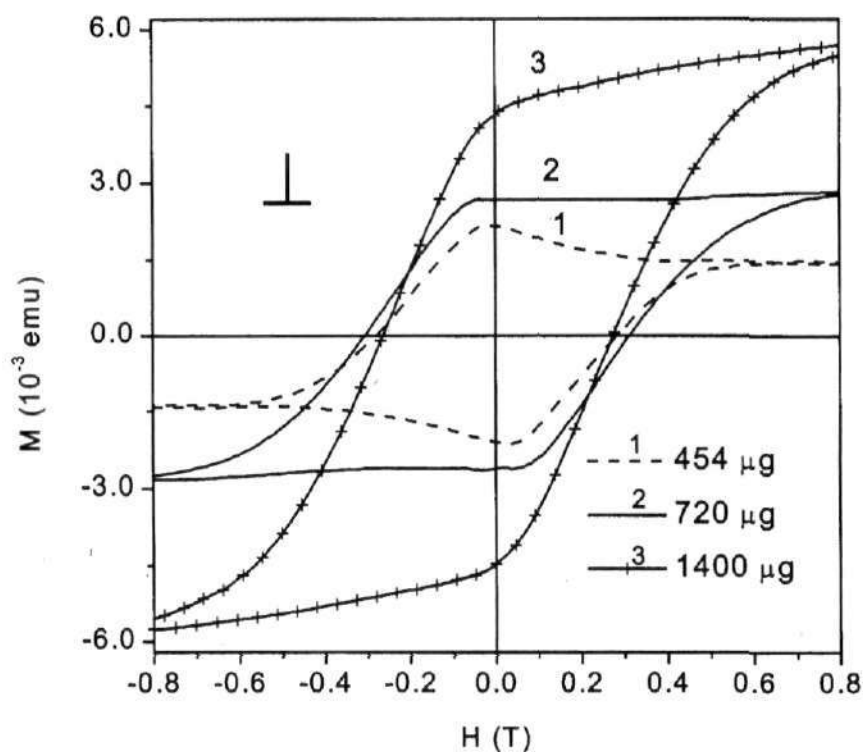


Figure 4.63: Hysteresis loops at 50 K for citrate capped $\gamma\text{-Fe}_2\text{O}_3$ films of different thickness with the substrate held perpendicular to the applied field direction.

essentially enclose the latter at all temperatures, indicating perpendicular anisotropy in the magnetization [94]. It is interesting that the squareness ratio of the loop, which is 0.89 at 300 K, reaches a value of 0.95 at 50 K along the perpendicular direction.

Figure 4.63 shows the hysteresis loops obtained at 50 K along the perpendicular direction for films with different loadings. The width and the height of the loops vary significantly with the loading. The coercivity value is 2.82 kOe for the 454 μg film and increases to 3.10 kOe when the loading is 720 μg , but decreases to 2.7 kOe on further increase of the loading to 1400 μg . The magnetic orientation in the latter film appears to be relatively poor, consistent with the presence of a large number of spherical aggregates (see Figure 4.59d).

The hysteresis loops obtained from the 300 μg octylamine capped $\gamma\text{-Fe}_2\text{O}_3$ nanocrystal film is shown in Figure 4.64. There is no appreciable change in the coercive field with the change in the orientation of the film. However, the remanence

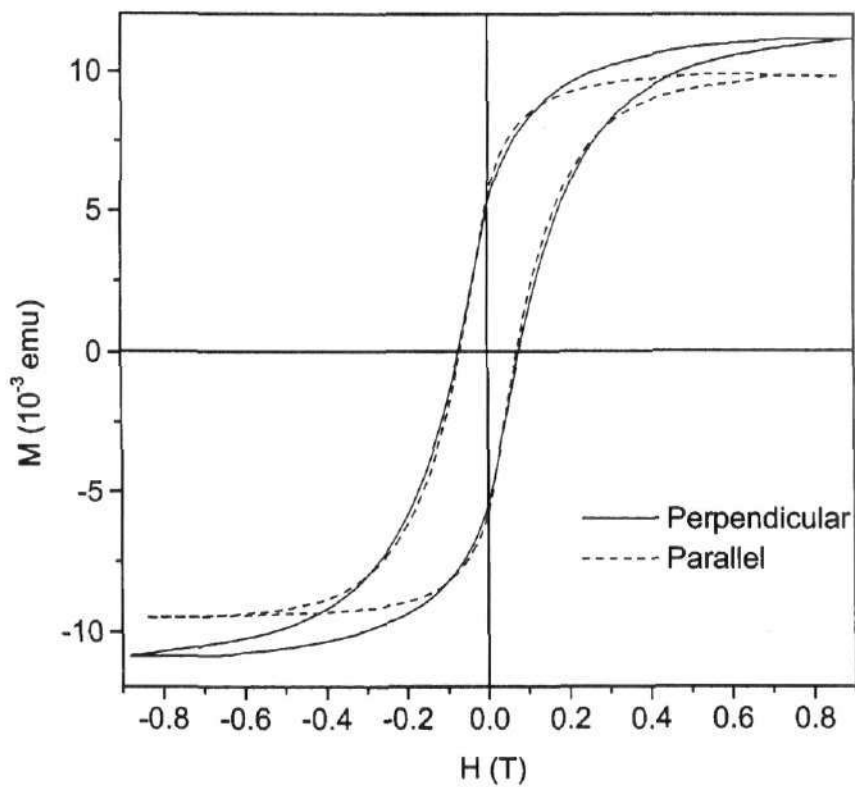


Figure 4.64: Hysteresis loops at 50 K for a 300 μg film of octylamine capped $\gamma\text{-Fe}_2\text{O}_3$ nanocrystals. The loops were corrected for the diamagnetic contribution from the substrate.

and the coercive field values are slightly higher than those of the corresponding frozen fluid which had a coercive field of 75 Oe and a remanence of 3×10^{-3} emu.

For the purpose of comparison, the collective behavior of the $\gamma\text{-Fe}_2\text{O}_3$ nanocrystals was ascertained by subtracting the contribution from the diamagnetic substrate. The values of the squareness ratio thus obtained are higher for the nanocrystal films than those of the powder or the frozen fluid. At 50 K for instance, the squareness ratios for the films are in the range of 0.61 to 0.89, while the value for the powder is 0.42. Changes in the demagnetization factor of the system could bring about such a difference [137, 196]. As mentioned earlier (see Section 1.6), magnetizing nanocrystals in the powder form is comparable to magnetizing spheres with the demagnetization value of 0.33. The demagnetization factor value is zero for the film of nanocrystals. Thus, the higher remanence values (squareness ratios) observed

in the case of the nanocrystal films are due to the lowering of the demagnetization factor. Although there is a small change in the squareness ratio in both parallel and perpendicular orientations with loading, the squareness ratio is always greater in the perpendicular orientation. The demagnetizing factor being nearly zero in these films, the observed difference could be due to the preferential orientation of the easy axis of magnetization of the nanocrystals perpendicular to the substrate [196]. The values of the magnetic anisotropy, estimated as the percentage of the excess area enclosed in a perpendicular loop, were 15%, 34% and 46% respectively, for the 454, 720 and 1440 μg films. These values serve as a measure of the perpendicular anisotropy in the citrate-capped $\gamma\text{-Fe}_2\text{O}_3$ films [230]. In the case of octylamine capped $\gamma\text{-Fe}_2\text{O}_3$ nanocrystals, the films show little change in coercivity with the change in the orientation, indicating a random orientation of the easy axis [168].

It may be argued that the observed anisotropy is due to the finite surface roughness present in the nanocrystal films that could give rise to a small perpendicular anisotropy. However, based on our estimate of the surface roughness and considering that the rougher films obtained in the cases of octylamine capped $\gamma\text{-Fe}_2\text{O}_3$ or the citrate capped $\gamma\text{-Fe}_2\text{O}_3$ on HOPG substrate do not exhibit such a behavior, we believe that surface roughness is unlikely to be responsible for the observed anisotropy.

While we are not in a position to ascertain the exact mechanism of perpendicular magnetization of the $\gamma\text{-Fe}_2\text{O}_3$ films, it is instructive to examine the important factors that govern the phenomenon. Ngo and Pileni [196] prepared drop-cast films of magnetic iron oxide nanocrystals on HOPG substrates and found no alignment of the magnetic axis, in the absence of an external magnetic field. With the field, they observed in-plane alignment of the magnetic moments. In the present study, we find that the nanocrystals spontaneously assemble on Si(100) substrates with their easy axis of magnetization perpendicular to the substrate. Previous studies involving different substrates for the assembly of semiconductor and metal nanocrystals have identified evaporation rates [137], van der Waals interaction between the particles and the substrate and capillary forces [231] as key parameters in bringing about changes in the microstructure. Indeed, the static dielectric constants of Si and

graphite, which determine the strength of the capillary and van der Waals forces are quite different (12 for Si and 5.6 for Graphite). Moreover, the chemical nature of the silicon surface differs considerably from that of graphite. Yet another factor that could influence the magnetic behavior is the relatively longer drying period required for the ferrofluid on the Si substrate. Earlier studies of the role of the substrate in influencing the magnetization of a deposited atomic thin film have shown that a combination of several anisotropies are required to produce noticeable perpendicular magnetization [232–234]. Of them, surface anisotropy and interfacial roughness are quite specific to a substrate [235,236] and it is possible that these factors are in play in the $\gamma\text{-Fe}_2\text{O}_3/\text{Si}(100)$ films discussed herein.

In conclusion, two-dimensional arrays of core-shell $\text{Pd}_{561}\text{Ni}_n$ nanocrystals have been prepared by using alkanethiols. The nanocrystals with higher Ni coverage tend to form multilayers or crystallites. Two-dimensional arrays have also been obtained with $\text{Pd}_{561}\text{Ni}_{3000}$ nanocrystals further covered by a Pd layer with the composition $\text{Pd}_{561}\text{Ni}_{3000}\text{Pd}_{1500}$. The structure of the $\text{Pd}_{561}\text{Ni}_{3000}$ array depends on nature of the head group of the surfactant, with the amine yielding an hexagonal array in contrast to the multilayered tapes or wires obtained with octanethiol. Octylamine capped $\gamma\text{-Fe}_2\text{O}_3$ nanoparticles tend to assemble into arrays with very short order. Relatively regular arrays are obtained with Fe_3O_4 nanoparticles capped with dodecylamine. Octylamine capped Co_3O_4 nanoparticles, however, yield good two-dimensional arrays extending to a few microns. The Co and Mn ferrite nanoparticles coated with octylamine exhibit small scale organization. We have demonstrated that citrate capped $\gamma\text{-Fe}_2\text{O}_3$ nanocrystals spontaneously assemble on Si(100) substrates with a preferential perpendicular ordering of the easy magnetic axis, yielding films with higher perpendicular magnetization. The magnetic anisotropy is sensitive to the film thickness. Octylamine capped $\gamma\text{-Fe}_2\text{O}_3$ nanocrystals, however, do not appear to form magnetically ordered films. The present results on the citrate-capped nanocrystals constitute the first demonstration of perpendicular magnetization in a nanostructure obtained by mesoscopic self-assembly.^{||}

^{||}Papers based on this study have appeared in J. Nanosci. Nanotech. (2001), Pramana - J. Phys. (2002). Another paper is submitted to Nanotech.

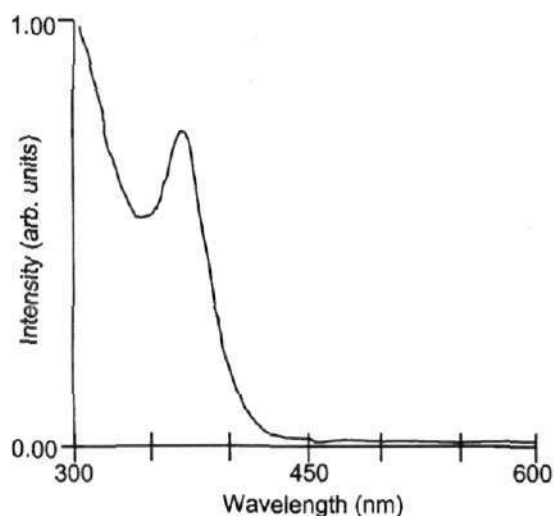


Figure 4.65: Electronic absorption spectra of CdS nanocrystals dispersed in heptane.

4.7 Layer-by-Layer assembly of metal and semiconductor nanocrystals

CdS nanocrystals have been prepared by using the reverse micelle technique as described in the experimental section. In Figure 4.65, the electronic absorption spectra of CdS nanocrystals dispersed in heptane is shown. The band at ~ 360 nm, indicates a diameter of 2.4 nm [208]. Pt nanocrystals stabilized with Tetraoctyl ammonium bromide were obtained by borohydride reduction of Pt ions transferred to toluene. The average diameter of the Pt particles was found to be 5 nm (as determined by TEM).

The deposition process is schematically illustrated in Figure 4.66. A monolayer of the dithiol (1,10-decanedithiol) was deposited on a polycrystalline Au substrate by immersing the substrate in a solution of dithiol. The film was subsequently immersed in a solution of Pt nanocrystals. These steps were repeated to obtain multilayered superlattices. After each deposition, the nanostructures were studied by means of XPS and STM. These experiments were a part of a larger study in our laboratory wherein, superlattices consisting of arrays of Au and Pt nanocrystals of different sizes were obtained on Au and Ag substrates [237]. The deposition of the

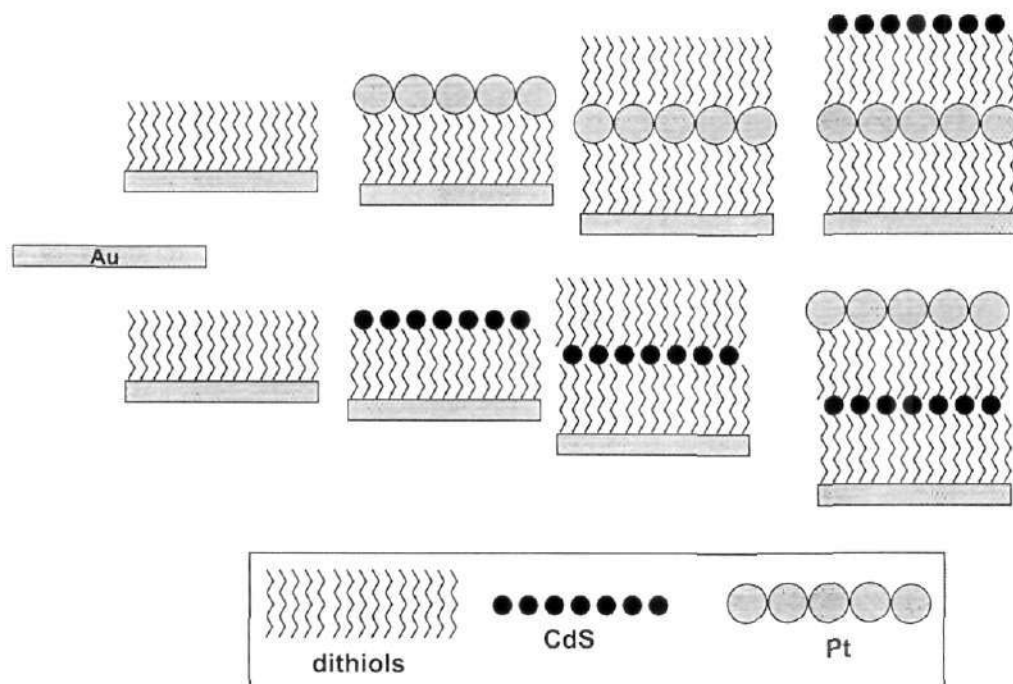


Figure 4.66: Schematic drawing depicting the layer-by-layer deposition of a heterostructure consisting of alternate layers of CdS and Pt nanoparticles with the layers being separated by dithiol molecules.

layers could follow any arbitrary order.

A scanning tunnelling microscopic study of a layer of 5 nm Pt particles after the first deposition revealed regular arrays of nanoparticles extending over 300 nm, which corresponds to the size of a typical flat terrace of the Au substrate. Imaging at lower scan size of 40×40 nm revealed the near regular spacing as 2 nm between spherical particles of 5 nm diameter (see Figure 4.67). Typical height of the features as estimated from STM z-values were $\sim 3 - 6$ nm, indicating that the layers are made of a monolayer of nanocrystals.

The core level XPS of a superlattice consisting of a layer of Pt and CdS nanocrystals is shown in Figure 4.68 after the first and second depositions along with that of the clean Au substrate. It is observed that the Au(4f) intensity decreases with the increase in the number of depositions. The substrate gets increasingly shadowed due to the limited escape depth of photoelectrons. The Pt(4f) level intensity is maximum after the deposition of Pt nanocrystals and shows a decrease

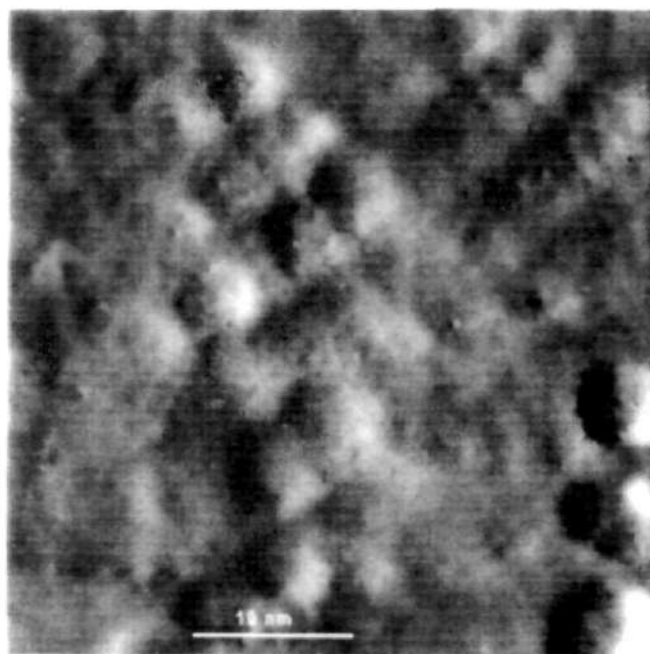


Figure 4.67: Scanning tunneling image of the first layer of the 5 nm Pt particles on a Au substrate.

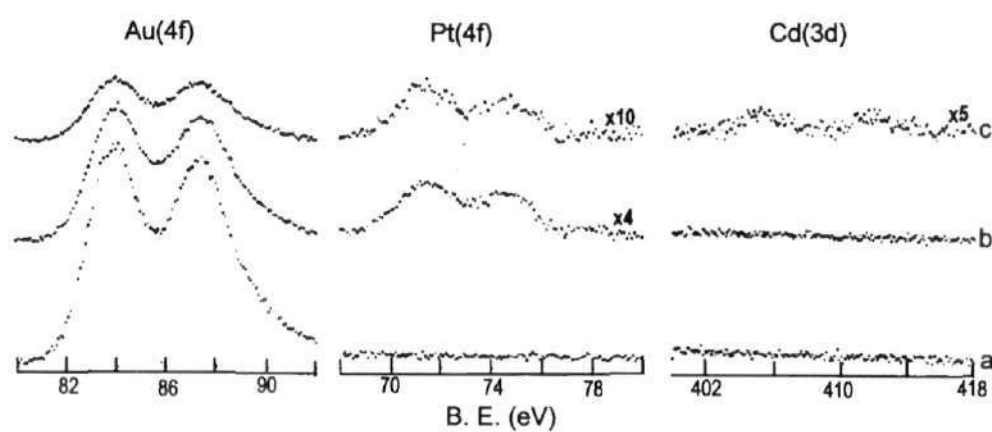


Figure 4.68: X-ray photoelectron spectra in the Cd(3d), Pt(4f), and Au(4f) regions for the CdS/Pt/Au system: (a) clean Au substrate, (b) after the deposition of the 5 nm Pt particles in the first layer, and (c) after the deposition of the 2.4 nm CdS particles in the second layer.

after the deposition of CdS nanocrystals. Following the second deposition, the Cd(3d) level which was previously absent comes up. The intensities of C(1s) and S(2p) levels of the dithiol (at 285.0 and 163.6 eV respectively) exhibit an increase with increase in number of depositions. It is thus apparent that the deposition proceeds by monolayer growth of nanocrystalline layers. Such depositions can be continued to upto five layers of particles. The order of deposition can be readily reversed and good superlattices of the form CdS-Pt-CdS could be obtained.

In conclusion, superlattices of arrays of CdS and Pt nanocrystals have been obtained by layer-by-layer deposition technique. CdS-Pt-CdS and Pt-CdS-Pt nanocrystal heterostructures have been made.**

4.8 Interaction of metal ions with lipoic acid capped Au and Ag nanoparticles

Lipoic acid capped Au and Ag nanocrystals were prepared by borohydride reduction of metal salts in the presence of lipoic acid as described in the experimental section. Au nanocrystals of mean diameters 7.5 ± 0.7 nm and 3.0 ± 0.4 nm were obtained by making use of metal/lipoic acid ratios of 1:1 and 1:2.5. In the case of Ag nanocrystals, the mean diameters were 5.0 ± 0.4 nm and 2.6 ± 0.4 nm for metal/lipoic acid ratios of 1:1 and 1:5 respectively. Stock solutions (1 mM) of CuSO₄, FeSO₄ (pH=3), NiNO₂ and acetates of Mn, Cd, Zn and Pb were used as sources of metal ions. Stock solutions of higher concentrations were employed in some cases. To study the effect of chelation of the metal ion to the lipoic acid groups that are bound to the metal nanocrystals, a few microliters of the stock solution were added to metal sols in a quartz cuvette. The changes that take place were followed by means of UV-visible spectroscopy. The reported concentrations are in terms of micromoles per liter (μ M).

Figure 4.69 shows two possible ways that Cu²⁺ ions can bind to a lipoic acid capped Ag nanocrystals. Figure 4.70 shows the changes in the absorption spectra of Ag nanoparticles of ~ 5 nm diameter capped by alpha-lipoic acid following the

**A Paper based on this study has appeared in J. Phys. Chem. (1999).

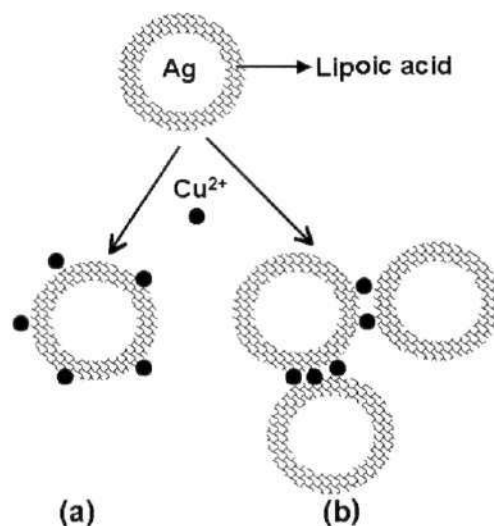


Figure 4.69: Schematic illustration showing the binding of metal ions to the carboxyl groups present at the tail of the amphiphile capping the metal nanoparticles. In (a), the metal ion is bound to the carboxyl end of one nanoparticle, but in (b), it binds to the carboxyl groups belonging to two nanoparticles, thus bridging between them.

addition of Cu^{2+} and Fe^{2+} ions. In the absence of metal ions, the plasmon band is observed ~ 430 nm. As the Cu^{2+} or the Fe^{2+} ions are added in the form of aqueous solutions, the plasmon band is dampened in proportion to the concentration of the metal ion (see Figure 4.70). After the addition of the metal ions, the plasmon band intensity immediately reaches a new value and the sol continues to exhibit the dampened band for extended periods of time (a few weeks), if left undisturbed. Several bivalent metal ions were examined. It was found that different metal ions cause the dampening of the plasmon band to different extents. For example, addition of $80 \mu\text{M}$ of $[\text{Cu}^{2+}]$ brings about a $\sim 60\%$ dampening of plasmon intensity while, on the other hand, addition of $230 \mu\text{M}$ of Fe^{2+} , brings about a decrease of $\sim 50\%$ (Figure 4.70). It is known that a change in the ionic strength causes aggregation of the sols, bringing about such changes in the plasmon band intensity. In the example above, the change in the ionic strength is around three times more in case of Fe^{2+} ions than in the case of Cu^{2+} ions but this is not reflected in the dampening of the plasmon band. We, therefore, consider the observed dampening of the plasmon band to arise from a process that is selective to a particular metal ion, involving the

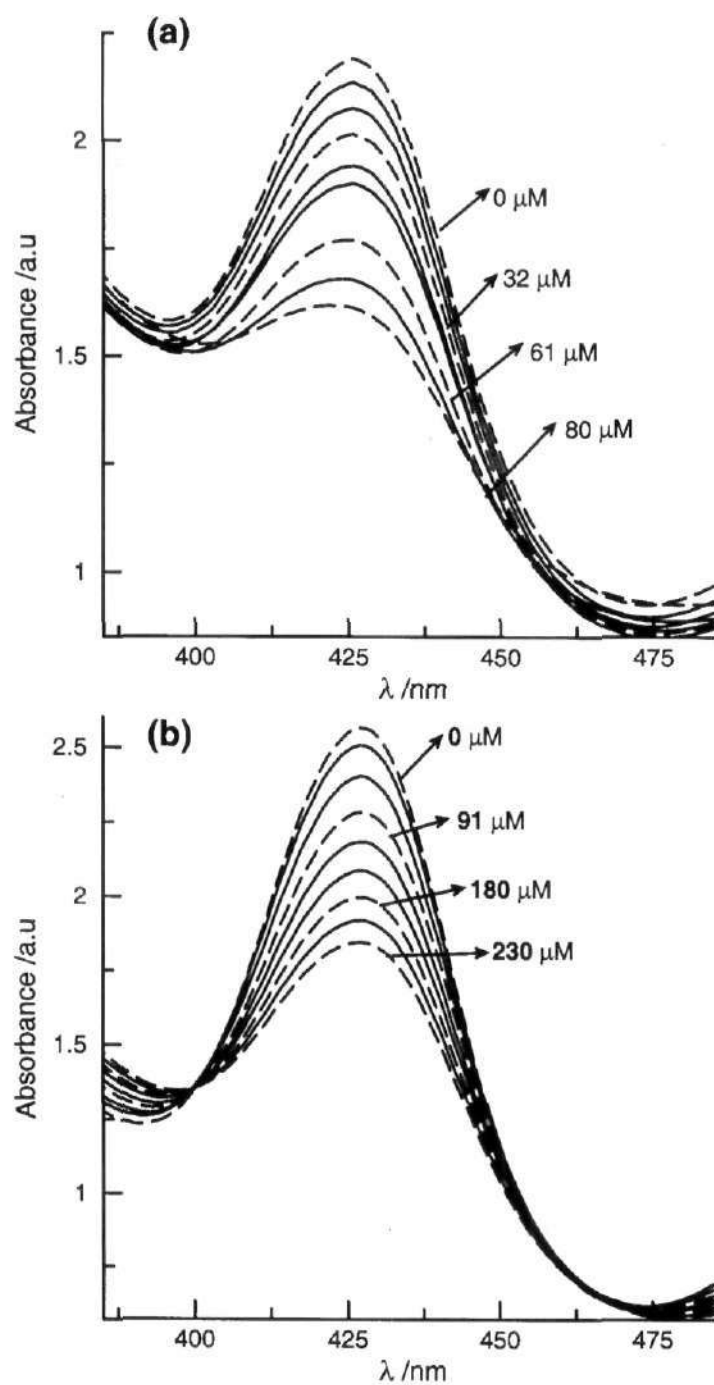


Figure 4.70: Electronic absorption spectra of ~5 nm Ag nanoparticles showing changes accompanying the addition of (a) Cu^{2+} and (b) Fe^{2+} . The concentrations of the ions are indicated.

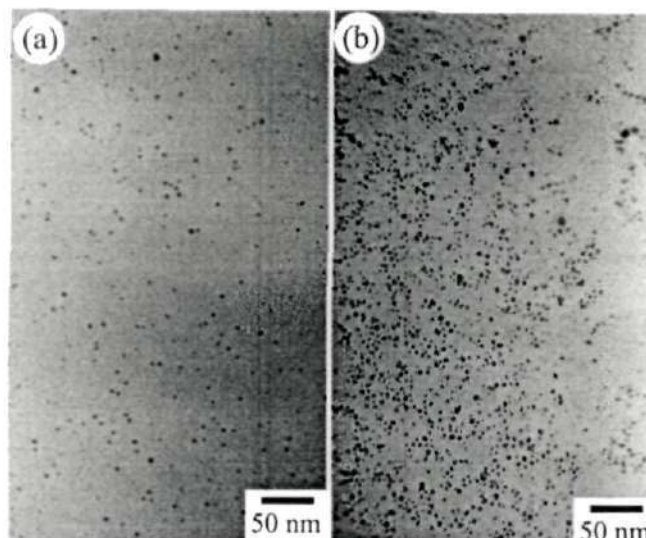


Figure 4.71: Electron micrographs of ~ 5 nm Ag nanoparticles (a) before the addition of Cu^{2+} and (b) in the presence of $80 \mu\text{M}$ Cu^{2+} .

surface carboxyl group rather than by ionic strength of the medium. Accordingly the sensitivity of the plasmon band varies from one metal ion to another.

In order to ascertain that this is indeed the case, we sought to remove the chelated metal ions by employing a ligand stronger than alpha-lipoic acid. Accordingly, by the addition of equimolar amounts of EDTA to Au and Ag sols containing chelated metal ions it was possible to enhance the plasmon band intensity to a value obtained in the absence of metal ions.

TEM studies shed further light on the above mentioned change undergone by the colloid. In Figure 4.71, we show typical TEM micrographs of the ~ 5 nm Ag nanoparticles before and after, the addition of Cu^{2+} ($80 \mu\text{M}$) ions. We see that even in the presence of Cu^{2+} ions, the nanoparticles remain isolated, with the aggregation limited to about 3% of the scanned area (throughout this study, no distinction between aggregation which is close, irreversible association of primary particles and agglomeration - loose, reversible association). This observation rules out aggregation as the cause of the observed dampening of the plasmon band. Theoretical investigations suggest that aggregates measuring a few hundred to thousand nanoparticles are required to obtain a substantive optical response [238].

The binding of metal ions appears to proceed more by the path a, rather than by the path b, in Figure 4.69.

Dampening of the plasmon band (along with accompanying changes in position and width) arising from the chemisorption of reactive molecules on the surfaces of nanoparticles [80, 239, 240] had earlier been attributed to charge transfer between the particle and the adsorbate. We have not found any change in the position or the width of plasmon band accompanying chelation of metal ions, but instead observe only a decrease in the band intensity. The existence of an isobestic point at 399 nm in Figure 4.70b and the near constant absorbance at 460 nm corroborate this view. Even where there is no isobestic point as in Figure 4.70a, there is little shift in the position of the width of the plasmon band. The trends were similar with different counter anions. Similar changes in the plasmon band intensity was observed in the case of Ag nanoparticles with a mean diameter of 2.6 nm following chelation. It can, therefore, be concluded that in the dilute metal ion concentration regime, the metal ions bind to the carboxyl functional group of the alpha-lipoic acid, which caps the nanoparticles and thereby cause the observed dampening of the plasmon band.

The effect of metal ions in dampening the plasmon band has been quantified by making use of the slopes of the plots of the plasmon band intensity against the metal ion concentration. We present such plots of the absorbance of the plasmon band of Ag nanoparticles at the absorption maximum against the concentration of metal ions in Figure 4.72. We also show the corresponding linear fits in this figure. The inset in Figure 4.72 shows that the intensity decrease can continue over an extended region of concentration in the case of weakly interacting metal ions such as Mn^{2+} and Ni^{2+} . The values of the slopes for the interaction of Cu^{2+} , Fe^{2+} , Cd^{2+} , Zn^{2+} , Pb^{2+} , Mn^{2+} and Ni^{2+} with ~ 5 nm Ag nanoparticles are 7.5, 3.8, 2.0, 1.8, 1.2, 0.5, $0.5 \times 10^3 \text{ M}^{-1}$ respectively. The slopes obtained for Ag nanoparticles with a mean diameter of 2.6 nm were 2.8, 0.6, 0.5, $0.2 \times 10^3 \text{ M}^{-1}$ for Cu^{2+} , Fe^{2+} , Mn^{2+} and Ni^{2+} ions respectively. Similar results were obtained when the counter ions of the Cu^{2+} , Ni^{2+} and Mn^{2+} ions were changed to chlorides. While the slopes of the absorption-concentration plots are higher when the particle diameter is larger, the effectiveness of chelation varies in the order $\text{Cu}^{2+} > \text{Fe}^{2+} > \text{Mn}^{2+} > \text{Ni}^{2+}$, independent of the

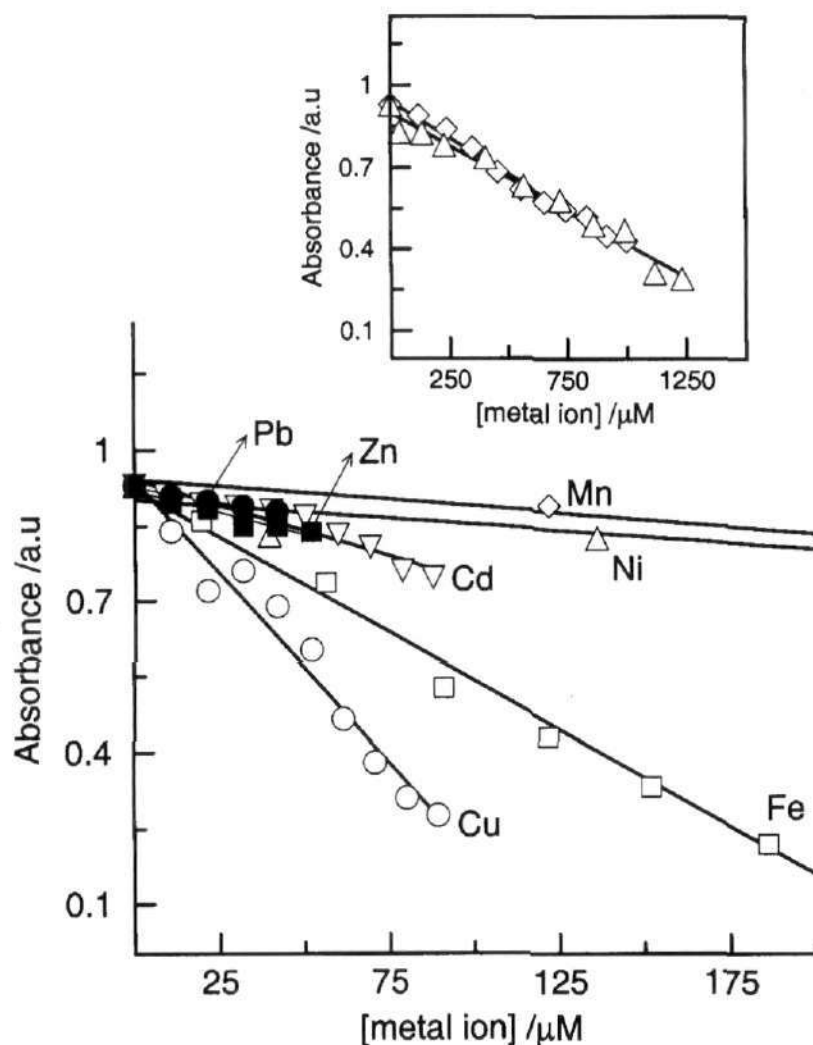


Figure 4.72: Variation in the absorbance of the plasmon band (at λ_{\max}) of ~ 5 nm Ag nanoparticles as a function of the concentration of metal ions. Linear fits are shown. The inset shows the data for Mn^{2+} and Ni^{2+} over an extended concentration range.

diameter of the Ag nanoparticles.

Figure 4.73 shows the results of our studies on the interaction of Cu^{2+} ions with Au nanoparticles. In Figure 4.73a, we present the changes in the absorption spectra of ~ 7.5 nm Au nanoparticles brought about by the addition of Cu^{2+} ions. A decrease in the plasmon band intensity is observed just as in the case of Ag nanoparticles. In Figure 4.73b, we show the change in the absorbance with the Cu^{2+} concentration for 7.5 nm and 3.0 nm Au nanoparticles. The slope is slightly greater

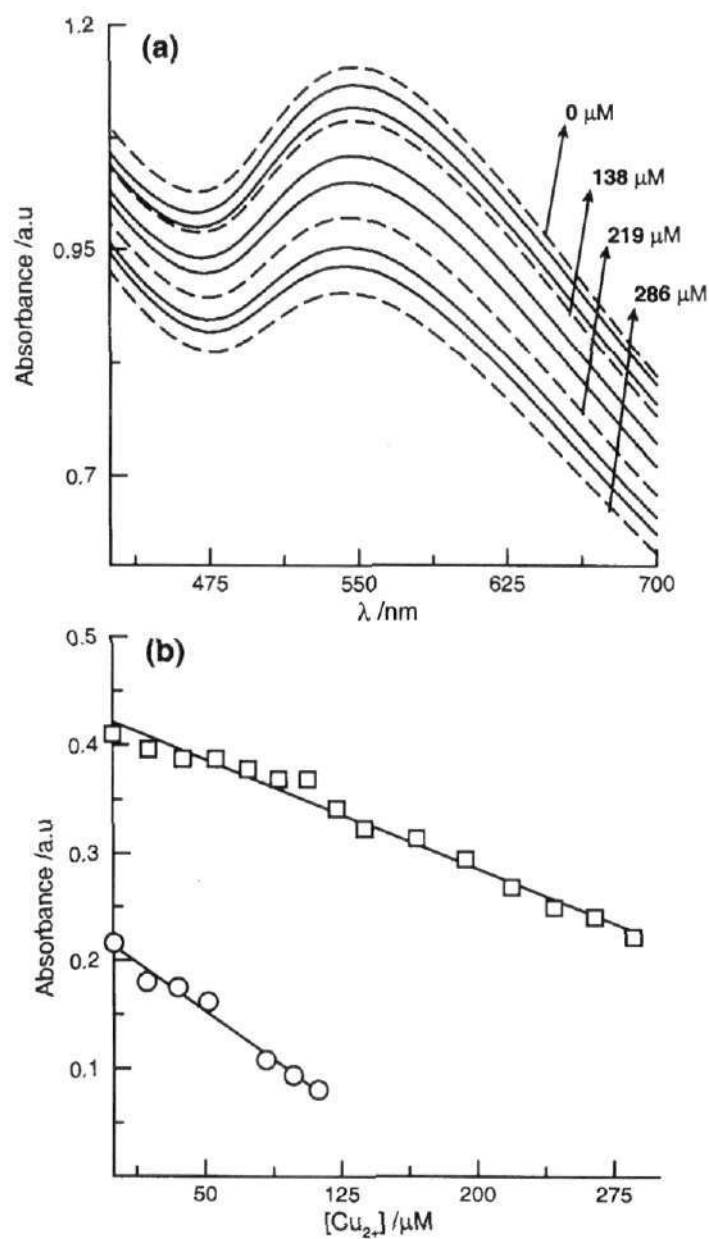


Figure 4.73: (a) Electronic absorption spectra of ~ 7.5 nm Au nanoparticles showing changes accompanying the addition of Cu^{2+} . (b) Plots showing the variation of absorbance of the plasmon band (at λ_{max}) of Au nanoparticles accompanying the addition of Cu^{2+} ions. The circles correspond to nanoparticles of ~ 7.5 nm diameter, and the squares correspond to ~ 3.0 nm diameter nanoparticles.

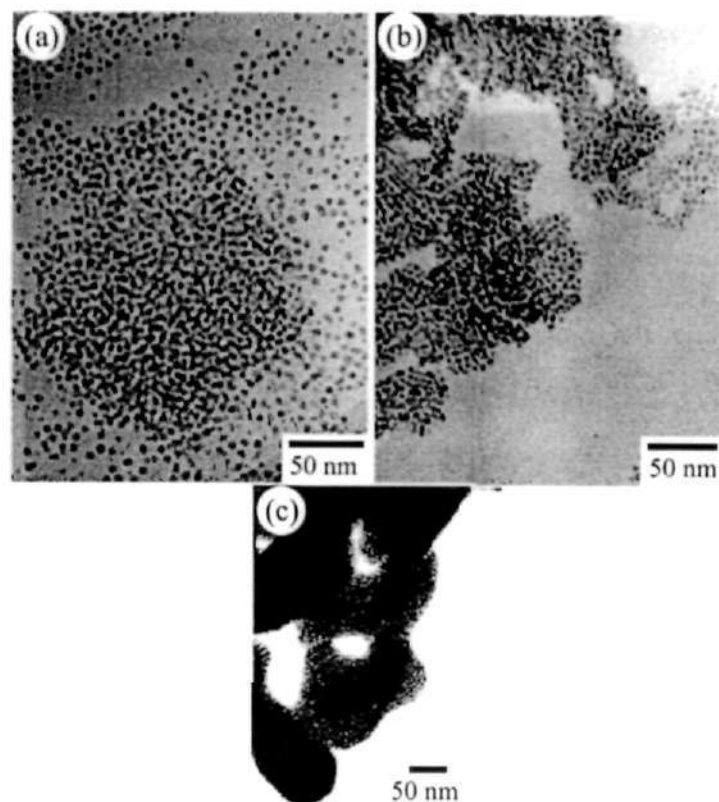


Figure 4.74: Electron micrographs of ~ 5 nm Ag nanoparticles after interaction with aqueous Cu^{2+} solutions that are (a) $120 \mu\text{M}$, (b) $200 \mu\text{M}$, and (c) $500 \mu\text{M}$.

in the case of the larger Au nanoparticles. Addition of Cu^{2+} ions to ~ 5 nm Ag nanoparticles beyond the dilute regime ($> 90 \mu\text{M}$) brings about different changes in the sol. The sols precipitate out after about $200 \mu\text{M}$ of Cu^{2+} has been added. The onset of precipitation is shifted to higher concentration upon addition of PVA (5%). TEM studies indicate that the nanoparticles form aggregates, with the extent of aggregation (measured as the fraction of particles belonging to an aggregate) increasing with concentration of the metal ions as shown by the micrographs in Figure 4.74. When the Cu^{2+} concentration is $120 \mu\text{M}$ (Figure 4.74a), $\sim 50\%$ of the nanoparticles form part of aggregates in contrast to the case of $80 \mu\text{M}$ Cu^{2+} , where the aggregation is limited to $\sim 3\%$ particles (see Figure 4.71b). Almost all the particles get aggregated when the concentration of Cu^{2+} is raised to $200 \mu\text{M}$. It is to be noted that the sols showed little sign of opalescence and remained stable during all the measurements discussed hitherto (in the Cu^{2+} ion concentration regime



Figure 4.75: Electron micrographs of ~ 7.5 nm Au nanoparticles after interaction with an aqueous $600 \mu\text{M}$ Cu^{2+} solution.

of $0\text{--}200 \mu\text{M}$). Further addition of Cu^{2+} ions, however, leads to precipitation. TEM images of the precipitate showed multilayered, close packed structures of nanoparticles (Figure 4.74c).

The above observations are supported by changes in the optical spectra of the nanoparticles. In the above concentration regime ($90 \mu\text{M} < [\text{Cu}^{2+}] > 200 \mu\text{M}$), the plasmon band is completely damped and the scatter at longer wavelengths, which was essentially constant in the dilute regime, increases progressively. In order to quantify the changes, we employ a slightly modified version of the flocculation parameter defined previously by Weisbecker et al. [201] for Au colloids. The flocculation parameter, defined here, for the case of Ag nanoparticles as the integrated area in the $550\text{--}750$ nm region, shows an increase with the metal ion concentration, coinciding with aggregation phenomena described previously. The change in the flocculation parameter could not be reversed by addition of EDTA and thus the chelation is irreversible. Addition of PVA stabilizes the sol and permits further addition of Cu^{2+} ions with higher values of flocculation parameter than that of the native sol. We thus have a regime of chelation, that is not reversible

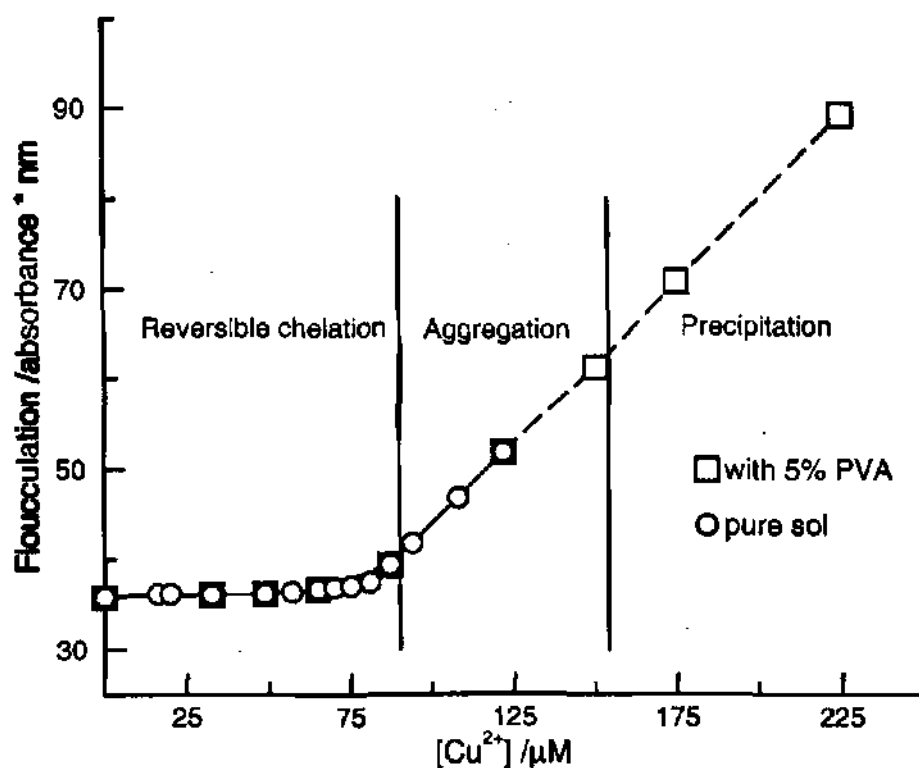


Figure 4.76: Variation of the flocculation parameter with the concentration of Cu^{2+} in the case of ~ 5 nm Ag nanoparticles.

by addition of stronger chelating agents above $90 \mu\text{M}$ of $[\text{Cu}^{2+}]$, followed by a regime where precipitation occurs (Figure 4.74c). In the case of Au nanoparticles, the region of irreversible chelation was also marked by aggregation as can be seen from the TEM micrograph in Figure 4.75.

The different regimes of metal ion interaction with alpha-lipoic acid capped Ag nanoparticles, delineated on the basis of the flocculation parameter is depicted in Figure 4.76. In the case of other metal ions such as Fe^{2+} and Cd^{2+} , the different regimes occur at concentrations different from those found with Cu^{2+} ions as expected on the basis of the slopes in the absorbance-concentration plots (Figure 4.72).

The observation that the aggregates and the precipitates are made of nanoparticles similar in dimensions to that of the colloid and the fact that the onset of aggregation depends on the metal ion used seems to suggest that the binding event

(chelation) is responsible for aggregation and precipitation. However, given that the aggregation and precipitation are irreversible and the stabilizing agent PVA is able to shift the onset of precipitation indicates that the ionic strength of the medium may indeed play a role. The actual factors leading to aggregation and precipitation, in the case of alpha-lipoic acid capped Au and Ag nanoparticles may well involve a combination of both these factors.

The present study shows three distinct regimes of interaction of metal ions with alpha-lipoic acid-capped Ag nanoparticles, the regime of low metal ion concentration being associated with reversible chelation and dampening of the plasmon band. Aggregation and irreversible chelation accompanied by an increase in the flocculation parameter characterize the next regime of intermediate metal ion concentration. Further increase in metal ion concentration results in precipitation.^{††}

4.9 Atomic force microscopy based method for patterning nanocrystals

A surface terminated by oxygen atoms is obtained when a piece of mica is freshly cleaved. Under ambient conditions, water molecules are attracted to this surface and are known to hop from one oxygen site to another. This hopping terminates after several steps and eventually (after a few days) results in condensation of a water layer on mica. Any change in the polarizability of the mica surface such as that produced by a scanning AFM tip, alters the dynamics of this process. Thus, scanning a Si₃N₄ cantilever results in instantaneous local condensation of water. As the cantilever is slowly scanned across the surface, the condensed water layer moves along with the tip, instead of sticking to the surface, forming a meniscus between the tip and the substrate. The meniscus formation process is sensitive to humidity and scan speed. As mentioned previously (section 2.9), Mirkin and co-workers have utilized this technique named “dip pen nanolithography” to create various nanostructured patterns, with molecules that chemically bind to the surface [203,241]. They have found that the cantilever coated

^{††}A paper based on this study has appeared in J. Phys. Chem. (2002).

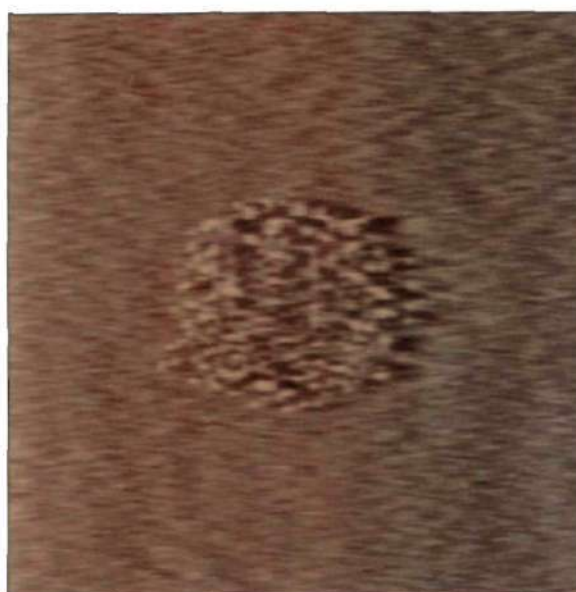


Figure 4.77: AFM image (scan area $6.8 \mu^2$) of a mica substrate showing condensation of microdroplets of water in a square shape with an area of $2 \mu^2$. The AFM image was acquired by scanning the area ($6.8 \mu^2$) with tip velocity of $122 \mu\text{m/s}$. Condensation of water was brought about by scanning the surface (scan area $2 \mu^2$) under ambient humidity conditions (40%) with tip velocity of $1 \mu\text{m/s}$ for 10 minutes.

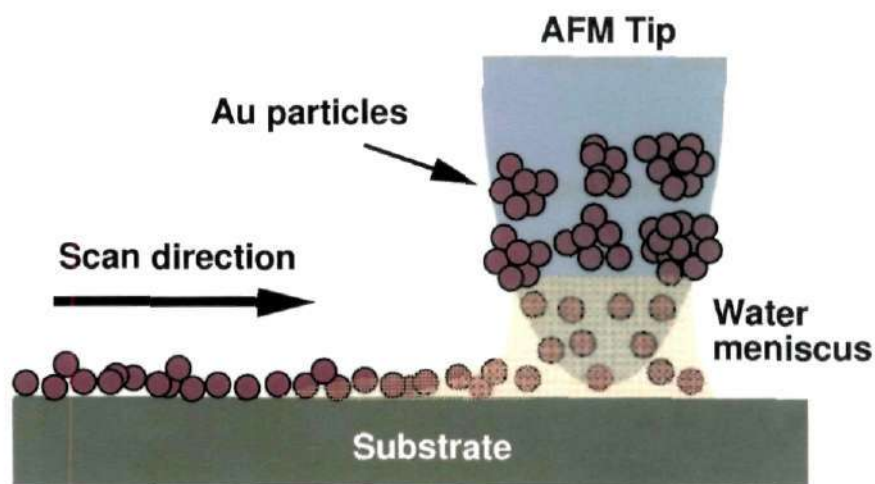


Figure 4.78: Schematic illustration of the "dip pen process". Au nanocrystals deposited on the cantilever dissolve in the water meniscus between the tip and the substrate. The dissolved nanocrystals are transferred to the substrate, when the tip is slowly scanned across the surface. Aggregates of nanocrystals are formed on the substrate upon evaporation of the water layer.

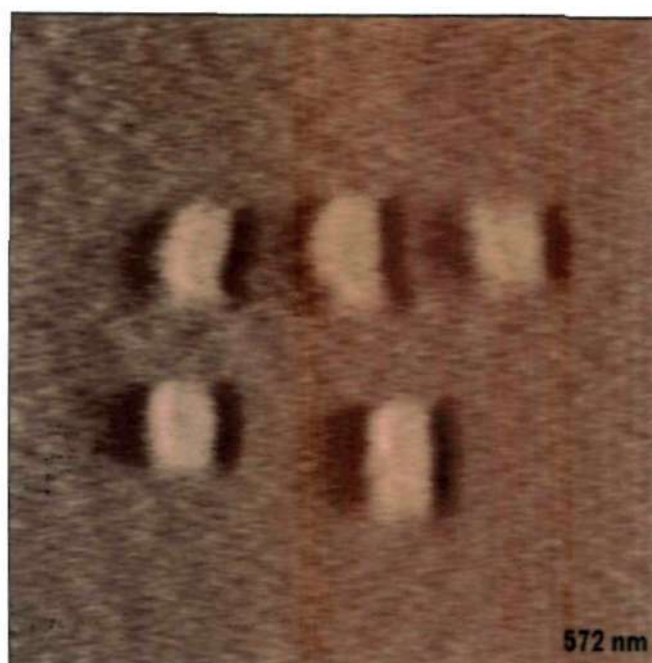


Figure 4.79: AFM images (in the lateral force mode) showing rectangles made of Pd nanocrystals. The rectangles have a constant interspacing of 100 nm in either the horizontal or vertical direction and were created by employing successive 66 nm by 100 nm scans interspersed with 100 nm scan offset either on the X or the Y axis. The scan size employed for obtaining the second rectangle at the bottom row was 66 by 120 nm. Also, the interspacing distance is 135 nm in this case. The total time required for creating the pattern was 45 minutes. Subsequent imaging was carried over a larger area with a tip velocity of 50 $\mu\text{m/s}$.

with the “ink” - the materials required for patterning can be used for both patterning and subsequent imaging. The patterning step is carried out with slow scan speeds (typically with tip velocities of 1 or 2 $\mu\text{m/s}$), while imaging is carried out at higher scan speeds.

In Figure 4.77, an AFM image of a mica substrate on which microdroplets of water have been made to condense in the form of a square of area $2 \mu^2$ by exploiting the meniscus that spontaneously forms at the interface of the tip and the mica substrate under ambient conditions is shown. Such patterns can be created with varied dimensions at any arbitrary area on the surface by exploiting the spatial resolution provided by AFM. We find that by utilizing the water meniscus,

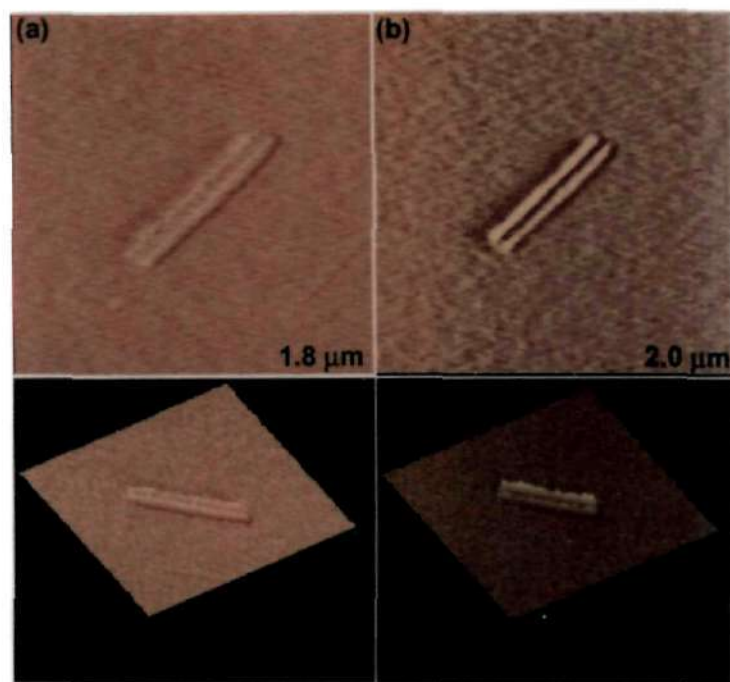


Figure 4.80: AFM images (in the lateral force mode) showing lines (35 nm by 750 nm) of (a) Au and (b) Pd nanocrystals. The corresponding surface plots are shown beneath. The lines were drawn by scanning the cantilever across an area of 35 nm by 750 nm with a velocity of 1 $\mu\text{m/s}$, under ambient conditions. Subsequent imaging was carried out over larger areas at a scan angle of 45° and velocities of 50 $\mu\text{m/s}$. The apparently greater height at the edges of these lines is due to the tendency of the lateral force microscopic technique to exaggerate frictional changes, that take place when one moves from the pattern to the substrate.

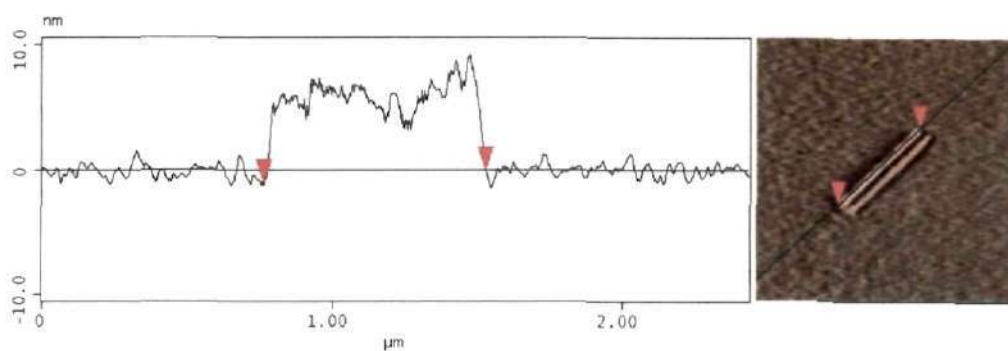


Figure 4.81: A plot of the cross sectional profile along a line made of nanocrystals shown in Figure 4.80. The area plotted is indicated in the AFM image alongside.

nanocrystals deposited on the tip can be transferred to the sample to generate a pattern defined by the scan area. The weak forces of interaction between nanocrystals and mica suffice to create stable patterns. For this purpose, magic nuclearity Pd₅₆₁ nanocrystals capped with PVP and Au nanocrystals capped with THPC (average diameter 2 nm) were employed. The nanocrystals were prepared and purified as detailed in the experimental section. The particles were deposited on the cantilever by immersing the cantilever assembly in the sol and subsequently blow drying it.

Figure 4.79 shows an AFM image of patterns consisting of four rectangles of dimensions 66 by 100 nm and one rectangle with a dimension of 66 by 120 nm positioned with a constant interspacing of 100 nm in either the horizontal or vertical direction. The last rectangle is placed at a distance of 135 nm from the other rectangle. The rectangles were obtained by scanning a cantilever coated with Pd nanocrystals for five minutes over an area of 66 nm by 100 nm at a scan rate of 1 Hz, then the cantilever was shifted by 100 nm along either the X or Y axis and scanning (at the slow rate) was resumed in the new area. The last rectangle was created by scanning an area of 66 by 120 nm after applying an X - shift of 135 nm. Finally, the area was imaged by the same cantilever employing higher scan rates. Each of these rectangles are filled with Pd nanocrystals. The individual particles are not resolved due to mild contact forces employed to image the patterned area. This pattern demonstrates how nanostructures can be created at a desired area and aligned with respect to each other by making use of the positioning capability of AFM. The sharp boundaries exhibited by the patterns and the close correspondence between the scanned area and the pattern dimensions indicate that the non-covalent, weak forces of interaction between the substrate and the particles are adequate to limit lateral diffusion (which would otherwise have resulted in patterns with no correspondence to the area scanned). In addition to rectangles, this method is also amenable to creating high aspect ratio structures such as lines. In Figure 4.80, lines of length 750 nm and 35 nm width patterned with Au and Pd nanocrystals are shown. Typical heights estimated from the z scale of AFM images were 6 and 12 nm (see Figure 4.81) and indicate that the patterns are probably made of more than one layer

of nanocrystals.

It is possible to distinguish patterns of nanocrystals from the condensed water by examining the stability of the obtained nanostructures. The water patterns tend to evaporate in about 30 mins under ambient conditions as against nanocrystal patterns which were stable for extended periods of time (for several hours under the ambient conditions). Indeed, the nanocrystal patterns are only destroyed by water vapor which spontaneously condenses on a mica surface exposed to the ambient and could be preserved by storing the mica substrate under vacuum. The patterns formed by water do not exhibit the sharp boundaries that the nanocrystal patterns do as can be seen by comparing the boundary between the pattern and the substrate in Figures 4.80 and 4.77. Further, the aqueous patterns are not continuous and are seen to consist of droplets of varied dimensions.

The nanocrystal patterns obtained had little dependence on the contact forces employed between the cantilever and the substrate. Other studies that use the dip-pen technique to transfer small molecules to a substrate have reported similar observations. It is believed that by holding the cantilever in contact with the substrate, it is possible to study the process of lateral diffusion of the nanocrystals. We found that holding the cantilever in contact with the surface does not result in patterns that show any sign of lateral diffusion. Instead, a small increase in the height of the features on the substrate was observed in both cases (Au and Pd nanocrystals). It is indeed surprising that the weak forces that exist between the PVP and THPC covered nanocrystals and the surface are strong enough to limit lateral diffusion. The details of such an interaction is not clear at present. Further, the two nanocrystal systems employed (THPC coated Au and PVP covered Pd) despite the difference in size and composition, exhibit little differences in the conditions required for patterning, the only real difference is that slightly longer contact times that are required to obtain good patterns of Au nanocrystals.

In order to independently ascertain that the patterns are indeed made up of nanocrystals, we have imaged the patterns by means of TEM. For this purpose, TEM grids were patterned with Au nanocrystals. A typical TEM image is shown in

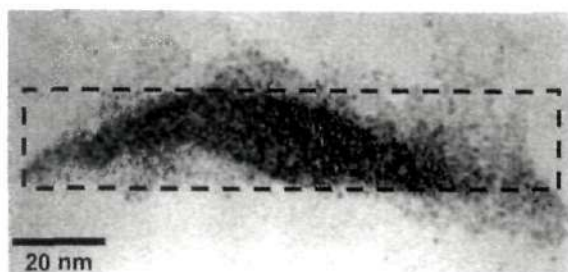


Figure 4.82: TEM image of pattern created on a TEM grid. The likely area where the cantilever was scanned is indicated.

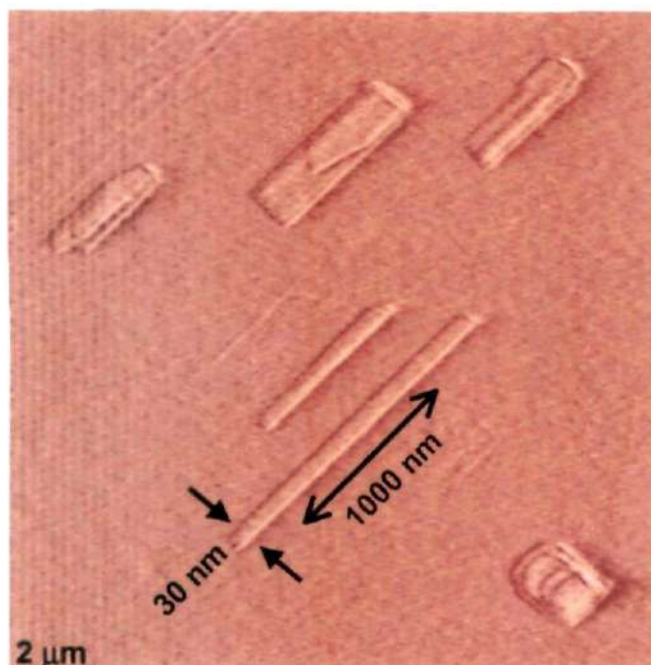


Figure 4.83: AFM images (in the lateral force mode) showing various patterns made of Au nanocrystals. The patterns were drawn by scanning the cantilever over the surface with a velocity of $1 \mu\text{m/s}$, under ambient conditions. Subsequent imaging was carried out over larger areas at a scan angle of 45° and velocity of $50 \mu\text{m/s}$.

Figure 4.82. It is observed that the pattern is indeed made up of nanocrystals and in several areas of the pattern, the nanocrystals are present in multilayers. However, on the TEM grid, the patterns are not sharp and exhibit a tendency to spread, unlike on mica. It is possible that substrate- nanocrystal interaction forces do not suffice to limit lateral diffusion. The relatively higher roughness of the TEM grid could also be a factor causing such a spread of the deposited nanocrystals.

4.9. Atomic force microscopy based method for patterning nanocrystals

It has to be noted that unlike in the experiments where chemical bond exist between the molecules and the substrate, the patterns obtained here are fragile and are destroyed by the indiscriminate condensing of water vapor which takes place when a particular region is scanned for a long time (over an hour) under the ambient conditions. Despite the above limitation, it has been possible to create several nanostructured features on the surface. In Figure 4.83, AFM images of a region of the substrate where several rectangles and lines of various aspect ratios and sizes have been patterned with Au nanocrystals is shown.

Recently, Su and Dravid have demonstrated that patterns of organic dyes can be obtained by using the noncovalent interactions between the substrate and the dyes [242]. However, the present study, to the best of our knowledge, is the first where high molecular mass material such as capped nanocrystals have been patterned directly on the substrates. The demonstration that weak forces of interaction are sufficient to create stable patterns circumvents the requirement for tailoring a chemical interaction between the substrate and the “ink” and thus significantly broadens the choice of nanocrystals and the substrates amenable to patterning.

In conclusion, we have shown that Au and Pd nanocrystals could be patterned on a mica substrate into features of nanometric dimensions by making use of the water meniscus between that forms spontaneously between an AFM tip and the substrate. The weak forces of interaction between the substrate and the nanocrystals suffice to limit lateral spread.

References

- [1] M. Faraday, *Philos. Trans. R. Soc. London.* 147, 145 (1857).
- [2] W. Ostwald, "Die Welt der Vernachlässigten Dimensionen", Steinkopf, Dresden, 1915.
- [3] G. Mie, *Ann. Phys.* 25, 377 (1908).
- [4] R. Gans, *Ann. Phys.* 31, 881 (1911).
- [5] R. Gans, *Ann. Phys.* 47, 270 (1915).
- [6] R. Kubo, *J. Phys. Soc. Jap.* 17, 975 (1962).
- [7] A. Einstein, *Ann. Phys.* 17, 549 (1905).
- [8] K. E. Drexler, "Nanosystems: molecular machinery, manufacturing, and computation", Wiley-Vch, Weinheim, 1992.
- [9] A. Henglein, *Ber. Bunsenges. Phys. Chem.* 903, 99 (1995).
- [10] "Clusters And Colloids: From Theory To Applications", Edited G. Schmid, Wiley-Vch, Weinheim, 1994.
- [11] F. Fievet, J. P. Lagier, B. Blin, B. Beaudoin and M. Figlarz, *Solid State Ionics* 32/33, 198 (1989).
- [12] R. Seshadri and C. N. R. Rao, *Mater. Res. Bull.* 29, 795 (1994).
- [13] G. Schmid, R. Peifel, R. Boese, F. Bandermann, S. Meyers, G. H. M. Calis and J. W. A. van der Velen, *Chem. Ber.* 114, 3634 (1981).
- [14] M. N. Vargaftik, I. I. Moiseev, D. I. Kochubey and K. I. Zamaraev, *Farad. Discuss.* 92, 13 (1991).
- [15] S. V. Gaponenko, "Optical Properties Of Semiconductor Nanocrystals", Cambridge University Press, Cambridge, 1998.
- [16] M. Rajamathi and R. Seshadri, *Curr. Opn. Sol. Stat. Mater. Sci.* 6, 337 (2002).
- [17] T. Trindade, P. O'Brien and N. L. Pickett, *Chem. Mater.* 13, 3843 (2001).
- [18] M. Green, *Curr. Opn. Sol. Stat. Mater. Sci.* 6, 355 (2002); A. C. C. Esteves and T. Trindade, *Curr. Opn. Sol. Stat. Mater. Sci.* 6, 347 (2002).
- [19] C. T. Dameron, R. N. Reese, R. K. Mehra, A. R. Kortan, P. J. Carroll, M. L. Steigerwald, L. E. Brus and D. R. Winge, *Nature* 338, 596 (1989).
- [20] P. Mukherjee, A. Ahmad, D. Mandal, S. Senapati, S. R. Sainkar, M. I. Khan, R. Ramani, R. Parischa, P. V. Ajayakumar, M. Alam, M. Sastry and R. Kumar, *Angew. Chem. Int. Ed.* 40, 3585 (2001).

References

- [21] M. Kowshik, W. Vogel, J. Urban, S. K. Kulkarni and K. M. Paknikar, *Adv. Mater.* 14, 815 (2002).
- [22] J. C. Hulteen and C. R. Martin, *J. Mater. Chem.* 7, 1075 (1997).
- [23] M.-P. Pileni, *J. Phys. Chem.* 97, 6961 (1993).
- [24] M. T. Reetz and W. Helbig, *J. Am. Chem. Soc.* 116, 7401 (1994).
- [25] S. A. Harfenist, Z. L. Wang, R. L. Whetten, I. Vezmar and M. M. Alvarez, *Adv. Mater.* 9, 817 (1997).
- [26] F. Mafuné, J.-y. Kohno, Y. Takeda and T. Kondow, *J. Phys. Chem. B* 106, 7575 (2002).
- [27] A. Koronowski, M. Giersig, M. Vogel, A. Chemseddine and H. Weller, *Adv. Mater.* 5, 634 (1993).
- [28] J. Neddersen, G. Chumanov and T. M. Cotton, *Appl. Spectrosc.* 47, 1959 (1993).
- [29] Y. Mizukoshi, K. Okitsu, Y. Maeda, T. A. Yamamoto, R. Oshima and Y. Nagata, *J. Phys. Chem. B* 101, 7033 (1997).
- [30] N. Herron, J. C. Calabrese, W. E. Farneth and Y. Wang, *Science* 259, 1426 (1993).
- [31] N. Zhu and D. Fenske, *J. Chem. Soc. Dalton Trans.* 1067 (1999); M. Bettenhausen, A. Eichhofer, D. Fenske and M. Semmelmann, *Z. Anorg. Allg. Chem.* 625, 593 (1999).
- [32] T. Vötsch, G. Reck, L. Katsikas, E. T. K. Haupt, B. Schulz and H. Weller, *Science* 267, 1476 (1995).
- [33] S. Beherens, M. Bettenhausen, A. C. Deveson, A. Eichhofer, D. Fenske, A. Lohde and U. Woggon, *Angew. Chem. Int. Ed.* 35, 221 (1996).
- [34] J. Turkevich, P. C. Stevenson and J. Hillier, *J. Discuss. Faraday Soc.* 11, 55 (1951).
- [35] L. Manna, E. C. Scher and A. P. Alivisatos, *J. Am. Chem. Soc.* 122, 12700 (2000).
- [36] X. Peng, L. Manna, W. Yang, J. Wickham, E. Scher, A. Kadavanich and A. P. Alivisatos, *Nature* 404, 59 (2000).
- [37] N. Pinna, K. Weiss, H. Sach-Kongehl, W. Vogel, J. Urban and M.-P. Pileni, *Langmuir* 17, 7982 (2001).
- [38] R. K. Baldwin, K. A. Pettigrew, J. C. Garno, P. P. Power, G. Liu and S. M. Kauzlarich, *J. Am. Chem. Soc.* 124, 1150 (2002).
- [39] Y.-W. Jun, Y.-Y. Jung and J. Cheon, *J. Am. Chem. Soc.* 124, 615 (2002).
- [40] S. Chen, Z. Fan and D. L. Carroll, *J. Phys. Chem. B* 106, 10777 (2002).

- [41] Y. Sun, B. T. Mayers, Y. Xia, *Nano Lett.* 2, 481 (2002).
- [42] C. J. Murphy and N. R. Jana, *Adv. Mater.* 14, 80 (2002).
- [43] C. J. Johnson, E. Dujardin, S. A. Davis, C. J. Murphy and S. Mann, *J. Mater. Chem.* 12, 1765 (2002).
- [44] N. R. Jana, L. Gearheart and C. J. Murphy, *Chem. Commun.* 617 (2001).
- [45] K. Esuni, M. Nawa, N. Aihara and K. Usui, *New. J. Chem.* 719 (1998).
- [46] Y. Sun and Y. Xia, *Adv. Mater.* 14, 833 (2002).
- [47] V. F. Puentes, K. M. Krishnan and A. P. Alivisatos, *Science* 291, 2115 (2001).
- [48] C. M. Niemeyer, *Angew. Chem. Int. Ed.* 40, 4128 (2001).
- [49] V. Chechik and R. M. Crooks, *J. Am. Chem. Soc.* 122, 1243 (2000).
- [50] P. Mulvaney, L. M. Liz-Marzan, M. Giersig and T. Long, *J. Mater. Chem.* 10, 1259 (2002).
- [51] J. Lin, W. Zhou, A. Kumbhar, J. Wiemann, J. Fang, E. E. Carpenter and C. J. O'Connor, *J. Solid. State. Chem.* 159, 26 (2001).
- [52] A. J. Sutherland, *Curr. Opin. Sol. Stat. Mater. Sci.* 6, 365 (2002).
- [53] H. Harai, H. Aizawa and H. Shiozaki, *Chem. Lett.* 8, 1527 (1992).
- [54] L. O. Brown and J. E. Hutchison, *J. Am. Chem. Soc.* 121, 882 (1999).
- [55] W. M. Pankau, K. Verbist and G. v. Kiedrowski, *Chem. Commun.* 519 (2001).
- [56] K. V. Sarathy, G. Raina, R. T. Yadav, G. U. Kulkarni and C. N. R. Rao, *J. Phys. Chem. B* 101, 9876 (1997).
- [57] K. V. Sarathy, G. U. Kulkarni and C. N. R. Rao, *Chem. Commun.* 537 (1997).
- [58] A. Kumar, A. B. Mandale and M. Sastry *Langmuir* 16, 9229 (2000).
- [59] D. I. Gittins and F. Caruso, *Angew. Chem. Int. Ed.* 40, 3001 (2001).
- [60] D. L. Gittins and F. Caruso, *Chemphyschem* 40, 3001 (2001).
- [61] A. I. Kirkland, D. E. Jefferson, D. G. Duff, P. P. Edwards, I. Gamesson, B. F. U. Johnson and D. J. Smith, *Proc. R. Soc. London A* 440, 589 (1993).
- [62] T. P. Martin, T. Bergmann, H. Göhlich and T. Lange, *J. Phys. Chem.* 95, 6421 (1991).
- [63] H.-G. Boyen, G. Kastle, F. Weigl, B. Koslowski, C. Dietrich, P. Ziemann, J. P. Spatz, S. Riethmuller, C. Hartmann, M. Moller, G. Schmid, M. G. Garnier and P. Oelhafen, *Science* 297, 1533 (2002).
- [64] P. A. Buffat, M. Flüeli, R. Spycher, P. Stadelmann and J. P. Borel, *Farad. Discuss.* 92, 173 (1991).
- [65] A. I. Kirkland, D. A. Jefferson, D. Tang and P. P. Edwards, *Proc. R. Soc. Lond. A* 434, 279 (1991).

References

- [66] J. O. Bovin and J. O. Malm, *Z. Phys. D: Atoms, Molecules and Clusters* 19, 293 (1991).
- [67] M. T. Reetz, W. Helbig, S. A. Quaiser, U. Stimming, N. Breuer and R. Vogel, *Science* 276, 367 (1995).
- [68] P. P. Edwards, R. L. Johnston and C. N. R. Rao in "Metal clusters in Chemistry", Edited P. Braunstein, G. Oro and P. R. Raithby, Wiley-Vch, Weinheim, 1998.
- [69] M. Rosenblit and J. Jortner, *J. Phys. Chem.* 98, 9365 (1995).
- [70] R. Busani, M. Folker and O. Chesnovsky, *Phys. Rev. Lett.* 81, 3836 (1998).
- [71] K. Rademann, O. D. Rademann, M. Schlauf, V. Even and F. Hensel, *Phys. Rev. Lett.* 69, 3208 (1992).
- [72] C. P. Vinod, G. U. Kulkarni and C. N. R. Rao, *Chem. Phys. Lett.* 289, 329 (1998).
- [73] C. P. Collier, T. Vossmeier and J. R. Heath, *Annu. Rev. Phys. Chem.* 49, 371 (1998).
- [74] "Nanoparticles and Nanostructured Films", Edited J. H. Fendler, Wiley-Vch, Weinheim, 1998.
- [75] "Single electron tunneling", Edited H. Grabert and M. H. Devoret, Plenum, New York, 1992.
- [76] S. Chen, R. S. Ingram, M. J. Hostetler, J. J. Pietron, R. W. Murray, T. G. Schaaf, J. T. Khoury, M. M. Alvarez and R. L. Whetten, *Science* 280, 2098 (1998).
- [77] S. J. Green, J. I. Stokes, M. J. Hostetler, J. Peitron and R. W. Murray, *J. Phys. Chem.* B101, 2663 (1997).
- [78] J. R. Pietron, J. F. Jicks and R. W. Murray, *J. Am. Chem. Soc.* 121, 5565 (1999).
- [79] S. Link and M. A. El-Sayed, *Int. Rev. Phys. Chem.* 19, 409 (2000); S. Link and M. A. El-Sayed, *J. Phys. Chem.* B105, 1 (2001).
- [80] P. Mulvaney, *Langmuir* 12, 788 (1996).
- [81] G. C. Papavassiliou, *Prog. Solid State Chem.* 12, 185 (1980).
- [82] D. C. Look, *J. Colloid Inter. Sci.* 56, 386 (1976).
- [83] http://diogenes.iwt.uni-bremen.de/~wriedt/Mie_Type_Codes/body_mie.type_codes.html
- [84] C. F. Bohren and D. R. Huffman, "Absorption and Scattering of Light by Small Particles", Wiley, New York, 1983.
- [85] M. Kerker, "The Scattering of Light and Other Electromagnetic Radiation", Academic Press, New York, 1969.

- [86] U. Kreibig and M. Vollmer, "Optical properties of metal clusters", Springer-Verlag, Berlin, 1995.
- [87] A. C. Templeton, J. J. Pietron, R. W. Murray and P. Mulvaney, *J. Phys. Chem. B* 104, 564 (2000).
- [88] C. A. Mirkin, R. L. Letsinger, R. C. Mucic and J. J. Storhoff, *Nature* 382, 607 (1996).
- [89] L. E. Brus, *J. Chem. Phys.* 79, 5566 (1983).
- [90] L. E. Brus, *J. Chem. Phys.* 80, 4403 (1984).
- [91] P. E. Lippens and M. Lannoo, *Phys. Rev. B* 39, 10935 (1989).
- [92] M. V. R. Krishna and R. A. Friesner, *J. Chem. Phys.* 95, 8309 (1991).
- [93] "Magnetic properties of Fine Particles", Edited J. L. Dormann and D. Fiorani, North-Holland, Amsterdam, 1992.
- [94] S. Chikazumi and S. H. Charap, "Physics of Magnetism", John Wiley, New York, 1964.
- [95] B. D. Cullity, "Introduction to Magnetic Materials", Addison-Wesley, 1972.
- [96] Q. A. Pankhurst and R. J. Pollard, *J. Phys. Condens. Matter* 5, 8487 (1993).
- [97] L. Neel, *Comptes-rendus des séances de l'Académie des sciences* 237, 1468 (1953).
- [98] E. D. Torre, "Magnetic Hysteresis", IEEE, New Jersey, 1992.
- [99] D. G. Rancourt, *Rev. Min. Geochem.* 44, 217 (2001).
- [100] Z. L. Wang, *J. Phys. Chem. B* 104, 1153 (2000).
- [101] C. B. Murray, C. R. Kagan and M. G. Bawendi, *Annu. Rev. Mater. Sci.* 30, 545 (2000).
- [102] A. N. Shipway, E. Katz and I. Willner, *Chemphyschem* 1, 18 (2000).
- [103] G. L. Hornayak, M. Krll, R. Pugin, T. Sawitowski, G. Schmid, J.O. Bovin, G. Karrson, H. Hofmeister and S. Hopfe, *Eur. J. Chem.* 3, 195 (1997).
- [104] A. P. Alivisatos, K. P. Johnsson, X. Peng, T. E. Wilson, C. J. Loweth, M. P. Burcher Jr. and P.G. Schultz, *Nature* 382, 609 (1996).
- [105] A. Kumar, M. Pattarkine, M. Bhadbhade, A. B. Mandale, K. N. Ganesh, S. S. Datar, C. V. Dharmadhikari and M. Sastry, *Adv. Mater.* 13, 341 (2001).
- [106] W. Vogel, S. Botti, S. Martelli and E. Carlino, *New J. Chem.* 749 (1998); Y. Dirix, C. Bastiaansen, W. Caseri and P. Smith, *Adv. Mater.* 11, 223 (1999).
- [107] S. W. Chung, G. Markovich and J. R. Heath, *J. Phys. Chem. B* 102, 6685 (1998).
- [108] M. Mitov, C. Portet, C. Bourgerette, E. Snoeck and M. Verelst, *Nature Mater.* 1, 229 (2002).

References

- [109] S.-W. Lee, C. Mao, C. E. Flynn and A. M. Belchar, *Science* 296, 892 (2002).
- [110] E. Dujardin, C. Peet, G. Stubbs, J. N. Culver and S. Mann, *Nano Lett.* 3, 413 (2003).
- [111] M. Brust, M. Walker, D. Bethell, D. J. Schiffrin and R. Whyman, *Chem. Commun.* 801 (1994).
- [112] N. Sandhyarani and T. Pradeep, *Chem. Mater.* 12, 1755 (2000).
- [113] R. L. Whetten, J. T. Khoury, M. M. Alvarez, S. Murthy, I. Vezmar, Z. Wang, P. W. Stephens, Ch. L. Clevend, W. D. Luedtke and U. Landman, *Adv. Mater.* 8, 428 (1996).
- [114] B. A. Korgel, S. Fullam, S. Connolly and D. Fitzmaurice, *J. Phys. Chem. B* 102, 8379 (1998).
- [115] N. Sandhyarani, M. R. Resmi, R. Unnikrishnan, K. Vidyasagar, S. Ma, M. P. Antony, G. P. Selvam, V. Visalakshi, N. Chandrakumar, K. Pandian, Y.-T. Tao and T. Pradeep, *Chem. Mater.* 12, 104 (2000).
- [116] S. Sun and C.B. Murray, *J. Appl. Phys.* 85, 4325 (1999).
- [117] C. Petit, A. Taleb and M.-P. Pileni, *J. Phys. Chem. B* 103, 1805 (1999).
- [118] M.-P. Pileni, *New. J. Chem.* 693 (1998).
- [119] K. Abe, T. Hanada, Y. Yoshida, N. Tanigaki, H. Takiguchi, H. Nagasawa, M. Nakamoto, T. Yamaguchi and K. Yase, *Thin Solid Films* 327-329, 524 (1998).
- [120] L. O. Brown and J. E. Hutchison, *J. Phys. Chem. B* 105, 8911 (2001).
- [121] B. A. Korgel and D. Fitzmaurice, *Adv. Mater.* 10, 661 (1998).
- [122] C. J. Kiely, J. Fink, M. Brust, D. Bethell and D. J. Schiffrin, *Nature* 396, 444 (1998).
- [123] C. J. Kiely, J. Fink, J. G. Zheng, M. Brust, D. Bethell and D. J. Schiffrin, *Adv. Mater.* 12, 639 (2000).
- [124] B. Kim, S. L. Tripp and A. Wei, *J. Am. Chem. Soc.* 123, 7955 (2001).
- [125] C. B. Murray, C. R. Kagan and M. G. Bawendi, *Science* 270, 1335 (1995).
- [126] O. I. Micic, K. M. Jones, A. Cahill and A. J. Nozik, *J. Phys. Chem. B* 102, 9791 (1998).
- [127] R. A. Mcmillan, C. D. Paavola, J. Howard, S. L. Chan, N. J. Zaluzec and J. D. Trent, *Nature Mater.* 1, 247 (2002).
- [128] M. D. Bentzon, J. van Wonterghem, S. Morup, A. Tholen and C. J. W. Koch, *Phil. Mag. B* 60, 169 (1989).
- [129] S. Sun and H. Zeng, *J. Am. Chem. Soc.* 124, 8204 (2002).
- [130] J. S. Yin and Z. L. Wang, *Phys. Rev. Lett.* 79, 2570 (1997).

- [131] M. Li, H. Schnablegger and S. Mann, *Science* 402, 393 (1999).
- [132] H. Zheng, J. Li, J. P. Llu, Z. L. Whang and S. Sun, *Nature* 420, 395 (2002).
- [133] P. C. Ohara and W. M. Gelbart, *Langmuir* 14, 3418 (1998).
- [134] T. Vossmeier, S.-W. Chung, W. M. Gelbart and J. R. Heath, *Adv. Mater.* 10, 351 (1998).
- [135] C. Stowell and B. A. Korgel, *Nano Lett.* 1, 595 (2001).
- [136] K. V. P. M. Shafi, I. Felner, Y. Mastai and A. Gedanken, *J. Phys. Chem. B* 103, 3358 (1999).
- [137] M. Maillard, L. Motte, A. T. Ngo and M.-P. Pileni, *J. Phys. Chem. B* 104, 11871 (2000).
- [138] M. Maillard, L. Motte and M.-P. Pileni, *Adv. Mater.* 16, 200 (2001).
- [139] M. Brust, D. Bethell, C. J. Kiely and D. J. Schiffrin, *Langmuir* 14, 5425 (1998).
- [140] R. Blonder, L. Sheeney and I. Willner, *Chem. Commun.* 1393 (1998).
- [141] Y. Liu, Y. Wany and R. O. Claus, *Chem. Phys. Lett.* 298, 315 (1998).
- [142] A. Samokhvalov, M. Berfeld, M. Lahav, R. Naaman and E. Rabani, *J. Phys. Chem. B* 104, 8632 (2000).
- [143] M. Gao, B. Richter and S. Kirstein, *Adv. Mater.* 9, 802 (1997).
- [144] M. Maillard, L. Motte, A. T. Ngo and M.-P. Pileni, *J. Phys. Chem. B* 104, 11871 (2000).
- [145] D. V. Talapin, E. V. Shevchenko, A. Kornowski, N. Gaponik, M. Haase, A. L. Rogach and H. Weller, *Adv. Mater.* 13, 1868 (2001).
- [146] M. Brust, D. Bethell, D. J. Schiffrin and C. J. Kiely, *Adv. Mater.* 7, 795 (1995).
- [147] V. Torma, G. Schmid and U. Simon, *Chemphyschem* 1, 321 (2001).
- [148] U. Simon, R. Flesch, H. Wiggers, G. Schn and G. Schmid, *J. Mater. Chem.* 8, 517 (1998).
- [149] M. Aslam, I. S. Mulla and K. Vijayamohanan, *Appl. Phys. Lett.* 79, 689 (2001).
- [150] R. H. Terrill, T. A. Postlewaite, C. Chen, C. D. Poon, A. Terzis, A. Chen, J. E. Hutchinson, M. R. Clark, G. Wignall, J. D. Londono, R. Superfine, M. Falvo, C. S. Johnson Jr., E. T. Samulski and R. W. Murray, *J. Am. Chem. Soc.* 117, 1237 (1995).
- [151] M. D. Musick, C. D. Keating, M. H. Keefe and M. J. Natan, *Chem. Mater.* 9, 1499 (1997).
- [152] Y. Liu, Y. Wang and R. O. Claus, *Chem. Phys. Lett.* 298, 315 (1998).
- [153] R. Parthasarathy, X.-M. Lin and H. A. Jaeger, *Phys. Rev. Lett.* 87, 186807 (2001).

References

- [154] J. Schmelzer Jr., S. A. Brown, A. Wurl, H. Hyslop and R. J. Blaikie, *Phys. Rev. Lett.* 88, 226802 (2002).
- [155] R. C. Doty, H. Yu, C. K. Shih and B. A. Korgel, *J. Phys. Chem. B* 105, 8291 (2001).
- [156] T. Ogawa, K. Kobayashi, G. Masuda, T. Takase and S. Maeda, *Thin Solid Films*, 393, 374 (2001).
- [157] R. G. Osifchin, W. J. Mahoney, J. D. Bielefeld, R. P. Andres, J. I. Henderson and C. P. Kubiak, *Superlattices and Microstructures*, 18, 283 (1995).
- [158] R. G. Osifchin, W. J. Mahoney, J. D. Bielefeld, R. P. Andres, J. I. Henderson and C. P. Kubiak, *Superlattices and Microstructures*, 18, 275 (1995).
- [159] G. Markovich, C. P. Collier, S. E. Hendricks, F. Ramacle, R. D. Levine and J. R. Heath, *Acc. Chem. Res.* 32, 415 (1999).
- [160] G. Medeiros-Ribeiro, D. A. A. Ohlberg, R. S. Williams and J. R. Heath, *Phys. Rev. B* 59, 1633 (1999).
- [161] A. Taleb, F. Silly, A. O. Gusev, F. Charra and M.-P. Pileni, *Adv. Mater.* 12, 633 (2000).
- [162] T. P. Bigioni, L. E. Harrell, W. G. Cullen, D. K. Guthrie, R. L. Whetten and P. N. First, *Eur. Phys. J. D* 6, 355 (1999).
- [163] M. V. Artemyev, U. Woggon, H. Jaschinski, L. I. Gurinovich and S. V. Gaponenko, *J. Phys. Chem. B* 104, 11617 (1999).
- [164] C. R. Kagan, C. B. Murray and M. G. Bawendi, *Phys. Rev. B* 54, 8633 (1996).
- [165] H. Döllefeld, H. Weller and A. Eychmüller, *J. Phys. Chem. B* 106, 5604 (2002).
- [166] M. V. Artemyev, A. I. Bibik, L. I. Gurinovich, S. V. Gaponenko and U. Woggon, *Phys. Rev. B* 60, 1504 (1999).
- [167] V. Russier, C. Petit, J. Legrand and M.-P. Pileni, *Phys. Rev. B* 62, 3910 (2000).
- [168] S. Sun, C. B. Murray, D. Weller, L. Folks and A. Maser, *Science* 287, 1989 (2000).
- [169] W. U. Huynh, J. J. Dittmer and A. P. Alivisatos, *Science* 295, 2425 (2002).
- [170] J. Lee, V. C. Sundar, J. R. Heine, M. G. Bawendi and K. F. Jensen, *Adv. Mater.* 12, 1102 (2000).
- [171] C. R. Martin and D. T. Mitchell, *Anal. Chem.* 322A (1998).
- [172] U. Simon, *Adv. Mater.* 10, 1487 (1998).
- [173] D. L. Feldheim and C. D. Keating, *Chem. Soc. Rev.* 27, 1 (1998).
- [174] "Single charge tunneling, coulomb blockade phenomena in nanostructures", Edited H. Graber and M. H. Devoret, Plenum, New York 1992, NATO ASI series B294.

- [175] "Molecular electronics" Edited J. Jortner and M. Ratner, Blackwell Scientific, London 1997, IUPAC A 'Chemistry for the 21st Century' monograph
- [176] A. O. Orlov, I. Amlani, G. H. Bernstein, C. S. Lent and G. L. Snider, *Science* 277, 928 (1997).
- [177] J. R. Heath, P. J. Kuekes, G. S. Snider and R. S. Williams, *Science* 280, 1717 (1998).
- [178] H. Abelson, D. Allen, D. Coore, C. Hanson, G. Homsy, T. F. Knoght, Jr., R. Nagpal, E. Rauch, G. J. Sussman and R. Weiss, Technical Report A. I. Memo 1665, Massachusetts Institute of Technology, Artificial Intelligence Laboratory, Aug. 1999.
- [179] D. Coore, R. Nagpal and R. Weiss, Technical Report A. I. Memo 1614, Massachusetts Institute of Technology, Artificial Intelligence Laboratory, Oct. 1997.
- [180] H. Abelson, D. Allen, D. Coore, C. Hanson, G. Homsy, T. F. Knoght Jr., R. Nagpal, E. Rauch, G. J. Sussman and R. Weiss, *Comm. of the ACM*, May 2000.
- [181] G. Viau, F. Fievet-vincent and F. Fievet, *J. Mater. Chem.* 6, 1047 (1996).
- [182] G. Viau, F. Fievet-vincent and F. Fievet, *Solid State Ionics* 84, 259 (1996).
- [183] G. Viau, F. Ravel, O. Acher and F. Fievet-vincent, *J. Appl. Phys.* 76, 6570 (1994).
- [184] J. Osuna, D. de. Caro, C. Amiens, B. Chaudret, E. Snoeck, M. Respaud, J. M. Broto and A. Fert, *J. Phys. Chem.* 100, 14571 (1996).
- [185] M.-P. Pileni, *Nature Mater.* 2, 145 (2003).
- [186] E. S. Smotkin, C. Lee, A. J. Bard, A. Campion, M. A. Fox, T. E. Mallouk, S. I. Webber and J. M. White, *Chem. Phys. Lett.* 152, 265 (1998).
- [187] J. G. A. Dubois, J. W. Gerritsem S. E. Shafranjuk, E. J. G. Boon, G. Schmid and H. van Kempen, *Europhys. Lett.* 33, 279 (1996).
- [188] C. Petit, T. Cren, D. Roditchev, W. Sacks, J. Jlein and M.-P. Pileni, *Adv. Mater.* 11, 1998 (1999).
- [189] V. Erokin, P. Facci, S. Carrara and C. Nicolini, *J. Phys. D. Appl. Phys.* 28, 2534 (1995).
- [190] P. C. Ohara, D. V. Leff, J. R. Heath and W. A. Gelwart, *Phys. Rev. Lett.* 75, 3466 (1995).
- [191] B. J. Alder and T. E. Wanwright, *J. Chem. Phys.* 27, 1208 (1957).
- [192] J. R. Heath, M. C. Knobler and D. V. Leff, *J. Phys. Chem.* B101, 189 (1997).
- [193] R. L. Whetten, M. M. Shafigullin, J. T. Khoury, T. G. Schaaf, I. Vezmar, M. M. Alvarez and A. Wilkinson, *Acc. Chem. Res.* 32, 397 (1999).

References

- [194] H. G. Fritsche, H. Muller and B. Fehrensen, *Z. Phys. Chem.* 199, 87 (1997).
- [195] H. Feld, A. Leute, D. Rading, A. Benninghoven and G. Schmid, *J. Am. Chem. Soc.* 112, 8166 (1990).
- [196] A. T. Ngo and M. P. Pileni, *J. Phys. Chem.* B105, 53 (2001).
- [197] A. T. Ngo and M. P. Pileni, *Adv. Mater.* 12, 276 (2000).
- [198] T. Nakanishi, B. Ohtani and K. Uosaki, *J. Phys. Chem.* B102, 1571 (1998).
- [199] Y. Kim, R. C. Johnson and J. T. Hupp, *Nano Lett.* 1, 165 (2001).
- [200] J. Simard, C. Riggs, A. K. Boal and V. M. Rotello, *Chem. Commun.* 1943 (2000).
- [201] C. S. Weisbecker, M. V. Merritt and G. M. Whitesides, *Langmuir* 12, 3763 (1996).
- [202] Y. Xia and G. M. Whitesides, *Angew. Chem. Int. Ed.* 37, 550 (1998).
- [203] L. M. Demers and C. A. Mirkin, *Angew. Chem. Int. Ed.* 40, 3069 (2001).
- [204] P. Braunstein, H. Lehner and D. Matt, *Inorg. Synth.* 7, 218 (1990).
- [205] T. Teranishi and M. Miyake, *Chem. Mater.* 10, 54 (1998); T. Teranishi, H. Hori and M. Miyake, *J. Phys. Chem.* B101, 5774 (1997).
- [206] G. Schmid, M. Harns, J. O. Malm, J. O. Bovin, J. V. Ruitentecik, H. W. Zandbergen and T. Fu, *J. Am. Chem. Soc.* 115, 2046 (1993).
- [207] F. Porta, F. Ragaini and S. Cenini, *Gazz. Chem. Ital.* 122, 361 (1992).
- [208] P. Lianos and J. K. Thomas, *Chem. Phys. Lett.* 125, 299 (1986).
- [209] M. Y. Han, L. Zhou, C. H. Quek, S. F. Y. Li and N. Huang, *Chem. Phys. Lett.* 287, 47 (1998).
- [210] L. Maya, G. Muralidharan, T. G. Thundat and E. A. Kenik, *Langmuir* 16, 9151 (2000).
- [211] A. T. Ngo and M. P. Pileni, *J. Phys. Chem.* B105, 53 (2001).
- [212] N. H. Furman, W. B. Mason and J. S. Pekola, *Anal. Chem.* 21, 1325 (1949).
- [213] A. J. Nam, A. Teren, J. A. Lusby and A. J. Melmed, *J. Vac. Sci. Technol.* B115, 2046 (1996).
- [214] C. Kittle, J. K. Galt and W. E. Campbell, *Phys. Rev.* 77, 725 (1950).
- [215] G. Schmid and S. Peschel, *New J. Chem.* 669 (1998).
- [216] M. Quinten, I. Sander, P. Steiner, U. Kreibig, K. Fauth and G. Schmid, *Z. Phys. D: Atoms, Molecules and Clusters* 20, 377 (1991).
- [217] W.J. Kaiser and R.C. Jaklevic, *IBM J. Res. Dev.* 30, 4 (1986).
- [218] M. Amman, R. Wilkins, E. Ben-Jacob, P. D. Amker and R. C. Jaklevic, *Phys. Rev.* B43, 1146 (1991).

- [219] M. Y. Han, L. Zhou, C. H. Quek, S. F. Y. Li and N. Huang, *Chem. Phys. Lett.* 287, 47 (1998).
- [220] J. Jortner, *Z. Phys. D: Atoms, Molecules and Clusters* 24, 247 (1992).
- [221] J. Jortner, Private Communication.
- [222] J. Fink, C. J. Kiely, D. Bethell and D. J. Schiffrin, *Chem. Mater.* 10, 922 (1998).
- [223] G. Schmid, M. Bäuml and N. Beyer, *Angew. Chem. Int. Ed.* 1, 39 (2000).
- [224] R. J. Speedy, *J. Phys. Condes. Mater.* 10, 4185 (1998).
- [225] D. Bargeman and F. V. V. Vader, *J. Electroanal. Chem.* 37, 45 (1972).
- [226] J. N. Israelachvili, "Intermolecular and surface forces", Academic press, London, 1992.
- [227] A. K. Santra, G. N. Subbanna and C. N. R. Rao, *Surf. Sci.* 259, 317 (1994).
- [228] B. H. Sohn and R. E. Cohen, *Chem. Mater.* 9, 264 (1997).
- [229] F. Gazeua, J. C. Bacri, F. Gendron, R. Porzynski, L. Y. Ruikher, V. I. Stepanov and E. J. Dubois, *J. Magn. Mater.* 186, 175 (1998).
- [230] S. A. Haque, S.-I. Itaya, Y. Yamamoto and H. Hori *Jpn. J. Appl. Phys.* 41, 2014 (2002).
- [231] L. Motte, E. Lacaze, M. Maillard and M.-P. Pileni *Appl. Surf. Sci.* 162-163, 604 (2000).
- [232] (a) D. A. Thompson and J. A. Best *IBM. J. Res. Develop.* 44, 311 (2000) ;
(b) K. Ouchi and N. Honda *IEEE Trans. Magn.* 36, 16 (2000).
- [233] T. Asahi, M. Ikeda, A. Takizawa, T. Onoue and T. Osaka *J. Magn. Mater.* 212, 293 (2000).
- [234] J.-R. Jeong, Y.-S. Kim and S.-C. Shin *J. Appl. Phys.* 85, 5762 (1999).
- [235] (a) A. Moschel and K. D. Usadel 1995 *J. Magn. Mater.* 140-144, 649 (1995); (b) L. Neel *J. Phys. Rad.* 15, 225 (1954).
- [236] P. Bruno *J. Appl. Phys.* 64, 3153 (1988).
- [237] K. Vijayasarathy, Ph. D. Thesis (2002), Manipal Academy of Higher Education (Mahe).
- [238] A. A. Lazarides and G. C. Schatz, *J. Phys. Chem.* B104, 460 (2000); A. A. Lazarides and G. C. Schatz, *J. Chem. Phys.* 112, 2987 (2000).
- [239] T. Linnert, P. Mulvaney and A. Henglein, *J. Phys. Chem.* B97, 679 (1993).
- [240] F. Strelow and A. Henglein, *J. Phys. Chem.* B99, 11834 (1995); F. Strelow, A. Fojtik and A. Henglein, *J. Phys. Chem.* B98, 3032 (1994); A. Henglein and D. Meisel, *J. Phys. Chem.* B102, 8364 (1998).
- [241] R. D. Piner, J. Zhu, F. Xu, S. Hong and C. A. Mirkin, *Science* 283, 661 (1999); C. A. Mirkin, *MRS Bull.* 535, July 2001.

References

- [242] M. Su and V. P. Dravid, *Appl. Phys. Lett.* 80, 4436 (2002).

Other publications of the author

- P. J. Thomas and G. U. Kulkarni, "Self-assembling bilayers of palladiumthiolates in organic media", Proc. Indian Acad. Sci. -Chem. Sci., 113, 611 (2001).
- B. C. Satish Kumar, P. J. Thomas, A. Govindaraj and C. N. R. Rao, "Y-junction carbon nanotubes", Appl. Phys. Lett. 77, 2530 (2000).

Reviews

- C. N. R. Rao, G. U. Kulkarni, P. J. Thomas and P. P. Edwards, "Size-dependent chemistry: Properties of nanocrystals", Chem. Eur. J. 8, 30 (2002).
- C. N. R. Rao, G. U. Kulkarni, P. J. Thomas and P. P. Edwards, "Metal nanoparticles and their assemblies", Chem. Soc. Rev. 28, 27 (2000).

In books

- G. U. Kulkarni, P. J. Thomas and C. N. R. Rao, "Mesoscale self-assembly of metal nanocrystals into ordered arrays and giant clusters", in "Supramolecular Materials Design" (Eds. W. Jones and C. N. R. Rao), Cambridge University Press (2002).
- G. U. Kulkarni, P. J. Thomas and C. N. R. Rao, "Mesoscopic organizations of metal nanocrystals", in "Encyclopedia of Nanoscience and Nanotechnology" World Scientific publishers (in press).
- G. U. Kulkarni, P. J. Thomas and C. N. R. Rao, "Mesoscopic assembly and other properties of metal and semiconductor nanocrystals", in "Chemistry of Nanomaterials" Wiley-Vch (in press).

G20.11
P02